Durham E-Theses

The nature and origin of disky elliptical galaxies

McDermid, Richard Morgan

How to cite:

McDermid, Richard Morgan (2002) *The nature and origin of disky elliptical galaxies*, Durham theses, Durham University. Available at Durham E-Theses Online: http://etheses.dur.ac.uk/4179/

Use policy

The full-text may be used and/or reproduced, and given to third parties in any format or medium, without prior permission or charge, for personal research or study, educational, or not-for-profit purposes provided that:

- a full bibliographic reference is made to the original source
- a link is made to the metadata record in Durham E-Theses
- the full-text is not changed in any way

The full-text must not be sold in any format or medium without the formal permission of the copyright holders.

Please consult the full Durham E-Theses policy for further details.

Academic Support Office, Durham University, University Office, Old Elvet, Durham DH1 3HP
e-mail: e-theses.admin@dur.ac.uk Tel: +44 0191 334 6107
http://etheses.dur.ac.uk

The Nature and Origin of Disky Elliptical Galaxies

by
Richard Morgan McDermid

A thesis submitted to the University of Durham
in accordance with the regulations for
admittance to the Degree of Doctor of Philosophy

The copyright of this thesis rests with the author. No quotation from it should be published without his prior written consent and information derived from it should be acknowledged.

Department of Physics
University of Durham
December 2002

A copyright of this thesis rests with the author. No quotation from it should be published without his prior written consent and information derived from it should be acknowledged.

1 6 JAN 2004

" *'Forty-two,' said Deep Thought, with infinite majesty and calm.*"
Douglas Adams

The Nature and Origin of Disky Elliptical Galaxies

By Richard Morgan McDermid

Abstract

The observational trend that disky elliptical galaxies exhibit younger luminosity-weighted ages than boxy ellipticals is investigated. The presence of a possible young stellar disk embedded in these galaxies is explored by comparing kinematics derived from the near-infrared Calcium II triplet (around 8600 Å) and Hβ (4863 Å) Balmer line, thought to be sensitive to older and younger stars respectively. Using synthetic stellar population spectra of these two wavelength regions, it is found that a young disk component produces observable differences in the kinematics derived from the two wavelength regions. Specifically, very young disks produce differences in the Gauss-Hermite coefficients, h_3 and h_4. Disks with an intermediate age produce offsets in the rotation velocities. Older disks produce clear two-component structure in the derived LOSVDs. Thus, diagnostic indicators are established which can be applied to observations.

A comparison is presented of the major- and minor-axis kinematics derived from the Calcium II triplet and Hβ absorption features for a small sample of disky elliptical galaxies with enhanced Hβ absorption strength, indicative of a young component. For two galaxies in the sample, NGC 584 and NGC 821, Hβ gives a rotation velocity higher than that from the Calcium II triplet. These offsets are not consistent with the spectral models, since the offsets in velocity are not accompanied by the expected offsets in the other LOSVD parameters. This implies that the disks have either formed over time with a modest star-formation rate; or that the young stars in these systems are present in both the disk and spheroid components.

From dynamical modelling of ground-based integral-field spectroscopy combined with HST STIS data, the disky elliptical NGC 821 is found to have a mass-to-light ratio of $4.12\pm$ 0.06 in I-band solar units, and harbours a central black hole of mass $(3.41 \pm 0.68) \times 10^7 M_\odot$. This black hole mass is consistent with Gebhardt et al. (2002), who use the same STIS data with their independent modelling code. The phase-space distribution of the orbits in the model shows evidence for a two-component structure, which corresponds to a slowly rotating spheroidal component superimposed with a flattened, strongly rotating component. This second component, which has properties similar to a disk, accounts for 15% of the total system mass. Applying the two-component stellar population models, a disk of this mass would have formed 6 Gyr ago to produce the observed Hβ absorption. Such a disk is not consistent with the long-slit observations, as no offset was found between the Calcium II triplet and Hβ velocity dispersions. However, this cannot be strongly excluded due to the effects of metallicity and disk velocity dispersion on the spectral modelling.

Preface

The work described in this thesis was undertaken between October 1999 and December 2002 whilst the author was a research student under the supervision of Prof. Roger L. Davies in the Department of Physics, at the University of Durham. This work has not been submitted for any other degree at the University of Durham or at any other University.

The majority of the work contained in this thesis is the author's own. The ISIS long-slit data was observed by Harald Kuntschner in October 1997. The MIDAS implementation of the routine, FCQ, used to determine the long-slit kinematics was written by Ralf Bender and Roberto Saglia. The integral-field data of NGC 821 were obtained as part of the *SAURON* survey of nearby early-type galaxies. The three-integral Schwarzschild dynamical modelling code used was originally written by Roeland van der Marel and Nicolas Cretton, and later adapted by Ellen Verolme and Michele Cappellari to incorporate integral-field data. The Multi-Gaussian Expansion routine was written by Michele Cappellari.

Acknowledgements

It is a privilege to be able to thank my supervisor, Roger Davies, for his expert guidance throughout the course of my PhD; for always providing me with opportunities to grow, both as a scientist and as a person. It is also a great pleasure to thank my 'other' supervisor, Harald Kuntschner, for his friendship, for his endless patience during my first encounters with data, and for teaching me the true meaning of the word 'carefully'. I hope that even a small amount of your diligence, organisation and skilful eye for detail has rubbed off onto me. I must also thank my 'administrative' supervisor in Durham, Tom Shanks, for his assistance during the final stages of the submission of this thesis.

I am indebted to Tim de Zeeuw for his support and encouragement during the course of my PhD, for careful reading of this manuscript, and for his hospitality at the Sterrewacht on many occasions. To my other colleagues and friends in the *SAURON* team, especially Eric Emsellem, Ellen Verolme, Michele Cappellari and Davor Krajnovic; thank you all for your invaluable contributions to this thesis. Without your investment of time and effort in me, I could never have completed this work.

I thank Alex Vazdekis for many enlightening discussions on stellar populations, and for supplying the Calcium II triplet SSP models in advance of publication. Likewise, I thank Karl Gebhardt for supplying STIS data on NGC 821 in advance of publication, and for his hospitality in Austin. I must also express huge thanks to the computer support in Durham, specifically Alan Lotts, Andrew Hunter, Peter Draper and Nigel Metcalfe, without whom this thesis would never have been produced.

Life as a PhD student in Durham would just not have been the same without my crazy office mates, all of whom deserve some of the blame for the production of this document. Dave, thanks for introducing me to all things IDL, and for always knowing everything all the time. Fiona, thanks for the dancing lesson in my first week, which really put me at ease... Amaya, thanks for the ham & stamp sandwich, and Dajana, thanks for your endless supply of chocolate and good vibes just when required. To Kev, Dave W, Rowena and Claudio, you all deserve my thanks just for putting up with my music. Thanks to Cosmic Physics five-aside for encouraging extra-curricular activity, even against all odds. Thanks also to Peder, Chris and Graham for your valued friendship over the years, and for making it possible to escape the realm of the nebulae once in a while.

Thanks must go to my family, who have always indulged me in my academic pursuits with unquestioning trust and belief. I am deeply grateful to my father, for teaching me that the questions are more important than the answers; to my mother, for my inner strength; and to my sister, for being the biggest influence in my life. Sincere thanks must also go to Hans and Evelyn, for providing me with opportunity, for taking such an active interest in my life, and for teaching me that there's a world outside my window.

Above all, I thank Kirsten, for being a source of constant love, support, encouragement and sanity. Somehow you have tolerated me throughout all of this. I promise, I won't do it again.

Contents

Abstract ii

Preface iii

Acknowledgements iv

Contents vi

List of Figures ix

List of Tables xii

1 Introduction 1

1.1 Introduction . . . 1

1.2 Properties of Elliptical Galaxies . . . 2

1.2.1 Isophote Shapes of Elliptical Galaxies . . . 3

1.2.2 Kinematic Properties of Ellipticals . . . 4

1.2.3 Star Formation History of Elliptical Galaxies . . . 6

1.3 Thesis Aims . . . 8

1.3.1 Young Disks in Elliptical Galaxies . . . 8

1.3.2 Dynamical Modelling of Integral-Field Spectroscopy of NGC 821 . 9

2 Application of Stellar Population Models 10

2.1 Introduction . . . 10

2.2 High Resolution Synthetic SSP Spectra . . . 11

2.3 Creating Two-Component Models . . . 13

2.3.1 Limitations of the Models . . . 14

2.3.2 Constraining the Models . . . 14

2.3.3 Creating and Analysing the Model . . . 16

2.4 Trends from the Models . . . 18

2.4.1 Complete LOSVD Parameters . . . 18

2.4.2 Differences Between the Ca II Triplet and Hβ Mean Velocities . . 20

2.4.3 Differences Between Mg b and Hβ Mean Velocities . . . 22

2.4.4 Dependence on Metallicity . . . 24

2.4.5 Dependence on Disk Velocity Dispersion . . . 26

2.5 Conclusions . . . 30

3 Galaxy Kinematics **33**
3.1 Introduction . . . 33
3.2 Long-Slit Spectroscopic Data . . . 33
3.2.1 The Instrument . . . 33
3.2.2 The Sample . . . 34
3.2.3 The Observations . . . 35
3.2.4 Basic Data Reduction . . . 35
3.2.5 Rebinning to Logarithmic Wavelength Units . . . 40
3.3 Measuring Galaxy Kinematics . . . 41
3.3.1 The Fourier Correlation Quotient . . . 41
3.3.2 Parameterising the LOSVD . . . 41
3.3.3 Monte Carlo Simulations . . . 44
3.3.4 Stellar Template . . . 48
3.4 Correcting for Nebular Emission Lines . . . 52
3.4.1 Introduction . . . 52
3.4.2 Detecting the Emission Lines . . . 54
3.4.3 Modelling the Emission Lines . . . 57
3.4.4 Reliability of Emission Correction . . . 58
3.4.5 Emission in the Sample Galaxies . . . 60
3.4.6 Effect of Emission Removal on Hβ Kinematics . . . 66
3.4.7 Profiles of Emission Line Properties . . . 66
3.5 Comparison of Ca II Triplet and Hβ Kinematics . . . 70
3.5.1 NGC 3379 . . . 72
3.5.2 NGC 584 . . . 76
3.5.3 NGC 720 . . . 83
3.5.4 NGC 821 . . . 84
3.5.5 NGC 1700 . . . 92
3.5.6 Conclusions from the Observations . . . 93
3.6 Discussion . . . 96
3.6.1 Why Are no Differences Detected? . . . 96
3.6.2 Constraining the Formation Scenario . . . 97
3.7 Conclusions . . . 98

4 Dynamical Schwarzschild Modelling of NGC 821 **100**
4.1 Introduction . . . 100
4.2 *SAURON* Observations and Data Reduction . . . 102
4.2.1 The *SAURON* Project . . . 102
4.2.2 The *SAURON* Instrument . . . 103
4.2.3 Observations . . . 106
4.2.4 Data Reduction . . . 106
4.2.5 Comparison with Long-Slit Data . . . 113
4.2.6 Other Data Sets . . . 116

4.2.7 PSF Measurement 121
4.3 MGE Mass Model 123
4.3.1 The MGE Formalism 124
4.3.2 The MGE Fit 126
4.4 Schwarzschild Dynamical Model 130
4.4.1 Generating the Orbit Library 131
4.4.2 Generating the Observed Kinematic Parameters 132
4.4.3 Fitting the Observational Constraints 134
4.4.4 Regularisation 135
4.5 Determining the Best Fit Parameters 136
4.6 Properties of the Best-fit Model 143
4.6.1 Comparison with Observational Data 144
4.6.2 Rotational or Pressure Support? 144
4.6.3 The Distribution Function 151
4.6.4 Decomposition of Phase Space 156
4.6.5 Comparison With Other Decomposition Techniques 162
4.7 Conclusions 165
4.7.1 Determining the Best-Fit Model 165
4.7.2 Global Properties of the Best Fit Model 167
4.7.3 Integral-Space Distribution 168

5 Conclusions **170**
5.1 Young Disks in Elliptical Galaxies 170
5.2 Dynamical Modelling of NGC821 171
5.3 General Discussion and Conclusions 172
5.4 Future Work 173
5.4.1 The *SAURON* Survey and Other IFU Studies 173
5.4.2 Modelling Dynamics and Stellar Populations 174

List of Figures

1.1 Modified Hubble Tuning Fork Diagram 2
1.2 Boxy and Disky Isophotes from Simulations 4
2.1 Young Component Contributions 16
2.2 Creating a Two-Component Model 17
2.3 Differences Between Calcium II triplet and Hβ Kinematic Parameters . . 19
2.4 Differences Between Calcium II triplet and Hβ Mean Velocities 21
2.5 Difference Between Calcium II triplet and Hβ LOSVDs 22
2.6 Example of Mg b Region and Fit 24
2.7 Differences Between Mg b and Hβ Kinematic Parameters 25
2.8 Dependence on Metallicity of Young and Old Components 27
2.9 LOSVD with a Dynamically Hot Disk 28
2.10 Effect of a Dynamically Hot Disk 29
3.1 Sky Residuals on N 584 and N 1700 39
3.2 Gauss-Hermite Coefficients 43
3.3 Disk + Bulge Model LOSVD 43
3.4 Monte-Carlo Simulations of Calcium II triplet Region 49
3.5 Monte-Carlo Simulations of Hβ Region 50
3.6 Template Residuals 52
3.7 Absorption Line Model Fit to NGC 584 56
3.8 Effect of Emission Subtraction 58
3.9 Check of NNLS 59
3.10 Emission Residuals for NGC 3379 Major-Axis 61
3.11 Emission Residuals for NGC 3379 Minor-Axis 61
3.12 Emission Residuals for NGC 584 Major-Axis 62
3.13 Emission Residuals for NGC 584 Minor-Axis 62
3.14 Emission Residuals for NGC 720 Major-Axis 63
3.15 Emission Residuals for NGC 720 Minor-Axis 63
3.16 Emission Residuals for NGC 821 Major-Axis 64
3.17 Emission Residuals for NGC 821 Minor-Axis 64
3.18 Emission Residuals for NGC 1700 Major-Axis 65
3.19 Emission Residuals for NGC 1700 Minor-Axis 65
3.20 Emission Correction Comparison 67
3.21 Emission Correction LOSVD Comparison 67

3.22 Emission Correction Test 68
3.23 Gas Kinematics for NGC 584 70
3.24 HST Colour-Index Image of NGC 584 71
3.25 Gas Kinematics for NGC 3379 72
3.26 NGC 3379 Major-Axis 73
3.27 NGC 3379 Minor-Axis 74
3.28 NGC 584 Major-Axis 78
3.29 NGC 584 Minor-Axis 79
3.30 NGC 584 Major-Axis: Central Regions 80
3.31 NGC 584 LOSVDs at 2″ 81
3.32 Applying SSP Models to NGC 584 82
3.33 NGC 720 Major-Axis 85
3.34 NGC 720 Minor-Axis 86
3.35 NGC 821 Major-Axis 87
3.36 NGC 821 Minor-Axis 88
3.37 NGC 821 LOSVDs at 3″ 89
3.38 Applying SSP Models to NGC 821 91
3.39 NGC 1700 Major-Axis 94
3.40 NGC 1700 Minor-Axis 95
4.1 *SAURON* Instrument Mounted on the WHT 102
4.2 *SAURON* Optical Design 104
4.3 *SAURON* Lens Map 105
4.4 NGC 821 *SAURON* Mosaic 107
4.5 Reconstructed Image 108
4.6 Wavelength Range 110
4.7 Two-Dimensional Signal-To-Noise Binning 112
4.8 Template Fit to NGC 821 113
4.9 *SAURON* Kinematic Parameter Maps for NGC 821 114
4.10 Comparison with González 1993 Data 116
4.11 Comparison with ISIS Data 117
4.12 Imaging Data 118
4.13 STIS Kinematic Profile 121
4.14 *SAURON* PSF 122
4.15 STIS PSF 124
4.16 MGE Sector Profile 128
4.17 MGE Fit to HST and CTIO Images 129
4.18 Maximum Flattening of MGE 130
4.19 Optimal Error on the Mass Constraints 136
4.20 Best-fit Model with 1960 Orbits 141
4.21 Best-fit Model with 3920 Orbits 141
4.22 Best-fit Model with 7840 Orbits 142
4.23 Comparison with Gebhardt et al. 2002 143

4.24 Comparison of Best-fit Model with *SAURON* Maps 145
4.25 Comparison of Best-fit Model with Extracted Long-Slit 146
4.26 Comparison of *SAURON* LOSVDs with Model Velocity Histograms . . . 147
4.27 Model Fit to STIS Kinematics 148
4.28 Intrinsic v/σ of the Best-Fit Model 149
4.29 Comparison of v/σ of NGC 821 with M32 150
4.30 Integral-Space Distribution for NGC 821 152
4.31 Chi-Squared as a Function of Regularisation 153
4.32 Regularised Integral-Space Distribution for NGC 821 154
4.33 Orbital Trajectories from Integral-Space 155
4.34 Comparison of *SAURON* Kinematics with Fourier Expansion 157
4.35 Data-Model Comparison for Fourier-Expanded Kinematics 158
4.36 Comparison of Integral-Space Distribution with Fourier-Expanded Kinematics 159
4.37 Deblending Integral-Space Components 161
4.38 Separation of Two Integral-Space Components 162
4.39 Reconstructed Integral-Space Components 163
4.40 Locating the Disk with MGE 166
4.41 Removing the Diskiness in NGC 821 166

List of Tables

3.1 ISIS spectrograph configuration 34
3.2 Galaxy Sample and Observations Summary 34
3.3 Summary of Galaxy Observations 35
3.4 Summary of Standard Star Observations 36
3.5 Monte Carlo Simulation Results 48
3.6 Best-Fit Kinematic Templates 51
4.1 *SAURON* Instrumental Set-up 105
4.2 Imaging Data 118
4.3 STIS Configuration 120
4.4 STIS Measurements 121
4.5 *SAURON* and STIS PSF Models 123
4.6 MGE Parameters 127
4.7 Orbital Grids 132
4.8 MGE Parameters for 19 Gaussians 165

Chapter 1 | *Introduction*

1.1 Introduction

In an astronomical context, galaxies are generally considered to be the most fundamental building blocks from which the universe is composed. The galaxy in which the Earth resides, the Milky Way (also referred to here as simply, 'the Galaxy'), has enchanted humans for thousands of years. Yet it is only in the past one hundred years that we have come to fully appreciate the cosmological significance of this iridescent ribbon of stars which encircles the night sky. Given the contrast in appearance between the band of the Milky Way to the apparently small, faint, nebulous objects which we now know are galaxies outside our own; it is no surprise that astronomers took some time to realise the two were the same type of structure seen from vastly different perspectives. This realisation was a key step in mankind's understanding of the incredible vastness of the Universe, and what a truly minute portion of this he occupies.

Study of these external galaxies has yielded crucial insights as to how the universe formed. A water-shed of contemporary cosmology was the discovery by Hubble & Humason (1931) that external galaxies are, in general, moving away from the Milky Way at enormous speeds. Moreover, distant galaxies recede faster than those nearby: the Universe is expanding. This naturally implies that, at some stage in the past, all galaxies were much closer together. This prompted the now commonly known 'Big Bang' scenario, in which the Universe was created by a single event around 15 billion years ago. Of course, the Universe we see now did not come ready-made from the Big Bang. Over the lifetime of the Universe, stars, galaxies, clusters of galaxies, and even clusters of clusters of galaxies, have all somehow formed to give the cosmological snapshot we see today.

Hubble was also one of the first to realise that the zoo of galaxy types he observed seemed to follow some kind of evolutionary path: the so-called Hubble Sequence (Hubble 1936). Figure 1.1 shows a slight variation on Hubble's original scheme, proposed by Kormendy & Bender (1996). It was once thought that galaxies evolved along this sequence from left to right, beginning their lives as elliptical objects, and developing into grand spiral structures. For this reason, objects on the left part of the fork diagram (E/S0 galaxies) were termed 'early-type' galaxies, and those to the right 'late-type'. Further study has revealed that, in fact, the general evolutionary trend is in the opposite sense, with elliptical galaxies being amongst the oldest stellar systems in the Universe.

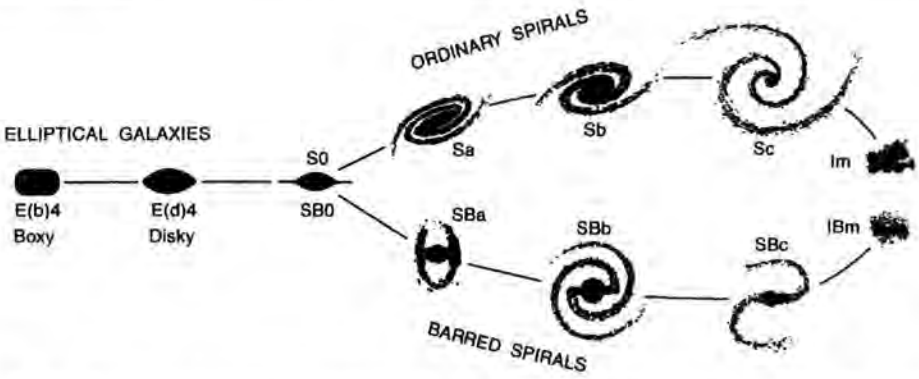

Figure 1.1: Revised 'Hubble tuning fork' diagram taken from Kormendy & Bender (1996): similar to Hubble's original proposed scheme (Hubble 1936), but with a distinction drawn between 'boxy' and 'disky' elliptical galaxies.

Determining the details of this seemingly simple progression between galaxies of different types is the principle aim of modern extra-galactic astronomy. Understanding this evolution, however, has implications which reach from the very creation of the Universe to its ultimate fate.

This thesis is concerned with objects which fall into the category of early-type objects, and more specifically, with 'disky elliptical' galaxies. In this introduction, a brief overview of the main characteristics of elliptical galaxies is given, as well as some consideration of the problems facing the current understanding of galaxy evolution. This Chapter concludes with a review of the thesis aims.

1.2 Properties of Elliptical Galaxies

Elliptical galaxies are conventionally perceived as being the simplest galactic systems; composed of a single component, dynamically simple, with a smooth and regular shape. They are relatively bright in the centre, but fade rapidly with increasing radius. They lack the dramatic features found in spirals, such as prominent disks and spiral structure; and contain little gas or dust. Consequently, there is little evidence for ongoing star formation, with no HII regions or young star clusters. Hubble & Humason (1931) first observed that elliptical galaxies are found to dominate the denser regions of the Universe, from rich clusters to small groups, with only a small fraction of isolated 'field' galaxies being ellipticals. This so-called 'Morphology-Density Relation' forms one of the key foundations in the understanding of galaxy evolution, and how galaxies interact with their environment (e.g., Dressler 1980).

This traditional view of elliptical galaxies being simple, quiescent objects began to change in the mid-1970s, when it became clear that, rather than being uncomplicated dynamical systems, elliptical galaxies exhibit a rich variety of shapes and internal dynamics. They are not, as Hubble had originally hypothesized, generally oblate, isotropic

rotators; but complex triaxial stellar systems. Thus it has become necessary to look at these objects more closely, and examine in fine detail their shape and structure which clearly hold essential information about their origin and evolution.

1.2.1 Isophote Shapes of Elliptical Galaxies

The elongation of isophotes of elliptical galaxies is characterised by their **ellipticity**, which also forms the basis of their morphological classification. Astronomers describe an isophote's ellipticity with the simple expression:

$$\epsilon = 1 - \frac{b}{a} \tag{1.1}$$

where a and b are the semi-major and semi-minor axes of the best-fitting ellipse respectively. Detailed surface photometry analysis of massive elliptical galaxies, however, has shown that their isophotes are, in general, *not* true ellipses (Peletier et al. 1990). These deviations from purely elliptical isophotes are not large, occurring at levels of at most a few percent. They are, however, significant and generally well determined.

We characterise the type of deviation, and hence the actual shape of the isophotes, by the terms **boxy** (thinner than an ellipse, with squarer ends), and **disky** (fatter than an ellipse, with more pointed ends). These terms can be quantified by expressing the fluctuations in intensity along the best-fitting ellipse as a Fourier series:

$$I(\phi) = I_0 + \sum_n A_n \sin n\phi + \sum_n B_n \cos n\phi \tag{1.2}$$

where $n \geq 3$. I is the intensity fluctuation, I_0 is the intensity of the best-fitting ellipse, ϕ is the angle measured from the major-axis of that ellipse, n is the order of the series, and A and B are coefficients describing the amplitude of the intensity deviations for a given order. In the case of axisymmetric isophotes, the most significant coefficient is B_4, with all other terms being generally smaller than the observational errors. We therefore define the dimensionless quantity $\mathsf{C4} = B_4/I_0$, which describes the 'diskiness' of the galaxy at a given position. If the isophote is disky, the C4 term will be positive; while a negative C4 value implies a boxy isophote. Although there is generally some radial dependence of this parameter, a single characteristic C4 value can be attributed to a galaxy as, for example, a luminosity-weighted mean of the complete profile (e.g., Bender et al. 1988).

The precise origin of these deviations is somewhat unclear, but many, seemingly unrelated, observed properties of elliptical galaxies are found to vary depending on the type and strength of the distortion. For example, disky galaxies are only weak sources of radio or X-ray emission, whereas boxy galaxies can be several orders of magnitude more powerful (Bender et al. 1989*a*).

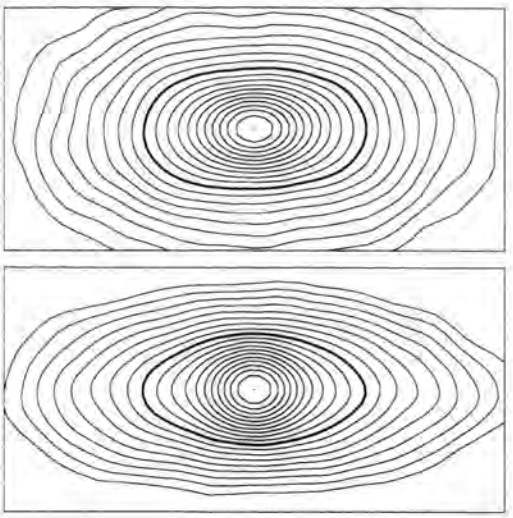

Figure 1.2: Representative isophotal contours of a simulated 1:1 merger remnant with boxy isophotes (upper panel) and a 3:1 merger remnant with disky isophotes (lower panel). The thick contour indicates the region where the C4 was determined. (Naab et al. 1999)

There is also a strong relation between the diskiness of a galaxy and its indicative rotation rate, $(v/\sigma)^*$ (see §1.2.2). Boxy galaxies show values of $(v/\sigma)^*$ which are much less than unity, implying that rotation is dynamically unimportant in these objects. Moreover, they often show significant rotation along the minor axis, indicative of triaxiality. For disky galaxies, $(v/\sigma)^*$ is generally close to unity, which, accompanied with negligible minor axis rotation, implies a rotationally supported object such as a disk.

This is supported by simulations of their formation scenarios. From disk-galaxy merger simulations (Naab et al. 1999, Bendo & Barnes 2000), it is found that equal-mass mergers lead to anisotropic, slowly rotating systems with preferentially boxy isophotes and significant minor axis rotation; whereas unequal-mass mergers result in rotationally supported ellipticals with disky isophotes and small minor axis rotation (Figure 1.2). It is clear, therefore, that isophote distortions hold important clues as to the nature and origin of elliptical galaxies.

1.2.2 Kinematic Properties of Ellipticals

Galaxy spectra are composed of the integrated light from many thousands of millions of stars, each with its own spectral characteristics and motion. The velocity of each star along the line-of-sight causes a Doppler shift in the stellar spectral lines. Because we observe the integrated light from many stars, with as many different velocities, spectral lines in the galaxy spectra appear to be broadened, simply because they are composed of many slightly shifted stellar features. By examining the *shape* of the absorption features,

we obtain information about the variation of stellar velocities present. This is called the Line-Of-Sight Velocity Distribution (LOSVD). For a population with isotropic motion, the profile shape will be close to that of a Gaussian function. Using this analogy, one can think of the mean velocity, v, as being the velocity at which the peak of the Gaussian occurs. From this we determine the rotation velocity relative to the systemic velocity. Also, the width of the Gaussian indicates the velocity dispersion, σ, which represents the random motions of the stars.

Rotation

It was once thought that elliptical galaxies were oblate isotropic rotators: systems flattened only by their rotation (e.g., Larson 1975). However, Bertola & Capaccioli (1975) and Illingworth (1977) found that the rotation of luminous ellipticals is not sufficient to explain the degree of flattening observed in these systems. We can quantify this by using the indicator $(v/\sigma)^*$ (where v is rotation velocity, and σ is velocity dispersion), defined as:

$$(v/\sigma)^* = \frac{(v/\sigma)}{(v/\sigma)_{\rm iso}} \tag{1.3}$$

where $(v/\sigma)_{\rm iso}$ is the value expected for oblate, rotationally flattened galaxies. A good approximation of $(v/\sigma)_{\rm iso}$ is:

$$(v/\sigma)_{\rm iso} = [\epsilon/(1-\epsilon)]^{1/2} \tag{1.4}$$

where ϵ is the ellipticity of the galaxy (Kormendy & Illingworth 1982). Bright ellipticals typically have a mean $(v/\sigma)^* \approx 0.4$, implying that they are supported by anisotropies in the velocity distribution. Conversely, Davies et al. (1983) found that intrinsically faint, low-luminosity ellipticals have $(v/\sigma)^* \approx 0.9$, and are flattened almost exclusively by their rotation.

Distinct Cores

Improvements in detector technology have allowed accurate measurements of the line-of-sight mean velocity and velocity dispersion with good spatial resolution. It has since been observed that elliptical galaxies exhibit a range of complex kinematic behaviour, contrasting with the long-standing view that ellipticals are dynamically simple. Most notable is the discovery of Kinematically Decoupled Cores (KDCs). It has been found that more than one-quarter of giant elliptical galaxies exhibit significant kinematic differences between their central regions and outer parts (e.g., Bender 1990), including counter-rotating components. Such features are often regarded as evidence of mergers (for a

review see Schweizer 1998), and such scenarios have been successfully simulated with resolved kinematics (Bendo & Barnes 2000).

The velocity dispersion profiles of these galaxies with distinct cores often do not appear unusual, although in some cases σ decreases towards the centre. Likewise the photometry generally gives no indication of any peculiarities, and no unusual colour gradients have been observed which distinguish these objects from ellipticals without a distinct core (Peletier et al. 1990, Carollo et al. 1997). With the advent of integral-field spectroscopy, it is possible to study in detail the properties of KDCs, as their spatial extent and orientation to the main body of the galaxy are well determined. Such studies (e.g., Davies et al. 2001) have shown that the stellar populations of KDCs can be both very similar to the rest of the galaxy, or show large contrasts. The connection between the dynamical properties of KDCs and their stellar populations is a crucial link to reveal the formation mechanisms involved.

1.2.3 Star Formation History of Elliptical Galaxies

Passive Evolution

Since the 1960's, with the work of Eggen et al. (1962), and the seminal papers of Larson (1975) and Toomre (1977), elliptical galaxies were widely believed to be old, coeval systems formed by dissipational collapse with a rapid, single burst of star formation around 15 Gyr ago, with little or no star formation since. Indeed, observational support of such a scenario remains considerable. For example, the well established **Colour-Magnitude Relation** (CMR) implies a physical link between the stellar populations of galaxies and their total stellar mass (e.g., Sandage & Visvanathan 1978, Larson et al. 1980). The widely accepted explanation of this appears to be the correlation of the stellar metal abundances and the total galaxy mass.

The principle empirical problem in testing this scenario is that the observational effects of a decrease in metallicity and a decrease in age are degenerate. Metal abundance variations are thought to be the more likely explanation because observations of the CMR in high-redshift clusters show a uniform shift towards bluer colours for galaxies of all magnitudes while maintaining a small scatter about the mean relation (Ellis et al. 1997, Kodama & Arimoto 1997, Stanford et al. 1997, Kodama et al. 1998). Hence the CMR has been interpreted as the result of an initial burst of star formation creating most of the stars in the galaxy, with passive evolution of the system thereafter; although Bower et al. (1998) found that some residual star formation would be consistent with the observed CMR scatter.

The tightness of the CMR for galaxies in clusters has been emphasised by Bower et al. (1992) as putting strong constraints on the possible spread in age amongst cluster ellipticals. Similarly the small spread in the relation found between the central Mg_2 line

strength and the central velocity dispersion, σ, in ellipticals (Bender et al. 1993, Ziegler & Bender 1997, Colless et al. 1999) has been interpreted as representing a range in combined age and metallicity (in the sense that the two are degenerate) of the order of 15% rms. Thus it would appear that many observations support the view that ellipticals are old, coeval, passively evolving systems with little or no recent star formation.

Late Star Formation in Ellipticals?

Since the late 1970's, there has been a growing body of evidence indicating that some elliptical galaxies have experienced recent star formation. Larson et al. (1980) showed that while cluster galaxies exhibit a tight CMR, those in the field show more scatter, which they attributed to late star formation in galaxies in low density environments. Similarly Schweizer et al. (1990), showed that galaxies with well-developed symptoms of past interactions, e.g., jets, shells, etc., have stronger Hβ absorption and weaker metal lines than those without. This is interpreted as the result of star formation in the disturbed objects. More evidence comes from the pivotal work of Butcher and Oemler (1978, 1984) who found that the fraction of blue galaxies in clusters of redshift $\sim$0.5 is much higher than it is at redshift zero; thus giving direct evidence that star formation in cluster environments continued until relatively recently.

In the past decade, a number of in-depth studies have attempted to model the spectral energy density of the integrated light of elliptical galaxies. These models are generally based on one or both of two principles: evolutionary and empirical population synthesis. One of the most popular models currently in use is that of Worthey (1994) which combines both techniques. By fitting a composite of stellar spectra from an extensive library to an observed galaxy spectrum, and assuming particular stellar isochrones, it is possible to model the spectral energy density of the object. This powerful technique is, however, prone to the same problems of degeneracy between the effects of age and metallicity as mentioned above, especially in luminous galaxies where the sensitivity of the measurements is reduced by the high velocity dispersions which broaden and blend absorption features. In order to break this degeneracy, spectral line-strength indices which are sensitive to age and not metallicity must be combined with indices which are sensitive to metallicity and not age. The problem then lies in determining which indices are most strongly dependent on one and not the other.

To this end, much work has been done, primarily through the creation of extensive spectral libraries such as that developed through the Lick/IDS project, a self-consistent collection of spectral observations compiled between 1972 and 1984 at the UCO/Lick Observatory. In his thesis, Worthey (1992) quantified the relative age and metallicity sensitivity of the different Lick/IDS line-strength indices, and found that, while many broadband colours were degenerate, certain lines were reliable indicators of either age or metallicity alone. Specifically, Hβ was found to be predominantly age-sensitive. A recently

published large sample of nearby early-type galaxies (Trager et al. 2000) indicates that luminous ellipticals span a wide range of Hβ absorption strengths over a small range in metallicity. Consequently, applying the models of Worthey (1994), this corresponds to a large range in *luminosity weighted* age, from older than 12 Gyr to as young as 2 Gyr. It is important to note that the luminosity-weighted average age does not represent the age of formation, or even the age of the last starburst. As young populations tend to be much more luminous, a small young population can dramatically influence these line strengths. This spread in Hβ absorption therefore suggests that some luminous elliptical galaxies contain a young component, and therefore have experienced recent star formation.

1.3 Thesis Aims

The general aim of this thesis is to explore the properties of disky elliptical galaxies in an attempt to understand their formation and evolution. This is carried out using a variety of observational and theoretical techniques, involving state-of-the-art data and models to explore the observational properties of these objects. This thesis divides roughly into two halves, which explore different aspects of disky elliptical galaxies.

1.3.1 Young Disks in Elliptical Galaxies

The first two chapters of this thesis are concerned with determining whether or not some disky elliptical galaxies harbour young, embedded stellar disks. De Jong & Davies (1997) found that galaxies with disky isophote distortions also tend to exhibit stronger Hβ absorption compared to their boxy counterparts. Applying stellar population models (e.g., Worthey 1994), this implies that disky galaxies tend to be younger than their boxy counterparts. This result was corroborated by Trager (1997) who, in his thesis, investigated the trend directly of luminosity-weighted age as a function of isophote diskiness. He found that, whereas boxy galaxies exhibit a wide range of ages, there is a paucity of old, disky ellipticals. This trend relates two seemingly independent observable properties of elliptical galaxies, and holds important information as to how the formation processes for boxy and disky ellipticals differ.

De Jong & Davies (1997) explain this trend as being due to the presence of an embedded stellar disk (giving rise to the disky isophotes) composed of a young stellar population (producing enhanced Hβ absorption). They find that the typical young, disky galaxy is consistent with a 2 Gyr old disk which contributes around 10% of the total galaxy mass, embedded in a 12 Gyr spheroidal component. This simple interpretation is able to reproduce the observed trend. However, it is somewhat indirect evidence for secondary star formation in embedded stellar disks housed in elliptical galaxies. It is an aim of this thesis to explore whether it is possible to directly measure the kinematics of different stellar

populations, and to apply this to determine the presence and nature of young disks in elliptical galaxies.

1.3.2 Dynamical Modelling of Integral-Field Spectroscopy of NGC 821

The second part of this thesis aims to explore the detailed dynamical properties of disky elliptical galaxies by applying general, three-integral axisymmetric dynamical modelling to an extensive two-dimensional kinematic data set from a panoramic integral-field spectrograph. Applying this powerful modelling technique to the unprecedented number of constraints supplied by integral-field spectroscopy allows many detailed aspects of the model to be studied which reveal the intrinsic structure of the galaxy in question.

The galaxy NGC 821 is a prime example of a disky elliptical, with strongly disky isophotes, and which appears to be consistent with axisymmetry, making it an ideal candidate for applying an axisymmetric dynamical model. The aim of this work is to construct a detailed dynamical model of this disky elliptical galaxy, and determine how the intrinsic dynamical properties relate to the disky nature of the galaxy's isophotes. More specifically, this work aims to determine if it is possible to distinguish the presence of a disk component in the orbital structure of this galaxy, and if so, to determine its physical characteristics, and gain insights as to how it has formed.

Chapter 2

Application of Stellar Population Models

2.1 Introduction

One of the principle aims of this thesis is to explore, in a direct manner, the relationships between the dynamical structure of disky elliptical galaxies and their stellar populations. The method employed is to use a specific spectral feature (which can be a single absorption line, or a set of lines) to derive kinematics which can then be related directly to the stellar populations most responsible for producing that feature. Untangling the mixture of kinematics and populations requires an understanding of how these two 'ingredients' affect the integrated spectral features we observe

Recent advances in the theoretical understanding of stellar structure and evolution, coupled with extensive stellar libraries using modern, high-quality observational data, have resulted in a variety of methods for predicting and quantifying the observational properties of stellar populations across a broad range of wavelengths. By using detailed models of the spectral energy distribution of stellar populations with different ages and metallicities, it is possible to test the hypothesis that kinematics derived using the Hβ and Ca II Triplet features are sensitive to different stellar populations. Furthermore, by creating composite populations with varying chemical and kinematic properties, it is possible to determine how sensitive this method is, allowing a more quantitative analysis of the observational results.

This chapter describes the application of single-age, single-metallicity stellar population (hereafter SSP) models to this analysis by creating composite models consisting of two different stellar populations with varying kinematic properties. These models are then analysed using the same method as for the observational data, allowing direct comparison between the model predictions and observational results. Section 2.2 provides background information on the SSP models being used. Section 2.3 describes how these SSP models were used to create two-component composite models, the choice of constraints, and the limitations of the models. Section 2.4 presents results from the analysis of the composite models, and Section 2.5 discusses the implications of these.

2.2 High Resolution Synthetic SSP Spectra

Population studies using broad band photometric colours found that the effect of an increase in the metallicity of a population was degenerate with that of an increase in age: the so-called **age-metallicity degeneracy** (e.g., Worthey 1994, Arimoto 1996). To have any hope of breaking this degeneracy, it is necessary to examine the galaxy spectra, and determine how different absorption lines behave with different population parameters.

To this end, several evolutionary stellar population synthesis models have been developed to predict the absorption line strengths of the integrated populations by using empirical fitting functions, which relate the stellar atmospheric parameters (effective temperature, $T_{\rm eff}$; surface gravity, $\log g$; and metallicity, $[{\rm Fe/H}] = \log({\rm Fe/H}) - \log({\rm Fe/H})_{\odot}$) with the measured index equivalent widths (e.g., Worthey 1994, Vazdekis et al. 1996). The stellar atmospheric parameters can come from either theoretical calculations of stellar atmospheres (as in e.g., Worthey 1994) or from an extensive empirical stellar spectral library (as in e.g., Vazdekis et al. 1996). Using a library of observed stellar spectra has the advantage that the atmospheric parameters are not dependent on imperfections in the adopted stellar structure theory. The limitations, however, come from the degree of completeness of the observed library, in terms of their coverage in spectral type, luminosity-class, and metallicity.

There are two sets of models used in this investigation, both based on extensive empirical stellar libraries. The models of Vazdekis (1999) are used to represent the spectral region around the Hβ feature at 4863 Å (the 'BLUE' models). For the near-IR Calcium II triplet, the recent models of Vazdekis et al. (2003) are used (the 'RED' models), which were kindly supplied by Alex Vazdekis in advance of publication. These models span the wavelength range 8350 - 9020 Å, centred around 8600 Å. Both sets of models are generated using the same principles, and are based on stellar libraries containing many of the same stars (although observed independently).

The BLUE models are based on the extensive stellar library of Jones (1998), which consists of over 680 stars observed with the same instrument, at high resolution (1.8 Å FWHM) and high signal-to-noise ratio (hereafter S/N), covering spectral types A - K and luminosity classes I-V in the metallicity range $-2.5 \leq [{\rm Fe/H}] \leq +0.5$, and O - M stars of near solar metallicity. The final synthetic spectra have the same resolution as the library, sampled at 0.6228 Å pixel^{-1}, corresponding to single-age populations of metallicities [Fe/H]= −0.7, −0.4, 0.0 and +0.2. For each metallicity, the models cover a range in ages from 1 to 17 Gyr, except for lower metallicities, which begin at 6 Gyr for [Fe/H]= −0.7 and 3 Gyr for [Fe/H]= −0.4 due to the limitations of the empirical library.

The RED models are based on a similarly extensive library of 706 stars, including significant overlap with previous studies of both the classic blue wavelength ranges (including all but three stars from the Lick/IDS Library: Burstein et al. 1984, Faber

et al. 1985, Burstein et al. 1986), and other Calcium II triplet studies (e.g., Diaz et al. 1989, Idiart et al. 1997). The library consists of high-quality data (S/N$\sim$ 100 Å^{-1} for field and open cluster stars, and S/N$\geq$ 15 Å^{-1} for globular cluster stars) observed at resolution comparable to the BLUE models (1.5 Å FWHM), covering a broad range of stellar types and atmospheric parameters (Cenarro et al. 2001). The resulting synthetic spectra are generated over the same age and metallicity range and intervals as the BLUE models, allowing direct use of the RED and BLUE models as parts of the same simple stellar population.

In general, the relative composition of elements heavier than helium in the models is close to solar, since the empirical approach implicitly includes the chemical enrichment history of the solar neighbourhood. More generally, detailed stellar libraries are intrinsically biased toward the stellar types available within our own galaxy (i.e., the old, metal-poor stars in globular cluster of the Galactic disk and halo, or the young, massive stars of the disk with solar or higher metallicities). This fact is important when applying the models to external galaxies, whose star formation histories may be significantly different to that of the Galaxy.

The understanding of the effects of non-solar abundance ratios on stellar populations has made significant advances in recent years (Weiss et al. 1995, Salaris & Weiss 1998, VandenBerg et al. 2000, Salasnich et al. 2000), with specific relevance to the 'α-enhancement' (where α refers to α-rich isotopes such as O, Mg, Si, Ca etc.) commonly observed in early-type galaxies, typified by the 'magnesium overabundance' (Faber 1973, Peletier & Valentijn 1989, Worthey et al. 1992, Henry & Worthey 1999). As Calcium is an α-element, the effects of non-solar abundance ratios may well be important to this work. However, the behaviour of the Calcium II triplet with respect to the classic α-enhancement indicators (e.g., Mg$\,b$) is not yet entirely clear (e.g., Peletier et al. 1999, Saglia et al. 2002).

The basic principle in constructing the population models is relatively straightforward. The stars living at the current epoch are composed of stellar populations with a mixture of ages and metallicities. It is instructive to decompose these stars into *single stellar populations* (SSPs), each having a single age and metallicity. These populations can then be used as building blocks to analyse composite populations.

To do this requires firstly theoretical isochrones which cover a similar range of metallicities as the stellar library. Each point on the isochrone represents a group of stars with known atmospheric parameters ($T_{\rm eff}$, log g, and [Fe/H]). A stellar spectrum is then selected from the grid of stellar observations (i.e., the spectral library) with matching parameters, and weighted using the assumed initial mass function (IMF: the relative number of newly-formed stars as a function of their initial mass). This is carried out along a number of points on a given isochrone, and the final spectrum, $SSP_\lambda(t,\ Z)$, corresponding to the SSP with age t, and metallicity Z, is given by integrating along the isochrone:

$$SSP_\lambda(t,\ Z) = \int_{m_l}^{m_u} S_\lambda(m,\ t,\ Z) F_{\lambda_{\rm ref}}(m,\ t,\ Z) N(m,\ t) dm, \tag{2.1}$$

where $S_\lambda(m,\ t,\ Z)$ is the observed spectrum corresponding to a star of mass m and metallicity Z that exists at the age assumed for the stellar population, t; $F_{\lambda_{\rm ref}}(m,\ t,\ Z)$ is the star's absolute flux at a certain reference wavelength, $\lambda_{\rm ref}$, used to scale S_λ; and $N(m,\ t)$ is the number of stars of this type, determined by the IMF (from Vazdekis 1999).

In this way, synthetic spectra of the SSPs are produced, allowing populations with different ages and different metallicities to be treated in the same manner as observational data. These synthetic spectra are produced both in the 'BLUE' region (4795 - 5465 Å) stretching from Hβ at 4863 Å to redder than Mg b at 5150 Å; and also in the 'RED' region (8350 - 9020 Å) around the Calcium II triplet centred around 8600 Å, at comparable resolutions (1.8 Å and 1.5 Å respectively).

2.3 Creating Two-Component Models

One of the main aims of this thesis is to explore the possibility that elliptical galaxies which exhibit disky isophotes and enhanced Hβ absorption do so because of the presence of a disk component composed of young stars. The observational approach to this is to compare the kinematics of such galaxies derived from absorption features which are thought to be sensitive to either old or young stars, chosen to be the Ca II triplet and Hβ respectively, and determine whether a disk component is more evident in one feature than another.

To test this technique, the SSP model spectra are used to create simple models of a young disk component superimposed on an old spheroidal population. This is done assuming some fractional contribution of each component to the total mass at a given radius, and applying some simple assumptions about the kinematics of the two populations, such that the final model is given by:

$$G_{D+S} = I_D S_{\lambda,D}(t_D,\ Z_D,\ v_D,\ \sigma_D) + I_S S_{\lambda,S}(t_S,\ Z_S,\ v_S,\ \sigma_S), \tag{2.2}$$

The subscript D or S in the above equation signifies the disk or spheroid component respectively; I is the fractional contribution *by mass* of the component (such that $I_D + I_S = 1$); and S_λ is the SSP synthetic spectrum of the component, with a given age, t (such that $t_D \leq t_S$), metallicity, Z, velocity, v, and velocity dispersion, σ.

SSP model spectra around both the Hβ region and the Ca II triplet region are combined in this way using the same parameters, effectively treating them as part of the same spectrum, and producing self-consistent two-component models in both wavelength

regions. In this way, the effects of varying the parameters (t, Z, v, σ) can be explored, and the results applied to the observations.

2.3.1 Limitations of the Models

The assumptions made in creating these two-component models are intentionally simplistic. The models are not designed to accurately recreate the dynamics and stellar populations of the data. They are used primarily to test whether it is possible to detect any kind of differences in the LOSVDs derived from these different spectral features, and how these differences relate to the intrinsic components. However, there are certain limitations to this approach which should be mentioned.

The components are consider to have solar metallicity. Based on the implication that the disk component in these galaxies formed at some later time to that of the spheroid, the metallicity of the two stellar populations is unlikely to be the same, solar or otherwise. Exploring a complete parameter space of metallicity for the two components, as well as age and kinematics, is very time consuming, and goes beyond the exploration of whether a young disk is visible by comparing the Hβ and Calcium II triplet kinematics. As a 'worst-case scenario', however, the case of a metal-rich young component superimposed on a metal-poor old component is discussed in §2.4.4.

The disk component is assumed to be edge-on, and primarily rotationally supported. It therefore has a low apparent velocity dispersion compared to the spheroid component, which has an impact on how easily the kinematic signatures of the disk and spheroid components can be separated. For simplicity, only one set of velocity dispersions is considered; specifically, the spheroid and disk have a dispersion of 200 $\mathrm{km\,s^{-1}}$ and 70 $\mathrm{km\,s^{-1}}$ respectively. The degree to which the results are dependent on the velocity dispersions is considered in §2.4.5, where a 'hot' disk is considered, with velocity dispersion of 110 $\mathrm{km\,s^{-1}}$, similar to the dispersion of the disk in NGC 821 determined by Scorza & Bender (1995).

Furthermore, it is assumed that the line-broadening due to the disk component is Gaussian in form. This is not true for an edge on disk, as the projection of the disk's rotation along the line of sight gives rise to an asymmetric LOSVD (Wagner et al. 1989). The effect is small, however (Bender 1990), and will not influence the results significantly.

2.3.2 Constraining the Models

Disky isophotes are thought to indicate the presence of a disk component superimposed on an oblate spheroid (e.g., Nieto et al. 1988, Bender et al. 1989*b*), although the inclination of the disk and the fractional contribution to the total light are not well constrained by the C4 parameter alone (Rix & White 1990). An underlying assumption in this investigation, however, is that the disks in these galaxies are near to edge on, and share the same

position angle as the main body of the galaxy. These are reasonable assumptions given the high apparent flattening of these objects (all are type E4 or higher), the negligible isophote twists within the radius of our kinematic measurements (Kuntschner 2003), and their generally strong major-axis rotation.

In order to create a two-component 'disk+spheroid' model, one must assume appropriate kinematics for the components. The conventional approach to this type of model is a low dispersion, high rotation velocity component (the disk) superimposed on a high dispersion, low rotation velocity component (the spheroid). The assumption that the disk is edge on implies that its apparent velocity dispersion is small (e.g., ≤ 100 km s^{-1}) and its rotation velocity, $v_{\rm disk}$, is close to the circular velocity, $v_{\rm circ}$, of the potential. Assuming the potential of an isothermal sphere, $v_{\rm disk} \approx v_{\rm circ} \approx \sqrt{2}\sigma$ (Binney & Tremaine 1987), which allows an estimate of the differences in rotation velocity and velocity dispersion that one can expect from a cold disk embedded in a pressure supported spheroid. The galaxies in this sample are luminous ($M_B \lesssim -20$), with typical velocity dispersions of around 200 km s^{-1}, giving a $v_{\rm disk} \approx 280$ km s^{-1}. Based on an oblate, isotropic rotator, the v/σ of an E4 galaxy is ≈ 0.8 (Binney & Merrifield 1998), implying a rotation velocity of ≈ 160 km s^{-1} for the spheroid. From these simple assumptions, one would expect a difference in rotation velocity of ~ 120 km s^{-1}. Davies et al. (1983) found that the typical v/σ for luminous ellipticals tends to be lower than that predicted by the isotropic, oblate spheroid model, implying that this velocity difference represents the lower limit of what may be expected.

In addition to having high C4 values, the galaxies in the sample were chosen to have enhanced Hβ absorption. Hence one would expect a representative model to display a similar strength of Hβ absorption. This allows the possible mass fractions of the young and the old populations to be constrained. For example, adding a 1 Gyr population to a 12 Gyr 'base' population, such that it contributes 1% of the total mass, results in the same measured *total* Hβ absorption strength (2.1 Å) as adding a 3 Gyr population to the same 12 Gyr population such that it represents 26% of the total mass. The mass fractions of the model components were established by trial and error; combining some fraction of young and old populations, and measuring the resulting Hβ line strength on the LICK system. This ensures that the combined Hβ line strength of models with different aged 'young' components remains the same.

Figure 2.1 shows the mass fractions of young components added to a 12 Gyr base population which produce a given combined Hβ absorption. The three values of Hβ which have been explored were chosen to be representative of the sample galaxies; namely Hβ= 2.11, 1.77 and 1.66 Å. The curves tend asymptotically to the age corresponding to the total Hβ strength, at which point, the disk population would account for 100% of the system mass: equivalent to the total luminosity-weighted age of the integrated system (denoted by the coloured vertical lines in Figure 2.1). Note that the ages given in this figure correspond to the ages given by the Vazdekis (1999) models, which are known to

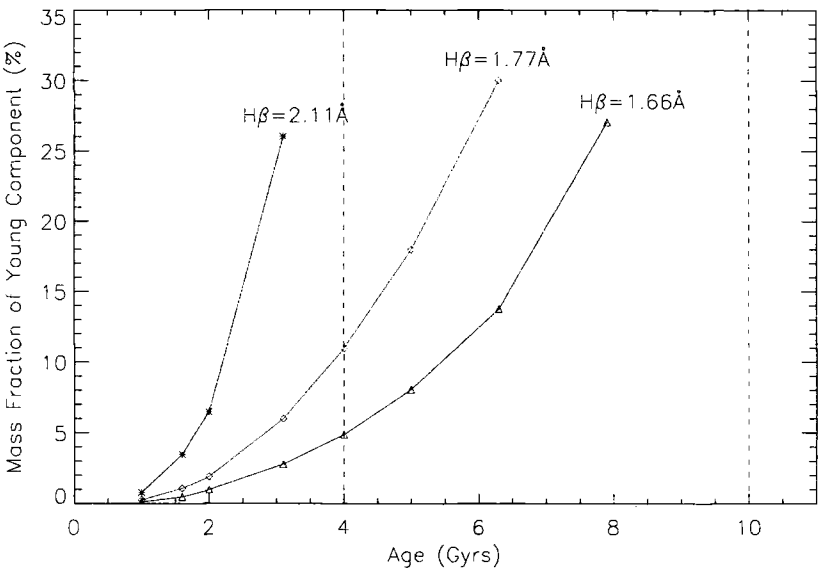

Figure 2.1: The required percentage of the total mass contributed by the young disk component, for different ages, which, when added to the 12 Gyr base population, results in the corresponding Hβ absorption strength. The coloured vertical lines represent the luminosity-weighted age corresponding to the given total Hβ absorption strength.

give systematically larger ages for the Hβ absorption strength than the González (1993) models (e.g., see Trager et al. 2000).

Mass fractions larger than $\sim$ 30% are not considered, as such massive thin disks are not supported by the photometry of these galaxies, given that the disk is only detectable by small-scale distortions in the isophotes. The mass fractions shown in Figure 2.1 are also applied to the SSP spectra of the Calcium II triplet using the same ages and metallicities as for the Hβ region.

2.3.3 Creating and Analysing the Model

The SSP model spectra are relatively fluxed, therefore the final model is created simply by weighting the young and old components by the corresponding mass fraction, and adding the two spectra together. Before the spectra are added, they are convolved with a Gaussian of the appropriate width to give the desired velocity dispersion, and shifted with respect to each other by some velocity in order to mimic the different rotation rates. Figure 2.2 gives a schematic representation of how the final composite model is produced. For this analysis, a velocity dispersion of 70 km s^{-1} is used for the disk component, and 200 km s^{-1} for the spheroid. The velocity difference between the two components was varied from 0 to 300 km s^{-1} in 10 km s^{-1} intervals, and the kinematics of the model were measured in both wavelength regions (RED and BLUE) at each step.

Kinematic analysis of the models was conducted following the same method used

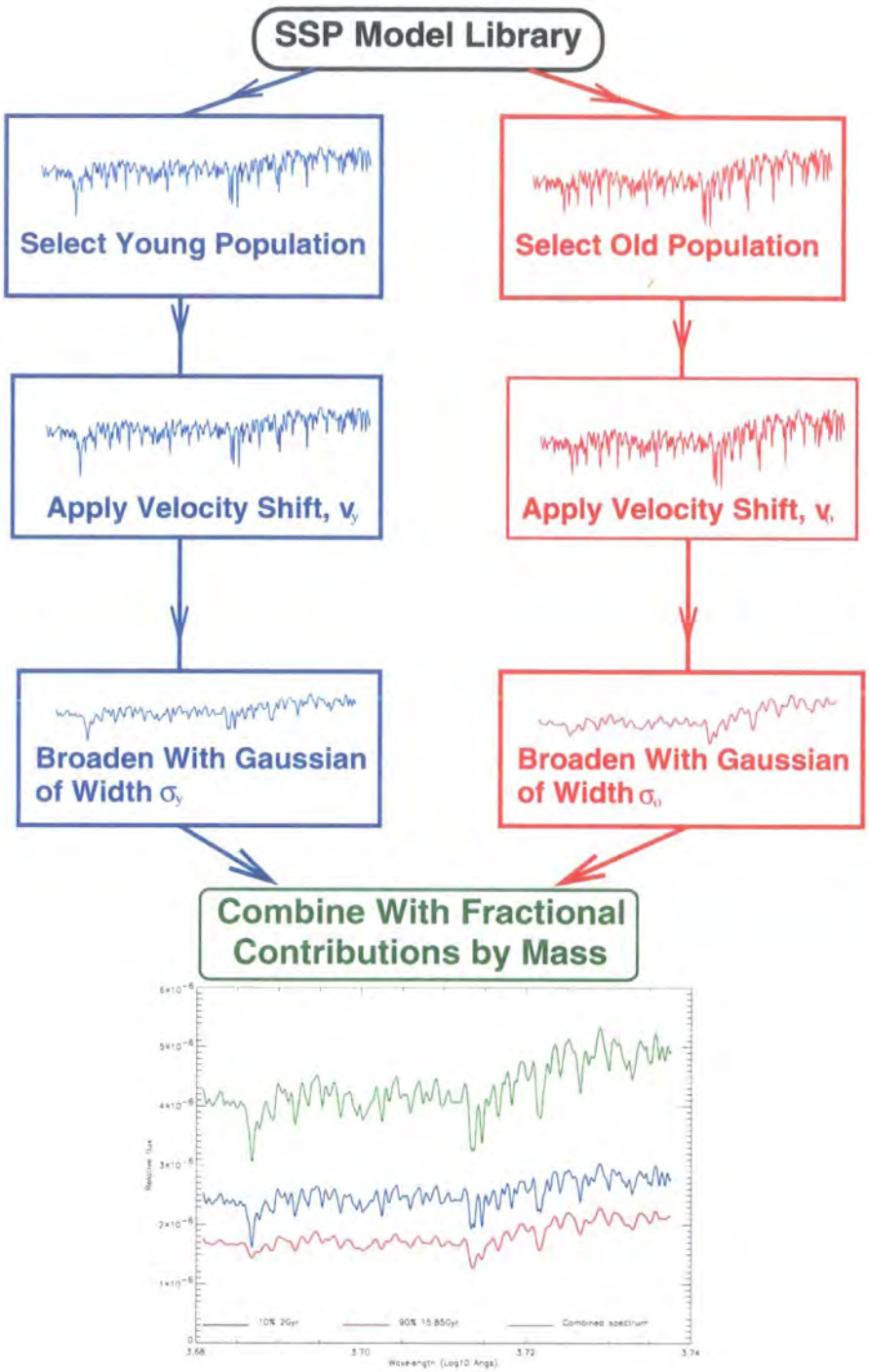

Figure 2.2: Schematic illustrating how SSP models are used to create a model spectrum of a galaxy with a young disk component superimposed on an old spheroidal population. An old and young population are selected from the library of SSP model spectra. Each is then shifted and broadened by an amount corresponding to the chosen kinematics. Both components are weighted by their relative mass fraction, and co-added to give the final model.

for the observations (see Chapter 3 for details). The Fourier Correlation Quotient (FCQ: Bender 1990) routine was used to determine the kinematic properties of the two-component models, with the velocity template 'stars' being chosen from the model library itself in order to minimize template mismatch effects. The templates which best represented the Hβ absorption line or Calcium II triplet lines of the models were used, and so generally templates of different ages were used to analyse the RED and the BLUE regions, even though they are essentially part of the same model.

2.4 Trends from the Models

2.4.1 Complete LOSVD Parameters

Figure 2.3 presents the differences between the LOSVD parameters, v, σ, h_3 and h_4, derived from the Calcium II triplet and Hβ, for the three values of integrated Hβ absorption being considered. The parameters are plotted for increasing velocity differences between the old spheroid and the young disk population, which is intended to represent the offset in velocity between a pressure supported spheroid and rotationally supported disk. The different colours correspond to models composed of different ages (and therefore mass fractions) of disk component added to the same 12 Gyr spheroid population.

The primary result of this simple modelling is that, for all of the models, there are measurable differences in the kinematics derived from the Ca II Triplet and Hβ features (i.e., for at least one of the four parameters, the difference between the Calcium II triplet- and Hβ-derived values is always larger than the typical measurement error). This implies that, in galaxies with properties similar to these models, comparing the kinematics derived from the Calcium II triplet and Hβ can reveal differences in the kinematic character of the young stars from the old, even for small mass fractions and moderate Hβ strengths.

As expected, the degree of difference observed in the kinematics depends on both the age and kinematics of the disk relative to the spheroid. However, it is not clear from the results given in Figure 2.3 exactly what the relationship is between the age or velocity of the disk, and the differences found in the LOSVD parameters. The parameter which seems to follow the most regular relationship with disk-age is the difference in mean velocity, $\bar{v}$, derived from the two spectral features. In order to understand how the intrinsic and 'observed' parameters are related, it is therefore instructive to consider only the behaviour of this one parameter. When comparing these model results with the observed kinematics presented in Chapter 3, however, one should keep in mind that, although more difficult to interpret, differences should also be found in the other LOSVD parameters.

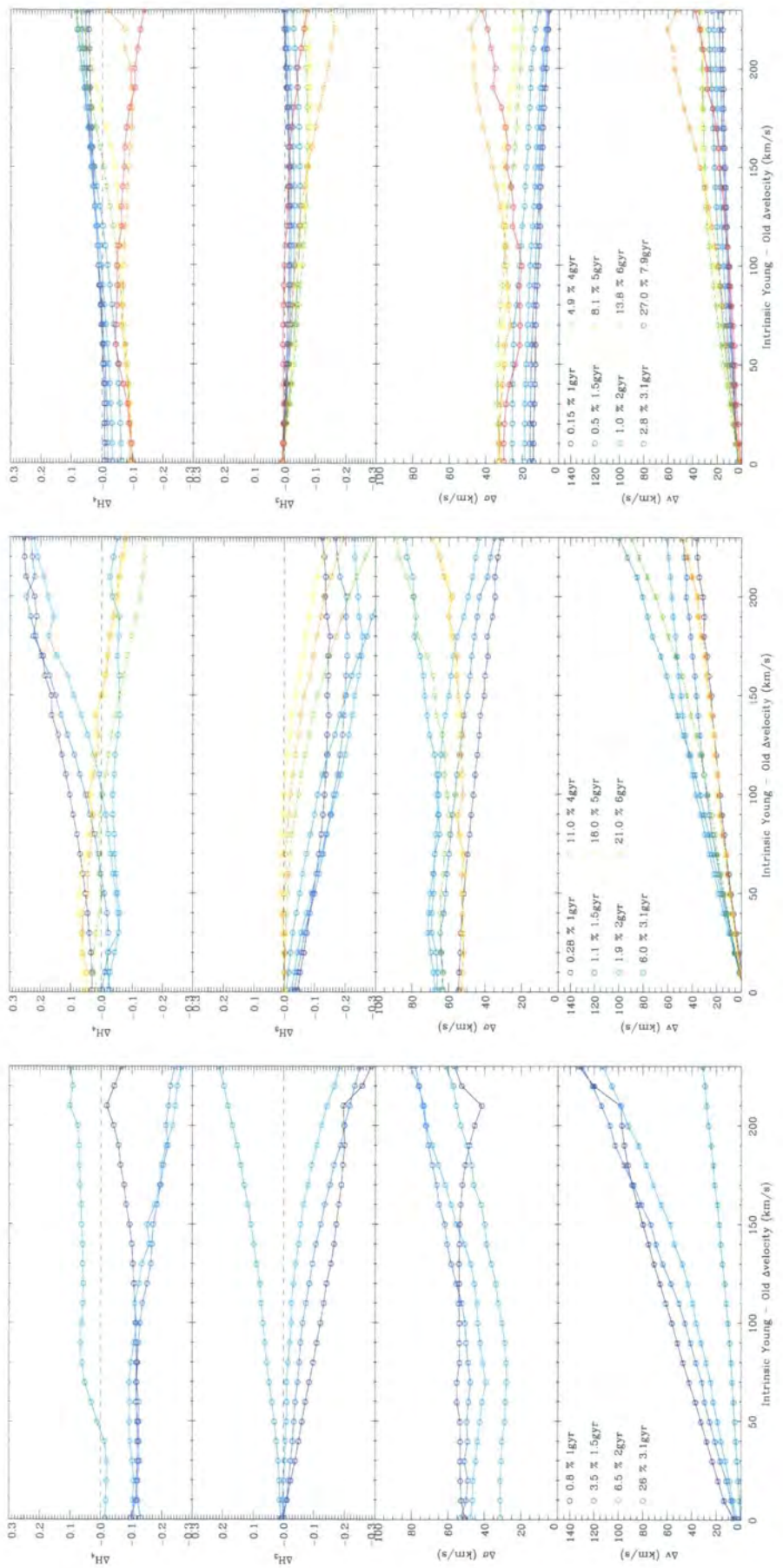

Figure 2.3: Comparison of LOSVD parameters measured using the Ca II Triplet ('RED') and Hβ ('BLUE') features for models with a total Hβ absorption strength of (a) 2.11 Å, (b) 1.77 Å and (c) 1.66 Å. Plotted are the recovered RED-BLUE parameter differences against the input intrinsic difference in velocity between the old spheroid and young disk components. Different symbols represent different mass fractions based on the total Hβ absorption strengths given in Figure 2.1. From these results, all the models plotted would show a measurable difference in at least one of the parameters for all values of the velocity offset between the disk and spheroid.

2.4.2 Differences Between the Ca II Triplet and Hβ Mean Velocities

Figure 2.4 gives results from the same models as Figure 2.3, but presents only the differences in mean velocity. Focusing on just this parameter illustrates more clearly the effect of superimposing different ages of young disk on the same old spheroid population. For example, to obtain an Hβ value of 2.11 Å, one can add a 26% by mass 3 Gyr population, or a 6.5% by mass 2 Gyr population to the 12 Gyr base population. The 3 Gyr disk component must be intrinsically rotating around 200 km s^{-1} faster than the old spheroidal population to produce a measurable difference (i.e., a difference larger than the typical measurement uncertainty) between the Hβ and Calcium II triplet velocities. The 2 Gyr disk, however, can be detected for an intrinsic difference of only 50 km s^{-1}. Applying the velocity difference based on the oblate, isotropic potential discussed in §2.3.2, a 2 Gyr disk rotating 120 km s^{-1} faster than the underlying 12 Gyr population would produce an observed difference between the Calcium II triplet and Hβ velocities of around 50 km s^{-1}. In this way we can place limits on the sensitivity to a given young population with certain kinematics, and, perhaps more importantly, determine the population ages and kinematics that may be present, but which *cannot* be detected using this technique.

Figure 2.4(a) shows that, for an Hβ equivalent width of 2.11 Å, the most easily detectable model is that which has the youngest disk component, with older disk components becoming less and less detectable. This is intuitively what one might expect, since for the youngest component, the spectra of the disk and spheroid are most different. However, Figures 2.4(b) and (c) show the youngest disks to be only as detectable as the oldest disks, whereas the intermediate-age disks (contributing $\sim 1-10\%$ of the mass) give the largest velocity differences. This can be understood by examining the LOSVDs themselves.

Figure 2.5 shows the LOSVDs for three different aged disks from the models in Figure 2.4(c), assuming an intrinsic disk-spheroid velocity difference of 150 km s^{-1}. The youngest disk (Figure 2.5, model a) has the lowest mass fraction, and also the lowest luminosity-weighted contribution to the total LOSVD. For this model, the difference between the Hβ and Ca II triplet LOSVDs shows up mainly in the *shape* of the LOSVDs, as opposed to their mean velocities, which are similar. As the disk becomes older (Figure 2.5, model b), its mass fraction must increase to maintain a constant Hβ absorption strength, and its relative contribution to the LOSVDs also increases. This is most prominent for the Hβ LOSVD, which develops a strong peak associated with the disk. This peak pulls the mean velocity of the Hβ LOSVD closer to the input disk velocity. The Ca II triplet LOSVD however only begins to show a distortion by the disk component, and its mean velocity remains close to that of the spheroid. For this model, the difference between the Hβ and Ca II triplet velocities is greatest. Finally, for the oldest disk (Figure 2.5, model c), the mass fraction is highest, and its luminosity weighted contribution begins to dominate both LOSVDs, making their mean velocities more similar, and the observed velocity difference becomes smaller.

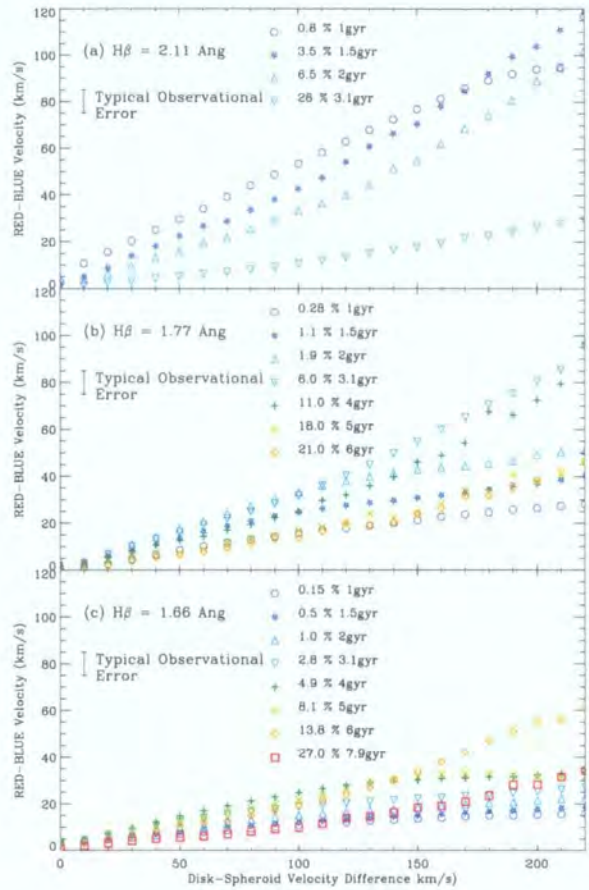

Figure 2.4: Comparison of velocities measured using the Ca II Triplet ('RED') and Hβ ('BLUE') features for models with a total Hβ absorption strength of (a) 2.11 Å, (b) 1.77 Å and (c) 1.66 Å. Plotted are the recovered |RED-BLUE| velocity differences against the input intrinsic difference in velocity between the old spheroid and young disk components. Different symbols represent different mass fractions based on the total Hβ absorption strengths given in Figure 2.1. Where the measured |RED-BLUE| velocity is larger than the typical measurement error (+/- 10 km s^{-1}, see Section 3.3.3), the young disk is detectable by comparing the RED and BLUE kinematics. From these results, all the models plotted would show a measurable difference in velocity if the young disk component is rotating more than 100 km s^{-1} faster than the old spheroid.

This explains why Figure 2.4 does not show a clear trend with age for all three total Hβ absorption strengths. The reason there is such a trend in Figure 2.4(a) is because the luminosity weighted contribution of the youngest disk component (0.8 % by mass of 1 Gyr) already dominates the Hβ LOSVD (equivalent to Figure 2.5, model b). Models with disks older than this produce LOSVDs tending to those of Figure 2.5 model (c), and so the measured velocity difference between the two LOSVDs decreases monotonically. If disks younger than 1 Gyr were to be considered for this Hβ strength, these disks would likewise become less visible, as in Figure 2.4(b) and (c).

By examining the LOSVDs derived from the two wavelength regions, one can understand what drives the trends shown in Figure 2.4. For most of the models considered, differences between the kinematics of the old and young populations are most obvious

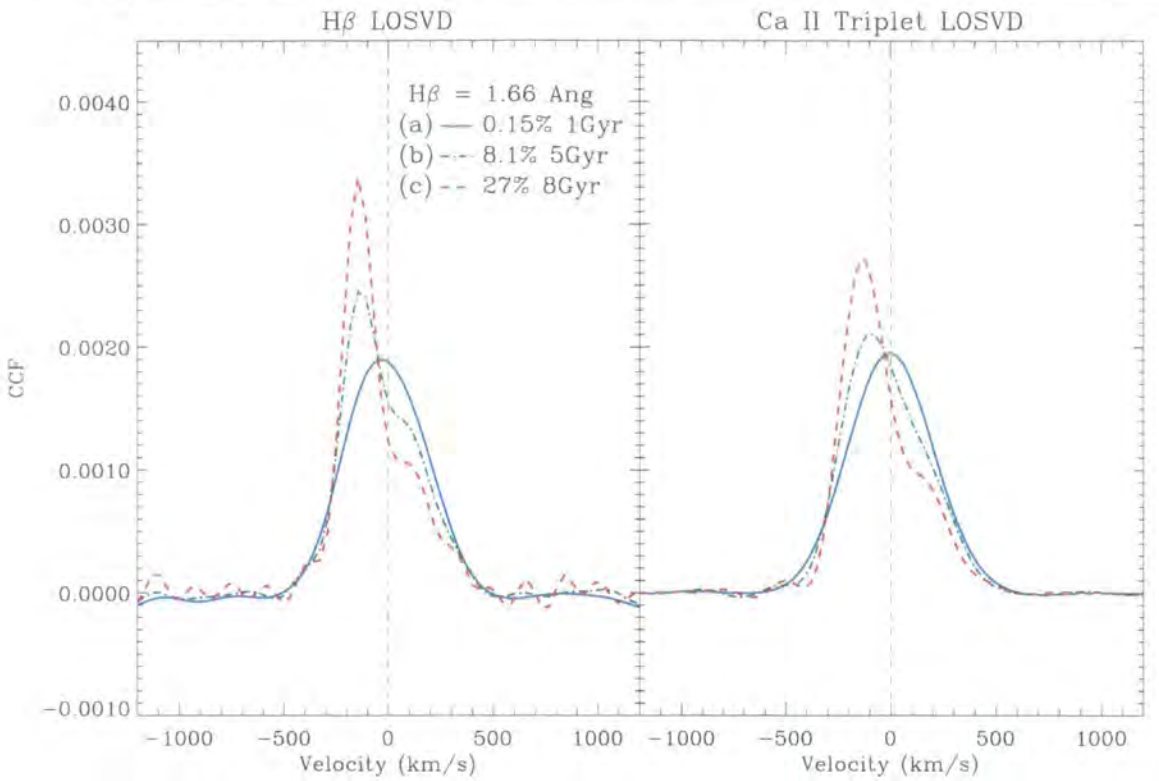

Figure 2.5: LOSVDs derived from the Hβ (left) and Ca II triplet (right) features for models with a total Hβ absorption of 1.66 Å (selected from Figure 2.4(c) with a velocity difference of 150 km s^{-1} between the young and old components). Note how the LOSVD shapes change as the age (and mass fraction) of the disk increases.

in the derived mean velocities. However, when no velocity difference is found, one must examine the LOSVDs themselves to detect either the small differences in shape caused by a very young, low mass fraction disk (evident in the higher-order h_3 and h_4 Gauss-Hermite parameters); or to detect the dominant signature of a low-dispersion peak due to an older, high mass-fraction disk.

2.4.3 Differences Between Mg b and Hβ Mean Velocities

So far, the investigation has been limited to comparing the kinematics derived from the Calcium II triplet and Hβ. This approach was adopted as it was hoped to provide the greatest sensitivity to the old and young populations respectively. Observationally, obtaining medium resolution spectra of these two spectral regions can, however, be costly in terms of observing time (requiring two sets of exposures on a galaxy for each wavelength region) or requires the use of a double-arm spectrograph. For this reason, it is worthwhile exploring whether there are alternative features which could be compared in the same way, but which are closer in wavelength.

Hβ is generally accepted to be one of the few absorption lines in the spectra of early-type galaxies which changes strongly as a function of age, but not of metallicity. The

models used in this investigation are composed of old and young populations with the *same* metallicity. Therefore differences in the kinematics derived from Hβ and the Calcium II triplet reflect specifically the different sensitivity of these two features to the *age* of the two populations.

There are currently no established age-sensitive features which lie near to (i.e., within a few hundred Ångströms of) the Calcium II triplet. Therefore, a feature or spectral region which is close to the Hβ feature, but which is not sensitive to young stars, should be investigated. A good candidate for such a region is that around the Mg b feature at 5175 Å. This region spans two features well known for their sensitivity to metallicity rather than age: Mg b itself and Fe5270. These two absorption features also tend to be prominent in the spectra of early-type galaxies, and should therefore provide a strong correlation peak when used with FCQ: essential for accurate kinematic measurements.

Figure 2.6 illustrates this wavelength region with a continuum-subtracted model and overplotted broadened template spectrum, which closely resembles the input 'galaxy' model. In practice, however, this region is prone to template-mismatching, as the abundance of magnesium compared to that of iron in luminous elliptical galaxies tends to be greater than that of the solar neighbourhood: the so-called 'magnesium overabundance' (e.g., Worthey et al. 1992, Weiss et al. 1995). Since only SSP models are considered here, this does not affect the analysis, as both 'galaxy' and 'template' spectra are drawn from a population with essentially the same metal content. For real observational data, however, using a template which well-represents this region of a galaxy's spectrum may be more difficult.

For simplicity, only the models with a total Hβ absorption of 2.11 Å are considered, as these resulted in the most apparent difference in kinematics derived from the Calcium II triplet and Hβ. If no differences are found for these models, then clearly there will be no differences for models with less total Hβ absorption.

Figure 2.7 presents the results of comparing the kinematics derived from Hβ and Mg b. This shows that there are differences, due to the different sensitivity of Hβ and the Mg b regions to the young component in the model. However, the resulting differences in mean velocity are not as large as those found using the Calcium II triplet, and differences in the higher-order parameters are likewise reduced compared to Figure 2.3.

Only the youngest disk can reliably be detected in the rotation velocity, although older components are apparent in the higher-order moments. This suggests that for disks which are much younger than the main body of the galaxy, it may be possible to detect differences between the Mg b and Hβ kinematics. However, for older disks, or galaxies with lower total Hβ absorption strengths, comparing these features is not as sensitive to the young disk component as comparing Hβ with the Calcium II triplet. Taking into account the effects of template mismatch, which plague kinematic measurements using the Mg b region, the conclusion is that using Mg b as a tracer of the old-component kinematics is

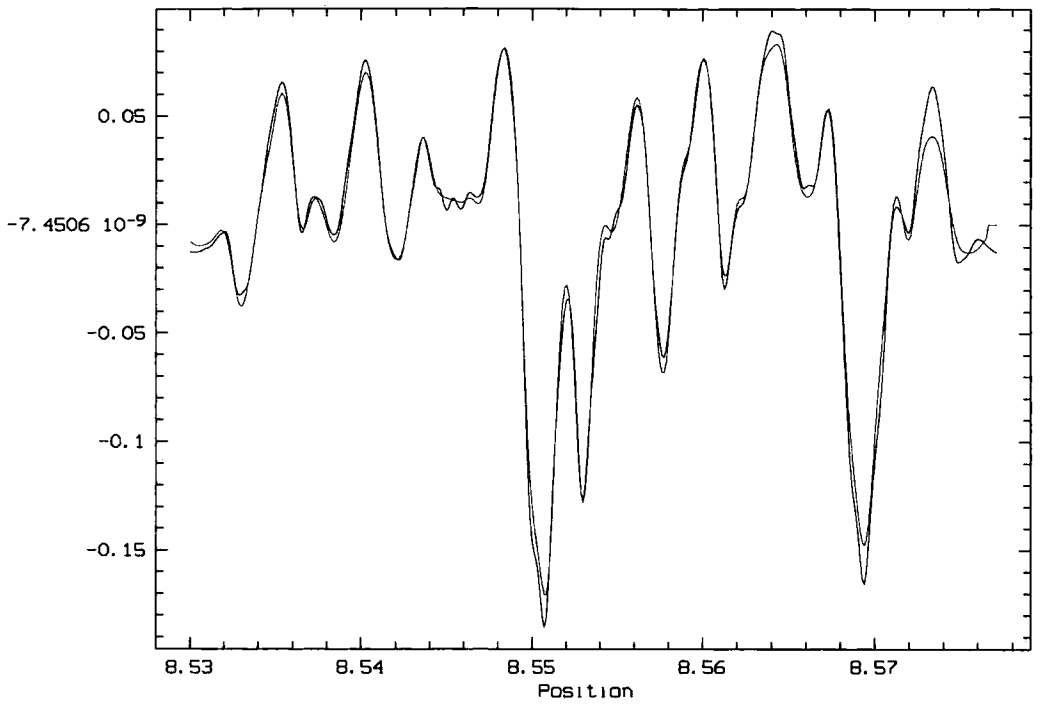

Figure 2.6: Example of the region around Mgb used to determine kinematics with which to compare with those from the Hβ feature. The composite model is shown (black line), overplotted with the broadened template spectrum (red line). Note that the quality of template-galaxy match here is difficult to achieve for real early-type galaxies due to the commonly observed 'magnesium overabundance' found in such galaxies.

less reliable than using the Calcium II triplet, although it may be useful where two very different populations are present.

2.4.4 Dependence on Metallicity

The principle results of this chapter are based on simple two-component models, where both the old spheroidal and young disk components have solar metallicity. It is known, and has already been discussed, that early-type galaxies do not generally exhibit solar metallicity. It is also unlikely that two components, formed at very different epochs, and possibly through different formation mechanisms, should have the same metal-enrichment.

For the purpose of detecting a young disk component embedded in an old population, perhaps the most significant metallicity effect is the age-metallicity degeneracy, implying that an increase in age has a similar effect on a stellar populations observable characteristics as an increase in metallicity. The Hβ feature is well known for its sensitivity to changes in age, and its insensitivity to changes in metallicity. The Calcium II triplet, however, is somewhat the opposite in character. Given this mixture of response to age and metallicity, it is instructive to investigate a simple example of a mixed-metallicity model.

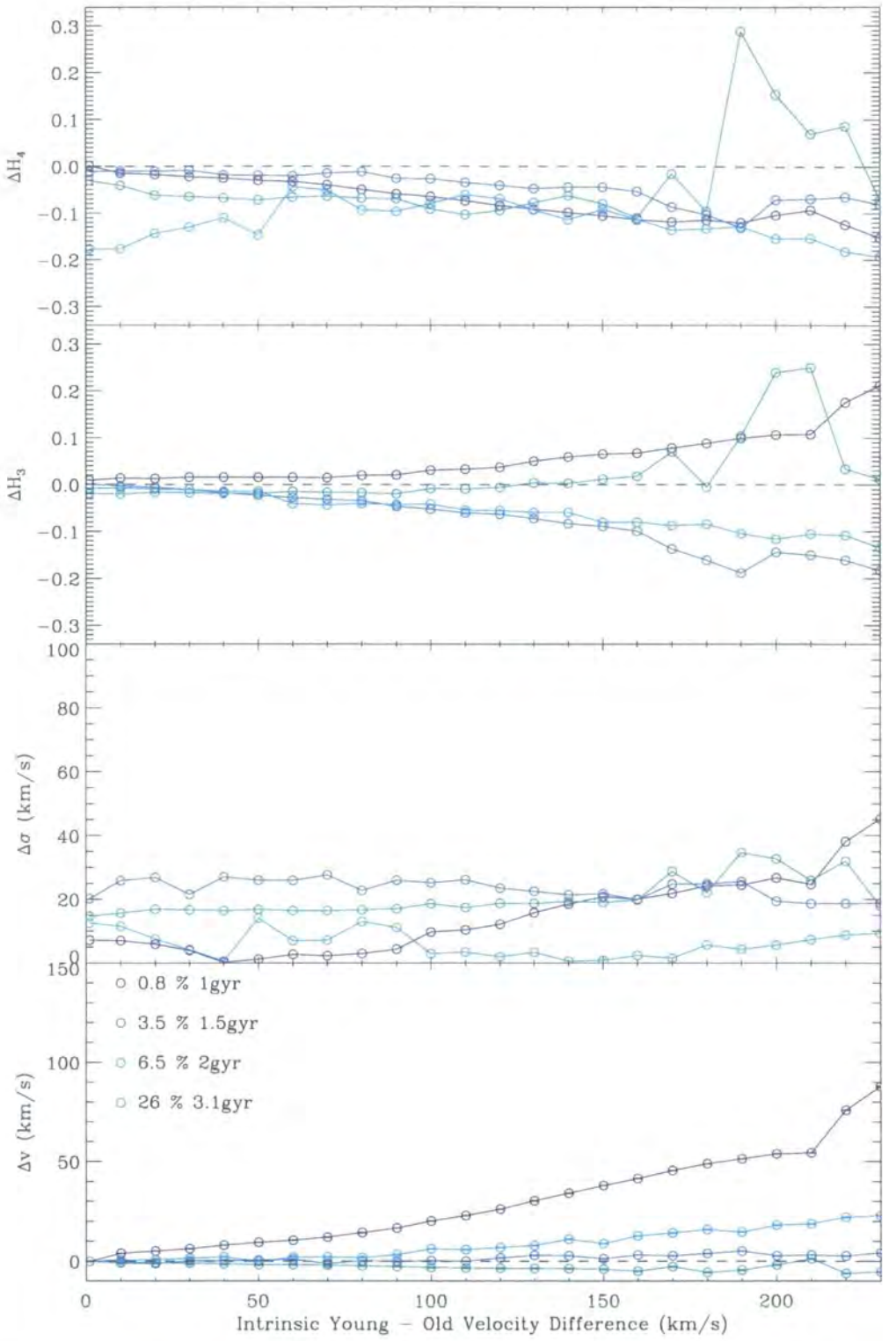

Figure 2.7: Determined differences between kinematic parameters derived using the Mg b region shown in Figure 2.6 and the Hβ absorption feature. There are differences found; however the size of these differences are much smaller than those found using the Calcium II triplet. The most reliably measured parameter is the mean velocity, which only shows a significant young disk signature for the youngest disk considered. This suggests that the Mg b region is only sensitive to components which are significantly younger than the rest of the galaxy in which it resides.

The most obvious case to determine how populations of different metallicity affect the detectability of a young component is to consider a metal-rich young disk population, superimposed with a metal-poor old spheroidal population. This scenario emphasises the effect of the age-metallicity degeneracy on the method of comparing the Calcium II triplet and Hβ kinematics. If the young disk component remains detectable within these models, then the effect of different metallicity components on the overall conclusions of this chapter should be small.

Figure 2.8 presents the differences between the kinematic parameters derived using the Calcium II triplet and Hβ, for models with a total Hβ absorption strength of 2.11 Å, using components of different (and non-solar) metallicities. The young disk component is metal-rich, having [Fe/H]= +0.2. The old spheroidal component, on the other hand, is metal-poor, with [Fe/H]= −0.7. This maximises the age-metallicity degeneracy effects on the kinematic differences determined, using the highest and lowest metallicity models available. As can be seen from Figure 2.8, there are still significant differences between the Calcium II triplet and Hβ kinematic parameters. The difference in mean velocity displays a similar trend as before, although here the gradient of the trend is around 2/3 less than that using solar metallicity components.

Therefore, metallicity effects *do* influence the degree of difference between the kinematics derived from the Calcium II triplet and Hβ features, making the technique less sensitive to underlying young components. However, there are still significant and measurable differences between the kinematic parameters, even in the case presented here with extreme metallicity differences. For models with lower total Hβ absorption strengths, the effect of metallicity will be more severe, pushing some young components which were just detected using solar metallicity components below the detection threshold. For galaxies with sufficiently strong Hβ, however, differences in the metallicity of the old and young components should not prevent a young disk component from being detected.

2.4.5 Dependence on Disk Velocity Dispersion

One of the key assumptions about the dynamics of the disk is that it is rotationally supported, and is viewed close to edge-on. This implies that the random motion in the disk is small, and the velocity dispersion of the disk along the line of sight is correspondingly narrow. This is in contrast to the spheroid component, which is assumed to be pressure-supported, and has a broad velocity dispersion. Since the two components have such different dispersions (the assumed values used for the velocity dispersion of the two components was 70 km s^{-1} for the disk, and 200 km s^{-1} for the spheroid), the disk contribution is more noticeable in the LOSVD. A disk which has a higher dynamical temperature (i.e., has more pressure support) will have a broader velocity dispersion, and its effect on the integrated LOSVD will be more subtle.

Figure 2.9 illustrates this by showing the components of the LOSVD for a cold (a) and

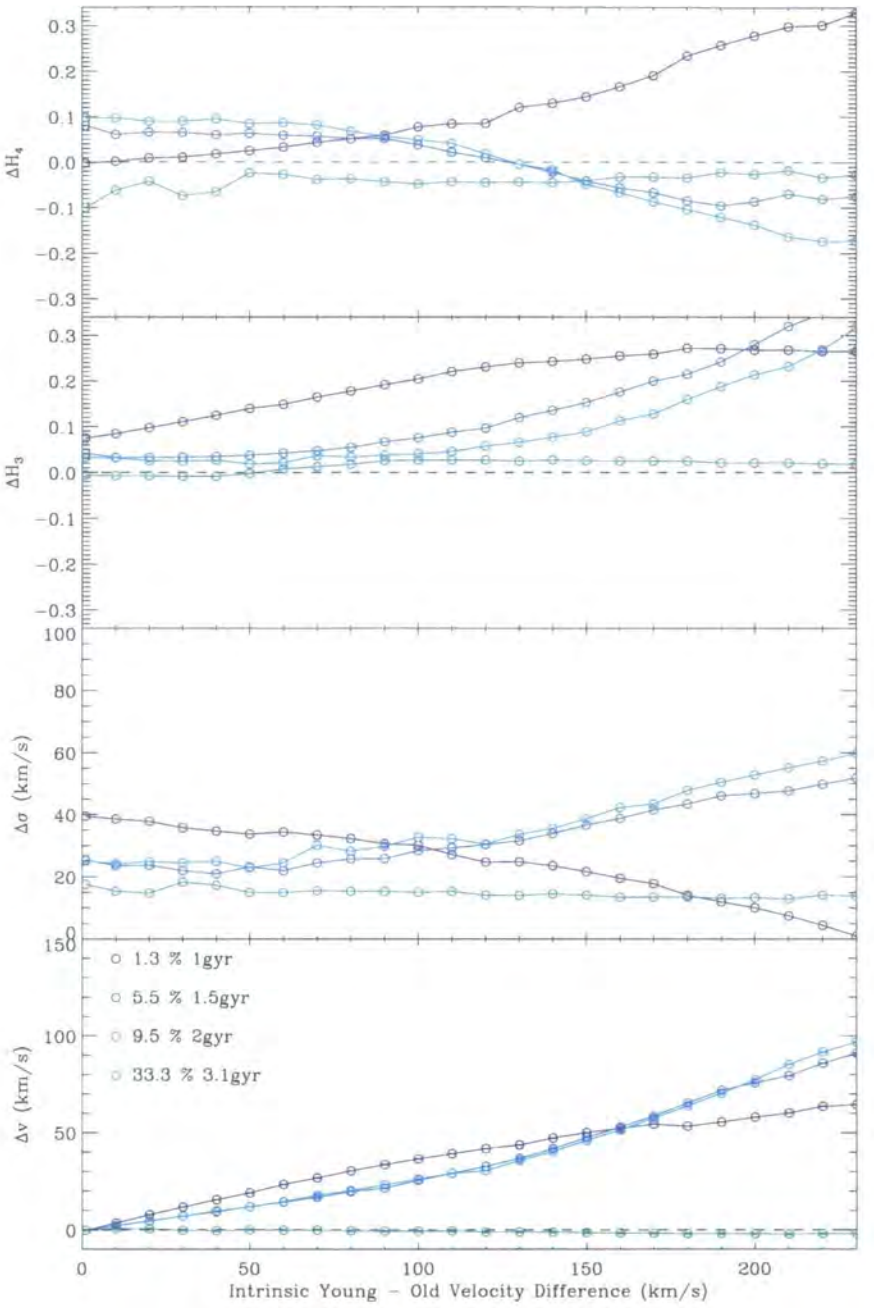

Figure 2.8: Determined differences between kinematic parameters derived using the Calcium II triplet and Hβ absorption features, for models with a total Hβ absorption strength of 2.11 Å. The young and old components have non-solar metallicities, such that the young population is metal-rich ([Fe/H]= +0.2) and the old population is metal-poor ([Fe/H]= −0.7). Such a configuration should maximise the effect of age-metallicity degeneracy on separating the kinematics of the old and young populations. There remain, however, significant and measurable differences between the Calcium II triplet and Hβ kinematics. The overall trends are very similar to those found using solar metallicity components (Figure 2.3), although the strength of the differences is somewhat diminished.

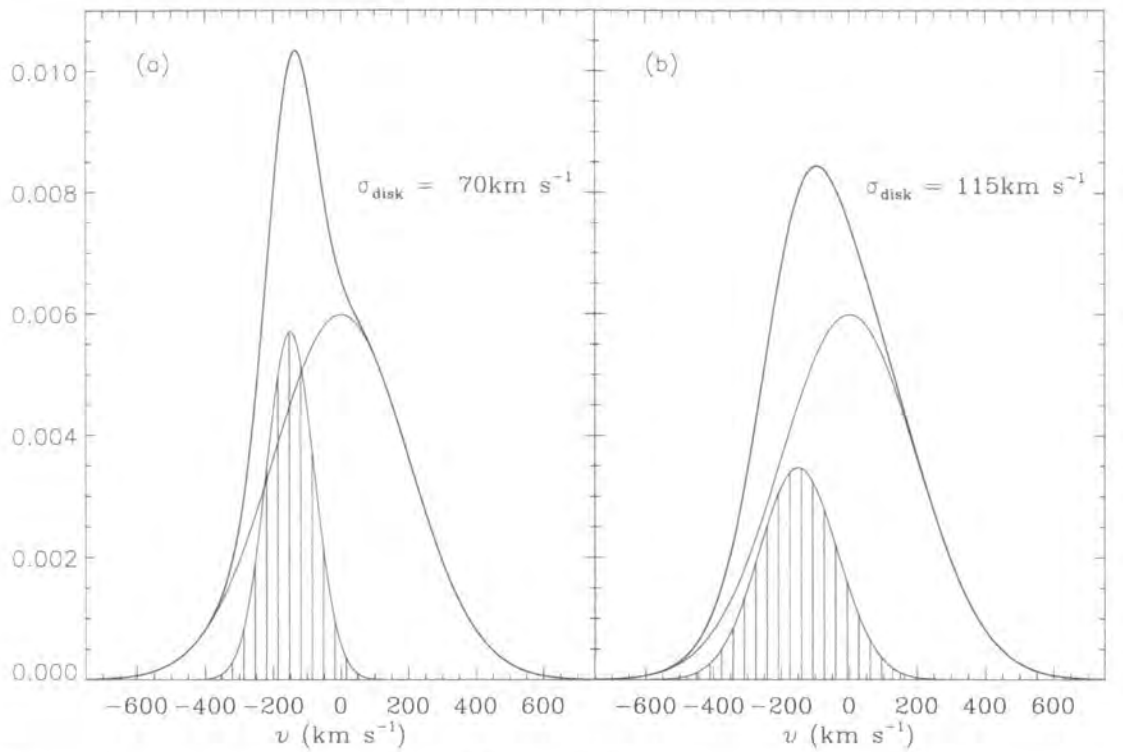

Figure 2.9: Comparison of simulated LOSVDs for a disk with velocity dispersion $\sigma_{\rm disk}$ = 70 km s^{-1} (a) and $\sigma_{\rm disk}$ = 110 km s^{-1}(b). The LOSVD of the disk component is denoted by the shaded Gaussian in each plot. The unshaded Gaussian represents the LOSVD of the spheroidal component ($\sigma_{\rm spheroid}$ = 200 km s^{-1}), and the thick solid line shows the combined LOSVD which would be observed. This demonstrates that a disk component with a low velocity dispersion results in a combined LOSVD which deviates more from a Gaussian, even though both disk components have the same integral.

hot (b) disk combined with the same broad spheroidal component. The cold disk gives rise to a distinct peak associated with the disk. The hotter disk has a more subtle effect on the total LOSVD, showing only as a slight deviation from a Gaussian. It is expected, therefore, that a hot disk will be more difficult to detect than a cold one. Consequently, the differences between the Calcium II triplet and Hβ kinematics may also be reduced, as the influence of the disk on the derived kinematic parameters becomes more subtle.

Observational evidence that the embedded disks in disky ellipticals can have appreciable pressure support comes from multi-component decomposition of the LOSVDs of such galaxies (e.g., Rix & White 1992). One example from the observational sample presented in this thesis, NGC 821, was studied in such a manner by Scorza & Bender (1995). They found that the disk component in this galaxy has a velocity dispersion of $\sim$ 110 km s^{-1}, and a peak rotation velocity of $\sim$ 150 km s^{-1}, giving a $(v/\sigma) \sim 1.4$. It is therefore instructive to construct similar models as before, but using a disk velocity dispersion of 110 km s^{-1}, as in NGC 821. This will illustrate how sensitive the resulting kinematic differences are to the degree of rotational support in the disk.

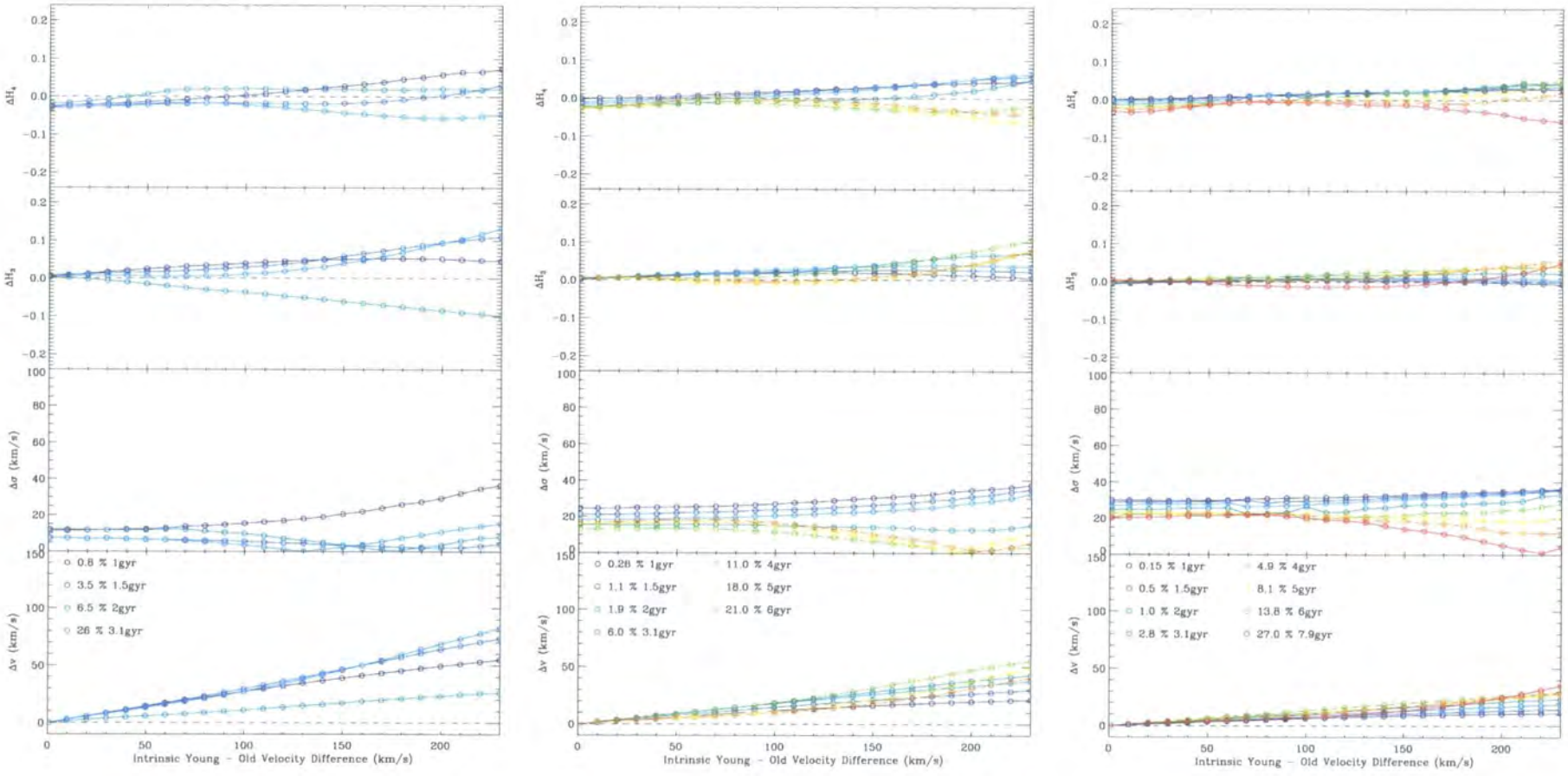

Figure 2.10: Same as Figure 2.3, but assuming a disk which is dynamically 'hot', having a velocity dispersion of 110 km s^{-1}(as was found for the disk in NGC 821 by Scorza & Bender (1995)). Note that the kinematic parameters derived from the two wavelength regions are more similar, and so the signature differences caused by the presence of a young, cold disk are less. This is especially evident for the model with the oldest total age (corresponding to Hβ= 1.66), where the differences between the parameters are close to the limit of the observational uncertainties.

Figure 2.10 presents the results for this test. All input parameters are the same as the models presented in Figure 2.3, except the velocity dispersion of the disk, which is now taken to be 110 $\mathrm{km\,s^{-1}}$ instead of 70 $\mathrm{km\,s^{-1}}$. It can be seen from this figure that the general effect is to reduce the amplitude of the differences observed between the Calcium II triplet and Hβ kinematics. The velocity differences (concluded to be a reliable first-order indicator of a young disk) show a similar trend to the previous results, but the gradient of the curves is reduced by a factor of ~ 2, meaning that a disk with the same rotation velocity, but with a velocity dispersion around 50% higher, will result in velocity differences about 50% lower.

More strongly affected are the h_3 and h_4 terms, which show significantly smaller differences for the hot disk models, especially where the Hβ absorption is relatively lower. This is due to the effect shown previously in Figure 2.9, that the two components of the LOSVD are more similar, and therefore their combined profile is generally less non-Gaussian for disks with the same velocity offset. The result of this is that the Gauss-Hermite terms cannot be used to put strong constraints on the presence of a young disk, especially where the total Hβ absorption strength is relatively low.

2.5 Conclusions

The purpose of this investigation was to determine whether different stellar populations in a galaxy, which have intrinsically different dynamical structure, can be detected by comparing the kinematics derived from the Calcium II triplet and Hβ absorption features. This was achievable through the use of state-of-the-art stellar population models spanning both the relevant features. These models not only predict colours and line-strengths, but provide actual synthetic spectra, which are extremely versatile, and can be analysed using the same techniques which are applied to observational data.

The specific scenario is that of a young disk embedded in an old spheroid: a situation for which there is observational support (de Jong & Davies 1997). The simplest approach to this problem is to assume a two-component galaxy: an old population in the form of a pressure-supported spheroid, combined with a single-burst young population in the form of a cold, rapidly rotating disk. If such a model yields no differences in the kinematics derived from the Calcium II triplet and Hβ features, then it is unlikely that a more contrived model, with e.g., a more complicated star formation history, will improve this situation, or place stronger constraints on observational results.

From observations of the galaxies in the sample, it is possible to place some constraints on the free parameters of the models, namely the kinematics of the two components, and their respective stellar populations. Three different composite stellar population scenarios were considered, spanning the range of integrated luminosity-weighted ages found the observational sample (Chapter 3). For each of these, disk populations of different ages were

investigated, and were found to give similar trends between the three different scenarios; however the absolute 'strength' of the disk signatures were found to vary considerably for different models.

From consideration of a young, dynamically cold disk embedded in an old, dynamically hot spheroid, there were generally found to be three indicators of the young disk:

1. For very young disks which contribute less than a few percent of the total system mass, the young disk is evident through small offsets in the Gauss-Hermite coefficients, h_3 and h_4.

2. For disks constituting between $\sim 2 - 10\%$ of the total mass, with a luminosity-weighted age of between $\sim 25 - 50\%$ of the total system age, the young disk component is most evident through differences in the rotation velocity derived from the Calcium II triplet and Hβ, in that Hβ shows a higher rotation velocity than the Calcium II triplet. Note that offsets for these models also exist in the Gauss-Hermite terms, but the velocity represents the lowest-order moment of the LOSVD, and can be more easily and securely measured.

3. For older disks, with ages greater than half that of the total luminosity-weighted age of the galaxy and mass fractions greater than $\sim 10\%$, the LOSVD parameters show only small differences. For these models, the disk is most evident by looking at the LOSVDs themselves, as it is dominated by the strong, narrow peak component of the disk, and shows clear two-component structure.

These indicators can be applied to observations as a diagnostic to constrain the possible presence of a young disk. These diagnostics also provide a means of quantifying upper or lower limits on the disk properties, such as its fractional mass contribution, age, and kinematic character.

The possibility of using absorption features less separated in wavelength (and therefore easier to observe) was also explored. The possibility of comparing Hβ kinematics with those derived from the nearby Mg b region was tested using the same models used for the Calcium II triplet investigation. Differences were found, but only for the case of a very young disk. The use of the Mg b region for real galaxies is further complicated by template mismatch problems due to the non-solar abundance ratios, or α-enhancement, often observed in early-type galaxies. The general conclusion is that, in extreme cases, a young disk can give rise to differences between kinematics derived from Hβ and Mg b. However, this technique is far less sensitive to such a component than comparing Hβ and Calcium II triplet kinematics.

Some consideration was given to the dependence of these results on the simplifying assumptions made in creating the models. Specifically, using disk and spheroid components with different, non-solar metallicities was considered. The test-case was that of

a metal-poor old component combined with a metal-rich young disk. Such a scenario emphasises the possible effects of the age-metallicity degeneracy. It was found that for such a scenario, the observed differences in the kinematic parameters are reduced. However, there are still significant and measurable differences, which implies that metallicity differences between the two components is a second-order effect.

The other assumption tested was that of the velocity dispersion of the disk. The disk is assumed to be rotationally supported, with a small velocity dispersion (taken to be 70 $\mathrm{km\,s^{-1}}$). For the disky galaxy NGC 821 (part of the observational sample of this thesis), Scorza & Bender (1995) found that the embedded stellar disk has a velocity dispersion of around 110 $\mathrm{km\,s^{-1}}$. The dependence of the model results on the assumed dispersion of the disk was investigated. As expected, for a disk with a higher dynamical temperature, the signature of the disk is more difficult to 'untangle' from that of the spheroid, as the shape of their intrinsic LOSVDs becomes more similar. Therefore, young disks are more difficult to detect if they are dynamically hot.

The overall conclusion to this chapter is that, by comparing the kinematics derived from the Calcium II triplet and Hβ absorption features, it is possible to detect the presence of a disk which is composed of young stars, as its kinematic signature (strong rotation, low velocity dispersion) is more evident in the Hβ kinematics than those from the Calcium II triplet. By comparing observations with the results from this modelling, it should be possible to constrain the possible presence of a young disk, and gain an insight as to how these disky galaxies form, and why they tend to show lower luminosity-weighted ages than their boxy counterparts.

Chapter 3 | *Galaxy Kinematics*

3.1 Introduction

From the application of stellar population models in Chapter 2, it was found that, for dynamically cold disks embedded in dynamically hot spheroids, using the Hβ and Calcium II triplet absorptions features can reveal differences in the stellar populations of the two components. Motivated by this finding, this chapter present an observational investigation of a small sample of disky elliptical galaxies which also show evidence of a young stellar population, indicating that they are ideal candidates for exploring the link between their dynamical structure and there stellar populations.

This chapter is arranged as follows: Section 3.2 summarizes the observations and the data reduction procedure. Section 3.3 describes the technique employed in this thesis to derive the galaxy kinematics from the observations. Section 3.4 describes the procedure for removing emission lines from the galaxy spectra, and presents gas kinematics for galaxies in the sample with strong emission features. Section 3.5 presents a comparison of the stellar kinematics derived from the Hβ and Calcium II triplet features, Section 3.6 presents a discussion of these results, and Section 3.7 concludes.

3.2 Long-Slit Spectroscopic Data

3.2.1 The Instrument

The long-slit spectra presented here were obtained using the ISIS spectrograph (Clegg 1992) mounted on the Cassegrain focus of the 4.2 m William Herschel Telescope (WHT) at the Observatorio del Roque de los Muchachos on La Palma, Canary Islands. This spectrograph was chosen due to its 'double-arm design, allowing two different wavelength regions, 'RED' and 'BLUE', to be observed at the same time. In this way, the Calcium II triplet (RED) and Hβ (BLUE) regions could be simultaneously observed at moderately high spectral resolution (< 1 Å pixel^{-1}), making efficient use of telescope time and minimizing instrumental and seeing differences between the two wavelength regions. The details of the instrumental parameters which were used are given in Table 3.1.

Arm	RED	BLUE
λ Range	8150 - 8950 Å	3800 - 5320 Å
Grating	600g/mm	600g/mm
Dispersion	0.79 Å pixel^{-1}	0.5 Å pixel^{-1}
Resolution	1.8 Å(FWHM)	2.0 Å(FWHM)
Spatial Scale	0.″36 pixel^{-1}	0.″22 pixel^{-1}
Detector	Tek1K	Loral2K
Gain	1.2 e^-/ADU	0.75 e^-/ADU
Read Noise	4.4 e^-	7.5 e^-

Table 3.1: ISIS configuration used for these data, based on a 1″ slit-width. The headings RED and BLUE refer to the settings used for the Calcium II triplet and Hβ wavelength regions respectively.

Name	Type	B_T	$< SB_e >$	σ_0	cz	Hβ	C4
(1)	(2)	(3)	(4)	(5)	(6)	(7)	(8)
NGC 584	E4	11.44	20.4	210	1802	2.08	2.2
NGC 720	E5	11.16	21.0	273	1745	1.77	0.84
NGC 821	E6	11.67	22.2	209	1735	1.66	3.1
NGC 1700	E4	12.20	21.2	234	3915	2.11	1.2
NGC 3379	E1	10.24	20.2	205	911	1.62	0.0

Table 3.2: Details of galaxy sample and observations. (1): Galaxy name, given from the New Galaxy Catalogue. (2),(3) and (4): Morphological classification, total B-band luminosity and effective surface brightness (de Vaucouleurs et al. 1991). (5) and (6): Central velocity dispersion and recession velocity in km s^{-1} (Smith et al. 2001). (7): Central (R_e/8) Hβ line index strength in Å (Trager et al. 2000). (8): Maximum C4 value from the data of Kuntschner (2003).

3.2.2 The Sample

The candidate galaxies in the sample were chosen as they exhibit enhanced Hβ absorption, and disky isophote distortions. They were selected from the González (1993) sample of elliptical galaxies with C4 > 0.5 and H$\beta \gtrsim 1.8$ Å, and hence are ideal candidates for testing the hypothesis that the diskiness of these galaxies can be attributed to a young disk component. The 'genuine' elliptical galaxy NGC 3379 was observed as it has purely elliptical isophotes and moderately weak Hβ absorption, and will be used as a 'control' galaxy to test the significance of any potential detections in the other galaxies. The whole sample has been chosen to be at approximately the same redshift, which enabled the relevant spectral features to be observed without altering the instrumental configuration. The velocity dispersions and surface brightness are appropriate for obtaining spatially resolved and accurate measurements across each galaxy. The general parameters of the galaxies in the sample are shown in Table 3.2.

Name	Date	Exposure Time	PA_{obs}	PA_{gal}
NGC 584	27th Oct. 1997	3600s	70°.0	55°.0
	27th Oct. 1997	3600s	160°.0	
NGC 720	28th Oct. 1997	3600s	141°.6	140°.0
	28th Oct. 1997	3600s	51°.6	
	28th Oct. 1997	1800s	141°.6	
	28th Oct. 1997	1800s	51°.6	
NGC 821	27th Oct. 1997	3600s	31°.5	25°.0
	27th Oct. 1997	3600s	121°.5	
NGC 1700	28th Oct. 1997	3600s	89°.1	90°.0
	28th Oct. 1997	3600s	179°.1	
NGC 3379	27th Oct. 1997	1200s	70°.0	70°.0
	28th Oct. 1997	1200s	160°.0	

Table 3.3: Summary of galaxy observations. The position angle of the observation is given (PA_{obs}), along with the major-axis position angle of the galaxy (PA_{gal}) as taken from the RC3 catalogue.

3.2.3 The Observations

The observations were made on two nights of generally good weather. Seeing ranged from 1-2″, but on average was better than $\sim 1''.5$. Calibration frames were taken on each night: biases and twilight exposures were taken at the beginning and end of each night; both tungsten flat-fields and arc-lamp frames were taken at each galaxy pointing to allow accurate fringing and dichroic corrections.

In order to determine the kinematic profile of each galaxy, several well-observed standard stars were observed, to be used as spectral templates for deriving the kinematics. The stars were chosen to be of G and K spectral type, as these are thought to be representative of a typical elliptical galaxy spectrum. Also observed were standard stars of earlier spectral type in order to produce accurate templates for any younger population which may be present.

Summaries of all galaxy and standard-star observations are given in Tables 3.3 and 3.4 respectively. The exposure times listed in Table 3.3 gave for each galaxy S/N$\gtrsim$ 100 per resolution element in the central regions, with S/N$\gtrsim$ 20 out to at least ≈ 0.5 R_e.

3.2.4 Basic Data Reduction

The data were reduced in the standard way, using mainly **IRAF** data reduction packages. This section briefly summarizes each of the basic reduction steps performed to calibrate the data.

Name 1	Name 2	Date	Exposure Time RED	BLUE	Spectral type	Vmag
HD 034411	HR 1729	27th Oct. 1997	60s	70s	G1.5 IV-V	4.71
HD 051440	HR 2600		60s	70s	K2 III	6.00
HD 052071	-		60s	70s	K2 III	7.11
HD 072324	HR 3369		70s	70s	G9 III	6.36
HD 184406	HR 7429		300s	300s	K3 IIIb	4.45
HD 186408	HR 7503		120s	120s	G1.5 Vb	5.96
HD 188056	HR 7576		90s	90s	K3 III	5.03
G 191-B2B*	-		180s	180s	DAw	11.6
HD 065934	-	28th Oct. 1997	90s	100s	G8 III	7.72
HD 069897	HR 3262		70s	80s	F6 V	5.14
HD 072324	HR 3369		90s	100s	G9 III	6.36
HD 074442	HR 3461		70s	80s	K0 III	3.94
HD 085503	HR 3905		60s	70s	K2 III	3.88
HD 086728	HR 3951		70s	80s	G3 Va	5.36
HD 184492	HR 7430		60s	70s	G8 IIIa	5.12
HD 186427	HR 7504		60s	70s	G3 V	6.20
HD 198858	-		60s	70s	K1 III	7.37
HD 217877	HR 8772		60s	70s	F8 V	6.68
G 191-B2B*	-		900s	900s	DAw	11.6

Table 3.4: List of observed standard stars, used as velocity templates, and (*) flux calibration. Name 1 refers to the entry in the Henry Draper Catalogue (Cannon & Pickering 1918), Name 2 refers to the entry in the Bright Star Catalogue (Hoffleit & Jaschek 1982). Exposure times are given for the RED and BLUE arms of the ISIS spectrograph individually. Stellar spectra types and V-band magnitudes are taken from the Simbad database. (This research has made use of the SIMBAD database, operated at CDS, Strasbourg, France http://simbad.u-strasbg.fr)

Preprocessing

The CCD bias level was removed using a median combined set of bias exposures taken at the beginning and end of each night of observations. frame-to-frame variations in the bias level were accounted for using the overscan region of each frame. Each exposure was then cropped to remove the overscan regions, as well as other border CCD rows and columns which contained no useful data.

Any regions of the CCD which did not collect charge, or were not read-out properly were determined from both the bias frames (for pixels with excessive charge) and continuum-lamp exposures (for non-responsive pixels). For all exposures, these pixels were interpolated across to prevent detrimental effects to the rest of the frame during subsequent reduction steps.

Flat Fielding

Variations in pixel efficiency were corrected for using a combination of continuum-lamp (for spectral flatness) and twilight-sky (for spatial flatness) exposures. The RED data suffered strong fringing effects, which occur when the thickness of the CCD substrate is of the order of the coherence scale of the incident light. This was found to be very stable over the course of the observations, and so it was possible to remove the fringing using a combination of all available continuum-lamp exposures, thus minimizing the noise introduced by the flat fielding process. The fringing variations were thus reduced from the 5% level, to much less than 1%.

In the BLUE arm, the transmission characteristics of the dichroic beamsplitter introduced structure in the data of the order 10% in intensity, and around 100 Å in the spectral direction, which could significantly bias the derived kinematics. The location of the structure on the CCD was found to be a strong function of telescope position, making it necessary to flat field the data using the single continuum-lamp exposure obtained at, or close to, a given galaxy pointing. In this way, the variations were reduced to a level of less than 1%.

Cosmic Ray Removal

Cosmic rays were removed from the data using the excellent CLEANEST routine of the $\mathrm{RED}^{\mathrm{uc}}_{\mathrm{m}}\mathrm{E}$[1] reduction software (Cardiel 1999). This package has a clear graphical user interface which allows cosmic rays to be accurately removed. Regions around galaxy centres and strong night-sky emission lines were excluded during the automated pass of the software, as these features can often be mistaken for cosmic ray events by the software,

[1] http://www.ucm.es/info/Astrof/reduceme/reduceme.html

and interpolated across by mistake. After an automated pass through the data, a second examination of the data was conducted. During the second iteration, no regions were excluded, and each suspected cosmic ray event found by the software was inspected 'by eye', and interpolated across if necessary.

Wavelength Calibration

The **IRAF** task identify was used to associate emission lines in the Cu-Ar-Ne arc-lamp exposures with their known laboratory wavelengths. The resulting dispersion function was determined for averaged strips across the CCD, to give a two-dimensional dispersion correction for each arc-lamp exposure. Each galaxy exposure was calibrated using the dispersion correction from the associated arc-lamp exposure taken at the same telescope position. The stellar observations were corrected using the nearest (in position and time) arc-lamp exposure, as calibrations were not obtained at every star position.

The typical uncertainty in the dispersion solution was between 0.05-0.1 pixels, equivalent to 0.04-0.08 Å for the RED data, and 0.03-0.05 Å for the BLUE data. Taking the mean wavelengths of the Calcium II triplet and Hβ absorption features as a reference, this corresponds to an intrinsic velocity uncertainty of $\lesssim 2.8\ \mathrm{km\,s^{-1}}$ and $\lesssim 3.1\ \mathrm{km\,s^{-1}}$ for the RED and BLUE data respectively.

Background Subtraction

Sky emission lines were removed from the data by using the regions at either ends of the slit, where the contribution from the galaxies is lowest, to constrain a straight-line fit across the galaxy profile (i.e., down a column of the CCD). This fit is performed at each wavelength bin, and is subtracted from the galaxy frame.

The sky emission lines differ grossly in character between the RED and BLUE wavelength regions. In the BLUE, there are few sky lines, and their intensity is generally small compared to the central brightness of the observed galaxy. Around the Ca II Triplet, however, there are many strong features, creating a 'forest' of sky lines. For this reason, accurately subtracting the sky emission lines is critical for this data.

Even though the wavelength calibration was conducted very accurately, the RED data exhibit sizeable residuals after sky subtraction. These residuals become more significant at larger radii, where the light from the sky lines dominates over the light from the galaxy. Whether these residuals fall on any of the three strong Calcium II triplet features depends on the recession velocity of the galaxy. For NGC 584 ($cz \sim 1800\ \mathrm{km\,s^{-1}}$), for example, the strongest sky residuals fall *between* the calcium lines [Figure 3.1(a)], and so the residuals do not interfere a great deal with the shape of the absorption line profiles.

For NGC 1700 ($cz \sim 3900$ km s^{-1}), however, the strong residuals fall *within* the strong absorption features [Figure 3.1(b)].

It is difficult to quantify the effect that these sky residuals will have on the final kinematics. The changes in intensity of the residuals are of a much higher frequency than the galaxy absorption lines, and the filtering of the spectrum in Fourier space should suppress the effect of these residuals on the derived kinematics. However, the errors on the Calcium II triplet kinematics are noticeably larger for NGC 1700 than for the other galaxies in the sample due to the effect of these sky residuals on the Calcium II triplet features (see e.g., Figure 3.39). NGC 1700 has the highest recession velocity of the sample.

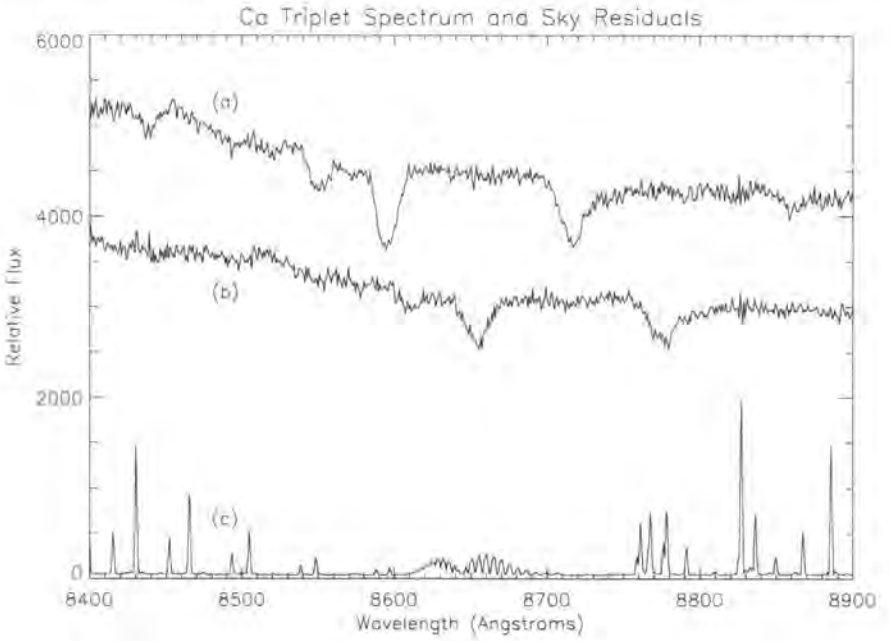

Figure 3.1: The central sky-subtracted spectra of (a) NGC 584 ($cz \sim 1800$ km s^{-1}) and (b) NGC 1700 ($cz \sim 3900$ km s^{-1}), with a representative spectrum of sky residuals (c). Note that the sky features between 8600 Å and 8800 Å lie mostly ***between*** the absorption lines in NGC 584, but lie ***inside*** the absorption features of NGC 1700. This gives rise to larger errors in the Calcium II triplet kinematics of NGC 1700 compared to the other galaxies in the sample, which have $cz \lesssim 2000$ km s^{-1})

Spatial Rectification

The data were corrected for any distortions in the spatial axis by tracing the peak of each galaxy's light profile across the CCD (i.e., along the spectral direction), and determining how the centroid of the light profile changes position. This is done by averaging several columns together (to improve the signal-to-noise ratio, and avoid the effects of velocity gradients in the absorption lines) before finding the peak of the profile, and repeating this process along the CCD. A polynomial is fitted to the resulting sequence of centroid coordinates, which then defines the transformation function used to rectify the data.

The distortion was found to be small in the RED data, with the centroid shifting only a few tenths of a pixel across the $\sim$ 1000 pixels of the detector. By comparison, the correction for the BLUE data was much larger, with the centroid shifting more than 12 pixels across the $\sim$ 4000 pixels of the detector.

Extracting 1D Stellar Spectra

In order to create kinematic template spectra with which to correlate with the galaxy spectra, it is necessary to extract a one-dimensional stellar spectrum from the 2D data frames. All the stars which were observed were 'trailed'; that is, the image of the star is allowed to move along the length of the slit, either by stopping the telescope tracking and letting the star drift along the slit, or by actively moving the telescope. This results in a large portion of the 2D frame containing light from the star, which can be combined to produce a very high S/N stellar spectrum.

In order to apply the spatial correction, it is necessary to 'trace' a peak of intensity across the CCD. Indeed, for the BLUE arm this is essential, as the slit is misaligned with the pixels of the detector by a significant amount. In the 2D stellar frames, there tend to be several distinct peaks in the intensity (where the star moved more fully into the slit), which can be used to trace the spectrum of the star across the CCD. For each exposure, each individual peak was traced and extracted using the **IRAF** task apall, then combined to generate a high-signal 1D stellar spectrum.

3.2.5 Rebinning to Logarithmic Wavelength Units

If a spectral feature, with rest wavelength λ_0, is observed at a wavelength λ, then the difference in velocity Δv of the source and the rest frame is given by:

$$\Delta v = c\left(\frac{\lambda_0 - \lambda}{\lambda}\right) = c\frac{\Delta\lambda}{\lambda}, \tag{3.1}$$

where c is the speed of light. Integrating this gives:

$$v = c\ln\lambda, \tag{3.2}$$

implying that velocity is proportional to the logarithm of wavelength. Therefore, before applying some analysis technique to determine the kinematics, it is necessary to rebin the spectra from wavelength units (Å) to logarithmic wavelength units ($\ln\lambda$). This rebinning was performed with the **IRAF** task dispcor, using a 5th order polynomial function to interpolate the wavelength axis onto a grid of points spaced linearly in $\ln\lambda$. This gave a final step-size of $\Delta v = 27.8$ km s^{-1} for the red-arm, and a comparable $\Delta v = 29.2$ km s^{-1} for the blue-arm.

3.3 Measuring Galaxy Kinematics

3.3.1 The Fourier Correlation Quotient

To derive the stellar kinematics of the galaxies in the sample, the well-established Fourier Correlation Quotient (FCQ) method (Bender 1990) was used. The FCQ method uses a combination of two principles: the Fourier quotient technique (e.g., Simkin 1974, Sargent et al. 1977) and the correlation method (e.g., Simkin 1974, Tonry & Davis 1979). Individually, these two techniques are well tested, and their advantages and problems are well known. For example, the correlation method, where a stellar template spectrum is 'matched' with a galaxy spectrum, producing a peak in the correlation function, is plagued by secondary peaks and the poorly definable effects of instrumental broadening. The Fourier quotient method, while more reliable in removing the instrumental broadening, suffers significantly with the problem of template mismatching. The FCQ method is designed to avoid, or at least minimize, the above effects.

This robustness to template mismatch is achieved by deconvolving the peak of the template–galaxy correlation function with the peak of the autocorrelation function of the template star, thus avoiding the characteristic 'ringing' in Fourier space due to template mismatch. Noise in the derived LOSVD is minimized through the use of an optimal filter (or 'Wiener' filter, after Wiener (1949)) in Fourier space, which utilizes the distinction between signal and noise in the Fourier domain. In principle, using the FCQ method robustly recovers the full LOSVD *independent* of template-mismatching (Bender 1990). This is important to the aims of this investigation, which seeks to measure small-scale differences in the derived LOSVDs, and so such systematic effects must be minimized.

3.3.2 Parameterising the LOSVD

The FCQ method derives the full LOSVD from the galaxy spectra. That is, for each velocity-bin of the data (equivalent to a spectral resolution element in the logarithmically-rebinned spectra), the luminosity-weighted contribution of stars along the line-of-sight having that velocity is recovered. From this distribution, it is possible to fit a Gaussian function, and determine the useful quantities of mean rotation velocity, $\bar{v}$, and velocity dispersion, σ.

Using large telescopes with modern, efficient spectrographs and detectors, it is possible to measure small, but distinct, deviations from the classical Gaussian approximation for the LOSVDs of elliptical galaxies. These deviations hold important information about the internal kinematics of the system, and thus being able to quantify these deviations in some general way allows a deeper understanding of how the object is supported.

Van der Marel & Franx (1993), and at the same time Gerhard (1993), proposed an elegant method for quantifying these deviations from a Gaussian, using an approach

similar to the standard practice of describing the higher-order moments of a distribution. Motivated by the fact that a Gaussian is a good low-order approximation to most realistic LOSVDs, they considered the Gauss-Hermite series[2]:

$$\mathcal{L}(v) = [\gamma\alpha(w)/\sigma]\sum_{j=0}^{N} h_j H_j(w), \quad w \equiv (v-\bar{v})/\sigma, \tag{3.3}$$

where γ is the line strength, the h_l are free parameters, $\alpha(y)$ is the standard Gaussian:

$$\alpha(y) = \frac{1}{\sqrt{2\pi}} e^{-\frac{1}{2}y^2}, \tag{3.4}$$

and the function $H_l(y)$ are the Hermite Polynomials, defined such that:

$$\int_{\infty}^{\infty} H_m(y)H_n(y)\alpha^2(y)\mathrm{d}y = \frac{1}{2\sqrt{\pi}}\delta_{mn}. \tag{3.5}$$

For any choice of (γ, v, σ) there exists a Gauss-Hermite series of the form equation 3.3 that fits the data. However, since we wish to quantify the deviations from a Gaussian, the series is fitted by first of all setting the parameters (γ, v, σ) to those of the best-fitting Gaussian. This is equivalent to setting (h_0, h_1, h_2) in equation 3.3 to $(1, 0, 0)$, resulting in a **truncated Gauss-Hermite** series of the form:

$$\mathcal{L}_{TGH}(v) = [\gamma\alpha(w)/\sigma]\{1 + \sum_{j=3}^{N} h_j H_j(w)\}, \quad w \equiv (v-\bar{v})/\sigma, \tag{3.6}$$

where symbols are as previously defined. The LOSVDs of most elliptical galaxies are adequately described by truncating the series at $N = 4$, although in the case of strong deviations from Gaussianity, terms with $N > 4$ become non-negligible. Figure 3.2 illustrates the effect of non-zero h_3 and h_4 coefficients on the shape of $\mathcal{L}_{TGH}(v)$. Notice that the wings of $\mathcal{L}_{TGH}(v)$ can be negative, which implies a non-physical LOSVD. This effect is usually within the measurement uncertainties in the distribution wings, but should be taken into account when considering the physical interpretation of these parameters.

Quantifying departures in the LOSVD shape from a Gaussian is specifically important to the aims of this thesis. In the case of a rotationally-supported disk which is embedded in the body of a slowly-rotating, pressure-supported spheroid, the integrated LOSVD can be strongly asymmetric. Figure 3.3 illustrates this, showing the resulting LOSVD from a model of two superimposed Gaussian components, overplotted with a Gaussian, and Gauss-Hermite polynomial functions. Clearly, asymmetries in the LOSVD can be indicative of a two-component kinematic structure. When comparing the kinematics

[2]using the notation of van der Marel & Franx (1993)

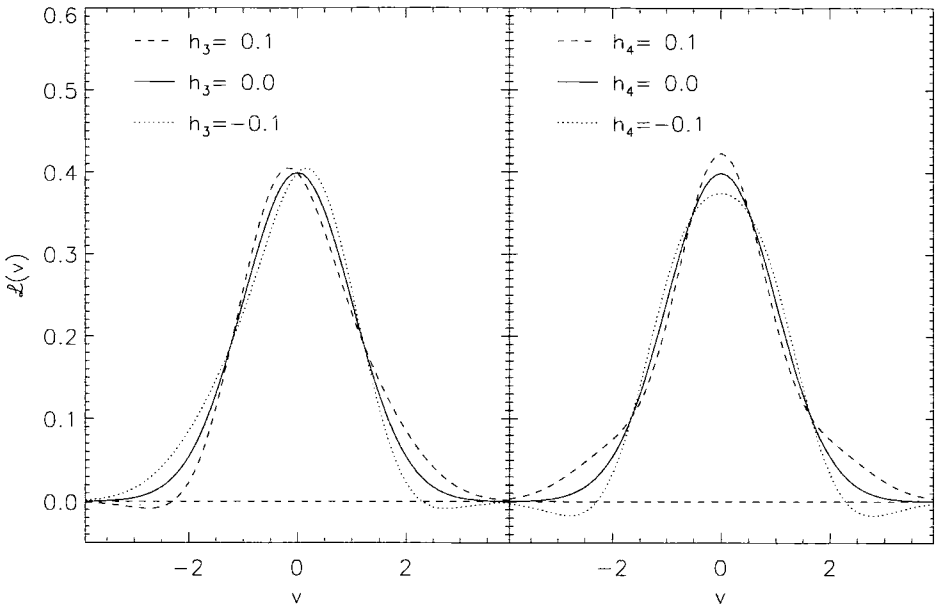

Figure 3.2: The function $\mathcal{L}(v) \equiv \alpha(v)[1 + h_3 H_3(v) + h_4 H_4(v)]$ used to describe departures from LOSVD Gaussianity, for various values of h_3 and h_4. The base Gaussian distribution has $\bar{v} = 0$ and $\sigma = 1$ in both panels. For curves in the left panel, $h_4 = 0$, and for the right panel, $h_3 = 0$. This illustrates how the h_3 term quantifies the asymmetric deviations from a Gaussian (similar to the skewness of the distribution); and how the h_4 term quantifies the symmetric deviation from a Gaussian (similar to the kurtosis of the distribution). Based on Figure 1 of van der Marel & Franx (1993).

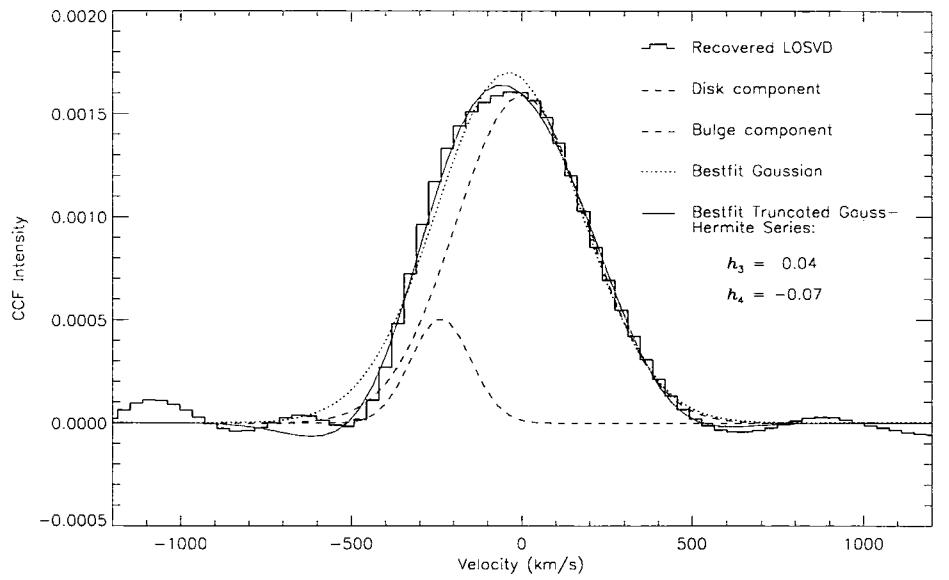

Figure 3.3: Recovered LOSVD (histogram) of a 'Disk + Bulge' model, in which the 'Disk' component (blue line) has a low intrinsic velocity dispersion, and is shifted in velocity with respect to the broad-dispersion, low velocity (pressure supported) 'Bulge' component (red line). Overplotted on the LOSVD is the best-fit truncated Gauss-Hermite series of the form equation 3.6 (green line), as well as the best-fit standard Gaussian (dotted line). The values of the higher-order coefficients, h_3 and h_4, are given. Clearly, the simple Gaussian does not represent the LOSVD as well as the Gauss-Hermite series.

derived from the two different wavelength regions, subtle differences in the shape of the LOSVDs between the two regions may provide evidence for the presence of a kinematic sub-component composed of a different stellar population.

3.3.3 Monte Carlo Simulations

In order to obtain accurate and reliable results from the FCQ code, there are a number of input parameters which must be optimised. These input parameters consist of: the wavelength region being used; the degree of tapering at the spectrum edges; the order of the function fitted to the continuum; the minimum signal-to-noise ratio (hereafter S/N) required for the radial binning; and the degree of filtering performed by the optimal, or 'Wiener' filter. These simulations also give a reliable indication of the true RMS error involved in obtaining the LOSVD, which is used to scale the internal error estimates given by the FCQ routine. Since the Calcium triplet and Hβ spectral regions are different in character, simulations were conducted for both regions individually.

Using a high S/N spectrum of one of the observed stars to create a synthetic galaxy spectrum, Monte Carlo simulations were performed to find the optimal value for each of these parameters. A number of input kinematic parameter values (i.e., $\bar{v}$, σ, h_3 and h_4) are explored for different input FCQ parameters and S/N. Since the FCQ parameters are not necessarily independent, a full 3-dimensional grid of parameters (apodisation, continuum order, and Wiener filter) was explored for different $(\bar{v}, \sigma, h_3, h_4)$ and a S/N of 60 Å^{-1}. Figures 3.4 and 3.5 present the results of these simulations. For each parameter, the results are shown from simulations in which the other parameters were fixed at their determined 'optimal' values. Finally, the variation of each parameter with S/N was explored, holding the input parameters at their optimal values.

Here, the purpose of each parameter, and its optimisation in each wavelength region through the simulations, is described. The combined results of the simulations are presented at the end of this subsection (Figures 3.4 and 3.5), along with a table giving the adopted 'optimal' input parameter values determined from the simulations (Table 3.5).

Wavelength Region

Since we are trying to isolate particular spectral features to be used in deriving the kinematics, we have to carefully select the spectral region we input to FCQ. Due to the nature of correlation methods, the accuracy of the derived LOSVD depends strongly on the number of absorption features in the spectrum, and the uniqueness of there distribution with wavelength.

For this reason, the Ca II triplet is an ideal region for our purposes. The three strong features are not evenly spaced, inhibiting false or resonant correlation peaks. The triplet

dominates the wavelength region, with no other strong features 'contaminating' the region with signal from other chemical elements (which may have a slightly different profile to the triplet lines). Therefore we obtain a correlation with high signal, low resonant noise, which comes almost exclusively from stars producing the Ca II triplet features.

In the case of the Hβ absorption line, however, things are not so straightforward. Firstly, it is only a single absorption feature[3] which, although a strong line, is not optimal for the correlation method. The spectra must be of a relatively higher S/N than the Ca II triplet to derive kinematics with the same accuracy.

Secondly, the Hβ line is surrounded on either side by relatively strong iron absorption features, which tend to come from older and metal-rich stars. Since we are using Hβ as an indicator of the kinematics of young stars, contamination from these iron lines must be kept to a minimum.

The precise wavelength regions used in deriving the kinematics was found through a process of trial and error. Initial estimates of appropriate regions to use were made, which were 'fine tuned' by running FCQ and altering the wavelength limits to ensure that the convolved template was as close a representation of the galaxy spectrum as possible. This was judged by overplotting the two continuum-subtracted, tapered spectra, and visually ensuring that they were as similar as possible. The wavelength ranges which were determined in this way for the two regions are given in table 3.5, quoted as the effective rest-wavelength values.

Apodisation

Since we are dealing with only finite spectral regions, the ends of the spectra form discontinuities which, when transformed into Fourier space, cause the power spectrum to run out to high frequencies. In order to avoid this additional 'noise' term, a tapering factor is applied to reduce the effect of these terminal discontinuities. This factor takes the form of a cosine bell, such that the ends of the spectrum are smoothly tapered to zero in the form of a cosine function. The degree of tapering is determined by the fraction of the total wavelength region to which the cosine bell is applied.

Figures 3.4 and 3.5 show the results for Monte-Carlo realisations of various apodisation fractions for the two wavelength regions. Note that for the longer wavelength coverage of the Calcium Triplet region, the results are insensitive to different amounts of apodisation. 15% was chosen to provide a reasonable amount of tapering, without introducing systematic errors. For the shorter Hβ region, however, the results are much more sensitive to the tapering fraction, and even a small fraction of spectrum given to the tapering has an effect on the recovered kinematics. For this region, the cosine bell was applied using only 5% of the spectrum.

[3]There are some weak iron absorption lines which also contribute to the Hβ absorption feature in early-type galaxy spectra, but their contribution is generally not significant (Burstein et al. 1984)

Continuum Order

Before transforming the spectra into Fourier space, the shape of the continuum of the galaxy and template-star must be subtracted to prevent it contributing to the low-frequency end of the Fourier transform. This involves fitting a low-order polynomial to the spectrum which follows the general shape of the spectrum without fitting to the spectral features.

This is achieved by incorporating a rejection scheme into the fitting process, whereby data points in the spectrum lying outside certain bounds of the initial best-fitting polynomial are discarded, and the function is fitted again to the reduced number of points for a number of iterations set by the user. The bounds are quantified as multiples of the standard deviation of the data around the fit. This 'sigma-clipping' process prevents the absorption features being fit by the function, as smaller bounds are defined for points below the fit than for above. Each subsequent fit rejects more points *below* the function than above, thus avoiding any fitting to the absorption lines.

An 'Occam's Razor' approach was taken in deciding which order of fit was appropriate, in that the lowest-order fit which yielded acceptable results was used. For the Calcium II triplet region, a 3rd-order polynomial was chosen to give the most satisfactory results. For the much shorter Hβ region, a simple 1st-order function of the form $y = ax + b$ was used.

Wiener Filter

The FCQ method works in the Fourier domain, where the process of deconvolution is equivalent to division. The quotient involves the peak of the galaxy-template correlation function as the nominator, which has a non-negligible noise component due to the limited `S/N` of the data. The denominator: the template autocorrelation function, is relatively noise-free by comparison, having been produced from very high `S/N` data of a bright template star.

Since the noise in the data can be assumed random, it has no frequency dependence, and therefore its Fourier spectrum covers the whole frequency domain with equal intensity. The transform of the template autocorrelation function, however, is confined to lower frequency channels. Therefore, at high frequencies, the noise term becomes strongly amplified by the low value of the denominator.

This problem is avoided by employing a filter in the Fourier domain. Specifically, it is possible to create an optimal filter which, when applied to the observed signal, results in the best approximation to the noise-free signal. The filter is 'optimal' in the sense that the difference between the filtered data and the true signal are minimized. If the true nature of the signal and noise are known, then the two can be extracted perfectly.

Since the filter is optimized in this way, small deviations from the true signal and noise functions cause only second-order discrepancies in the recovered signal. Consequently, it is adequate to describe the signal and noise components with smooth, simple models which can be fitted to the noisy input signal and thus provide the form of the optimal filter.

In practice, the signal component of the noisey galaxy-template correlation function can be well-fitted by a Gaussian function. The noise is taken to have a 'white' spectrum, giving a constant in Fourier space. Combining these two models yields the optimal filter. The implementation of the Wiener filter used in the FCQ routine provides a factor, W, which controls the degree of filtering applied by scaling the width of the Gaussian function used to model the signal component. A value of $W = 1$ corresponds to 'optimal' filtering, which uses the best-fit Gaussian fitted to the galaxy-template correlation function. Larger values of W imply correspondingly broader Gaussians used to describe the correlation, and result in less filtering.

Figures 3.4 and 3.5 illustrate that the resulting kinematic parameters are rather sensitive to the filtering parameter, W; especially the higher-order h_3 and h_4 terms. This has been noted by other authors (e.g., Joseph et al. 2001), and is a result of the assumed Gaussian form of the Wiener filter. If this filter is too strictly enforced, the intrinsic non-Gaussian part of the signal is strongly suppressed, resulting in an inaccurate determination of the higher-order terms. Similar to Joseph et al. (2001), a value of $W = 2.0$ was found to be the optimal choice between filtering out unwanted noise, and maintaining the intrinsic low-level signal of a non-Gaussian profile in both wavelength regions.

Optimal Signal to Noise Ratio

Due to the characteristically steep light profiles of elliptical galaxies, the S/N of the data drops rapidly with increasing radius from the galaxy centre. Thus, in order to maintain the minimum signal required to accurately measure the kinematics, the data must be rebinned in the radial direction by combining individual spectra at each spatial element until the minimum required signal is achieved. This minimum amount of signal is determined via the Monte Carlo simulations by finding the lowest S/N which still produces kinematics within the chosen accuracy limits.

Since reliably measuring the higher-order h_3 and h_4 terms requires a higher S/N than for measuring the mean velocity and velocity dispersion, the radial bins are correspondingly larger for these terms, as more spatial elements must be summed together. The result of this can be seen in the more sparse sampling of data points for these terms in the kinematic profiles given in §3.5.

The accuracy of the kinematic measurements depends not only on the S/N, but also on the number of absorption lines in the spectrum. The more absorption features present, the

more information there is about the LOSVD of the stars producing them. For the Calcium triplet kinematics, there are three strong features to base the measurements on, whereas in the Hβ region, the region is dominated by the single Hβ absorption feature. Therefore, to obtain equally accurate measurements in both regions, a higher S/N is required for the Hβ region to compensate for the small number of features being used. The aim is to measure velocities and velocity dispersions with a standard error of $\sim \pm 5$ km s^{-1}, and $\sim \pm 0.05$ in h_3 and h_4 where the quality of the data will allow.

From Figure 3.4 it can be seen that these accuracy limits are achievable for the Calcium II triplet region for S/N= 40 Å^{-1} for v and σ, and S/N= 60 Å^{-1} for h_3 and h_4. The simulations may suggest that h_3 and h_4 can be recovered with this accuracy at even lower values of S/N; however, these simulations fail to take into account the effects of template mismatch, and sky subtraction residuals. Around the Calcium II triplet region, the latter of these can be significant. Therefore, a more conservative estimate is adopted.

Figure 3.5 illustrates the effect of using the shorter Hβ wavelength range (note that the vertical scales in Figure 3.5 are different to those in 3.4). In order to meet the accuracy criteria, it is necessary to use higher S/N values. Although this limits the radial extent of the data more, using this short wavelength region optimises the sensitivity to a young population. For $\bar{v}$ and σ, S/N= 50 Å^{-1} is sufficient for a $1-\sigma$ error distribution of ± 5 km s^{-1}. For the higher-order terms, however, it is necessary to use S/N= 70 Å^{-1}, accounting for possible additional systematic errors due to template mismatch effects.

Parameter	Ca II Triplet	Hβ
Apodisation	15%	5%
Continuum Order	3	1
Wiener Filter	2.0	2.0
$(S/N)_{\bar{v},\sigma}$	40	50
$(S/N)_{h_3,h_4}$	60	70
Wavelength Region	8400-8800 Å	4820-4960 Å
$\Delta\bar{v}$	0.6	1.8
$\Delta\sigma$	0.6	0.8
Δh_3	0.5	1.2
Δh_4	0.5	1.2

Table 3.5: Values adopted for various FCQ input parameters, as well as the rest wavelengths of the spectral regions used to derive the kinematics, and the scale factors applied to the internal FCQ error estimates, given by the Δ terms.

3.3.4 Stellar Template

Although the FCQ method is much less sensitive to template mismatching than other correlation methods, using a template which is a poor representation of the spectrum of the galaxy can still introduce systematic errors to the derived kinematics. For this reason, a range of stellar types were observed in order to provide a choice of templates and thus increasing the likelihood of using a representative template.

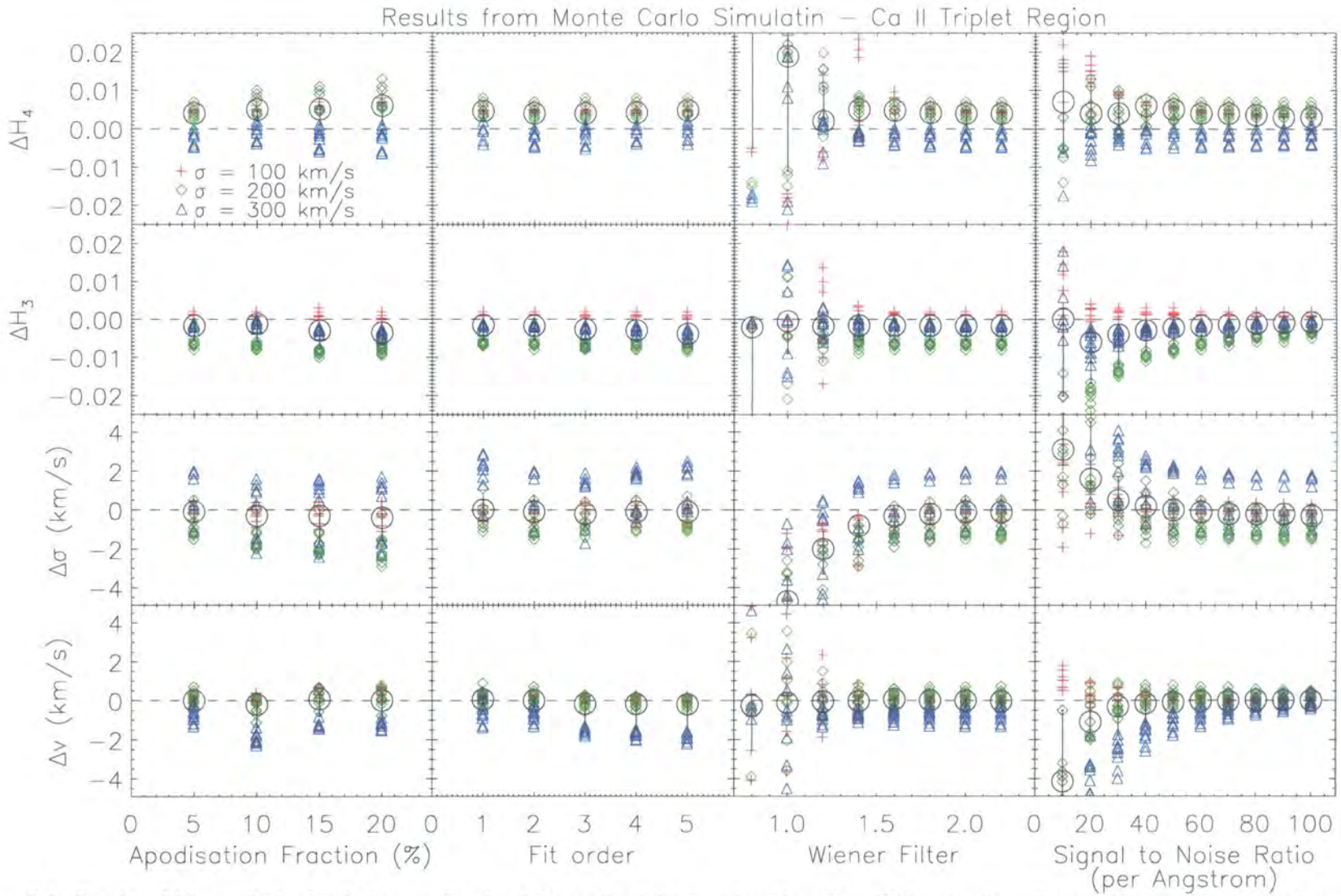

Figure 3.4: Results of Monte Carlo simulations on for the Calcium II triplet wavelength region. Different coloured symbols represent simulations of different intrinsic velocity dispersions. The large open circle represents the median of the distribution of points for a given parameter, with the error bar enclosing the 34% of points above and below the mean. The apodisation, fit order and Wiener filter plots are each given holding the other two factors at their 'best' value, and for a S/N of 60 Å^{-1}. (See text for detailed description of the simulations)

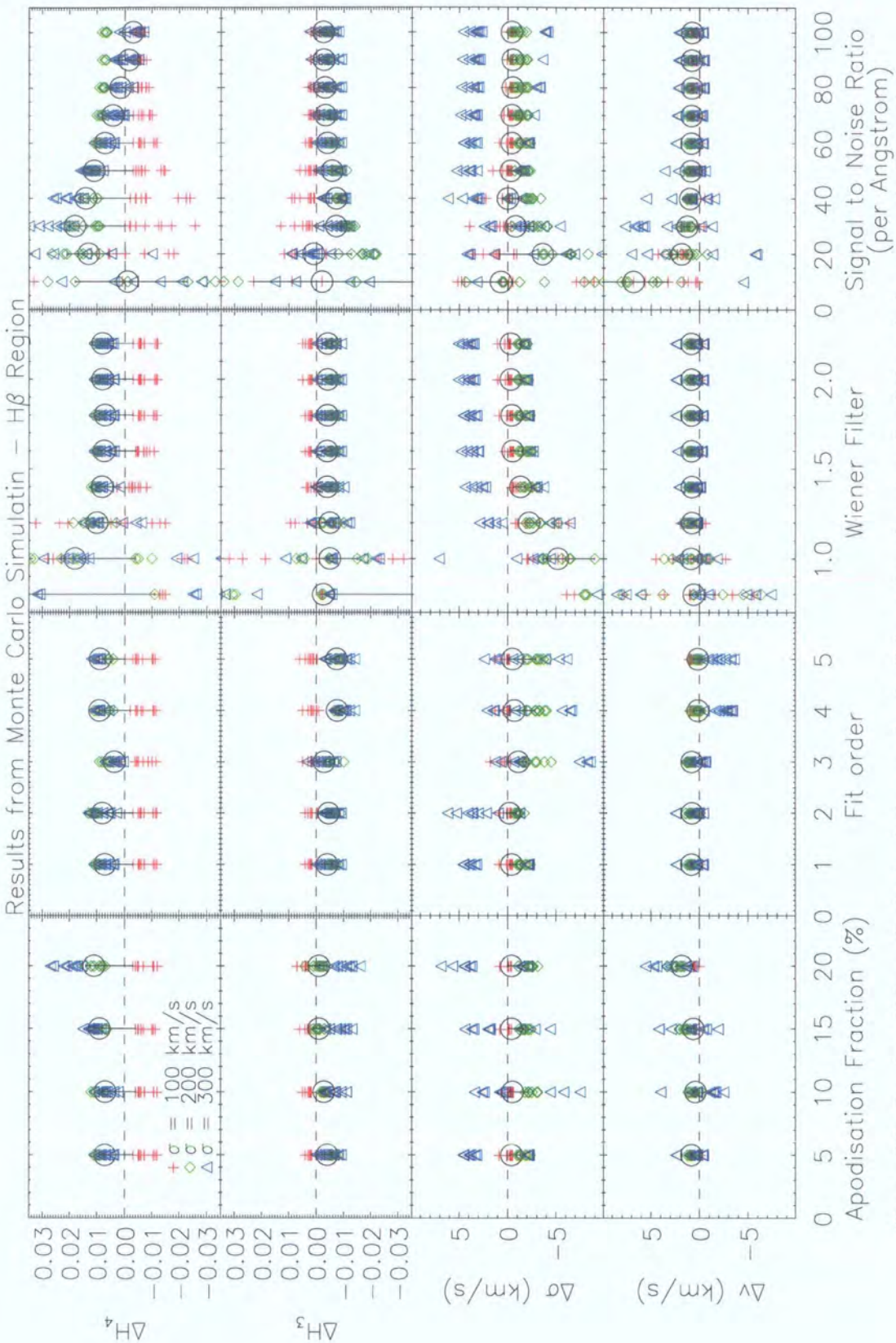

Figure 3.5: Results of Monte Carlo simulations on for the Hβ wavelength region. Symbols and plots are as in Figure 3.4.

A more subtle effect is that the choice of template can bias the derived kinematics towards that of the stellar population in the galaxy which has a similar spectral type to the template. Such an effect is important if we have a galaxy with two or more stellar populations which are kinematically distinct, such as in the case of a young disk embedded in an old spheroid. This effect is difficult to quantify and account for, as we do not know what populations are present *a priori*. For the purpose of this analysis, however, the effect should be negligible, as we are basing our measurements on individual spectral features (i.e., Hβ and the Calcium II triplet), rather than many different features which all must be represented in the template star in the correct proportions. In this way, our analysis is 'fine tuned' to the kinematics of the stars producing a particular feature, rather than of a complex mixture of spectral features.

The star used as template for any given galaxy was selected on the basis of how well it represented the galaxy spectral region being studied. The 'quality' of representation was determined by using the star as a template, convolving its spectrum with the resulting broadening function from FCQ, and evaluating the quality of fit to the galaxy spectral region based on the sum of the square of the residuals of the fit.

From this simple technique, a general trend with spectral type was found. Figure 3.6 (a) and (b) show, for the two wavelength regions, the values of the squared residuals between the major-axis spectrum of NGC 720 and templates of different spectral types. The residual values are plotted against the approximate surface temperature for templates of a given spectral type. For both wavelength regions, there is a weak trend of the quality of fit with spectral type. More specifically, the cooler K Giants are better fit to the near-infrared Calcium Triplet, where as the hotter G Giants fit better around the bluer Hβ feature. One expects such a trend from a simple consideration of Wien's Displacement Law, since cooler stars emit most of their light at redder wavelengths. This trend also illustrates the fact that, by studying these two wavelength regions, we are sensitive to different *stellar types*. However, we cannot deduce from this simple approach that there are necessarily different *stellar populations*, as the G and K giants may simply form part of the same population, created at the same epoch, and from similarly enriched material.

Galaxy Name	Ca II Triplet	Hβ
NGC 584	K3 III	G9 III
NGC 720	K3 III	G8 III
NGC 821	K2 III	G9 III
NGC 1700	G9 III	G8 IIIa
NGC 7454	G8 III	G3 V
NGC 3379	K1 III	K2 III

Table 3.6: Spectral types of template stars which best fit the given wavelength region for each galaxy in the sample. Note that the Calcium II Triplet is generally better represented by stars cooler than those which best represent the Hβ region.

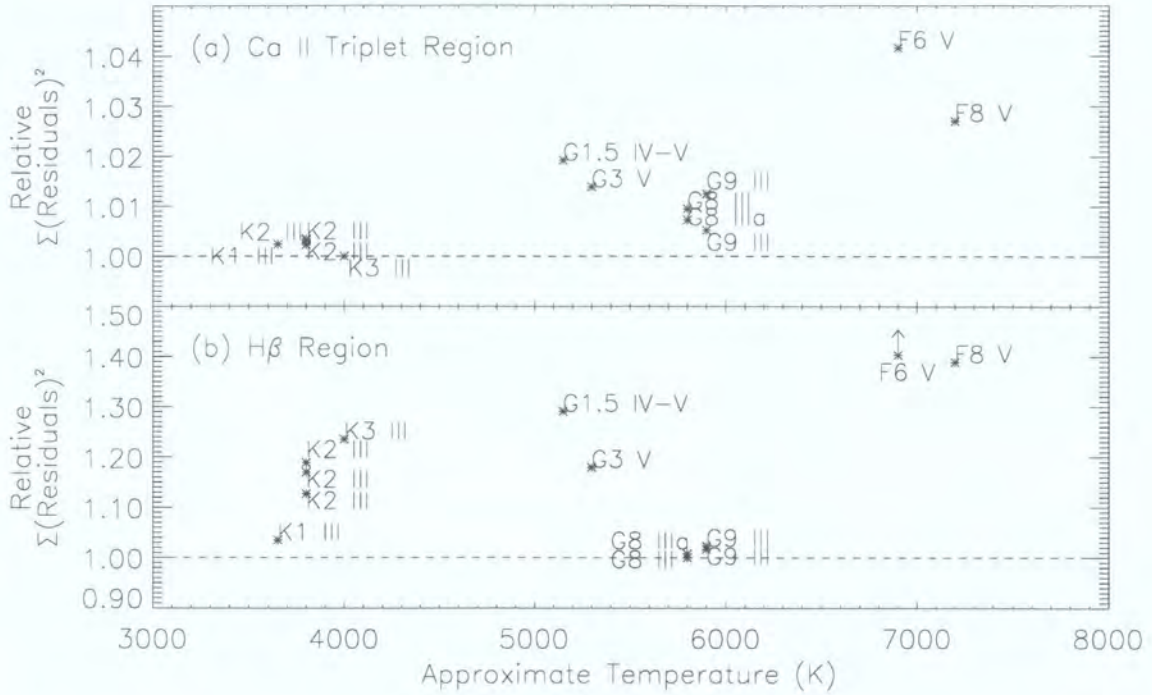

Figure 3.6: Relative value of the sum of the squared residuals of broadened template spectra of different spectral types subtracted from the spectrum of NGC 720 around (a) the Calcium II triplet features, and (b) the Hβ feature. The abscissa gives the approximate surface temperature of the template star based on its spectral type (taken from Binney & Merrifield (1998)). The residuals have been normalised by the minimum value. This shows that templates of different spectral type are needed for the different spectral regions. For clarity, in plot (b) the F6 V template has been plotted as an arrow, indicating that its true value lies beyond the limit of the y-axis.

Based on this analysis, the template star resulting in the smallest residuals was used as the final kinematic template. Different stars were selected in this way for different galaxies. Table 3.6 gives for each galaxy in the sample the spectral type of the best fitting template star for both wavelength regions.

3.4 Correcting for Nebular Emission Lines

3.4.1 Introduction

Previously thought to be devoid of gas, elliptical galaxies are now known to exhibit a significant and complex inter-stellar medium. The presence of *cold* ($< 100\ K$) gas is inferred from thermal emission in the far-infrared (Knapp et al. 1989), as well as H I 21 cm (e.g., Knapp et al. 1985) and CO line emission (e.g., Wiklind & Rydbeck 1986). Evidence of a *hot* ($\geq 10^6\ K$) gas component comes via X-ray emission (e.g., Brown & Bregman 1998). *Warm* gas at intermediate temperatures ($\sim 10^4\ K$) is revealed through optical emission from ionised elements such as hydrogen and oxygen. It is this warm gas component which affects this analysis.

Over half of elliptical and lenticular galaxies have been shown to contain a substantial amount of ionised gas (Phillips et al. 1986, Kim 1989, Buson et al. 1993, Goudfrooij et al. 1994, Caon et al. 2000). There have been numerous excitation mechanisms proposed for generating the observed emission: photoionisation by hot, young stars (Kim 1989, Shields 1991); photoionisation by hot, old post-AGB star (Binette et al. 1994); heat transfer from the hot gas to the cold gas component (Sparks et al. 1989); photoionisation directly by the x-ray emission (Donahue & Voit 1991); radiation originating from an active galactic nucleus (Fosbury et al. 1982); and shock-wave heating (Heckman et al. 1989). The ionisation mechanisms which are dominant, however, and how their relative importance changes from one object to another, is still an open issue.

The origin of the ionised gas is also somewhat uncertain. The gas can be considered as either of *internal* origin, for example, simply as a result of stellar mass-loss; or *external* origin, being deposited by a cooling flow, or accreted as the result of a merger with a gas-rich galaxy. Clues to the origins of the ionised gas come from its chemical composition, although interpreting this requires a full understanding of the ionisation process itself (Binette et al. 1994).

Other clues come from the dynamical structure of the gas. This information is less specific than the chemical composition of the gas, but it is perhaps more straightforward to relate the gas to its internal or external origins. To this end, several studies have found that the rotation of the stellar and gaseous components are very often misaligned, even anti-parallel, with sometimes more than one gaseous component (e.g., Caon et al. 2000, Pignatelli et al. 2001, Corsini et al. 2002). Such findings support an external origin for the gas, having been accreted from some kind of galaxy-galaxy interaction.

Emission lines in ellipticals are generally quite weak, with the exception of giant central-cluster galaxies (cD galaxies). Furthermore, their detection and measurement is made more difficult by the fact that many of the emission lines from the ionised gas are also present in absorption in the spectrum of the parent galaxy. It is for this same reason, however, that detecting the emission is important to this work, since these emission lines (if present) can significantly alter the shape of the absorption lines around which they occur. Ordinarily, for the purpose of obtaining stellar kinematics, small amounts of emission can be tolerated without significant loss of accuracy, since they constitute only a small portion of the spectral region being used to obtain the LOSVD. However, since only a very small spectral window is being used, if there is any appreciable level of emission present, it may have a significant effect on the kinematics derived.

Specifically, the Hβ Balmer line is often found in weak emission, as well as absorption. For example, in his investigation of stellar populations in early type galaxies, González (1993) found that [OIII]$\lambda\lambda$4959, 5007 emission was clearly detectable in around half the nuclei in his sample, and that most of these galaxies also displayed detectable Hβ emission (see his Figure 4.10). González (1993) corrected for this emission for the purposes of obtaining true absorption strength measurements. The Hβ emission effectively 'filled in'

the absorption line, giving a systematically lower equivalent width. He corrected for this by establishing an empirical relationship between the equivalent width of [OIII] emission, and that of Hβ emission, such that the decrease in equivalent width of Hβ due to emission in-filling was taken to be equal to 0.7 times the equivalent width of [OIII] emission.

For the purpose of kinematics, however, such a correction is not possible, as the effect of the emission is to alter the *shape* of the Hβ absorption line, as well as the depth. Thus, to correct for the effect of the emission on the kinematics requires attempting to *remove* the emission lines from the absorption lines by means of modelling the shape of the two components. This section describes the process undertaken to detect and, if necessary, remove the presence of emission lines from the galaxy spectra. In galaxies which exhibit significant amounts of emission, analysis of their gas kinematics and the intensity of the emission is also presented.

3.4.2 Detecting the Emission Lines

The technique used to separate the absorption from the emission features was to represent the stellar absorption spectrum as a linear combination of template spectra which are redshifted and broadened to the same mean velocity and velocity dispersion as that of the line of sight through the galaxy. Clearly, this is a circular argument: to properly determine the stellar kinematics, the emission must be removed; but to remove the emission requires knowledge of the stellar kinematics.

To avoid this problem, the stellar kinematics were firstly determined using a wavelength region close to Hβ, but which is known to be relatively unaffected by emission. For this purpose, the wavelength region from just redward of the [OIII]λ 5007 emission line, up to, and including, the Fe5270 iron absorption feature was used. This region includes distinctive features, such as Mg b, as well as the Fe5270 line, and so is well suited for determining kinematics. The region is not totally devoid of emission features, with possible [NI]$\lambda\lambda$5198, 5200 doublet emission affecting the Mg b absorption feature (Goudfrooij & Emsellem 1996). Unlike the kinematics derived using primarily the single Hβ feature, however, this region has several strong absorption features whose contributions will make the derived kinematics much more reliable, and less susceptible to the effects of this emission.

It should be noted that the final purpose of this work is to compare kinematics from the Hβ feature alone, since this feature is sensitive to young stars. Using a region consisting of features with characteristics very different to those of Hβ to estimate the kinematics of the stellar absorption component introduces a bias towards the kinematic signature of older and/or more metal-rich stars. This unavoidable bias, however, is considered negligible compared to the effect that a detectable amount of emission would have on the derived LOSVD.

Once an estimate of the stellar kinematics has been made, the model of the galaxy's absorption spectrum, $G_a(\lambda)$, is given in principle by:

$$G_a(\lambda) = \sum_{i=1}^{m} a_i S_i(\lambda), \tag{3.7}$$

where $S_i(\lambda)$ are individual shifted and broadened absorption spectra taken from a suitable library, and a_i are the relative contributions of the i'th spectrum to the final model. Therefore, fitting the galaxy absorption spectrum is a linear least-squares problem, which requires solving the above equation such that:

$$\|aS - G_a\| = \text{a minimum}, \tag{3.8}$$

where G_a is the n vector describing the observed galaxy absorption spectrum, S is the $n \times m$ array of shifted and broadened absorption spectra, and a is the m vector containing the solution coefficients. The solution is made more physical by solving the problem as a non-negative least-squares (NNLS) problem, such that there cannot be negative contributions from the library (i.e., each element of a must be greater than or equal to zero). The NNLS fit was performed using a FORTRAN90 algorithm based on the original work of Lawson & Hanson (1974).

It is important that only the regions of the galaxy spectrum unaffected by emission are used to constrain the NNLS fit. Where emission lines do not fall directly in absorption features, this does not affect the quality of the fit a great deal, since at least *part* of the absorption feature can be used to constrain the fit. In the case of Hβ, however, the result of omitting the emission region from the NNLS fit is that the Hβ *absorption* line is effectively unconstrained. This can be a severe problem, since Hβ is the most strongly age-sensitive feature within the wavelength region being considered, and so the NNLS fit is free to fit a variety of different-aged components which may not necessarily be present in the galaxy. For this reason, it is necessary to use a library of spectra which are generally similar in character to the galaxy. Where the signal to noise of the input galaxy spectrum is low, however, even using a 'reasonable' spectral library can result in spurious fits. It was necessary, therefore, to visually inspect the result of the NNLS fit before accepting it.

The spectral library used in this investigation is composed entirely of the single stellar population (SSP) model spectra of Vazdekis (1999) as used in Chapter 2. These spectra are models of stellar populations composed of a single metallicity, formed at the same epoch, therefore having the same age. The library consists of a grid of SSP models with different ages (from 1 - 17 Gyr) and metallicities ([Fe/H]= $-0.7, -0.4, 0.0$(i.e., solar) and+ 0.2). SSP models were used rather than an empirical library of observed stars and galaxies, in the hope of allowing a more physical interpretation of the weights assigned to each library spectrum.

Small differences in the continuum shape of the galaxy and the library can create a systematic offset in the fit which can result in a poor overall fit to the absorption lines. To avoid this, both the library and galaxy spectra are normalised by their continuum before running the NNLS fit. The shape of the continuum does, however, hold some information about the stellar populations in the galaxy, which is lost by removing this shape before the fit. This doesn't affect the quality of the emission correction, but should be kept in mind when interpreting the weights given to each SSP model in the fit.

Once an acceptable fit to the absorption spectrum of the galaxy is made, this fit is subtracted from the galaxy spectrum, which should leave, in principle, only the noise spectrum combined with the signature of any emission lines present. Figure 3.7 shows the result of fitting the SSP model library to a central spectrum of NGC 584. The shaded regions indicate the portions of spectrum used in the NNLS fit. Note that the region around the three suspected emission lines: [OIII]$\lambda\lambda$4959, 5007 and Hβ; are not included in the fit. The 'window' around these features is taken to be ± 700 km s^{-1} about the wavelength of the emission feature shifted to the systemic velocity of the galaxy.

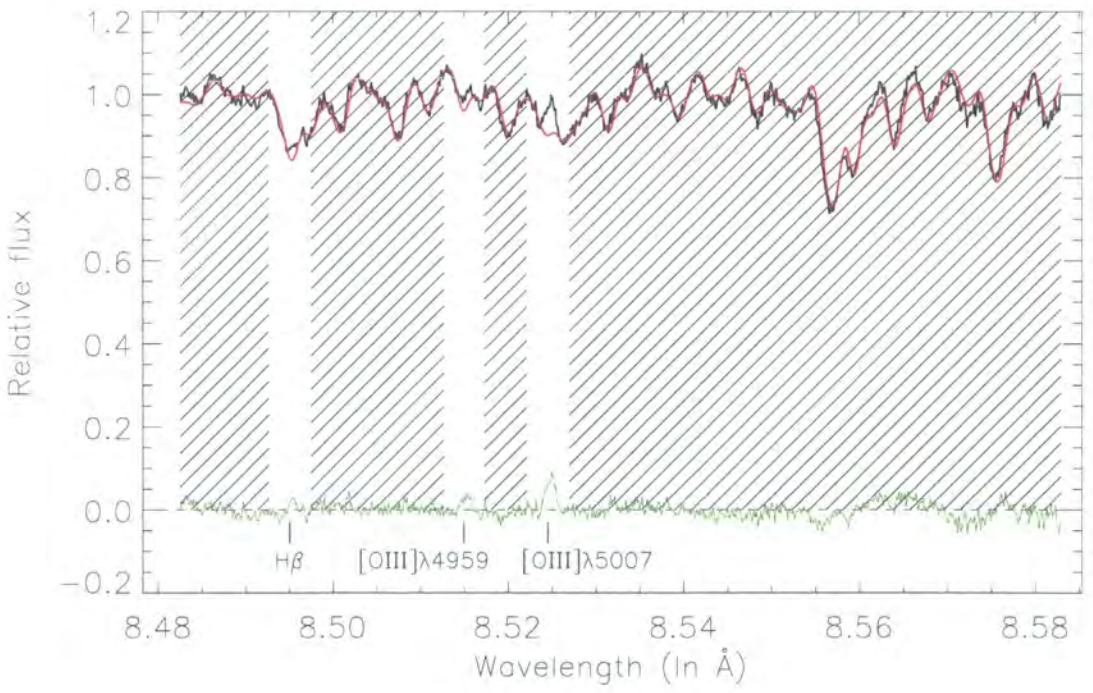

Figure 3.7: Example of fit (red line) to the central absorption spectrum of NGC 584 (black line). Subtracting the absorption model clearly reveals the emission features in the residual spectrum (green line). The emission features can then each modelled by e.g., a Gaussian function, which is then subtracted from the original spectrum.

3.4.3 Modelling the Emission Lines

In order to subtract the emission lines from the galaxy spectrum, it is necessary to model the emission component. Once an acceptable fit to the absorption spectrum of the galaxy has been subtracted, the emission lines are modelled by fitting a Gaussian function to each of the distinct peaks in the residual spectrum. The emission spectrum, G_e, is then described by the sum of N Gaussians:

$$G_e(\lambda) = \sum_{i=1}^{N} I_i e^{-\frac{1}{2}[\frac{\Delta\lambda_i}{\sigma_i}]^2}, \tag{3.9}$$

where I_i is the normalisation of the i'th Gaussian. $\Delta\lambda_i = \lambda - \lambda_i$, where λ_i is the mean wavelength, in Ångströms, of the i'th emission feature, and is related to the line-of-sight velocity, $v_{\rm los}$, of the i'th emission line by:

$$v_{\rm los} = c\frac{\lambda_{i_0} - \lambda_i}{\lambda_{i_0}} = c(\lambda'_{i_0} - \lambda'_i), \tag{3.10}$$

where c is the velocity of light, λ_{i_0} is the rest wavelength of the i'th emission line, and λ' implies units of ln(Ångström). Similarly, σ'_i, the dispersion of the Gaussian (in ln(Ångström) units), is related to the line-of-sight velocity dispersion by:

$$\sigma_{\rm los} = c\sigma'_i. \tag{3.11}$$

From Figure 3.7, the three strongest emission lines within the range of the data are: Hβ λ4863 Å, and the two [OIII] lines at λ4959 Å and λ5007 Å. Therefore, there are three emission lines to be fitted with Gaussians in the model (i.e., $N = 3$ in equation 3.9). Since the lines are quite weak, and are sufficiently separated in wavelength not to contribute any flux to each other, they can be fitted independently by dividing the residuals spectrum into three segments centred around the feature and treating each as a separate, single Gaussian. Once the (I, λ, σ) have been found for each of the emission lines, the three Gaussians are combined to form a single model emission line spectrum, which is be subtracted from the original data.

Figure 3.8 illustrates the effect of removing the emission line model from the galaxy spectrum, showing the original spectrum, the effective fit to the emission features, and the corrected spectrum which is used to determine the final kinematics. Clearly, removing the emission lines can have a non-negligible effect on the spectrum, especially for the Hβ absorption feature, which can have a significantly different shape before and after the correction. This should have a measurable effect on the kinematics derived.

Where the emission features were too weak to be reliably detected, no Gaussian was fitted. The threshold used was that the peak of the Gaussian must be greater in amplitude

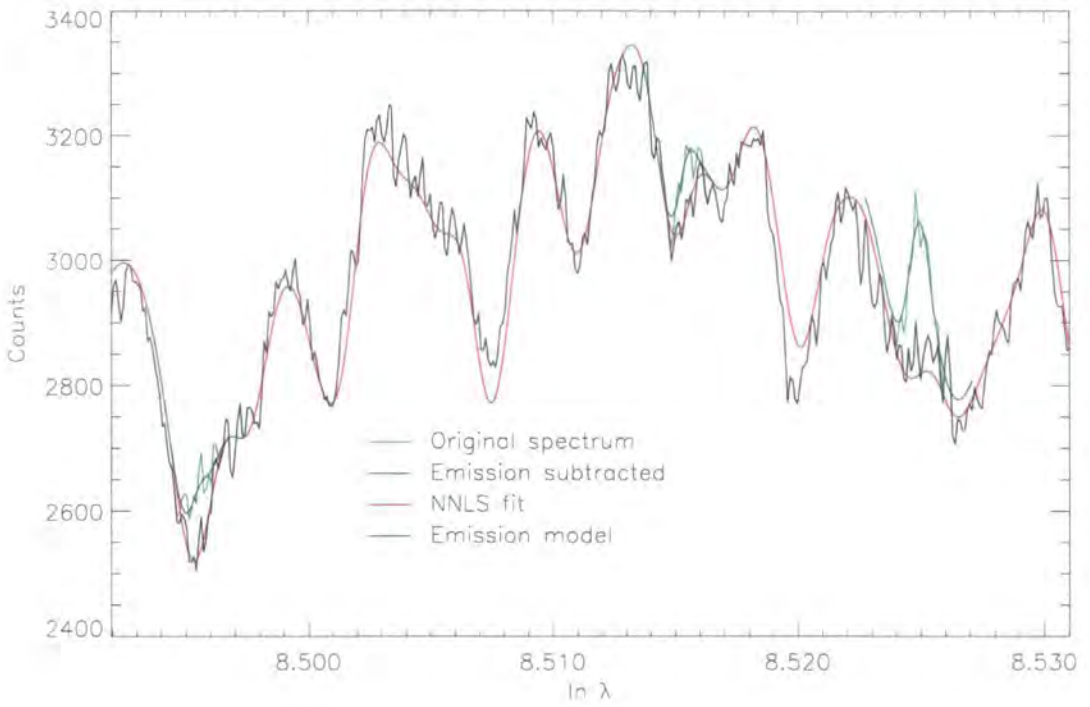

Figure 3.8: Example of a central spectrum of NGC 584 before and after the subtraction of the emission model. The original spectrum is shown (green line) overplotted with the smooth fit of the model absorption spectrum (red line) and emission spectrum (blue line). The resulting emission-subtracted spectrum is given by the black line. It is this spectrum which is used to derive the final kinematic parameters. This shows that the effect subtracting the emission from the Hβ feature is significant in this case.

than one standard deviation of the noise around the same spectral region. Also, to avoid fitting to noise peaks in the data, Gaussians with a dispersion less than a single pixel in wavelength, or larger than half the total width of the spectral window being used in the fit, were also rejected. This helped to minimize false features being fitted and removed from the data, however, the fits were also checked by eye to ensure reasonable results.

3.4.4 Reliability of Emission Correction

In order to test whether the peaks in the residuals of the galaxy spectra can be attributed to nebular emission lines, and are not caused simply by a poor fit to the absorption spectrum, it is possible to carry out the same process outlined above, but on an emission-free, synthetic galaxy spectrum. By using an SSP models from the library itself, it is also possible to determine to what extent the weights of the fitted library spectra given by the NNLS routine actually relate to the galaxy's stellar populations. For example, if the NNLS solution fits a galaxy as 70% 12 Gyr plus 30% 2 Gyr, this could be evidence that the galaxy cannot be represented with a single-age population, and perhaps harbours a young stellar component.

To test whether the emission-line signature could arise as a result of poor signal to noise, varying amounts of white noise were added to an emission-free synthetic galaxy spectrum, and the fitting process was conducted. The synthetic galaxy consists of a single 12 Gyr, solar metallicity, SSP model broadened by a Gaussian with an effective dispersion of 200 km s^{-1}.

The top half of Figure 3.9 shows the input spectra with varying signal-to-noise ratio, and the corresponding fit to the absorption lines via the NNLS routine described above. The residuals are plotted in the bottom half of Figure 3.9, and illustrate that, even for low signal to noise ratios, there are no peaks in the residuals which are as strong as those detected in the sample galaxies. Even around the Hβ region, where the fit is very poorly constrained, the absorption line is fitted well, without over-estimating the strength of the line and hence creating false 'emission line' signatures.

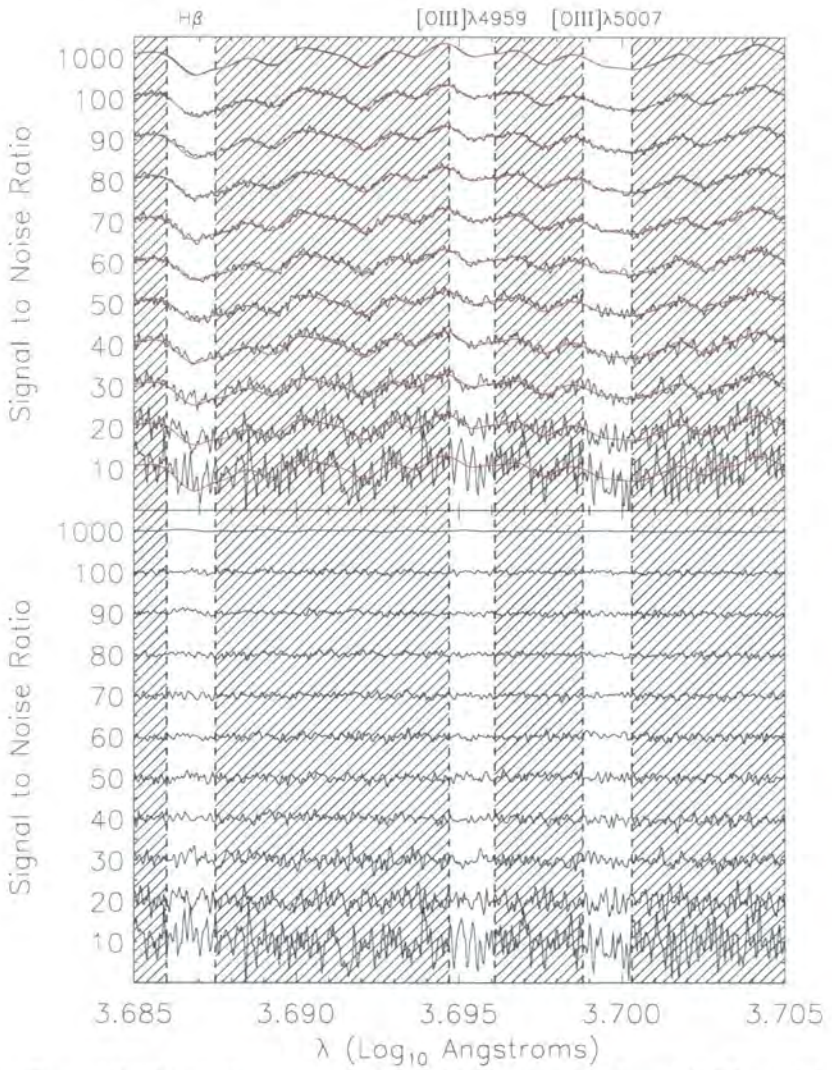

Figure 3.9: Top plot shows the emission-free, Gaussian-broadened SSP model with different signal-to-noise ratios, overplotted with the resulting NNLS fit. The bottom plot shows the residuals of these fits for the corresponding signal-to-noise ratios. Even for low signal-to-noise ratios, the fit does not result in false emission line signatures resulting from a poor fit.

One of the reasons for using a grid of SSP models as the library of absorption spectra was to allow a straightforward interpretation of the weights attributed to the spectra as an indication of the stellar populations in the galaxy. By examining the distribution of weights assigned to the synthetic galaxy spectrum, it is possible determine how reliable such an interpretation would be.

The SSP model used in the above simulations was a single, 12 Gyr, solar metallicity population. This exact model is contained within the library being fitted, along with the full range of ages and metallicities available to the library. If the weights from the NNLS routine can be interpreted directly as an indication of the populations which are present, there should be only one weight, which should be assigned to the 12 Gyr, solar metallicity model.

However, this is not the case. Even for the spectrum with virtually no added noise, the result of the NNLS fit consists of two components: 8% 6 Gyr + 92% 13 Gyr (both solar metallicity). Even by including the Hβ absorption feature in the NNLS fit to better constrain the choice of age, the same resulting weights are found, only with a slightly lower fraction of the 6 Gyr component. The reason that the original input population is not perfectly recovered is most probably due to the loss of the continuum information, as all spectra are normalised by the continuum before performing the fit. One way to reduce this effect would be to not remove the continuum information, but include a simple polynomial term in the linear combination during the NNLS fit which would correct for differences in the continuum shapes. However, even then, interpreting the weights of the combination is only a first-order indication of populations which may be present.

3.4.5 Emission in the Sample Galaxies

All galaxies in the sample were examined for emission lines. To increase the reliability of discovering these faint emission lines, the templates were fitted to the two-dimensional long-slit data after binning in radius to a minimum S/N. The S/N of the data correspond to the same S/N as that used to determine the Hβ kinematics (i.e., S/N $\geq$ 55). Figures 3.10-3.19 show the residual images after subtraction of the model absorption spectrum. Where emission lines are present, the show up as white features above the noise level. At the extremities of the radial dimension in these images, the fit to the spectrum of the galaxy (and especially to the Hβ feature) tends to be poorer due to the lower signal to noise ratio. Where the signature of emission is obviously from a poor fit of the library to the data, no emission model was subtracted from the data.

From Figures 3.10-3.19, it can be seen that, of all the galaxies in this sample, only NGC 584 shows any significant amount of Hβ emission. Only this galaxy has had a model of the emission spectrum fitted and subtracted before deriving the kinematics given in §3.5. A brief discussion of the emission line residuals is given in the caption of each figure.

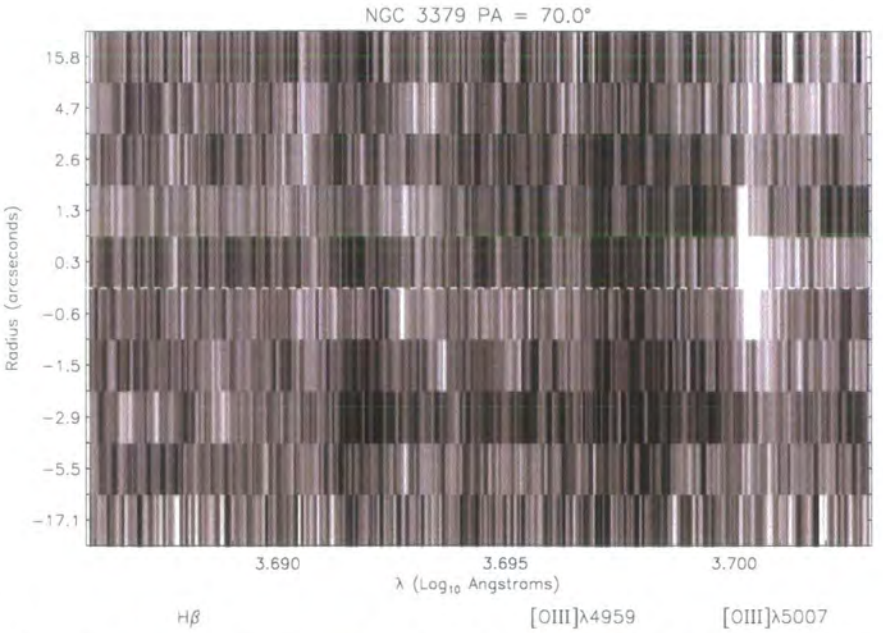

Figure 3.10: Two-dimensional residuals for NGC 3379 along the major-axis. The pixels have been stretched in radius for clarity. The white dashed line indicates the galaxy centre. Note that the radial spacing is not linear, as the spectra have been binned radially to obtain a minimum signal-to-noise ratio of ~ 50, similar to the binning for the kinematics presented in § 3.5. The central [OIII]λ5007 emission can clearly be seen in this galaxy, which extends to around $2''$ on the major-axis. The [OIII]λ4959 is barely visible on this image, and no Hβ emission is detectable above the noise level.

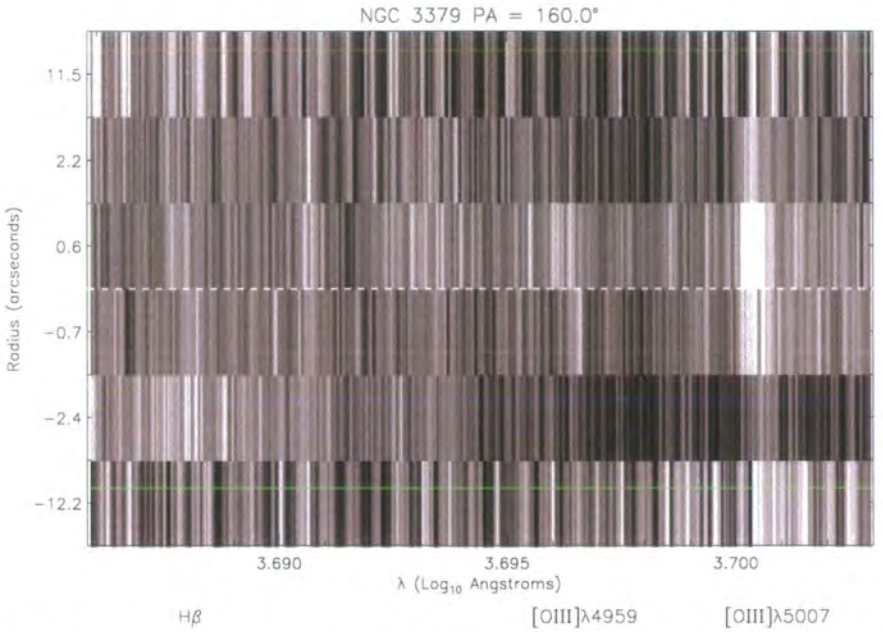

Figure 3.11: Same as Figure 3.10, but along the minor-axis. Again, the central [OIII]λ5007 emission can clearly be seen, with little evidence of [OIII]λ4959 or Hβ emission above the noise level.

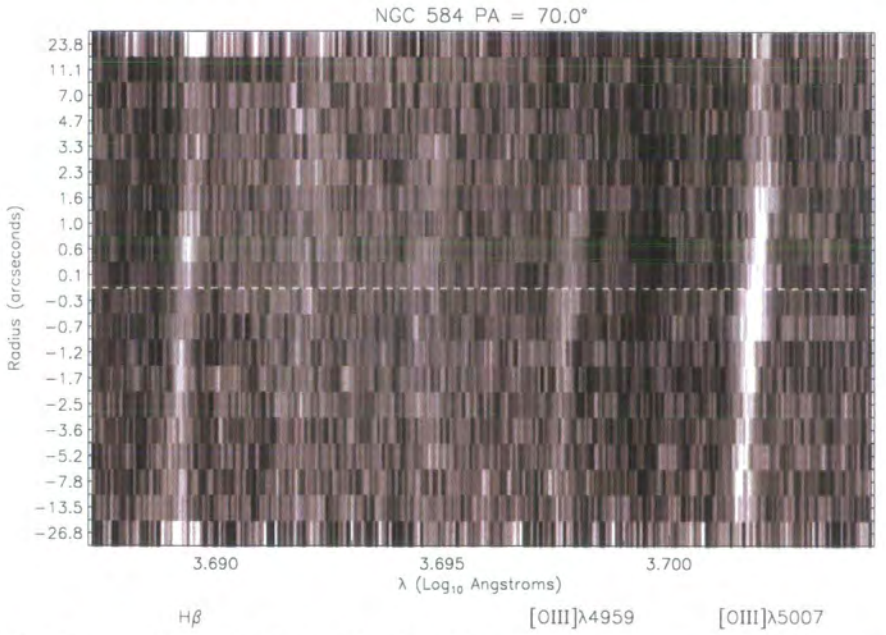

Figure 3.12: Same as Figure 3.10, but for NGC 584 close to the major-axis. The rotation of the gas can clearly be seen in the [OIII]λ5007 line, as well as the fainter [OIII]λ4959 and Hβ lines. The apparently strong Hβ emission in the largest radial bins are due to a poor fit to the Hβ absorption feature do to low signal-to-noise.

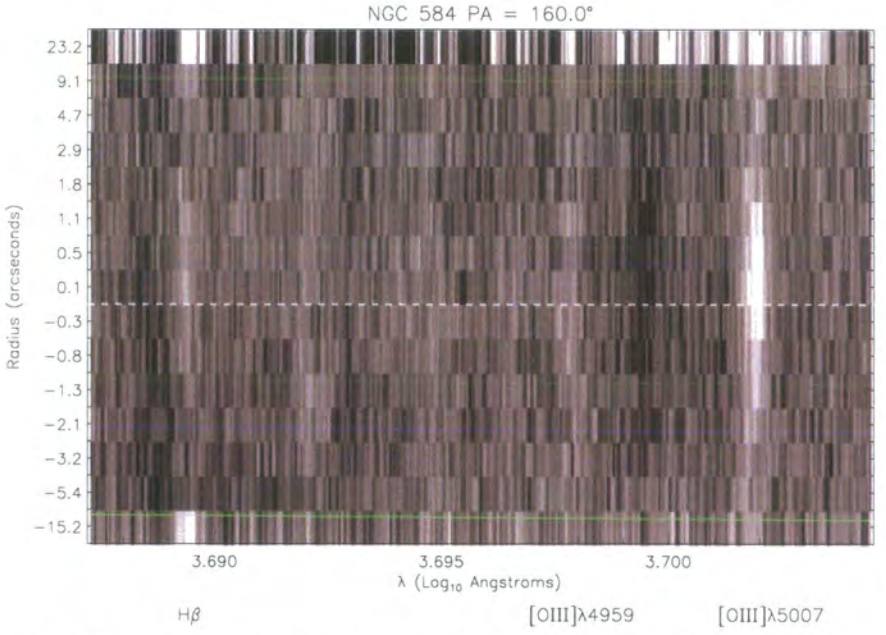

Figure 3.13: Same as Figure 3.10, but for NGC 584 near the minor-axis. From this image, there doesn't appear to be much rotation of the gas along the minor-axis, and the emission is less radially extended.

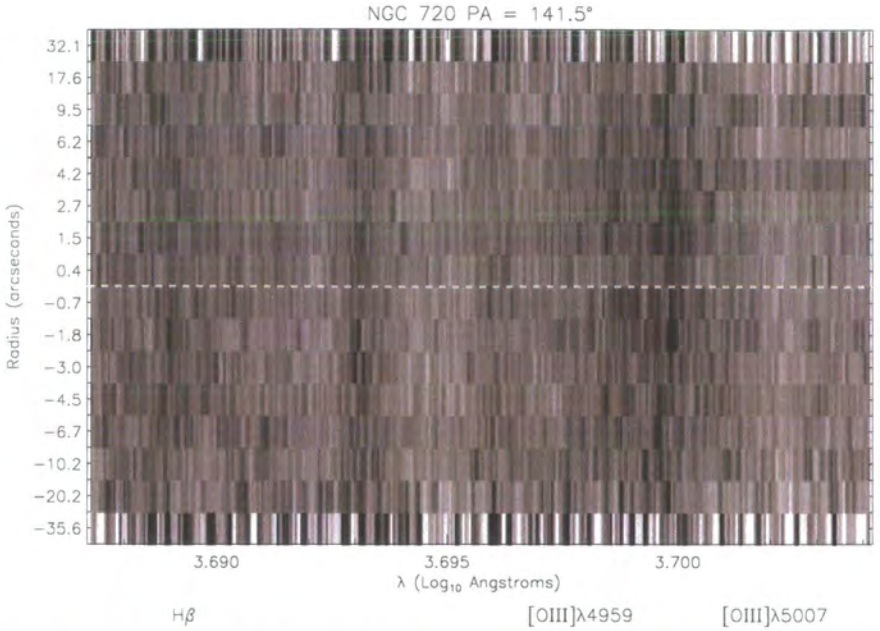

Figure 3.14: Same as Figure 3.10, but for NGC 720 along the major-axis. There is no detectable emission features above the noise level.

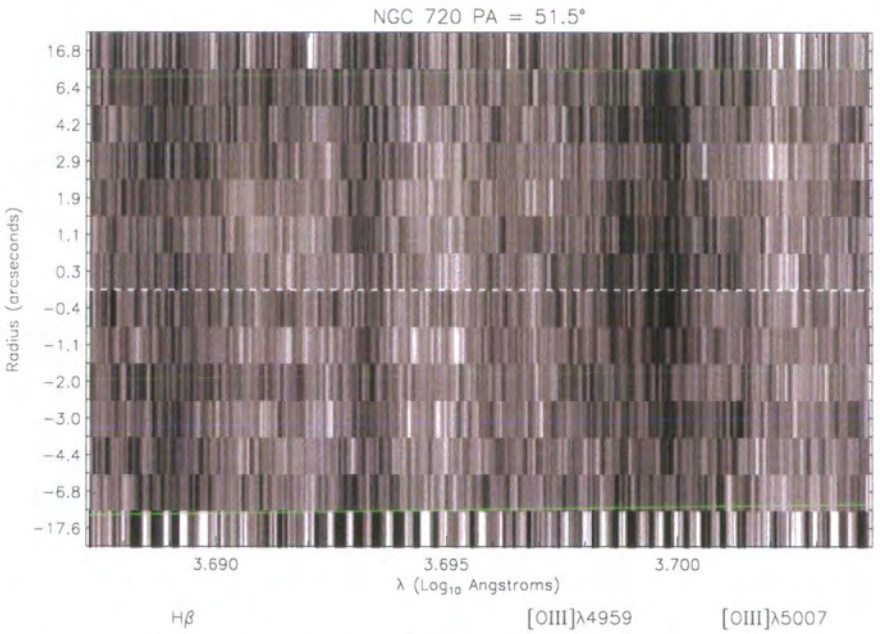

Figure 3.15: Same as Figure 3.10, but for NGC 720 along the minor-axis. Again, no emission is detected.

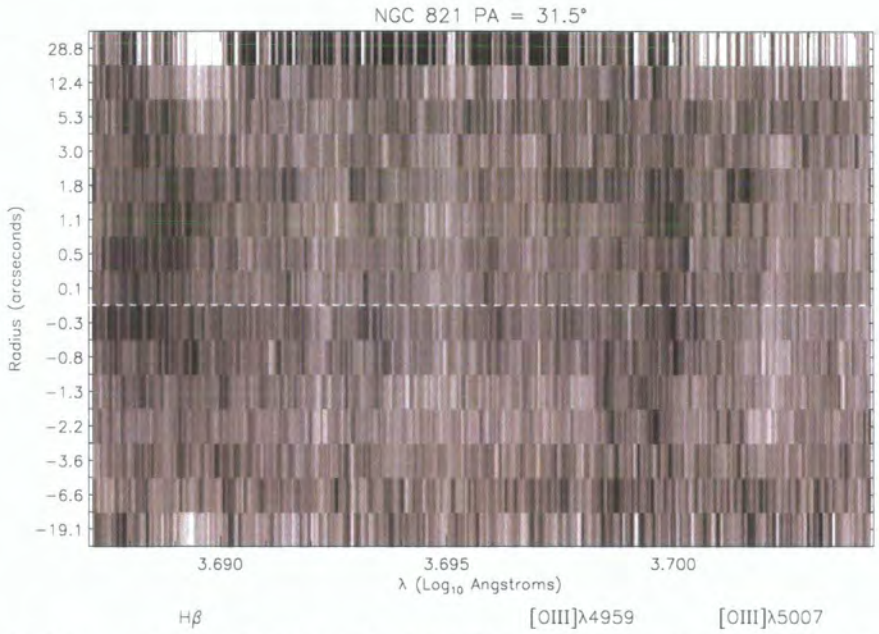

Figure 3.16: Same as Figure 3.10, but for NGC 821 along the major-axis. There is some faint [OIII]λ5007 emission visible, however, this is at a very low-level compared to the noise of the image. There is no detectable Hβ emission.

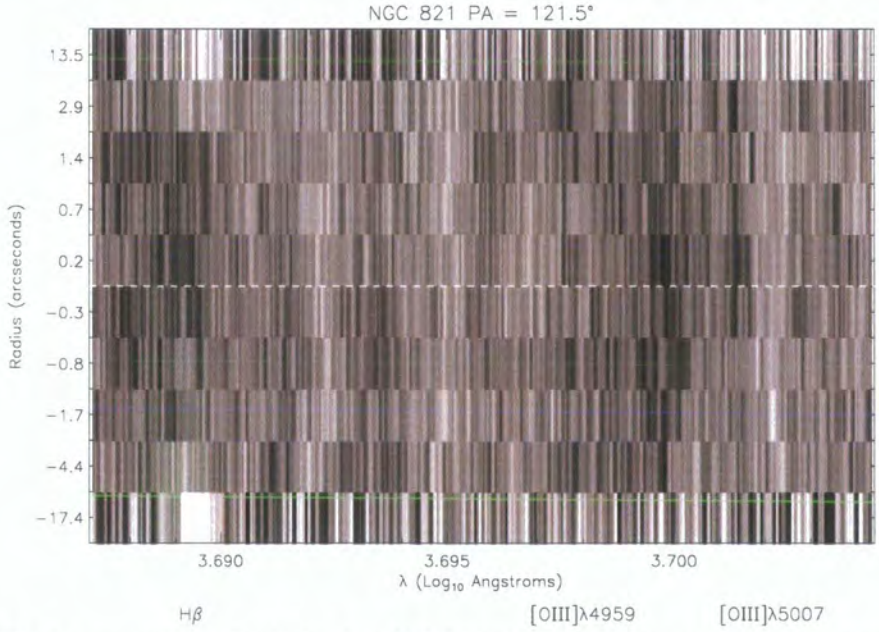

Figure 3.17: Same as Figure 3.10, but for NGC 821 along the minor-axis. As for the major-axis, there is perhaps some weak [OIII]λ5007 emission, but no detectable Hβ emission.

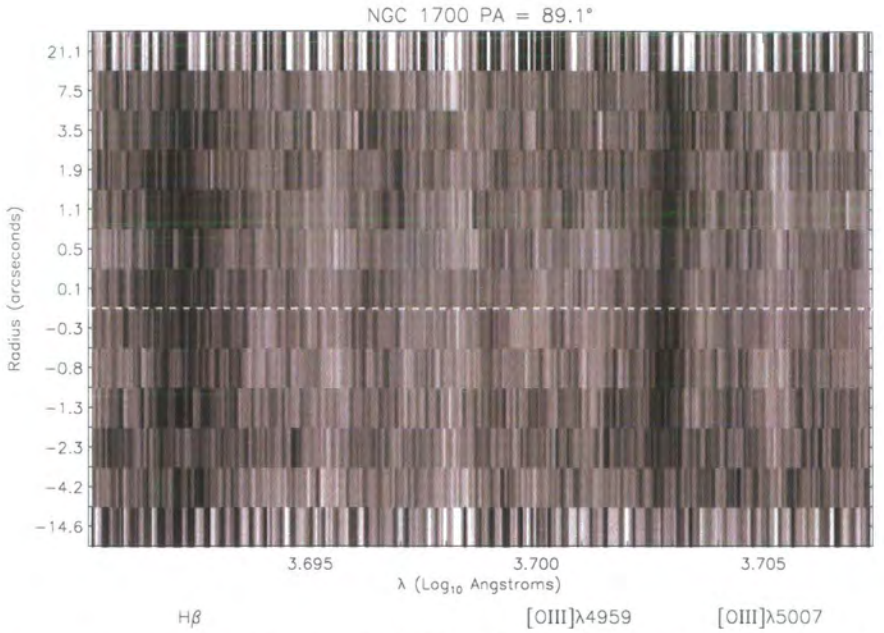

Figure 3.18: Same as Figure 3.10, but for NGC 1700 along the major-axis. There is some faint [OIII]λ5007 emission, but no evidence for significant Hβ emission.

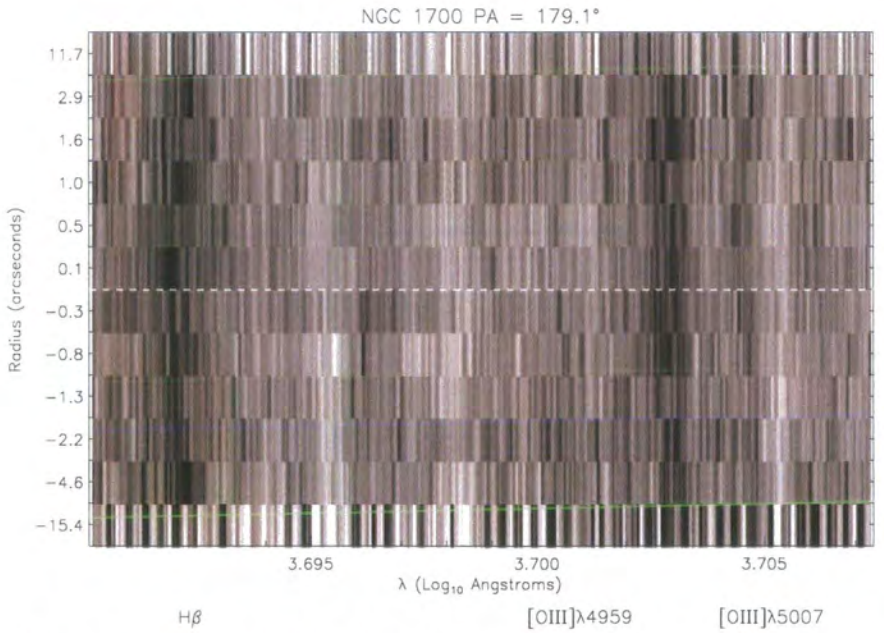

Figure 3.19: Same as Figure 3.10, but for NGC 1700 along the minor-axis. As with the major-axis, there is some faint [OIII]λ5007 emission, but no detectable Hβ emission.

3.4.6 Effect of Emission Removal on Hβ Kinematics

The only galaxy to have a measurable amount of Hβ emission is NGC 584. Other galaxies, including NGC 3379, show signs of [OIII]λ5007 emission, but no significant Hβ emission. This is not very surprising, as the emission spectra of H II regions are strong in H I recombination lines, but the strength of [OIII]λ5007 and [OIII]λ4959 lines can differ greatly (Osterbrock 1989, Carrasco et al. 1995). As a result, only the spectra of NGC 584 are corrected for Hβ emission before deriving the stellar kinematic profiles presented in §3.5. The effect and success of removing the Hβ emission is now discussed.

Figure 3.20 shows the kinematics derived from the Hβ region before and after the emission correction. The Hβ emission is generally very low, and removing this emission only effects the h_4 term of the stellar kinematics significantly. Where the emission is strongest, the corrected h_4 terms become less negative, implying that the LOSVDs are less flat-topped without the emission filling in the base of Hβ absorption feature. Figure 3.21 confirms this, showing the derived LOSVD at 2″ radius before and after the emission correction.

To check that this is not merely an effect of removing non-Gaussianity from the spectrum, as opposed to actually subtracting true emission, the fitting process was conducted on a synthetic emission-free galaxy spectrum with a strongly negative h_4 term. After subtracting the Gaussian-broadened model, the residual spectrum shows no features which can be mistaken for emission lines (Figure 3.22). This supports the interpretation that the residual features being subtracted are due to nebular emission. The Hβ kinematics given in §3.5 have therefore been corrected for emission.

3.4.7 Profiles of Emission Line Properties

The emission lines detected in NGC 584 and NGC 3379 show an extended structure, i.e., emission was detected at more than one radial position. It is therefore possible, using the information from the Gaussian fits, to determine intensity and kinematic profiles for the gas. For both galaxies, the strongest of the three lines is always [OIII]λ5007 Å, and so this line was used to estimate the velocity and velocity dispersion of the gas. Since the emission is generally very weak, only a single Gaussian could be reliably fit to the emission line.

The resulting kinematic profiles are given in Figures 3.23 to 3.25, as well as the equivalent width of the [OIII]λ5007 Å line, and the ratio of the [OIII]λ5007 and [OIII]λ4959 equivalent widths. This ratio was found empirically to be $\simeq 3$ by Ho et al. (1993) from a sample of low-ionisation nuclear emission-line regions (LINERs), which is the value predicted by theoretical transition probabilities (Bowers & Deeming 1984). In general, the values of this ratio found in this work agree with this value, although the uncertainties are large due to the difficulty in measuring the weak signature of the [OIII]λ4959 emission.

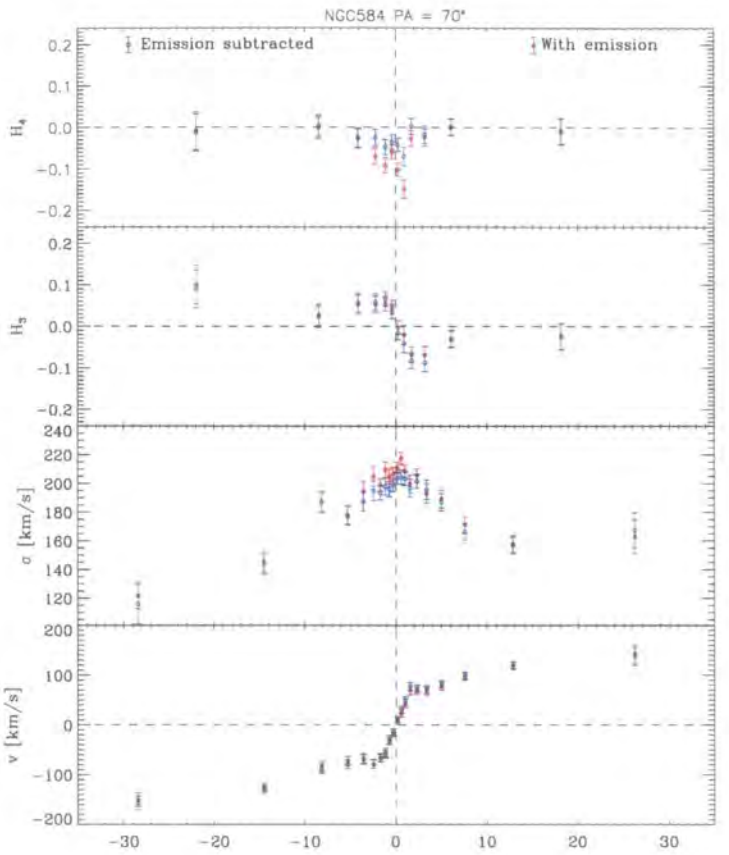

Figure 3.20: Comparison of NGC 584 kinematics before (red points) and after (blue points) subtraction of the emission line model. Only the h_4 parameter is significantly affected, implying that the LOSVD becomes less flat-topped in the absence of the Hβ emission.

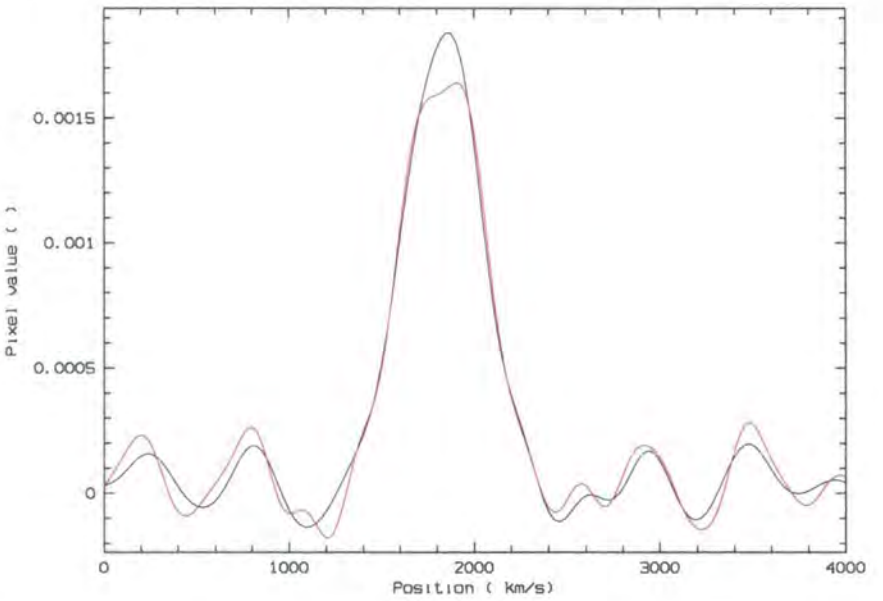

Figure 3.21: Comparison of LOSVDs of NGC 584 at 2″ radius before (red line) and after (black line) subtraction of the emission line model. This illustrates the effect of the Hβ emission on the shape of the LOSVD.

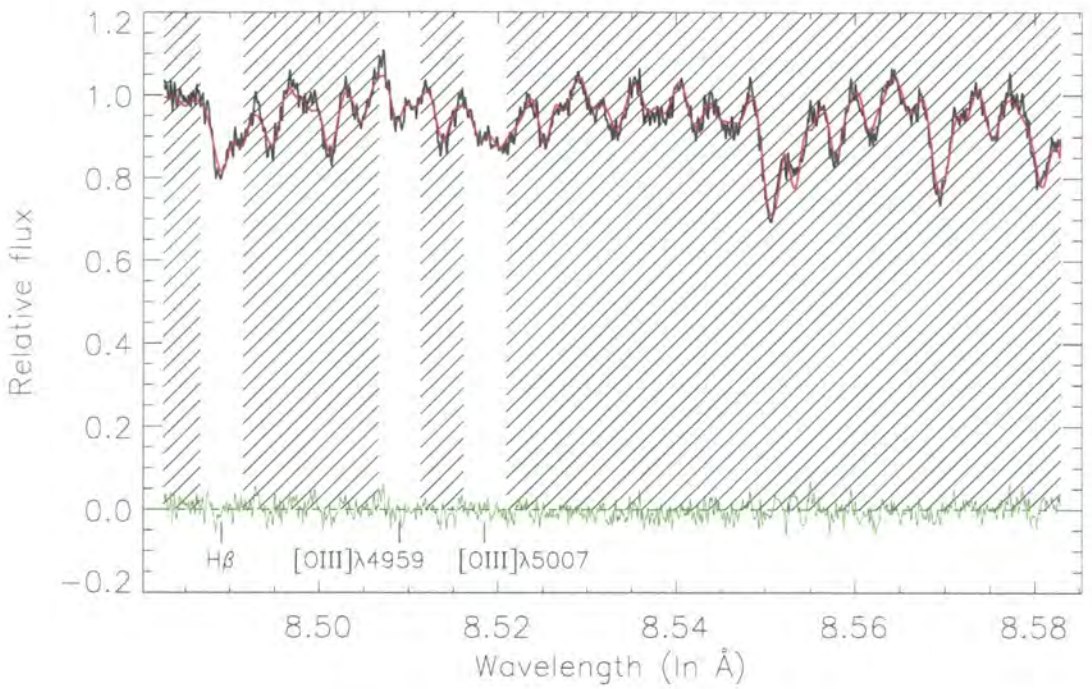

Figure 3.22: Resulting fit and residual spectrum of an emission-free model with an intrinsic h_4 value of -0.2. This illustrates that the residuals peaks found for NGC 584 (see Figure 3.7) are not caused by significant intrinsic non-Gaussianity of the absorption lines.

Errors for the gas properties were derived via Monte Carlo simulations of the residual-fitting program. For each radial bin, a synthetic emission residual spectrum was created by adding random noise to a noise-free Gaussian profile, resulting in a spectrum with the same signal-to-noise ratio as the data. Thirty realisations were generated for each radial bin, from which the rms variation in velocity and velocity dispersion were determined, as well as for the measurement of equivalent widths.

A brief synopsis of the profiles of emission line properties is given below.

NGC 584

The major-axis rotation of the gas in NGC 584 is clearly seen in the residual image after the absorption spectrum has been subtracted (Figure 3.12). By fitting the emission lines, it is possible to quantify this rotation. Figures 3.23(a) and (b) present the mean velocity and velocity dispersion profiles derived from the strong [OIII]λ 5007 line for the major- and minor-axes of NGC 584 respectively. Also plotted is the integrated flux under the fitted Gaussian as a function of radius, indicative of the general strength of the emission flux. The equivalent stellar kinematics are overplotted for reference.

From Figure 3.23(a), the gas can be seen to be rotating in the same sense as the

stars, but rises to its peak rotation velocity more steeply than the stars. Beyond 10″, the errors on the velocity become large, as the intensity of the emission falls rapidly. Along the minor-axis (Figure 3.23(b)), the gas also seems to follow the dynamics of the stars, showing a little rotation.

From the equivalent width measurements, it can be seen that the ionised gas component is rather flattened (i.e., more extended along the major-axis than the minor-axis), much like the stellar body of the galaxy. Taking the error-weighted mean velocity dispersion to be ~ 100 km s^{-1}, and the peak rotation velocity of the gas as ~ 200 km s^{-1}, $v/\sigma \sim 2$ for the gas, indicating that there is a high degree of rotational support, suggesting that the gas may take the form of a disk.

Warm gaseous components are often observed to co-exist with a similarly distributed dust component (Michard 1999). NGC 584 was detected by the IRAS satellite in the 100μ pass-band with a flux of 0.590 ± 0.102 Jy (taken from the NED database), suggesting that this galaxy has some form of thermal component. Figure 3.24 shows a colour-index image of NGC 584 using archival HST data. This image was made simply by taking the logarithm of the ratio of two images taken with different filters. Here, the FW814 and FW555 filter were used, roughly corresponding to I- and V-band respectively. This image shows a central structure which is brighter in the I-band than in the V-band, typical of a dust component. The dust component doesn't appear to be as extended as the nebular emission, being contained within the central $2-3''$. However, it does seem to be similarly flattened, suggesting the two may be related.

The presence of gas and dust in this galaxy is evidence that there may be some ongoing star-formation in the central regions. The dynamics of the gas, and distribution of the dust, suggest that the star-forming regions and material may be distributed in a disk rotating around the minor-axis. However, from the weak Hβ emission, it would appear that the rate at which mass is being transformed into stars is rather low.

NGC 3379

Figure 3.25 presents the emission line profiles for (a) the major-axis and (b) the minor-axis of NGC 3379. The emission in NGC 3379 appears more centrally concentrated than in NGC 584, and the overall strength of the emission is also less. However, it is still possible to detect some rotation along the major-axis (Figure 3.25(a)), and some evidence for rotation along the minor-axis (Figure 3.25(b)). This is consistent with the findings of Pastoriza et al. (2000), who used the stronger H_α and [NII]λ6584 lines to determine the gas kinematics. They find a peak rotation on the major-axis of ~ 200 km s^{-1}, and a value of ~ 100 km s^{-1}on the minor-axis. Although the uncertainties on the data presented here are large, it can be seen that these values are of a similar order.

The fact that the gas kinematics do not follow that of the stars may suggest an external

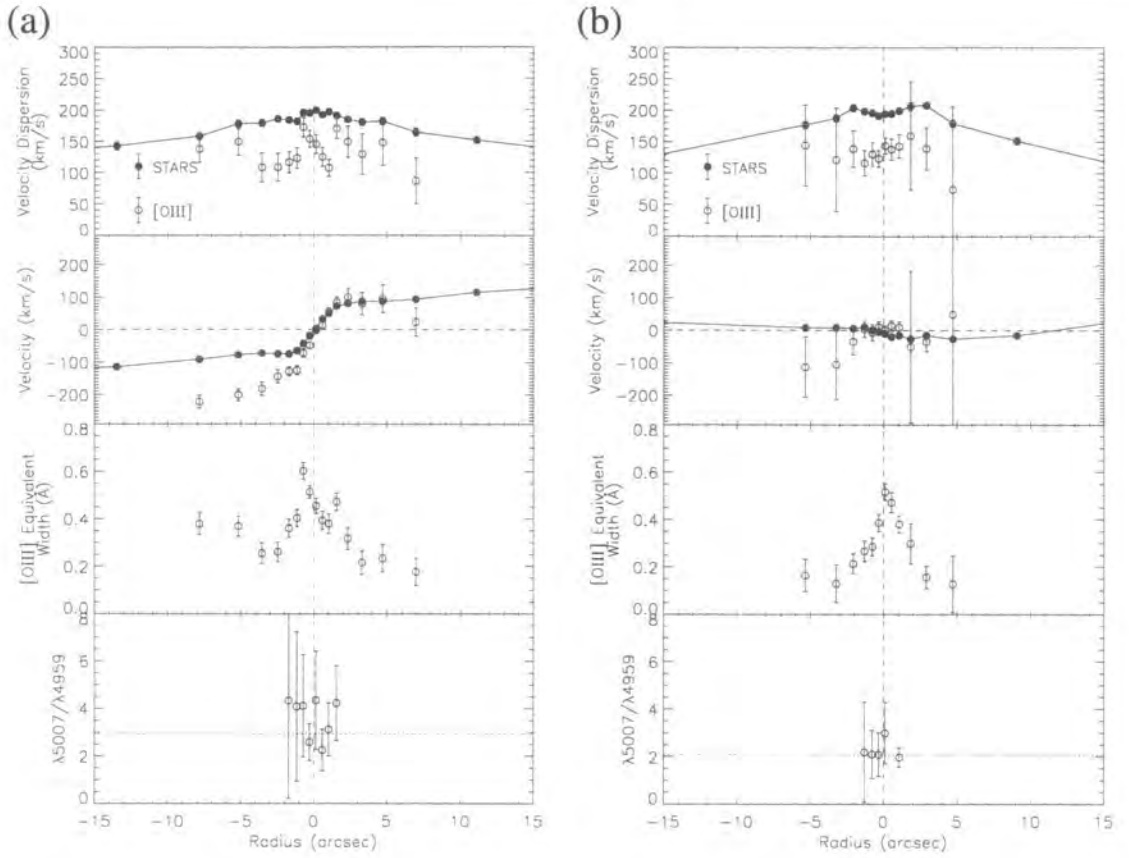

Figure 3.23: Emission line profile derived from the [OIII] emission line residuals of NGC 584 near the (a) major-axis, and (b) minor-axis. On the major-axis, the gas rotates in the same sense as the stars, but with a higher rotation velocity, and lower dispersion, suggesting that the gas is in the form of a rotationally-supported disk. On the minor-axis, there is little rotation, supporting the interpretation that the gas is in equilibrium with the stars, and rotating about the minor-axis. The equivalent width of [OIII]λ 5007 is given, as well as the ratio of [OIII]λ 5007/[OIII]λ 4959. The horizontal line in the latter plot indicates the error-weighted mean of this ratio. Where the [OIII]λ 4959 was too weak to measure reliably, no ratio is given. The values are generally close to the predicted ratio of 2.96 determined from theoretical transition probabilities (Osterbrock 1989).

origin for the gas, being acquired by the accretion of a gaseous body with a different angular momentum. Given the large uncertainties on the measurements, however, it is difficult to draw firm conclusions about the origin of the gas in NGC 3379.

3.5 Comparison of Ca II Triplet and Hβ Kinematics

Once the input data for the FCQ routine is fully reduced, and the input parameters for the routine have been optimised through the Monte Carlo simulations, the stellar kinematic profile of each galaxy can be derived. In this section, the major- and minor-axis kinematics derived from the Calcium II triplet and Hβ features are presented for each galaxy in the sample. The kinematics from the two wavelength regions are plotted together on the same figure to allow the profiles to be easily compared. Each galaxy is presented and discussed individually, with further analysis where necessary.

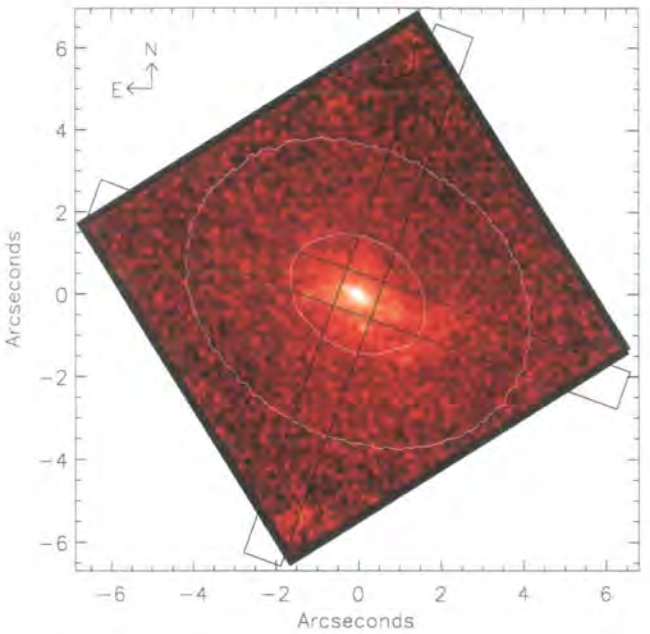

Figure 3.24: Colour-index image of NGC 584 using WFPC2/HST. Only the PC1 chip is shown. Lighter colours imply regions which are brighter in the F814W filter than in the F555W. These regions are due to obscuration of the bluer light by dust in the galaxy. Two representative isophotes are shown (white lines) to illustrate the orientation of the galaxy. Boxes are overplotted to represent the major- and minor-axis slits of the ISIS spectrograph, showing that the dust is more extended along the major-axis than the minor. This is also found for the emission.

Figures 3.26 to 3.40 present the major- and minor-axis parameterized LOSVD profiles. The major-axis profiles also present how the C4, or 'diskiness', parameter varies as a function of major-axis radius. This illustrates the radii at which the disky component is most apparent, and therefore where one may expect to see the most significant differences in the Calcium II triplet and Hβ kinematic profiles which would be due to a young disk component.

The C4 data is given from both ground-based and space-based HST imaging data, as the central C4 values in the ground-based data are severely effected by atmospheric seeing effects, which tend to 'smooth out' the disky distortions. For clarity, the HST C4 data has been rebinned to a sampling of 0.″5, with the error-bars indicating the degree of scatter within the bin. The intrinsic measurement errors on the HST data are generally $\lesssim 0.005$. The ground-based data is taken from CTIO imaging of Kuntschner (2003). The space-based data is taken from the Hubble Space Telescope data archive. The C4 values themselves were all derived using the IRAF package, **GALPHOT** (Franx et al. 1989*b*).

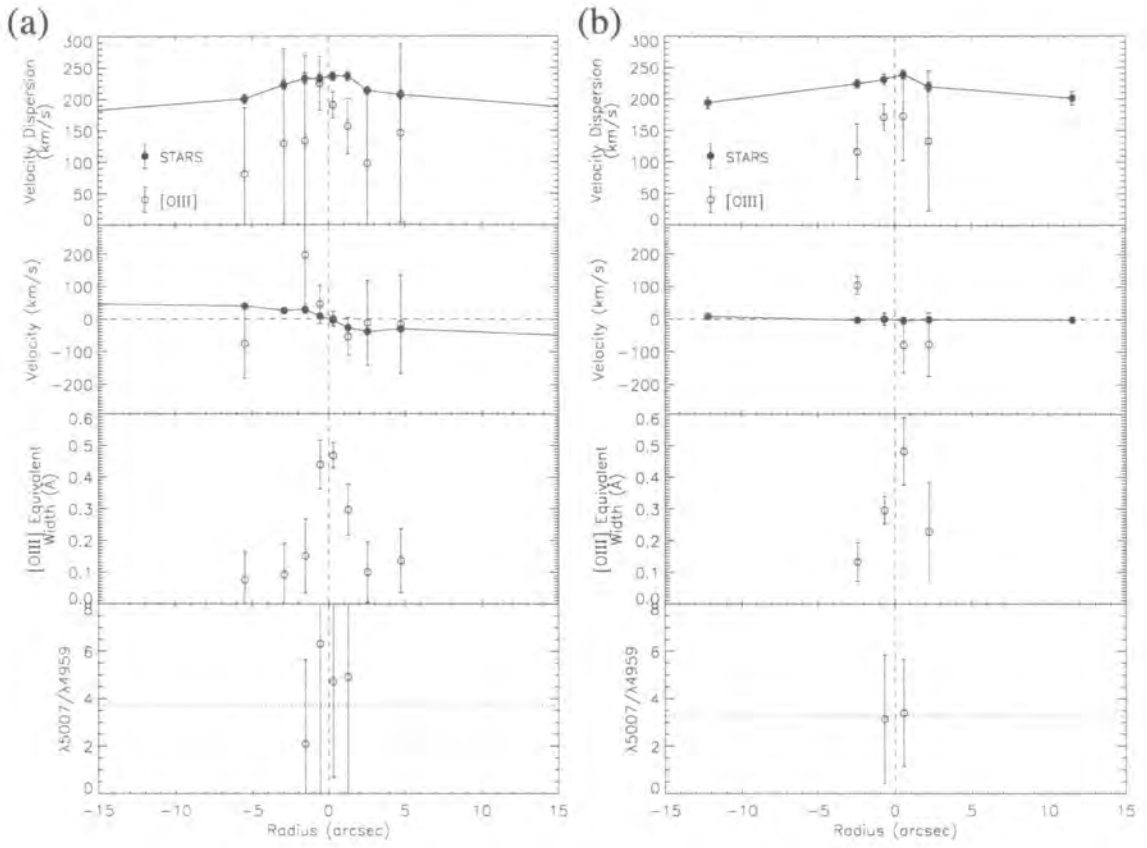

Figure 3.25: Emission line profile for NGC 3379 along the (a) major-axis and (b) minor-axis. On the major-axis, the gas rotates in the same sense as the stars. On the minor-axis, however, there is some weak evidence for rotation which is not observed with the stars. If present, this minor-axis rotation would be consistent with the findings of Pastoriza et al. (2000) based on the stronger H_α and [NII]λ6584 lines; however, the signature is too weak here to draw any firm conclusion. The equivalent width of [OIII]λ 5007 is also given as a function of radius, showing the gas to be concentrated within the central 5″ on both axes. The ratio of [OIII]λ 5007/[OIII]λ 4959 is roughly consistent with 2.96 (Osterbrock 1989), however the errors are large due to the weak signature of the [OIII]λ 4959 line.

3.5.1 NGC 3379

NGC 3379 is included here as our control object. This galaxy is an extremely well studied object, and as such has well established and characterised properties. It has a stereotypical $r^{1/4}$ brightness profile (de Vaucouleurs & Capaccioli 1979), almost perfectly elliptical isophotes, and colours characteristic of an old stellar population (Peletier et al. 1990, Trager et al. 2000). Even though there exists strong evidence that this galaxy is in fact a misclassified S0 galaxy (e.g., Statler & Smecker-Hane 1999, hereafter SSH99), it is still a good example of a galaxy which we would not expect to contain a young component associated with disky isophotes. This data provides a benchmark for the quality of our results, and the scale of differences between the Calcium II triplet and Hβ kinematics which can arise even in the absence of a young disk.

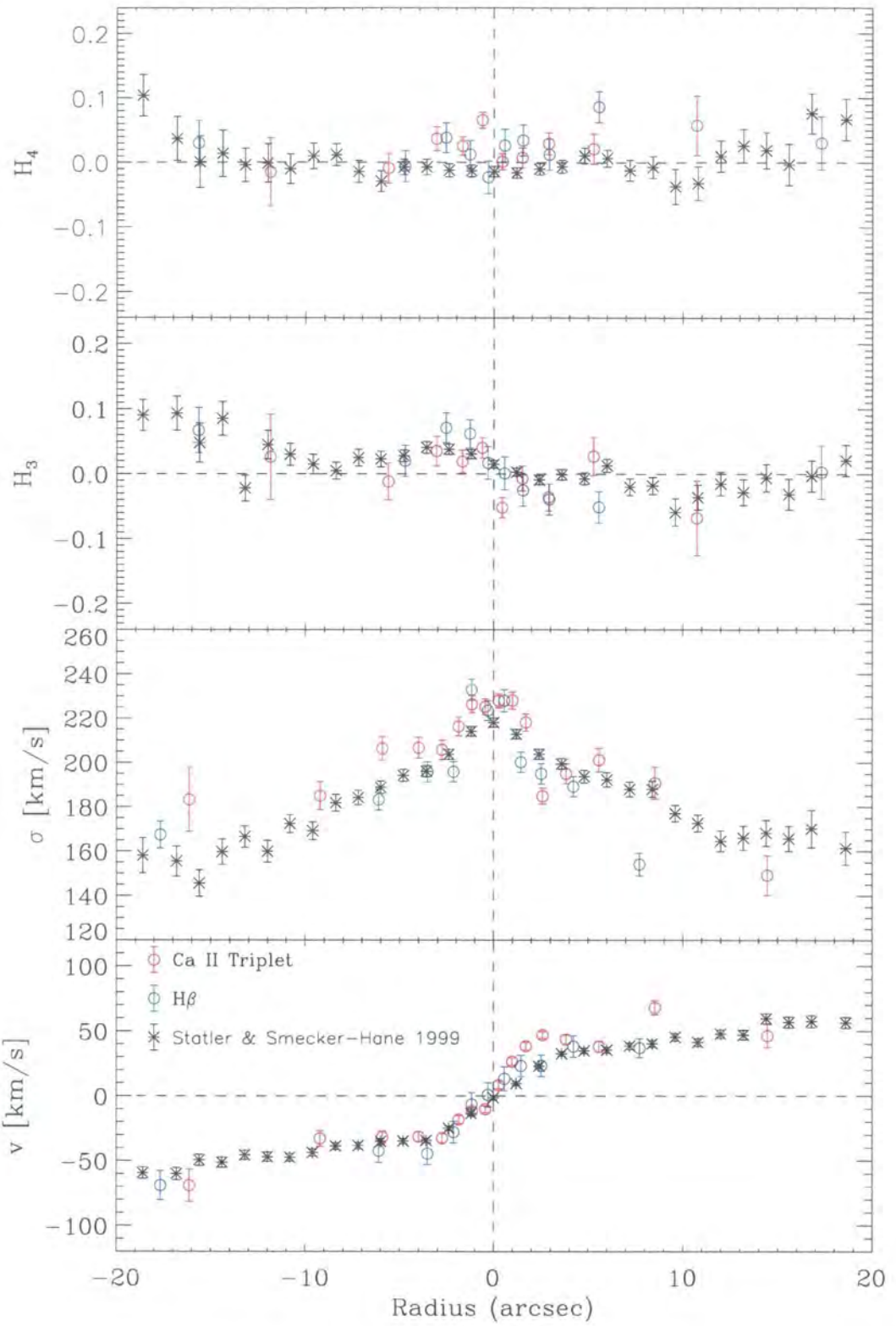

Figure 3.26: Comparison of Calcium II triplet (red circles) and Hβ (blue circles) kinematics with the data of SSH99. All three data sets are in good agreement, showing that the data presented in this work are of good quality, and free of significant systematic errors.

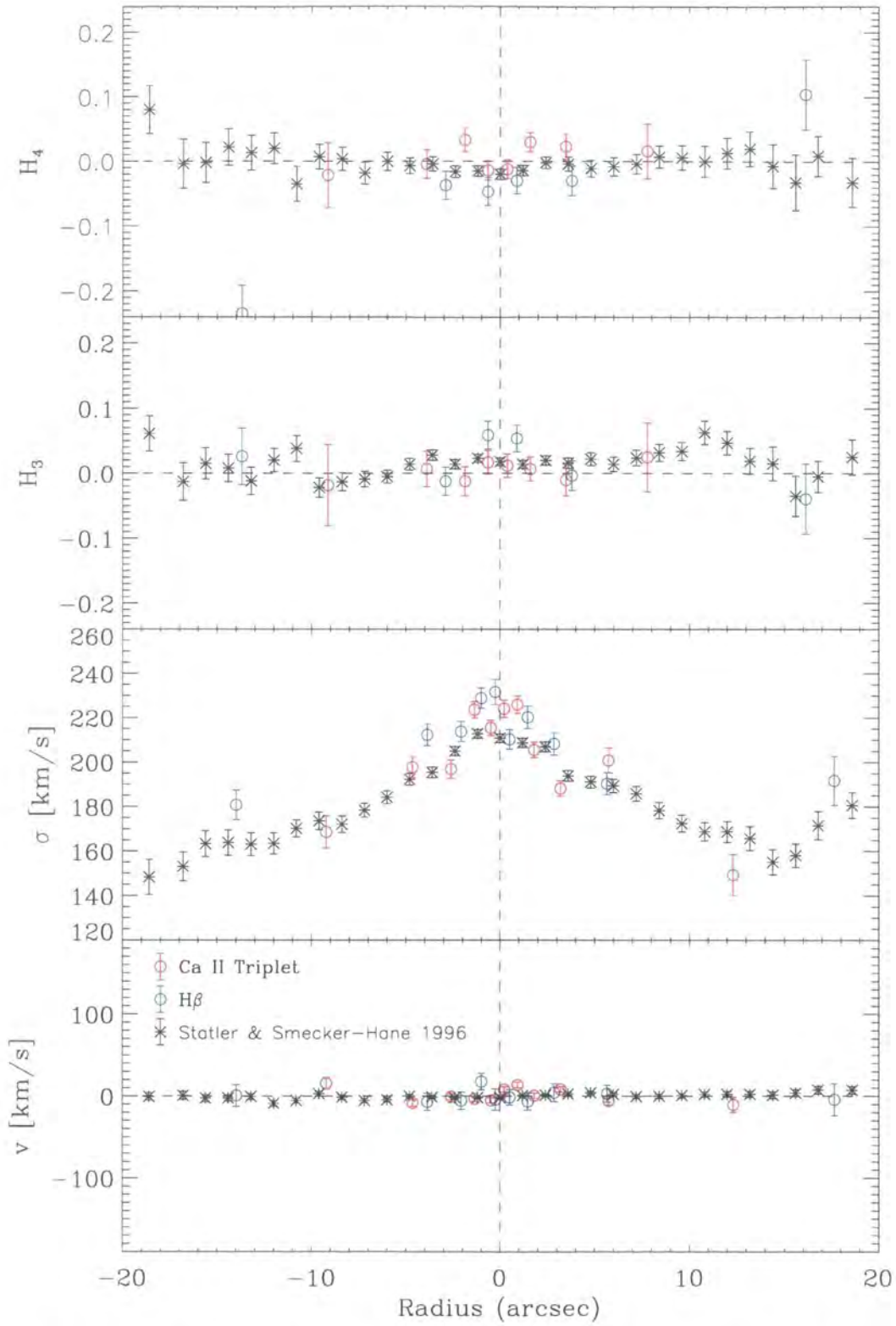

Figure 3.27: Same comparison as Figure 3.26 but for minor-axis of NGC 3379. Again the three data sets are in generally good agreement, with the notable exception of the central regions, where the ISIS data show a larger velocity dispersion than the SSH99 data. This is probably due to a smaller PSF for the ISIS data (see text).

As a well-studied control object, it is appropriate to compare the quality of data presented here with the work of other independent authors. SSH99 publish excellent quality data of this galaxy at a number of position angles. Although there are differences in the instrumental set-up (specifically the spatial and spectral resolution of the data), comparison of the two data sets gives a clear indication of the quality of the kinematics presented here.

Figure 3.26 presents the major-axis kinematics profiles of NGC 3379 derived from the Calcium II triplet and Hβ features of this work, overplotted with the major-axis profile of SSH99. The data compare very well, although clearly the SSH99 data extend to larger radii, since the total integration time used was much longer (4x1800s exposures, as opposed to 1x1200s exposure in this work).

Figure 3.27 presents the same comparison as before, but this time for the minor-axis of NGC 3379. Again, the SSH99 data are much deeper, but the three data sets are in good agreement. The most noticeable discrepancy in Figure 3.27 is within the central 2″, where the SSH99 data reach a central velocity dispersion value of $\sim$ 210 km s^{-1}, compared to a value of $\sim$ 225 km s^{-1} for the ISIS data. The ISIS value is consistent with the dispersion measured at the same position on the major-axis. The SSH99 major-axis data also has a higher central value for the major-axis ($\sim$ 220 km s^{-1}), suggesting that the discrepancy is due to a difference in observing conditions, rather than a problem with the ISIS minor-axis data. The agreement of the three minor-axis data sets at larger radii supports this, suggesting that the ISIS data were obtained in better seeing.

These comparisons demonstrate two important aspects of the data:

1. The data are in agreement with a completely independent data set, demonstrating both the quality of the data and of the kinematics presented in this work.

2. The kinematics derived from the Calcium II triplet are generally consistent with the kinematics derived from the Hβ feature, as well as the more extended blue wavelength region used by SSH99. This is expected for this galaxy, as there is no corroborating evidence from stellar population studies that NGC 3379 has a young component. Therefore, the comparison of the Calcium II triplet and Hβ kinematics appears free from any serious systematic effects which may influence this analysis.

It can be seen from this comparison that there are, however, radii at which the Calcium II triplet and Hβ kinematics are not consistent with each other. However, these inconsistencies are not mirrored on the opposite side of the profile, suggesting that such offsets are due simply to noise in the data. It is expected that the effect of intrinsically different stellar dynamics and populations should produce axisymmetric offsets in the profiles, rather than asymmetric effects.

3.5.2 NGC 584

NGC 584 is a prime example of a young, disky galaxy. The central Hβ absorption is relatively strong ($\sim$ 2.11 Å), giving an average luminosity weighted age of 2.5 – 2.8 Gyr (Trager et al. 2000). The photometric properties of this galaxy are quite complex, with a steady change in position angle from 60° to 70° between a radius of 20″ and 70″, suggesting that the galaxy may be triaxial. Furthermore, there are three significant peaks in the C4 term at 1.″5, 13″ and 30″ (see Figure 3.28), indicating that there may be several distinct components (Scorza & Bender 1995). Unfortunately, the slit position angle for the 'major-axis' observations was set to the *outer* PA of 70°, whereas the data only extends to 30″, within which the PA is essentially constant at 60°. Hence the 'major axis' data is in fact 10° offset from the true major-axis of the galaxy's central regions. As a result, the 'major-axis' rotation velocity (see Figure 3.28) is underestimated by a few percent, and the 'minor-axis' shows evidence of rotation (see Figure 3.29). The slit-misalignment can also be seen in the colour-index image, Figure 3.24. Hereafter, this slit-misalignment is implied by reference to the major- and minor-axes of NGC 584.

The inner-most two of the C4 peaks are covered by our kinematic data, and so it is at these points where we would expect to see the largest contribution of the disk to the kinematics. From the results of the spectral modelling in Chapter 2, the primary evidence for a young, disky component should appear as differences in the major-axis rotation velocity derived from the two wavelength regions. Specifically, the Hβ kinematics should show a higher rate of rotation than that from the Calcium II triplet. Figure 3.28 shows that at a radius of 13″, the rotation velocities derived from the two regions are consistent within the errors; although the number of data points at this radius is small due to the S/N constraints.

At a radius of 2″, the number and quality of data points are much higher, and therefore it is possible to compare the Calcium II triplet and Hβ kinematics more closely. On inspection of Figure 3.28, there does appear to be some connection between this inner-most peak in C4 values and the kinematics. The radius of this C4 peak ($\sim$ 2″) corresponds to the point at which the rotation velocity begins to change rapidly. This is also reflected in the h_3 term, which shows a peak at this radius. The kinematics from the two wavelength regions at this radius do show small, but detectable, differences.

Figure 3.30 shows an enlargement of Figure 3.28 around the central region. The velocity derived from the Hβ feature shows a slightly higher value at around 1.″5 on both sides of the galaxy, suggesting that this difference is somehow systematic. The difference is small, with a value of around $10 - 15$ km s^{-1}. The h_3 term also shows evidence for a systematic difference between the two wavelength regions, with the Hβ h_3 values reaching a slightly higher peak value, and falling back towards zero more slowly with radius than the Calcium II triplet values.

These differences are small, and are close to the limit of the uncertainties in the data.

The velocity dispersion also shows differences between the two wavelength regions which appear more significant (for example, at $-2''$ the Hβ dispersion is 20 km s^{-1} higher than that from the Calcium II triplet). However, these differences are not symmetric about the galaxy centre like the velocity and h_3 offsets. Thus, differences in the dispersion values are put down to under-estimated uncertainties in the data.

From the spectral modelling in Chapter 2, it was shown that further evidence of a young disk component could be determined from examining the LOSVD's themselves, as opposed to their parameterized properties. Figure 3.31 shows the LOSVDs extracted from the two wavelength regions at the radius corresponding to this central C4 peak. Although this peak in the C4 term is only resolved by the HST data, and was not used in establishing the original Hβ - diskiness trend of (de Jong & Davies 1997), it is still instructive to examine this region, as the signal-to-noise of our kinematic data at this point is high, allowing accurate LOSVDs to be derived.

Figure 3.31 shows that the two LOSVDs are consistent with each other within the uncertainties, and that they lack the obvious narrow peak of a high-mass disk (such as that in Figure 2.5(c)). The distributions are not exactly the same, however. The Hβ LOSVD shows broader wings than the Calcium II triplet LOSVD. These regions are sensitive, however, to the continuum subtraction. From the Monte-Carlo simulations presented in §3.3.3, it has already been shown that the Hβ kinematics are sensitive to how the continuum is removed, as the wavelength region is small, and so the continuum cannot be well-determined. For this reason, the broad wings in Figure 3.31 should be treated with caution, as they are most likely due to systematic uncertainties.

The uncertainties on the LOSVDs were calculated from 100 realisations of the galaxy spectra assuming a Poisson noise distribution. The error bars at each velocity bin represent $\pm$ one standard deviation of the resulting distribution of LOSVDs. This method tends to underestimate the true amount of noise involved, as well as not accounting for systematic errors involved in extracting the LOSVD. Hence these error bars represent a lower limit to the true uncertainties.

Therefore, NGC 584 displays marginal evidence of a young disk component, given mainly by a slightly higher rotation velocity derived from Hβ at $\pm 2''$ compared to that of the Calcium II triplet. By examining the actual LOSVDs at this position, there is no evidence of a strong two-component structure in the Hβ LOSVD compared to that of the Calcium II triplet, although the LOSVDs (from both wavelength regions) are noticeably asymmetric, typical of a disk. Applying the results from the simple spectral modelling presented in Chapter 2, it is possible to rule out the presence of a disk which is older than half the total luminosity-weighted age of the system, as this would be clearly visible as a strong two-component structure in the Hβ LOSVD, which is not observed.

The small difference in rotation velocity is found to be at most 15 km s^{-1}. From Figure 2.4(a), a difference between the observed Hβ and Calcium II triplet rotation velocities

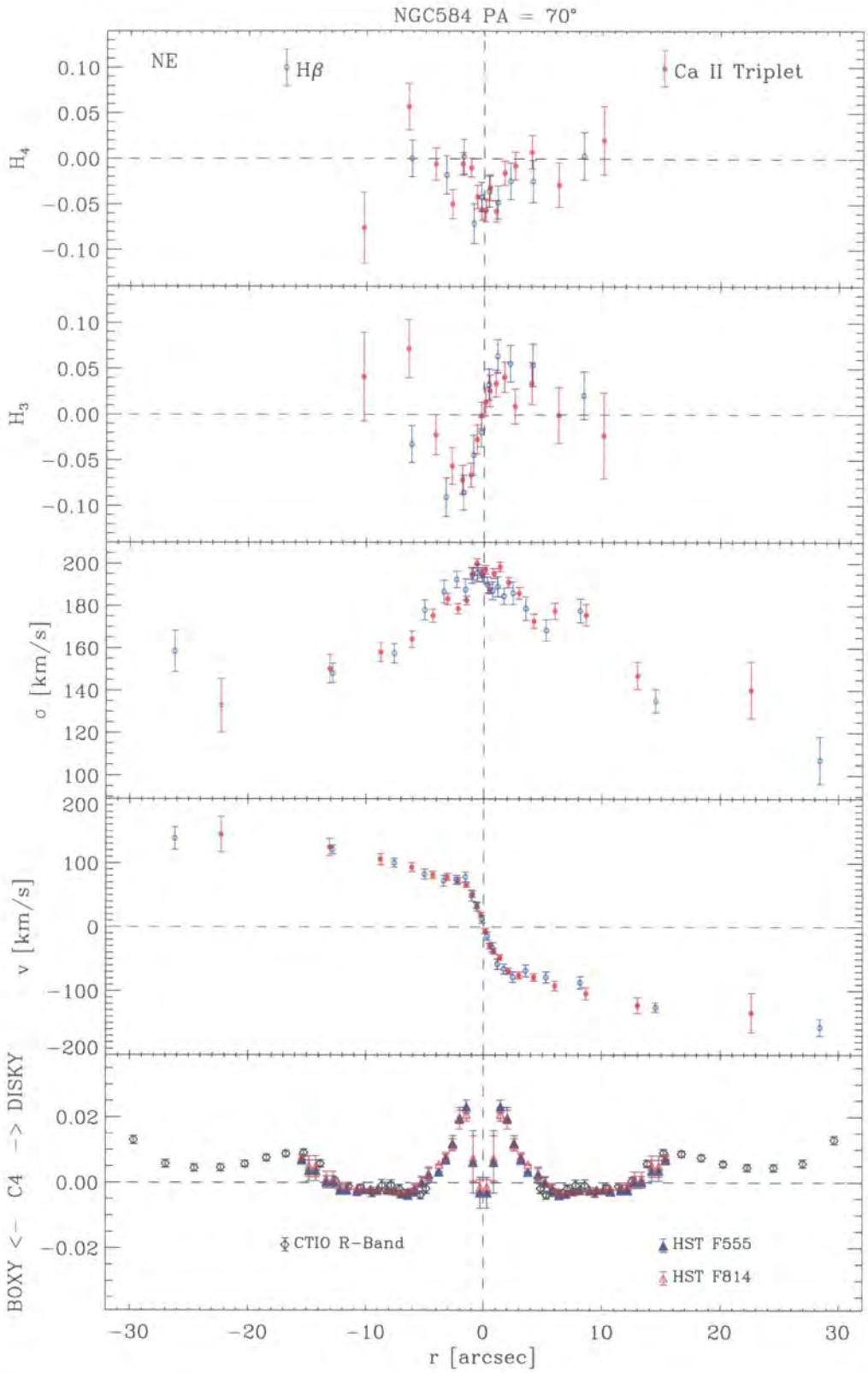

Figure 3.28: Parameterized LOSVD profile for the major-axis of NGC 584. The high rotation velocity, and steep velocity gradient across the centre, indicates that this galaxy has a high degree of rotational support. This behaviour is mirrored in the h_3 term, which suggests the presence of a central disk component. There is suggestive evidence of a slightly higher peak rotation velocity derived from Hβ than from the Calcium II triplet at $\pm \sim 2''$.

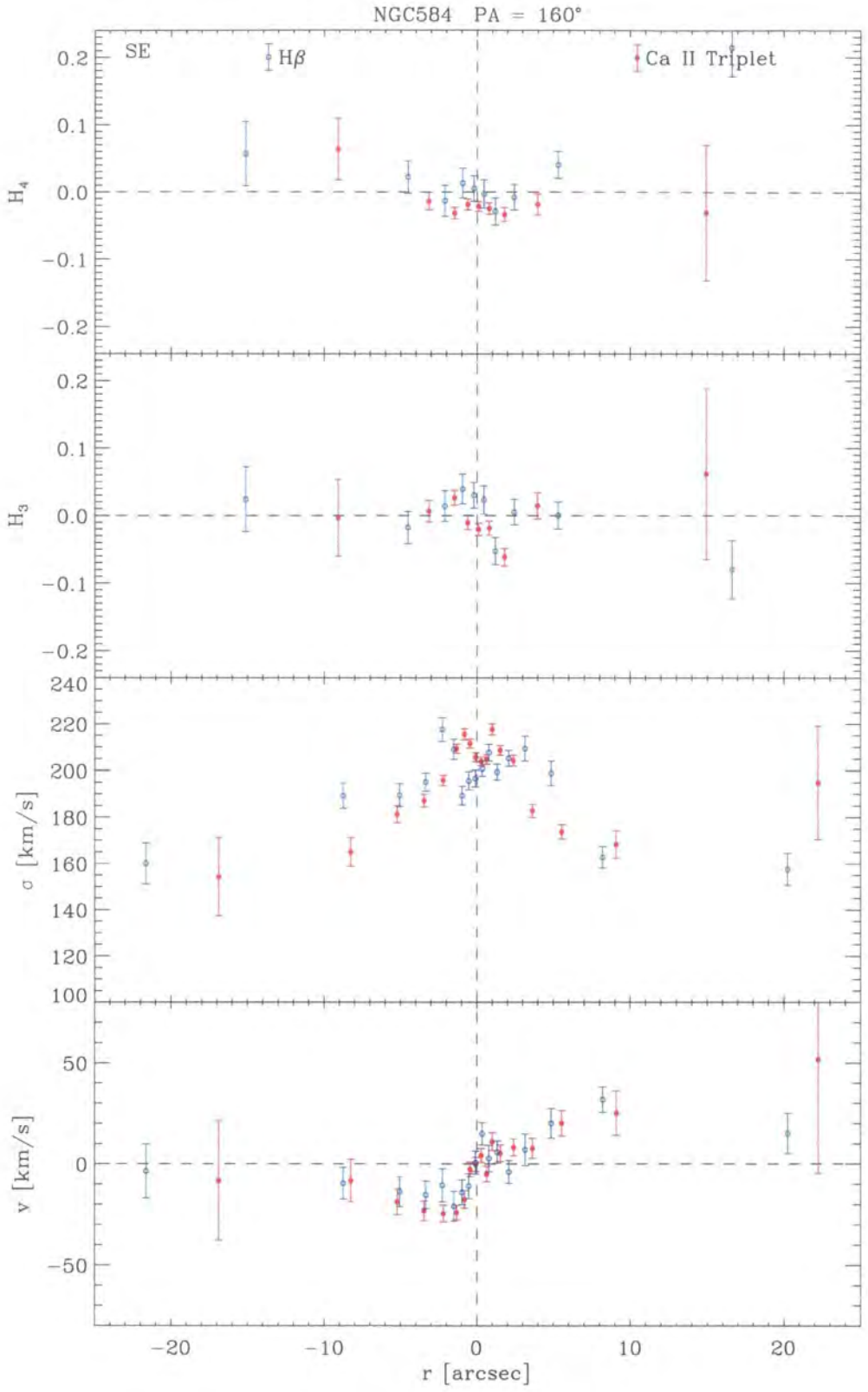

Figure 3.29: Parameterized LOSVD profile for the minor-axis of NGC 584. The apparent minor-axis rotation is due to the 10° offset in PA of the slit. The rotation velocity tends towards zero at larger radii, suggesting that this galaxy may be triaxial, supported by the known isophote twist observed in the photometry.

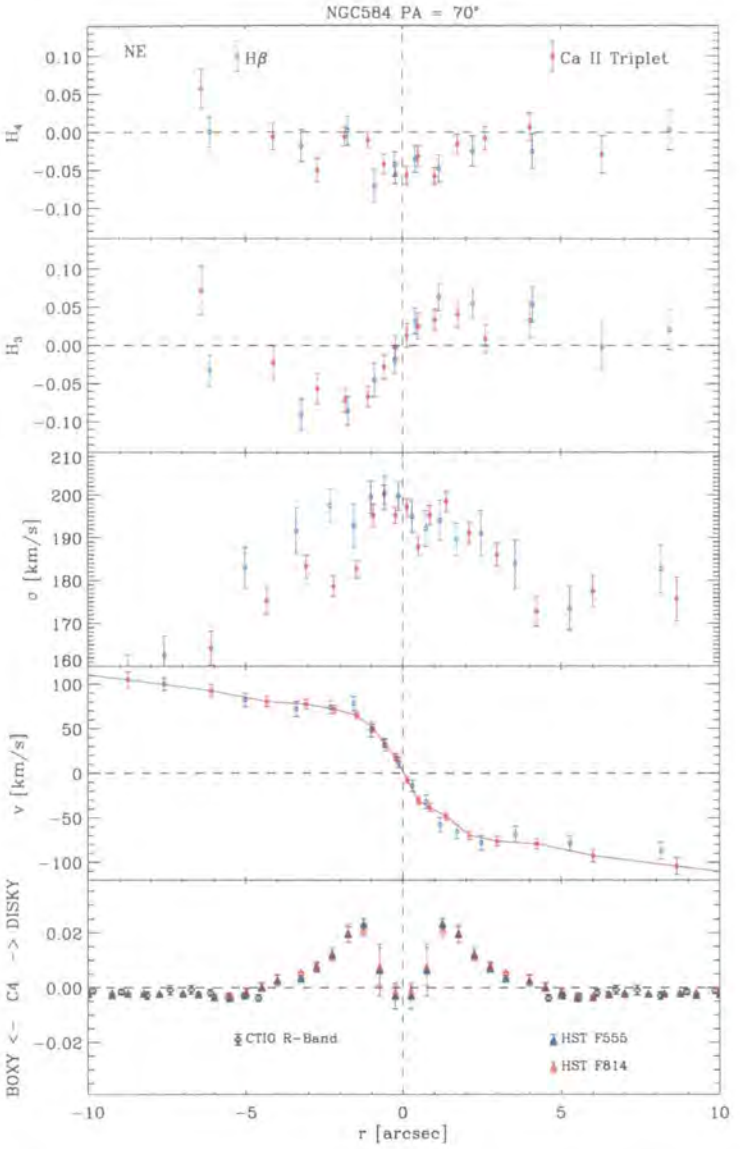

Figure 3.30: Parameterized LOSVD profile for the major-axis of NGC 584 within the central $\pm 10''$. The Calcium II triplet velocity profile is plotted as a line to show the small offsets between the velocities derived from the two wavelength regions. The Hβ velocity profile shows a higher rotation velocity at a radius of $1 - 2''$, which corresponds to a peak in the central C4 parameter.

of this size corresponds to an intrinsic velocity difference between the young disk and old spheroid from 20 km s^{-1} for a 1 Gyr disk, up to 50 km s^{-1} for a 2 Gyr disk. To differentiate between these models requires the higher moments of the LOSVD, namely the velocity dispersion, h_3, and h_4 terms.

Figure 3.32 shows the same results from the spectral modelling as Figure 2.3, but for the range of models relevant to NGC 584. Based on the observed 15 km s^{-1} difference in the Hβ and Calcium II triplet rotation velocities, and the lack of a strong second peak in the LOSVD, the relevant models consist of a population of 2 Gyr or younger, with an intrinsic velocity difference between the disk and spheroid of up to 50 km s^{-1}. Examining

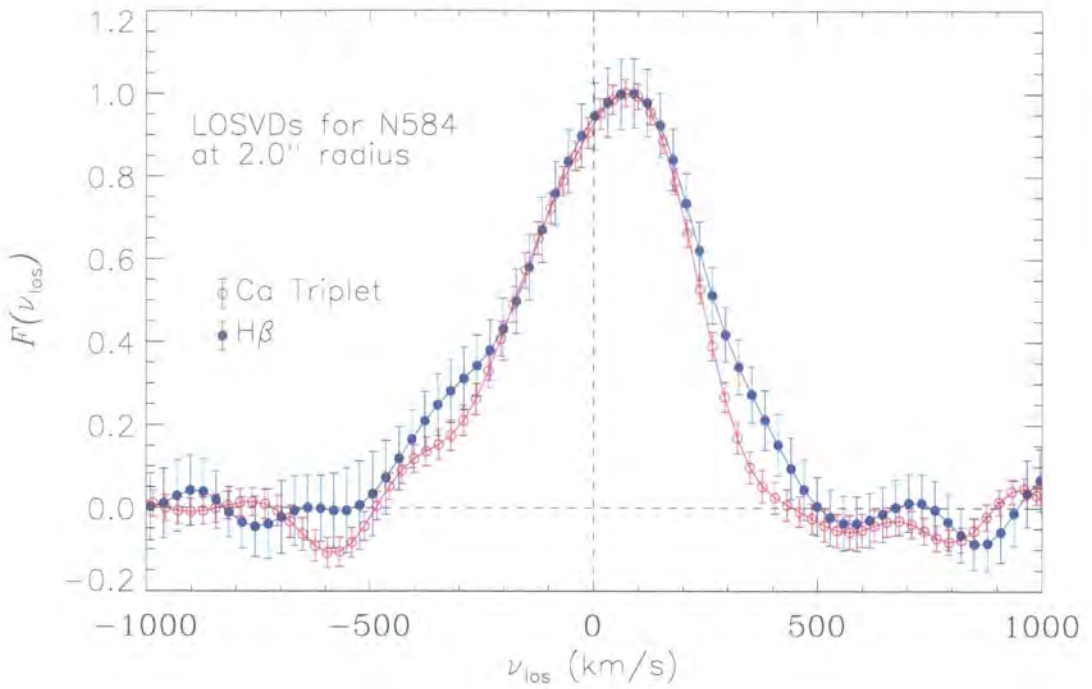

Figure 3.31: Comparison of the actual LOSVDs derived from the Calcium II triplet (red points) and Hβ (blue points). The distributions are very similar, especially around the peak, where the measurements are most secure. The Hβ LOSVD appears to have broader wings on *both* sides of the distribution, suggesting that this is not caused by secondary components, but by difficulties with the continuum subtraction due to the short wavelength range.

the other LOSVD parameters for such models, it is clear that one should expect to observe differences in these parameters as well. The difference between the Calcium II triplet and Hβ velocity dispersions, for example, are of the order $50 - 60$ km s^{-1} for all models; this is not evident in the observations. There are small differences in the h_3 term, for which there is some evidence in the observations. However, there should also then be significant differences in the h_4 term, which is not observed.

Therefore, NGC 584 presents something of a conundrum. On one hand, there are tantalising differences in the observed Calcium II triplet and Hβ kinematics: primarily in the rotation velocities, but also in the h_3 terms. These differences are, however, marginal given the uncertainties. The LOSVDs from the two spectral regions are similar, and show no strong two-component structure as was found for models of older, high-mass fraction disks. Therefore a younger, less obvious disk component may be present. The higher-order moments of the LOSVDs, however, do not support this, implying that all models considered in Chapter 2 can be excluded.

The conclusion is, therefore, that NGC 584 shows some evidence for harbouring a disk composed of stars which are younger than the underlying spheroidal component, as there are small velocity offsets between the Calcium II triplet and Hβ kinematics. This

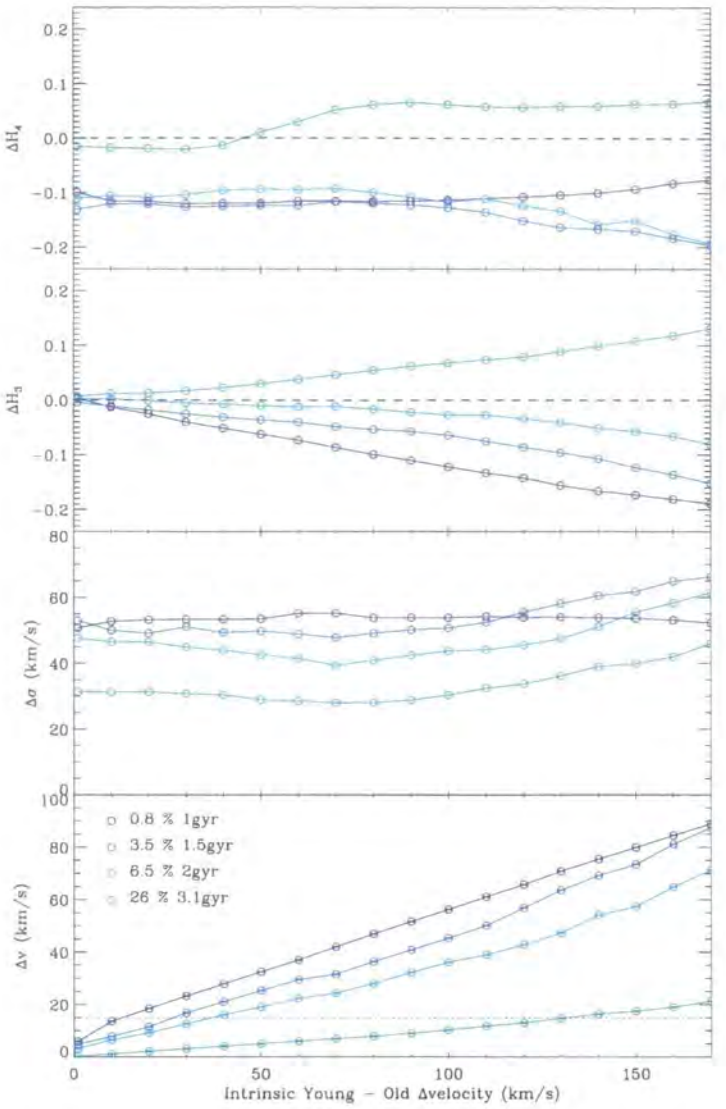

Figure 3.32: Model predictions from Chapter 2 for a two-component population with total Hβ absorption strength of 2.11 Å, consistent with the central Hβ absorption of NGC 584 (Trager et al. 2000). Plotted are the differences between the Calcium II triplet and Hβ kinematic parameters, as described in Chapter 2. The observed difference in the rotation velocities derived from Hβ and the Calcium II triplet is at most $\sim$ 15 km s^{-1}, which is overplotted in the bottom panel as a dotted line. This intersects the model curves at a large range of intrinsic disk-bulge velocity offsets depending on the assumed age of the disk population (shown as different colours). For example, if the disk is composed of a 1 Gyr population, the disk is predicted to rotate 10 km s^{-1} faster than the bulge in order to produce the observed 15 km s^{-1} offset. For such a disk, sizeable offsets in velocity dispersion and the h_4 term are also predicted, but not observed. Indeed, for all of the models which intersect with the observed velocity offset, there are offsets in the other kinematic parameters which are not observed in the data. Based on this evidence, all of the models considered can be excluded.

component is not, however, consistent with the simple model of a rotationally-supported component composed from a single, recent burst of star formation considered in Chapter 2, as the other kinematic indicators are not found.

3.5.3 NGC 720

NGC 720 is a bright, highly flattened, and relatively isolated (Dressler et al. 1986) elliptical. The Hβ absorption strength is moderately strong ($\sim$ 1.77 Å), with a luminosity-weighted age of around 5 Gyr (Trager et al. 2000), corresponding to the models shown in Figure 2.4(b). The isophotes show a peak in the C4 term within the central few arcseconds (resolved with HST), falling quickly to zero with increasing radius, and rising slowly again to a value of around 0.01 at 40″(see Figure 3.33).

The most notable aspect of the major-axis kinematics of NGC 720 is the lack of strong rotation. The peak rotation velocity is only $\sim$ 50 km s^{-1} which, compared to the other galaxies in the sample, is quite modest, and is not indicative of the presence of a disk component. The galaxy is also a 'core profile' galaxy from HST studies (Lauer et al. 1995, Faber et al. 1997), which are generally found to be slowly rotating systems with *boxy* isophotes. Although the C4 values are not very high for NGC 720, the only significant deviations from zero are towards *disky* isophotes. Therefore, this galaxy does not sit squarely with either models of slowly rotating 'core' galaxies with boxy isophotes, or more rotationally supported galaxies with disky isophotes.

The kinematic data are not of high enough quality at the outer C4 peak to constrain the possible presence of a young disk. In the central regions, however, the signal-to-noise ratio of the data is much higher, and we may expect to detect the signature of a central young disk with some degree of confidence. On the major-axis, the rotation velocity within the central $\pm 3''$ appears to fall to zero, as does the h_3 term, implying that the core region does not rotate about the minor-axis as the outer parts do. At the same position, the C4 values show a peak resolved by HST. There is no kinematic evidence, however, that this peak should be due to a near edge-on, central stellar disk rotating about the minor-axis.

On the minor-axis, however (Figure 3.34), there is evidence of rotation in the mean velocity profile. This is most prominent in the Calcium II triplet velocities, although the Hβ velocity is similar. The rotation is small in amplitude: estimated as $\pm \lesssim 20$ km s^{-1} from the Calcium II triplet data; but seems to show a peak at around $3 - 5''$. There appears, therefore, to be a weak decoupled core in this galaxy, which has a rotation-axis misaligned from that of the outer parts of the galaxy. This decoupled core has never been reported in previous literature. Whether or not this minor-axis rotation relates to the C4 peak, however, is not clear.

The disky isophote distortions which made this galaxy appropriate for this project occur at a radius for which the kinematic data is of too poor quality to determine the small kinematic differences required to constrain the presence of a young disk. There is a central peak in the C4 values derived from HST photometry. From Figures 3.33 and 3.34, however, there is no evidence of systematic differences in the kinematics derived from the Calcium II triplet and Hβ which may indicate the presence of a young disk around this

peak. Therefore, within the range of the observations, the presence of a disk component composed of exclusively young stars is ruled out.

3.5.4 NGC 821

NGC 821 was included in the observed sample due to its strongly disky isophotes, and has the highest C4 value of the sample. The presence of a disk component in this galaxy was confirmed by Scorza & Bender (1995, hereafter SB95), who performed a double-Gaussian decomposition of the LOSVD using the photometric disk-to-bulge ratio as an additional constraint. This did not, however, address the issue of a separate stellar population associated with this disk. The Hβ absorption in this galaxy is only moderate ($\sim$ 1.66 Å, the lowest of the disky sample), giving a luminosity weighted age of around 8 Gyr (Trager et al. 2000). This galaxy therefore corresponds to the models shown in Figure 2.4 model (c).

SB95 find that the embedded disk component is relatively 'hot', with a $v/\sigma \sim 1.5$, with a velocity dispersion $\sigma_d \sim 110\ \mathrm{km\,s^{-1}}$ and a velocity difference between the disk and bulge of $\sim 100\ \mathrm{km\,s^{-1}}$. In Chapter 2 it was shown that a disk which has a relatively large velocity dispersion can significantly reduce the detectability of a young disk component, as the disk and spheroid LOSVDs become more similar. Using the disk parameters from SB95, the maximum predicted difference in rotation velocity which one can expect is $\sim 15\ \mathrm{km\,s^{-1}}$, which is rather close to the limiting accuracy of the observations.

From Figure 3.35, the major-axis rotation velocities derived from the two wavelength regions do seem to show a small systematic offset, in the sense that the Hβ shows slightly higher rotation velocities between 2″ and 10″. The difference is small, reaching a maximum of $\sim 15\ \mathrm{km\,s^{-1}}$ at about 4″. However, the radius at which the C4 reaches a maximum is 16″. At this radius, the Calcium II triplet and Hβ velocities appear to be consistent, although the kinematic errors are too large, and the number of data points too few, to reliably constrain velocity differences $< 20\ \mathrm{km\,s^{-1}}$.

Along the minor-axis, Figure 3.36 shows that there are differences in the Calcium II triplet and Hβ kinematic parameters. These differences do not occur on either side of the galaxy as one might expect for a true, systematic difference however, and therefore are put down to underestimated uncertainties in the data.

It has already been shown that older, higher-mass fraction disks are most evident as a strong secondary component in the Hβ LOSVD. Figure 3.37 presents a comparison of the Hβ and Calcium II triplet LOSVDs at a radius of 3″ from the galactic centre along the major-axis. This corresponds to the position at which the offset in rotation velocity are observed in Figure 3.35. There is a small offset in the peak velocities, which probably accounts for the offset in $\bar{v}$. This slight difference in the LOSVDs may indicate the presence of a component with a higher rotation velocity which is more apparent in

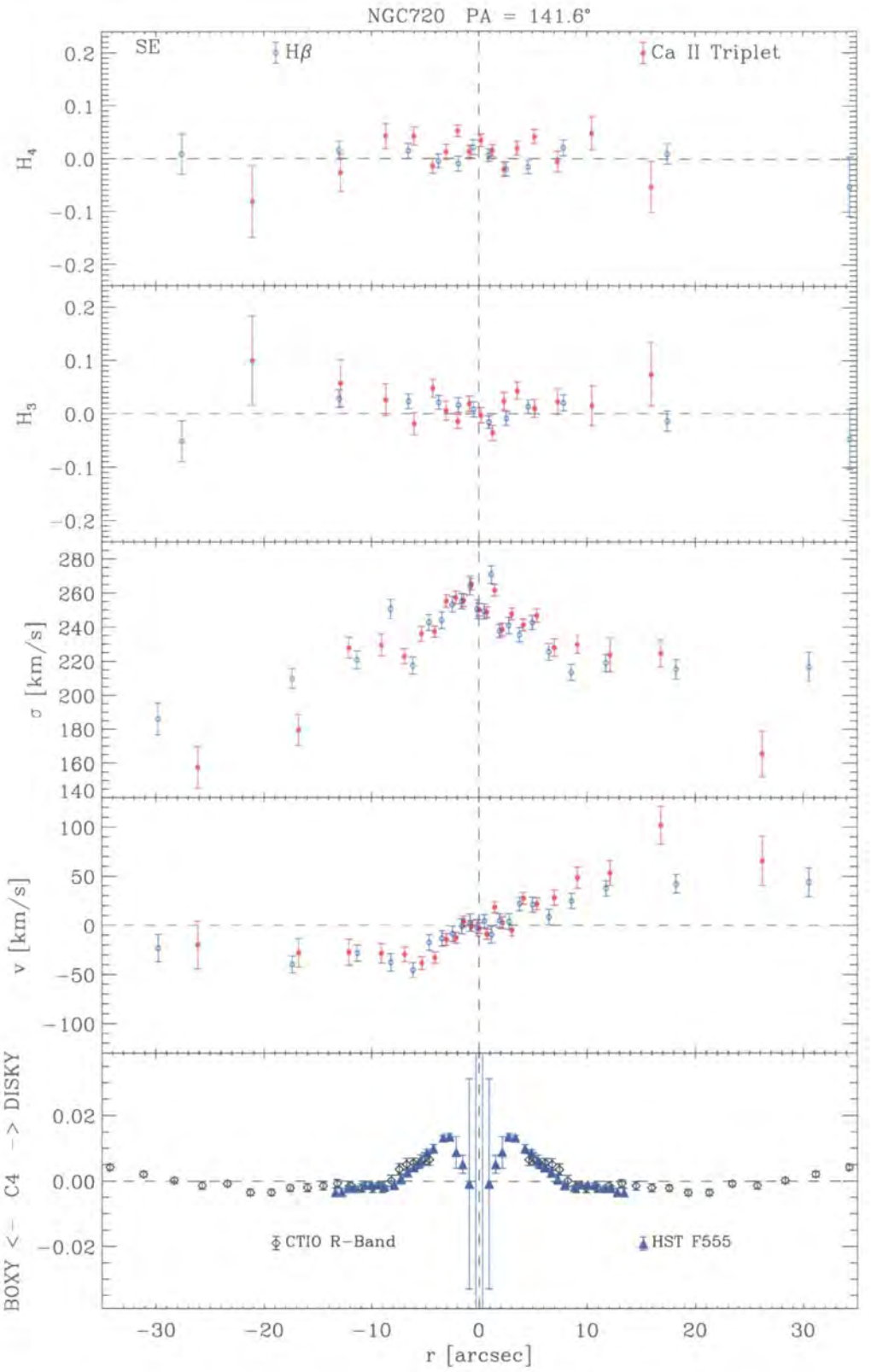

Figure 3.33: Parameterized LOSVD profile for the major-axis of NGC 720. The rotation velocity is not as high as for other galaxies in the sample, indicating that the galaxy may be more pressure-supported within the extent of this data. The C4 term begins to rise with increasing radius to a peak at $\sim 40''$, however the kinematic data are not of high enough quality at this radius to constrain a young component. The central HST data shows a central peak in the C4 parameter, which seems to correspond to where the rotation velocity flattens out within $\pm \sim 3''$. The increase in C4 is therefore not due to a central disk rotating about the minor axis.

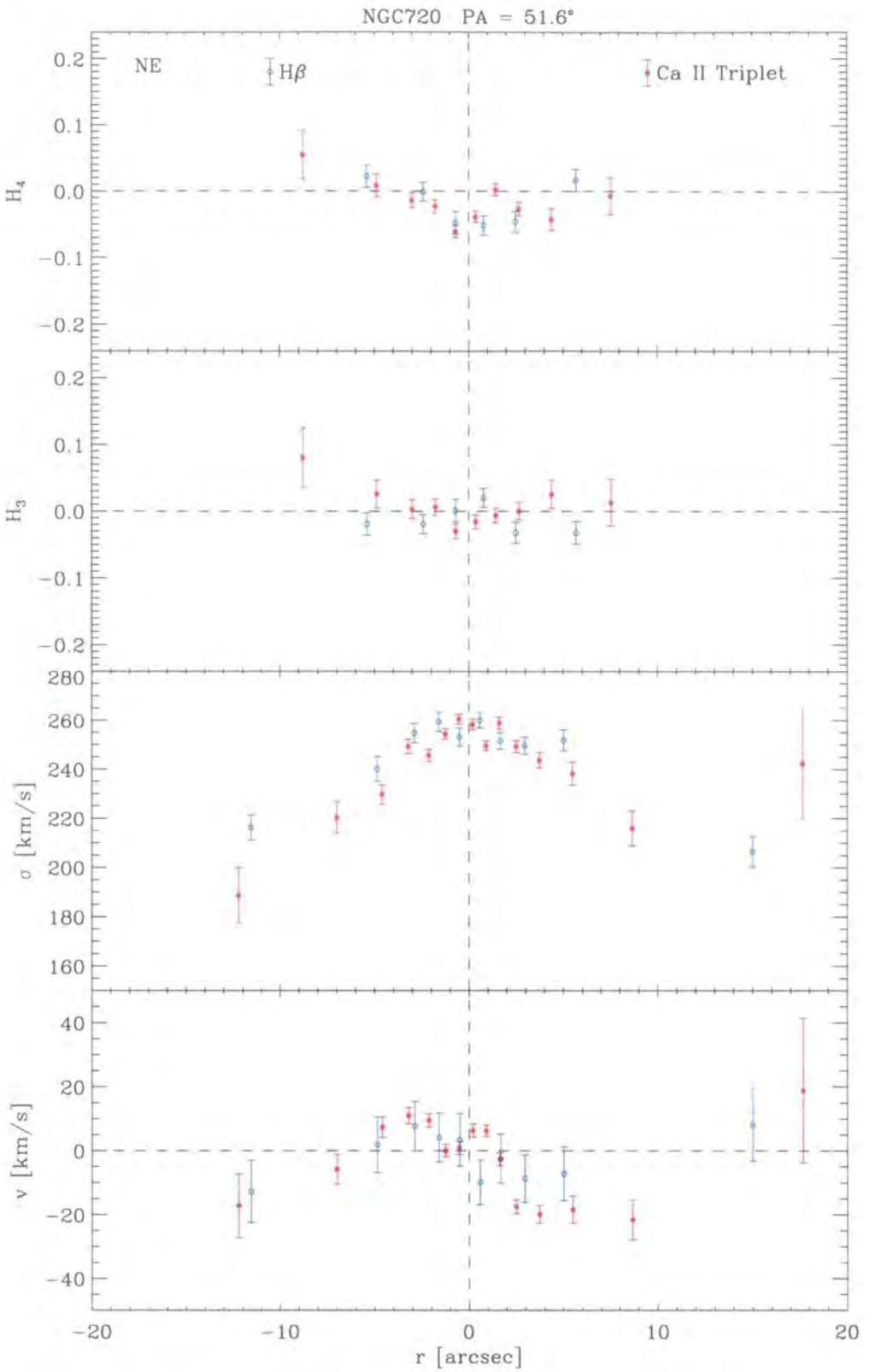

Figure 3.34: Parameterized LOSVD profile for the minor-axis of NGC 720. The rotation velocity within the central $\sim 5''$ appears to show evidence of rotation about the minor axis. This is not due to a clear slit misalignment as with NGC 584, as the PA of the observations is consistent with ground-based photometry. The minor-axis rotation appears to be real, therefore, and may be associated with the central C4 peak resolved by HST (see Figure 3.33)

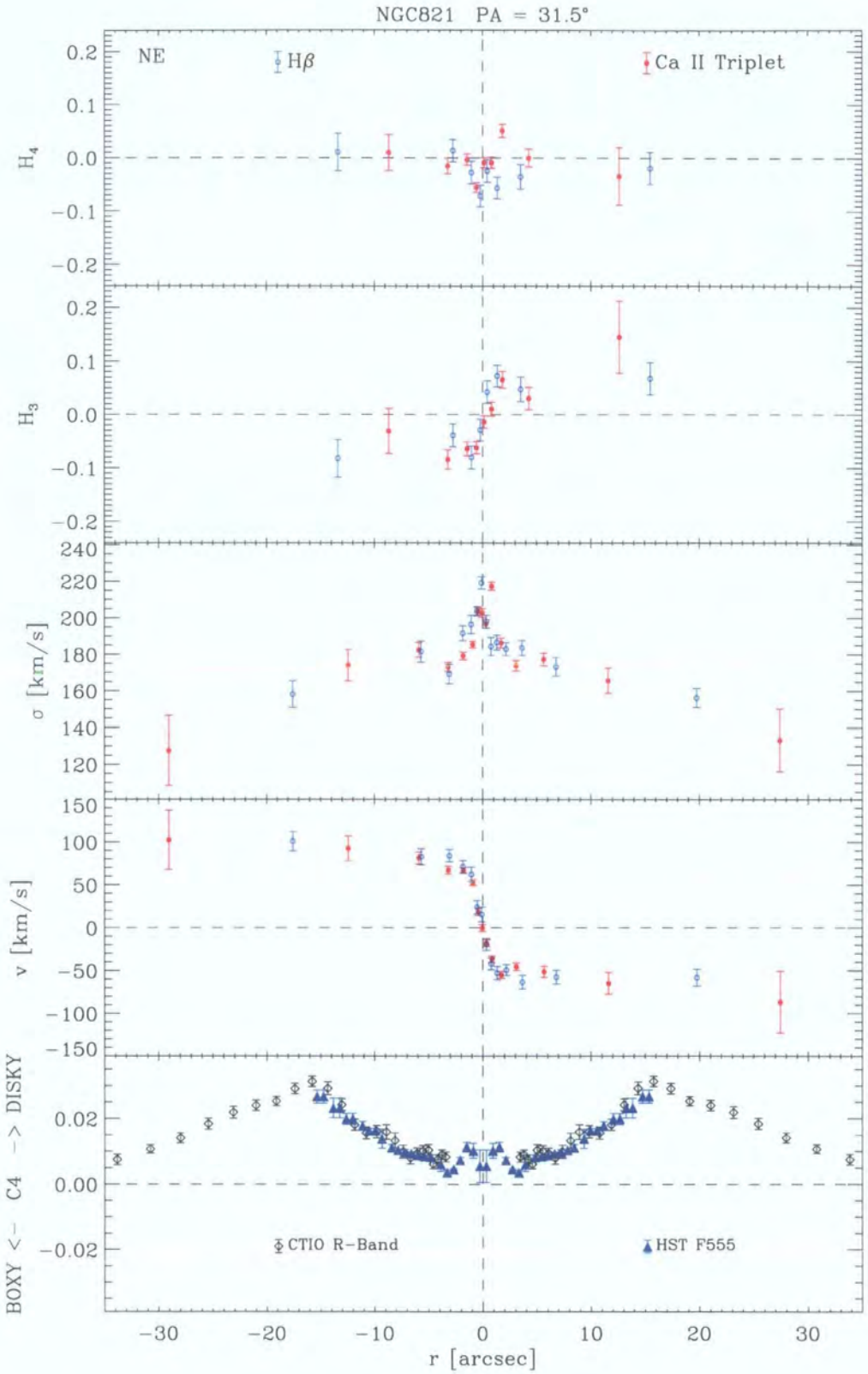

Figure 3.35: Parameterized LOSVD profile for the major-axis of NGC 821.

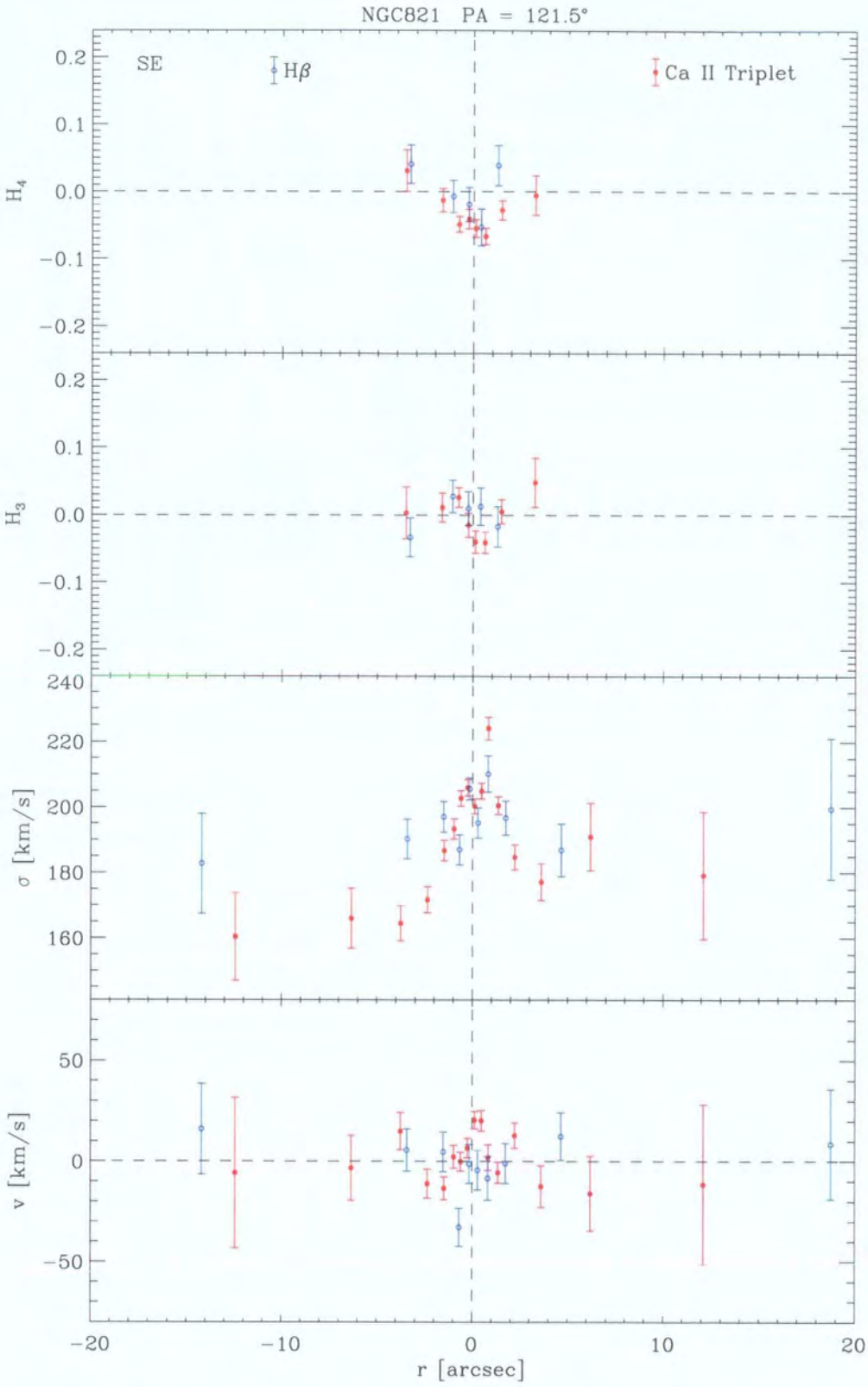

Figure 3.36: Parameterized LOSVD profile for the minor-axis of NGC 821

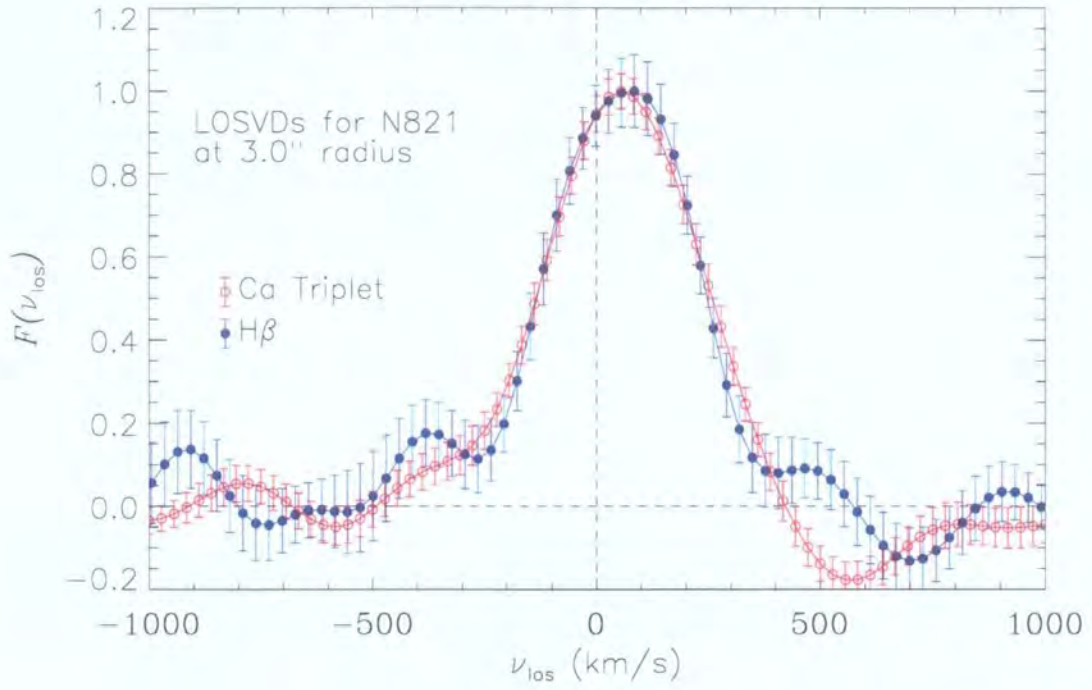

Figure 3.37: Comparison of the actual LOSVDs derived from the Calcium II triplet (red points) and Hβ (blue points) for NGC 821 at 3″ along the major-axis. The distributions are consistent within the uncertainties; however, the Hβ LOSVD (blue points) does show a slightly higher peak velocity than the Calcium II triplet LOSVD (red points), which accounts for the 20 km s^{-1} higher mean velocity derived from Hβ at this radius (Figure 3.35). This could indicate the presence of a high-rotation velocity component which is more apparent in Hβ than the Calcium II triplet. The uncertainties, however, are too large for this interpretation to be secure.

Hβ than the Calcium II triplet. The difference in the LOSVD shapes is, however, much smaller than those predicted by the modelling for a high-mass disk (Figure 2.5), even taking into account the larger disk velocity dispersion. Therefore, models older than 6 Gy are ruled out.

Applying the models of Chapter 2, an observed maximum velocity difference of 15 km s^{-1} between the Calcium II triplet and Hβ measurements is consistent with a range of intrinsic velocity differences between the disk and bulge component, depending on the stellar population of the disk. For a 4 Gyr disk contributing 5% of the total mass, this observed difference implies an intrinsic difference of 110 km s^{-1} between the disk and bulge. For a disk of 8 Gyr, providing over a quarter of the total mass, the intrinsic difference could be as high as 160 km s^{-1}. Likewise, a very young disk composed of a 2 Gyr population would imply an disk rotating more than 200 km s^{-1} faster than the spheroid component.

Assuming SB95's value of 100 km s^{-1} for the intrinsic velocity difference between the spheroid and disk, it is possible to cross-compare the *observed* velocity difference and the *intrinsic* velocity difference. Figure 3.38 illustrates this by showing the observed velocity difference of 15 km s^{-1} (horizontal dotted line), as well as the intrinsic velocity

difference between the spheroid and disk of 100 $\mathrm{km\,s^{-1}}$ (vertical dotted line) from SB95. In principle, where the lines intersect determines the age of the disk population, under the assumptions of the spectral modelling in Chapter 2. Given the uncertainties, however, the point of intersection provides only an indication of models which may be consistent with the observations.

From Figure 3.38 it is possible to exclude some of the models considered. The small observed velocity offset is estimated here as 15 $\mathrm{km\,s^{-1}}$ which, given the uncertainties, is probably an upper limit. At an intrinsic difference of 100 $\mathrm{km\,s^{-1}}$, however, all the models result in apparent offsets in velocity of less than 15 $\mathrm{km\,s^{-1}}$, thus none are excluded in this way.

From examination of the LOSVD at the radius at which the velocity offsets are found, it was possible to exclude the oldest disk models, as the LOSVDs did not have a clear two-component structure, or were not dominated by a possible disk component. Models with disks younger than $\sim$ 2 Gyr are also unlikely, as to produce an observed velocity difference of 15 $\mathrm{km\,s^{-1}}$, the disk would need to be rotating more than 150 $\mathrm{km\,s^{-1}}$ intrinsically faster than the spheroid component, which is not observed by SB95. These very young disks are not strongly excluded, however, as the assumed observed velocity differences here is only an upper limit. It is possible that the observed velocity difference is significantly less than 15 $\mathrm{km\,s^{-1}}$, allowing for younger disks with intrinsic velocity differences closer to the value of SB95.

The models which lie closest to both the observed velocity difference between the Calcium II triplet and Hβ kinematics presented here, and the intrinsic disk-spheroid velocity offset determined by SB95, are disks with an intermediate age of $3 - 5$ Gyr. For an observed velocity difference of $\sim$ 15 $\mathrm{km\,s^{-1}}$, these disks imply intrinsic offsets of $\sim 100 - 140$ $\mathrm{km\,s^{-1}}$, roughly consistent with SB95. For such models, the observed differences in the h_3 and h_4 terms are small (< 0.05), and the only other parameter for which significant offsets are found is in the velocity dispersion, which shows an apparent difference of $\sim$ 20 $\mathrm{km\,s^{-1}}$ for intermediate aged disks. This offset is in the sense that Hβ gives a lower velocity dispersion than the Calcium II triplet, as Hβ is more sensitive to the lower-dispersion disk component. Such an offset in the observed velocity dispersions are not, however, apparent in the observations. Indeed, the velocity dispersion is remarkably consistent between the two regions. Combining the constraints imposed by both the small observed velocity differences, and the lack of observed offsets in the velocity dispersion parameter, suggests that the disk in NGC 821 is not completely consistent with any of the SSP models considered here.

To conclude, the presence of a disk in NGC 821 has already been shown by SB95, however the nature of the stellar population of the disk component was not considered. From the data presented here, the disk is equally apparent in the kinematics derived from both the Calcium II triplet and from the Hβ absorption feature. For example, the h_3 Gauss-Hermite coefficient, known to be sensitive to the presence of a disk component, is

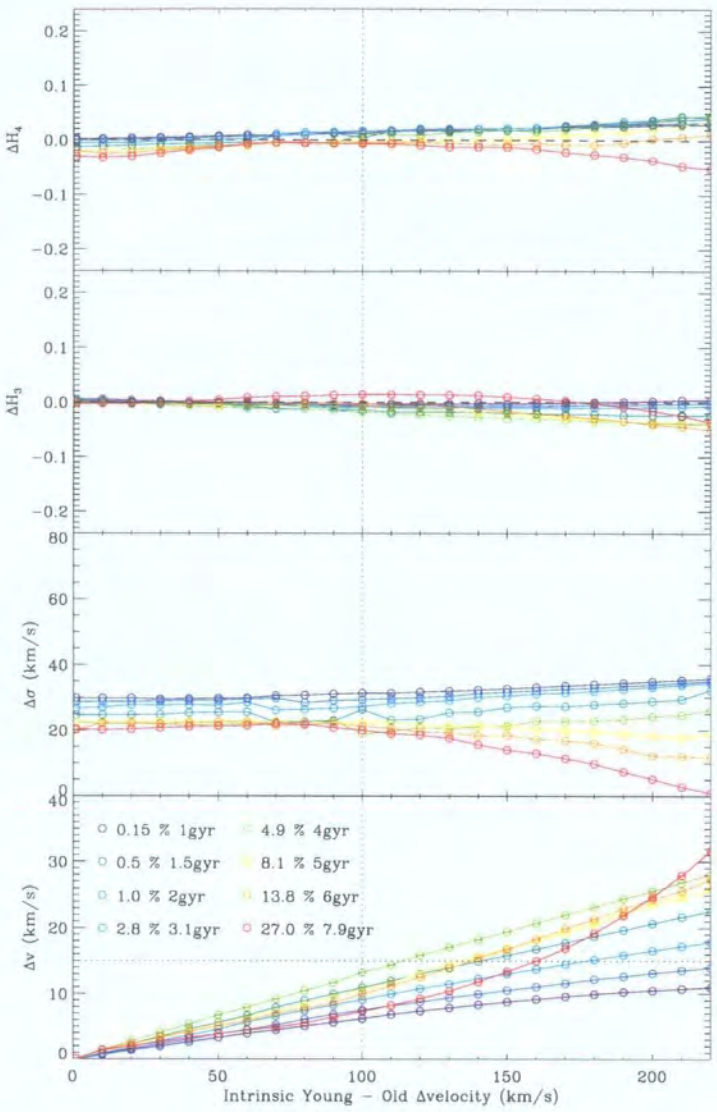

Figure 3.38: Model predictions from Chapter 2 for a two-component population with total Hβ absorption strength of 1.66 Å, consistent with the central Hβ absorption of NGC 821 (Trager et al. 2000).

equivalent from both wavelength regions. The only evidence for a distinct disk population comes from a small, but systematic offset between the Hβ and Calcium II triplet rotation velocities. Comparing the LOSVDs shows that this is not due to a disk population older than 6 Gyr, as this would show as a strong two-component structure. From comparison of the observed velocity difference with those predicted by the modelling of Chapter 2, it is possible to further exclude disk populations younger than $\sim$ 2 Gyr, as these would imply intrinsic velocity differences between the disk and spheroid far in excess of that found by SB95. The small observed velocity difference is most consistent with disks of intermediate age (3-5 Gyr) which contain 3-8% of the total mass of the galaxy. However, the models predict also a measurable offset in the velocity dispersion ($\sim$ 20 km s^{-1}) which is not observed. NGC 821 does, therefore, show tentative evidence for a disk component

composed of a different stellar population to that of the spheroid component. This disk is not, however, fully consistent with any of the single-burst disk models presented here.

3.5.5 NGC 1700

NGC 1700 is a superficially ordinary elliptical, with several features which make it a good candidate for housing a possible young, kinematically distinct component. Firstly, the galaxy exhibits relatively strong central Hβ absorption (= 2.11 Å, corresponding to the models shown in Figure 2.4(a)), giving a luminosity-weighted age of around 2 – 3 Gyr (Trager et al. 2000). This, and other consistent age estimates from independent techniques (Brown et al. 2000), implies that NGC 1700 contains a young component of some description. The presence of tidal tails (Schweizer & Seitzer 1992) implies the galaxy has been involved in a merger in the past 6 Gyr. Secondly, kinematic analysis reveals a counter-rotating core (Franx et al. 1989*a*, Statler et al. 1996): strong evidence for a past merger or accretion event (Schweizer et al. 1990, Bender & Surma 1992) which could lead to the formation of a young, kinematically distinct component.

Figures 3.39 and 3.40 present the major- and minor-axis kinematic profiles for NGC 1700 respectively. The kinematically decoupled core (hereafter KDC) can clearly be seen in the major-axis profile, showing a velocity amplitude of ± 40 km s^{-1}. The KDC also shows a clear impression on the velocity dispersion, which shows a distinct dip coincident with the KDC's peak velocity, as well as the h_3 term, which varies in step with the rotation velocity in the sense that h_3 has the opposite sign to $\bar{v}$. The minor-axis profile is devoid of such dramatic features, with no evidence of rotation. This implies that NGC 1700 is close to axisymmetric within the extent of these observations.

An initial comparison of the kinematic parameters derived from the two wavelength regions reveals several points. Firstly, the errors in the Calcium II triplet data points increase rapidly with radius. This is due to the effect of the sky-subtraction residuals which fall within the main absorption features. Secondly, the data are of best quality where the C4 parameter implies *boxy* isophotes. Where the C4 values are disky, the data points are few. The few kinematic data points which do coincide with disky isophotes (i.e., between $3-20''$) do not show strong evidence of inconsistencies which would indicate a young disk.

It is still interesting to consider whether the KDC can be composed of a distinct stellar population, which should be evident in a similar way to a young disk. The kinematics derived from the two wavelength regions are remarkably consistent, even across the decoupled core. There are some small inconsistencies between the two profiles, notably with the velocity dispersion. However there are no symmetric or systematic differences outside the observational uncertainties in any of the parameters.

Applying the results of the SSP models from Chapter 2 directly to the KDC in

NGC 1700 is not straightforward. The models were based on a disk component superimposed on a spheroid, which assumes intrinsic kinematics for these components which may not be relevant to the KDC. Indeed, the KDC appears to be associated with boxy isophotes, rather than disky isophotes, suggesting that the KDC is not in the form of a central disk. Therefore, it is not possible to apply the results from the spectral models as directly as was done for NGC 584 or NGC 821. However, it can be concluded that the KDC in NGC 1700 is not composed purely of a stellar population which is significantly younger than the rest of the galaxy, as its dynamical signature is equally apparent in both the Calcium II triplet and Hβ kinematics. The presence of a young *disk*, on the other hand, is not strongly constrained by this data, as the data quality is not high enough where the disky distortions are strong.

3.5.6 Conclusions from the Observations

From the simple spectral modelling presented in Chapter 2, it was shown that a cold, rotationally supported disk composed of a young stellar population, superimposed on an old, pressure supported, slowly rotating population, would be detectable by comparing the kinematics derived from the Calcium II triplet and Hβ absorption features. It was found that there were three indicators of a young disk component when comparing the kinematics from these two wavelength regions:

1. Offsets in the higher-order moments of the LOSVD. This is sensitive to disks younger than 25% of the total system age, which typically contain a very small fraction of the galaxy mass.

2. Higher Hβ rotation velocities. This is sensitive to disks aged between 25% and 50% of the total galaxy age, containing typically 2-10% of the galaxy mass.

3. Strong two-component structure in the LOSVD. This is sensitive to high-mass fraction disks, typically older than half the total age of the galaxy, and containing $> 10\%$ of the galaxy mass.

In all but two of the sample galaxies, none of the above indicators provide evidence of a young disk component. The two galaxies in question, NGC 584 and NGC 821, show tentative evidence of small offsets in the rotation velocities derived from the two wavelength regions, in the sense that Hβ gives a slightly higher rotation velocity than the Calcium II triplet.

Comparing the kinematic profiles for these galaxies with the corresponding model parameters, however, it is possible to exclude a number of possible young-disk models. The offsets in velocity are generally accompanied by measurable offsets in the higher-order moments of the LOSVD, namely the velocity dispersion, h_3 and h_4 parameters. For

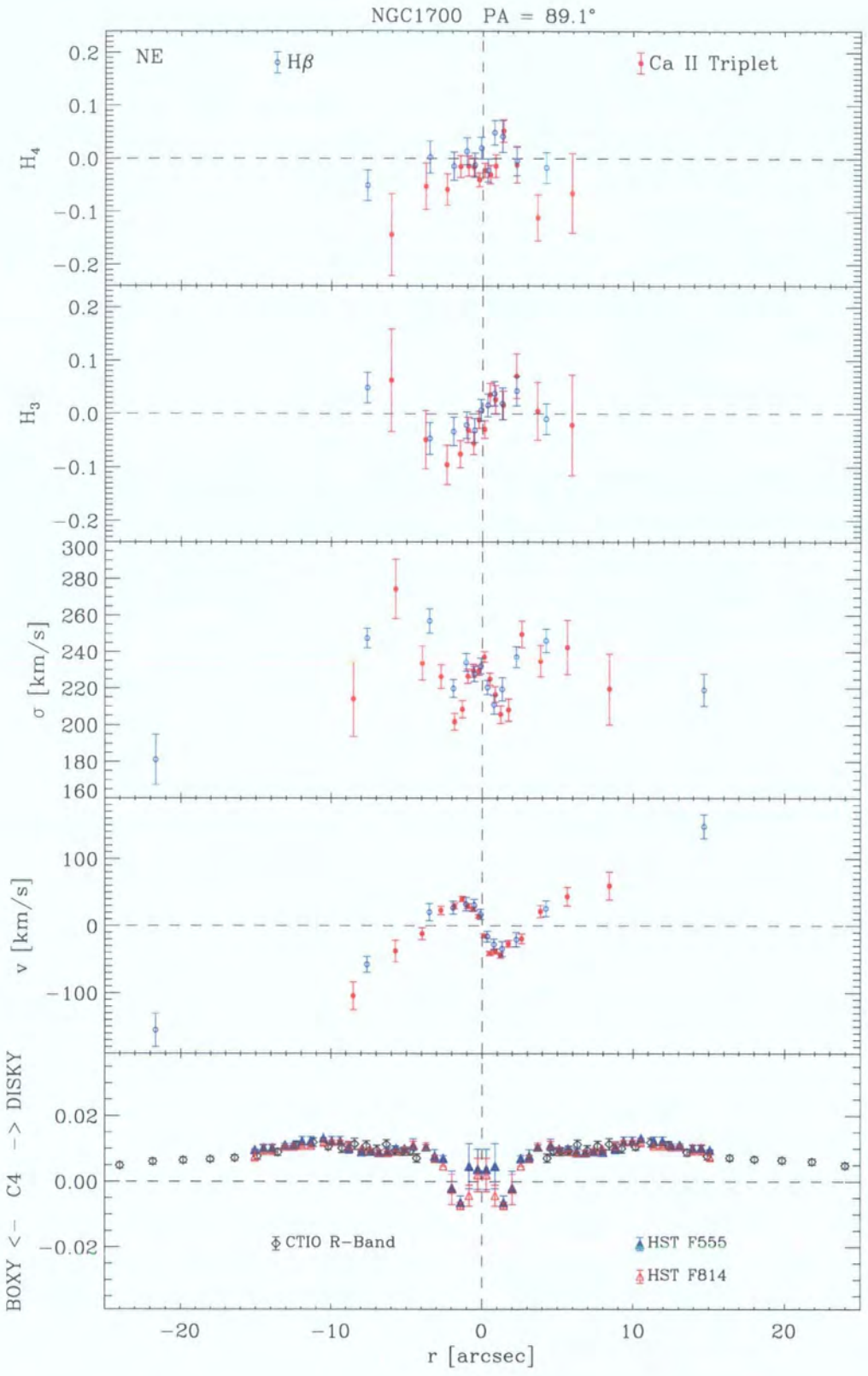

Figure 3.39: Parameterized LOSVD profile for the major-axis of NGC 1700

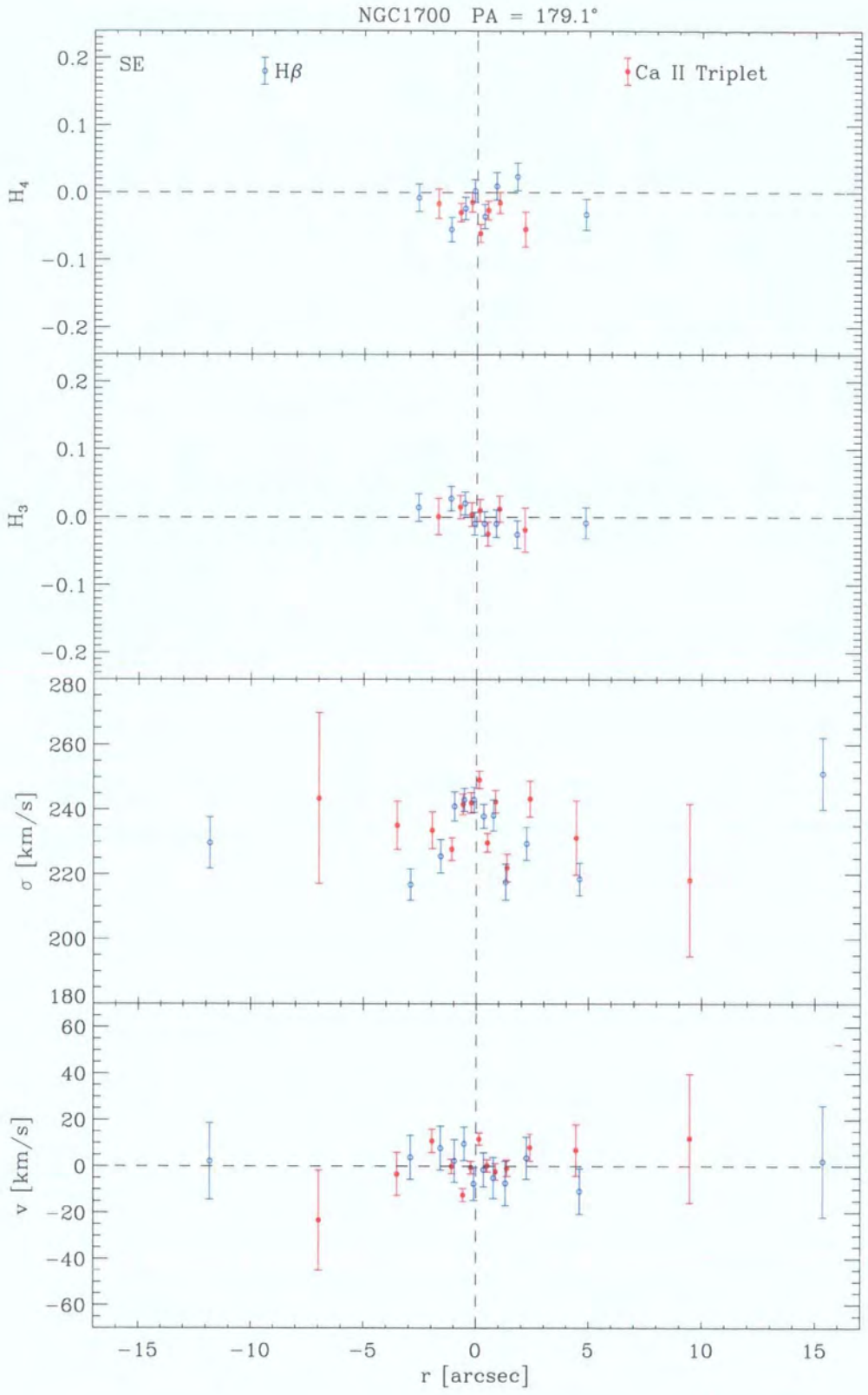

Figure 3.40: Parameterized LOSVD profile for the minor-axis of NGC 1700

NGC 584, these offsets in the other kinematic parameters are not observed, and therefore disks composed purely of a population older than 1 Gyr are strongly excluded by the observations.

For NGC 821, it is only possible to exclude disks which are 6 Gyr or older (therefore $\geq$ 14% by mass) based on examining the shapes of the LOSVDs. The disk component in NGC 821 is known to have a higher velocity dispersion than that assumed in the original disk+spheroid models, which makes the LOSVDs of the disk and spheroid more similar, and therefore more difficult to separate. The models most consistent with the observations are those of intermediate aged disks comprising 3-10% of the galaxy mass. Such models predict also offsets in the velocity dispersion, however, which are not observed. Thus, NGC 821 may indeed house a disk component with a distinct stellar population. This population is not consistent, however, with the single-burst models considered here.

3.6 Discussion

3.6.1 Why Are no Differences Detected?

Comparing the observational results and model predictions, it would seem that the young population contained in these galaxies does not exclusively take the form of a cold, rotationally supported disk. One possibility is that the young disks in these galaxies have some degree of pressure support, as in the case of NGC 821, thus resulting in smaller velocity differences between the 'disk' and 'spheroid' components, and a less pronounced difference between the shape of the disk and spheroid LOSVDs. From Chapter 2, it was shown that the dispersion of the disk can be a significant factor in determining the degree of difference between the Calcium II triplet and Hβ kinematics, especially where the overall Hβ absorption is not very strong.

The assumption of solar metallicity for both the disk and spheroidal components is most likely inaccurate, given that the two components form at completely different epochs. A proper exploration of the parameter space of different disk and spheroid metallicities, as well as ages and kinematics, is beyond the scope of this thesis. The worst-case scenario of a metal-rich young disk population superimposed on a metal-poor old spheroidal population was considered in Chapter 2. One would perhaps expect that there is a smaller contribution from the disk population, since the old population is contributing more to the Hβ absorption. However, the Hβ absorption is still too strong to be accounted for by the old population, even though it is metal poor. Alternatively, since the disk population is metal-rich, accounting for the additional Hβ absorption requires a larger mass fraction to be added (since the Hβ absorption is weaker than in the solar-metallicity case), therefore the disk still contributes a sufficiently large fraction of the light to create differences in the Ca II Triplet and Hβ kinematics. Therefore, consideration only of solar metallicity components is not expected to affect the conclusions of this work.

Due to the small differences in the kinematics that must be measured, data with high S/N and spatial resolution is required at the position where the peak in the C4 term occurs. Although the data meet these criteria in the central regions where the galaxy is bright, there is not always adequate S/N at larger radii to detect velocity differences down to 10 $\mathrm{km\,s^{-1}}$ without creating large radial bins which dilutes the disk signature. However, the total integration times for this data were not especially long (generally 3600s with a $1''$ slit on a 4m-class telescope), and increasing the data quality to meet these criteria would require a modest investment of observing time.

3.6.2 Constraining the Formation Scenario

The fact that there are no clear offsets between the observed kinematics derived from the two different wavelength regions provides constraints on how these galaxies have formed, and on the origins of the diskiness-Hβ trend. There has been much theoretical work recently on explaining the formation of disks in ellipticals via collisionless merging of disk galaxies (Naab et al. 1999, Bendo & Barnes 2000, Naab & Burkert 2001). Isophote shapes of the remnants are predicted to be determined simply by the mass ratio of the progenitor disk galaxies, with disky isophotes arising from merger mass ratios of 3:1 or greater. Explaining the observed kinematic properties proves less straight forward however, and the shapes of the remnant LOSVDs differ between studies.

Modelling only the gas component of a gas-rich merger event, Barnes (2002) shows that extended gas disks can form for a variety of merger mass ratios. It is suggested that, were such disks to form stars, they would be apparent primarily as a low-dispersion, high-rotation velocity component in the LOSVDs of these galaxies. Furthermore, since these stars would have formed as a result of the merger, the disk would be composed of younger stars than the rest of the galaxy, and that line profiles of different spectral lines may show this. The question remains, however, over the origin of the Hβ-diskiness relation. Barnes (2002) finds that these extended gas disks can also form in equal mass mergers, which are thought to result in boxy ellipticals. Why then do disky ellipticals appear younger than boxy ellipticals?

Bekki (1997) found that the rapidity of gas consumption by star formation in a merger has a profound effect on the isophotal shape of the resulting elliptical galaxy. The rate at which gas is converted to stars controls the amount of dissipation involved in the merger. This in turn determines the final isophotal shape, with more dissipation (and therefore a lower star formation rate) resulting in more disky isophotes. Furthermore, the role of dissipation in determining the merger outcome can be more significant than that of the initial mass ratio. Springel (2000) simulated equal mass mergers involving stellar and gas dynamics, as well as a phenomenological prescription for star formation. In these models, when gas was excluded from the simulation, remnants with predominantly boxy isophotes were produced. With gas included, the remnants' isophotes tended to be disky.

This suggests that the degree of dissipation involved in the merger is the dominant factor in determining the morphology of the remnant elliptical. Where dissipation plays a minor role, then the mass ratio of the merger can determine the outcome.

This interplay between dissipational and collisionless processes may give us clues to the origin of the Hβ-diskiness trend. Disky galaxies are found in a range of environments, whereas a high fraction of boxy ellipticals are found in the centre of clusters, where galaxies involved in merging have already had a large fraction of their gas removed by ram-pressure stripping and star-formation. Mergers of such galaxies would be largely collisionless, although not necessarily between galaxies of equal mass. In less dense environments, however, galaxies tend to be richer in gas, making dissipational processes more important. Thus, even equal mass mergers may produce disky ellipticals.

The importance of dissipation in determining the shape of remnant elliptical is intrinsically linked to the star formation rate (SFR) of the merger. If there is a high SFR during the merger, then all the gas is turned quickly into stars, rendering dissipation dynamically unimportant. If the SFR is low, however, the gas may play an important role in shaping the remnant elliptical. We would expect such differences in the star formation history to manifest themselves in the fossil evidence of the stellar populations in the remnant.

In the simple modelling presented in Chapter 2, it was assumed that the disk component formed instantaneously from a single burst of rapid star formation. It is possible, however, that the disk was formed in a more extended period of star formation, and is therefore composed of a range of stellar ages which result in the same combined, luminosity weighted age. The result of this would be that the disk contains both old stars and young stars, allowing a significant contribution of light in both red and blue wavelength regions, which is indeed what we find in this work.

3.7 Conclusions

This Chapter presents major- and minor-axis kinematic profiles for a small sample of disky, Hβ-enhanced galaxies observed simultaneously around both the Calcium triplet and Hβ spectral features. No strong differences between the kinematics derived from these two regions were found, although two galaxies show marginal evidence for a disk component composed of a distinct stellar population. This suggests that the observed galaxies do not resemble our simplistic two-component models, but instead have more complex star formation histories. It is found that the embedded disks in the sample galaxies are equally apparent in the kinematics derived from both wavelength regions, suggesting that the disks are composed of a range of stellar ages. This indicates an extended star formation history associated with the disk component, supporting theoretical findings from simulations of galaxy mergers that dissipation promotes diskiness.

From this work, it is evident that combining stellar populations and kinematics in a direct way can link together a galaxy's dynamical and chemical history, thus constraining the formation processes involved. Through the use of integral-field spectrographs (IFSs), future observations will obtain full spatial and spectral coverage of galaxies; linking morphological and dynamical structure to the distribution of stellar populations. One such project is already underway. The SAURON project is a systematic survey of a representative sample of early type galaxies, using a wide-field IFS, SAURON, on the William Herschel Telescope on La Palma. Early findings from this project (Bacon et al. 2001, Davies et al. 2001, de Zeeuw et al. 2002) indicate that, similar to this work, complex dynamical structure is not always clearly reflected in the stellar populations. Clearly, linking stellar populations directly with stellar dynamics is the first step in understanding why this should be the case.

Chapter 4

Dynamical Schwarzschild Modelling of NGC 821

4.1 Introduction

In the past two decades, our understanding of the internal structure of elliptical galaxies has increased dramatically. The discovery that bright elliptical galaxies rotate too slowly to be flattened only by their rotation (Bertola & Capaccioli 1975, Binney 1976, Illingworth 1977), while low-luminosity ellipticals are consistent with being oblate isotropic rotators (Davies et al. 1983), marked an early turning-point in the conventional view that elliptical systems were dynamically simple. Around the same time, Binney (1978) used the tensor virial theorem to demonstrate that ellipticals could be flattened without significant rotation, since their shape can be supported by an excess of random motions in the equatorial plane compared to the perpendicular direction, quantified by the anisotropy of their velocity dispersion tensor.

As discussed in previous chapters, detailed photometric observations of deviations from pure elliptical isophotes divide elliptical galaxies into two sub-classes of object: 'boxy' and 'disky' (Bender 1988, Peletier et al. 1990). Conventional interpretation of these isophote shapes is that the pointed isophotes in disky ellipticals indicate the presence of a faint, nearly edge-on embedded stellar disk, with a correspondingly higher degree of rotational support, and a structure typically consistent with axisymmetry. Alternatively, boxy isophotes imply that the galaxy is supported by various degrees of velocity anisotropy, and is indicative of a triaxial figure.

This simple interpretation is complicated by the fact that it is not certain that, from photometric considerations alone, the pointedness of disky isophotes is truly indicative of a faint stellar disk. Pointed isodensity surfaces can also result from single-component mass models with axisymmetric or triaxial potentials alike (de Zeeuw et al. 1986). N-body simulations of mergers and dissipational collapse have found that isophotes of remnants can appear either disky or boxy when viewed at different orientations (Stiavelli et al. 1991, Hernquist 1993, Heyl et al. 1994).

Therefore, it is necessary to study the detailed properties of these objects. Of particular relevance to this thesis are objects with disky isophotes. To test the hypothesis that such galaxies have a two-component 'disk + bulge' structure, it is instructive to explore how well such a model describes the observational constraints, both photometric and kinematic. Much work has been conducted in this direction, with a view to deconvolving the two component structure with some assumption about the physical form of either one or both components (e.g., Rix & White 1990, Rix & White 1992, Scorza & Bender 1990, Scorza & Bender 1995). The standard approach is to describe the spheroidal component as a pressure-supported, slowly rotating component with a classic $R^{1/4}$, or **de Vaucouleurs** light profile; and the disk as a razor-thin, rotationally supported component with an **exponential** light profile.

While such a model is often a good first approximation to the behaviour of many of these objects, one would prefer to study the dynamical structure in a more general way, without assuming a specific model for the components. One such route is to build general dynamical models (i.e., with the minimum possible assumptions, and with no specific form in mind) from which it may be possible to study the intrinsic orbital structure of the galaxy. One such type of dynamical model is that based on Schwarzschild's (1979) orbit superposition technique, which builds a dynamical picture of the galaxy by combining, in some optimal way, a variety of different stellar orbit trajectories. From this, it may be possible to associate particular orbital families or characteristics with the global properties of the galaxy, and thus 'decompose' the galaxy from a more physically motivated perspective.

Driven by this, this chapter presents an investigation of the disky elliptical NGC 821, using sophisticated modelling techniques combined with state-of-the-art integral-field spectroscopic and photometric data, to examine the orbital structure of this galaxy, and determine the nature of any dynamical sub-structure which may exist. By understanding the dynamical structure of this galaxy, and combining this with the consideration of stellar populations presented in Chapter 3, it is possible to gain insights as to the formation mechanism of this object, and disky elliptical galaxies in general.

This chapter has the following structure: the proceeding subsections introduce the concepts of the Schwarzschild dynamical model and integral-field spectroscopy. §4.2 describes the *SAURON* observations and data reduction, as well as all other data sets used in constraining the model. §4.3 describes the technique used to generate a mass model for the galaxy, §4.4 describes the application of the three-integral Schwarzschild code, and §4.5 presents the best-fitting model with comparison to other work. §4.6 presents the detailed properties of the best-fitting model, and §4.7 concludes.

4.2 *SAURON* Observations and Data Reduction

The *SAURON* integral-field data for NGC 821 was obtained as part of the representative sample of early type galaxies surveyed by the *SAURON* project. As a member of the team, the author has been involved in several of the observing runs required to complete the sample, and has reduced the data for NGC 821 from the 'merging' of individual exposures, to the production of the input kinematics for the Schwarzschild model. This section gives a brief outline of the project, the instrument, the observations, the data reduction techniques, and the analysis tools used. A comparison of the *SAURON* data with the long-slit data of NGC 821 presented in Chapter 3, as well as that of an independent author, is presented. Finally, the other data sets used in the model are summarized: specifically ground-based imaging, and space-based imaging and spectroscopy.

4.2.1 The *SAURON* Project

The *SAURON* project is a collaborative project undertaken by Observatoire de Lyon, Leiden Observatory, and the University of Durham, for the systematic study of the stellar and gaseous kinematics and the line-strength distributions of nearby early type galaxies. The project is centred around the *SAURON* (Spectrographic Areal Unit for Research on Optical Nebulae) IFU (Bacon et al. 2001), mounted on the Cassegrain focus of the 4.2m William Herschel Telescope (WHT), La Palma (Figure 4.1).

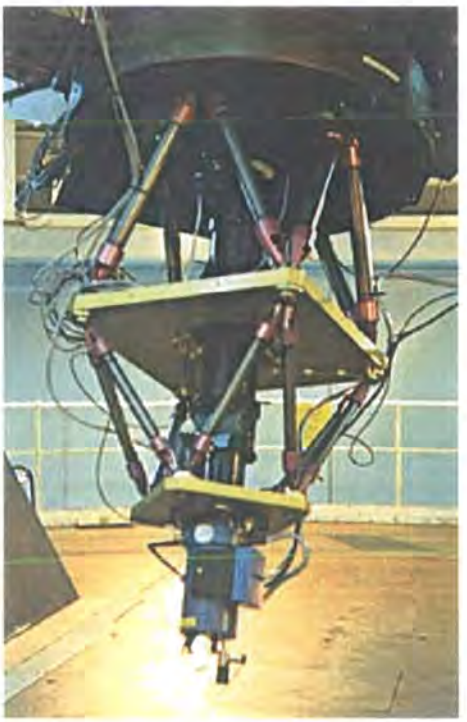

Figure 4.1: Photograph of the *SAURON* IFU mounted at the Cassegrain focus of the WHT.

The aim of the project is to survey the kinematics and stellar populations of a representative sample of 72 nearby E, S0, and Sa galaxies drawn from both cluster and field environments. The objectives of the survey include determining the intrinsic shape of the galaxies, their orbital structure, the mass-to-light ratio as a function of radius, the age and metallicity of their stellar populations, and the frequency of kinematically decoupled cores and demography of nuclear black holes. For galaxies with nebular emission lines, it is possible to examine the distribution and kinematics of ionised gas in these galaxies, providing observational clues to the links between stellar and gaseous processes, as well as ionisation mechanisms and nuclear activity.

Early results from the survey illustrate in graphic detail that early-type galaxies are far from dynamically simple systems, with a large number of kinematically misaligned or decoupled components observed (e.g., Davies et al. 2001, de Zeeuw et al. 2002), many of which were previously unknown, and certainly were not as well-quantified. Indeed, it is somewhat surprising that a sample, based only on ellipticity and magnitude, does not contain more 'normal' elliptical galaxies of the smooth, featureless systems one might expect.

Preliminary stellar population analysis also reveals a complex star formation history for many of the sample galaxies. Connecting star formation processes with the dynamical structure of elliptical galaxies is one of the key goals of the *SAURON* project. Only by establishing the connection between these properties can a full understanding of galaxy formation and evolution begin to form.

An important part of the *SAURON* project is to analyse the two-dimensional maps with state-of-the-art dynamical modelling techniques, such as the Schwarzschild orbit superposition method described in this chapter (e.g., van der Marel et al. 1998, Cretton et al. 1999). Applying data of this type and quality to such methods yields strong constraints on the structure of early-type galaxies, providing insights to their formation and evolution. The first results from this modelling process (Verolme et al. 2002) have shown that *SAURON* data provides a powerful constraint to the models, and can be used to extend their interpretation beyond what was possible with previous long-slit data. As the number of galaxies modelled from the sample increases, it is expected that statistically significant conclusions on the dynamical structure of early-type galaxies can be drawn.

4.2.2 The *SAURON* Instrument

SAURON is a purpose-built IFU based on a single lenslet array design pioneered by the TIGER spectrograph (Bacon et al. 1995), and later developed for OASIS (Bacon et al. 2001). Figure 4.2 illustrates the optical layout of the instrument. When *SAURON* was designed, special emphasis was put on maximising the field of view. For a pure lenslet IFU, this is determined by the spectral coverage on the CCD (a compromise between wavelength range and spectral resolution), the spacing between spectra from each lens,

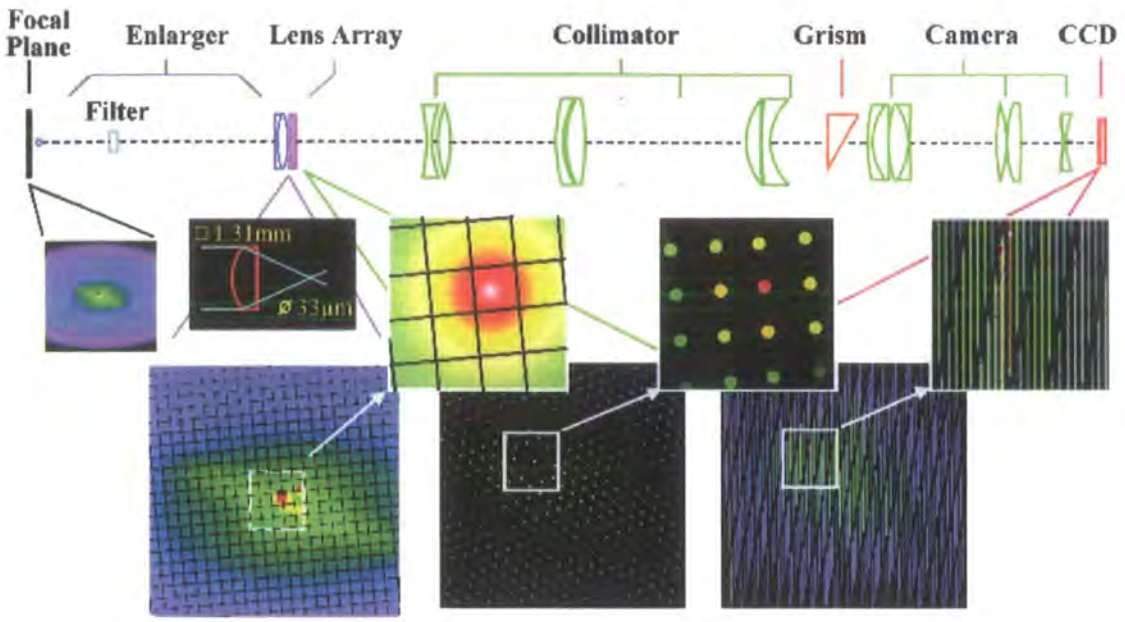

Figure 4.2: Schematic of the *SAURON* optical train. The key optical elements are displayed from the telescope focal plane (left) to the detector plane (right). The image of a galaxy is shown at each major stage: the telescope focal plane (showing the galaxy image), the entrance to the lens array (showing the image sampled by the lenses), the exit plane of the lens array (showing the micropupil images) and the detector plane (showing the dispersed micropupil images). Each has a corresponding enlargement for clarity. The insert at the lens array shows the detailed light path within a microlens. (Taken from Bacon et al. 2001)

the physical size of the detector, and the effective lenslet size on the sky. For the 4.2m WHT, using the 13.5 μm pixels of the 2kx4k EEV 12 detector, this results in a maximum lenslet size of around $1''$ for a camera aperture slower than $f/1.8$ (Bacon et al. 2001).

SAURON maximizes the spatial and spectral coverage by allowing up to 10% overlap between adjacent spectra, but maintaining reliable extraction of the spectra by accurately modelling the **cross-dispersion profile** (i.e., the light profile of each spectrum perpendicular to the wavelength axis). The wavelength range itself is carefully chosen to provide key diagnostic absorption and emission features whilst maintaining good spectral sampling. The region from 4800-5400 Å was chosen, as this region includes several strong absorption features (important for deriving kinematics) including the age-sensitive Hβ feature and metal-sensitive Mg b and Fe lines. In the presence of gas, this region also includes [OIII], Hβ and [NI] emission lines, allowing gas distributions, kinematics and excitation levels to be determined.

The resulting field of view is $41''$ x $33''$, observed with a filling factor of 100% (i.e., complete spatial coverage within the field), and sampled with $0\farcs94$ x $0\farcs94$ spatial elements. This is the low resolution (LR) mode of the instrument. A different enlarger is also available, which provides a finer spatial resolution of $0\farcs27$ x $0\farcs27$ across a $9''$ x $11''$ field: the high resolution (HR) mode. For the purpose of the *SAURON* survey, however, the

Parameter	Value
Spatial Sampling	0.″94 x 0.″94
Field of View	33″x 41″
Spectral Resolution (FWHM)	4.2 Å
Grism	514 lines mm^{-1}
Spectral Sampling	1.1 Å pix^{-1}
Instrumental Dispersion	105 $km\,s^{-1}$
Wavelength Range	4810-5350 Å
Detector	EEV 12 2148x4200 pixels
Pixels Size	13.5 μm

Table 4.1: Summary of *SAURON* instrumental set-up in the low resolution (LR) mode used for the survey observations.

HR mode is not used, and all further references to the instrument or data assume the LR mode. Table 4.1 gives the details of the generic instrumental set-up of *SAURON* used for the survey.

Even with this comparatively large field of view (for an IFU), the target objects generally still contribute a significant amount of light at the edges of the field. Therefore, in order to allow accurate subtraction of the background sky spectrum, there is another enlarger centred 1.′9 from the centre of the main field, which is then imaged onto one side of the lenslet array (see Figure 4.3. In this way, the sky background is observed simultaneously with the object, allowing accurate sky-subtraction. In total, there are 1431 object lenslets and 146 sky lenslets.

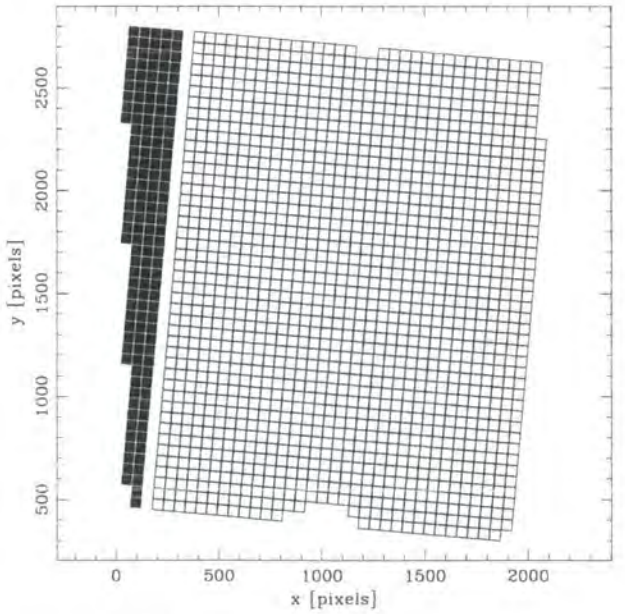

Figure 4.3: Schematic showing the effective positions of the lenslets on the CCD. Open squares represent the object lenses, solid squares represent the offset 'sky' lenses. The scale is in pixels of the EEV 12 detector (13.5 μm per pix.). (Taken from Bacon et al. 2001)

4.2.3 Observations

SAURON observations of NGC 821 were obtained between the 8th and 14th of October, 1999, during the second observing run of the *SAURON* project. One of the principle aims of the *SAURON* survey is to obtain data on the sample galaxies out to 1 effective radius (R_e: the radius inside of which contains half the light of the galaxy) in two or less pointings[1] where possible; otherwise, out to $0.5R_e$. NGC 821 has a rather large apparent size on the sky, with $R_e = 50''$. Hence, to map this galaxy to $\pm 1R_e$ would require more than two pointings, even with no overlap between the two fields. Therefore, the observations only go out to $\frac{1}{2}R_e \equiv 25''$. The resulting mosaic of the two pointings (each represented by a green rectangle) is shown in Figure 4.4.

Due to the precise placement of the spectra, an exposure time of 1800 seconds was considered optimal to minimize the effects of instrumental flexures and data-loss due to cosmic ray events, while maintaining a reasonable signal-to-noise ratio of each exposure. Each pointing therefore consisted of three individual 30 minute exposures, each slightly offset (by a small, non-integer number of spatial elements) from the other. This gives a 'drizzling'-style sampling, allowing the combination of exposures to be sampled at a higher effective spatial resolution (see §4.2.4). The final data-cube consists of 2956 individual spectra, covering a near-rectangular area of approximately $60'' \times 30''$ with a spatial sampling of $0''.8$ pix^{-1}.

Although the individual exposures are quite short, the nature of the data is such that instrumental flexures can have a drastic effect on the quality of the data extraction. Knowing precisely where the spectra are falling on the CCD is crucial in applying the model of the cross-dispersion profile. For this reason, wavelength calibration exposures of a neon arc-lamp are taken between each 1800s exposure. Although time-consuming, this ensures an accurate calibration and extraction of the spectra. At the beginning and end of each night, a series of at least five continuum-lamp exposures were obtained which were used to build the *extraction mask* (see §4.2.4); at least ten bias frames were also taken at the beginning and end of each night.

4.2.4 Data Reduction

Due to the complexity of the *SAURON* data format, to obtain the optimal quality of information from the data requires the use of specifically designed software based on the standard methods of data reduction, but which can deal effectively with a contiguous three-dimensional data-cube. The reduction and analysis of the *SAURON* data is done using the purpose-built XSauron software, developed by the Observatoire de Lyon, which is based on the publicly-available XOasis software (Bacon et al. 2000) designed for

[1] A 'pointing' refers to one or more exposures taken at approximately the same position in order to observe an area equivalent to a single *SAURON* field

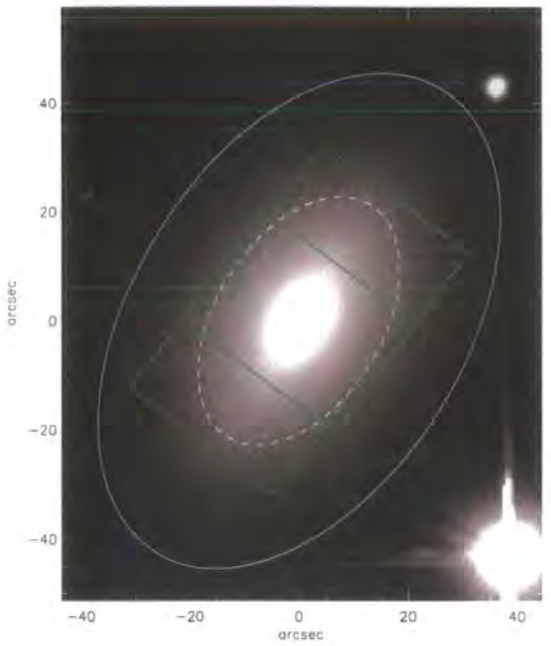

Figure 4.4: *SAURON* object fields (green boxes) overplotted on image of NGC 821 showing the two pointings of the mosaiced field. The solid curve corresponds to an ellipse with the same mean flattening and position angle as NGC 821 at a semi-majoraxis of 50″, equivalent to one effective radius (R_e). The dashed line is the same, but for a semi-majoraxis of $\frac{1}{2}R_e$.

SAURON's versatile predecessor instrument, OASIS. A fuller description of the XSauron software package is given in Copin (2000) and Bacon et al. (2001). The basic reduction outline for a single exposure is as follows:

- **CCD Preprocessing** This includes overscan, bias and dark current subtraction.
- **Extraction of the Spectra** Creating and applying the extraction mask based on the detailed instrument model.
- **Wavelength Calibration**
- **Flat-fielding** Includes spectral and spatial flattening.
- **Cosmic Ray Removal**
- **Common Spectral Resolution** Degrade all spectra to the lowest common spectral resolution of all exposures.
- **Sky Subtraction**

Each of these steps is described in detail in Bacon et al. (2001), and for the data presented here, were conducted by a semi-automated pipeline based at the Observatoire de Lyon. All further reduction and analysis steps were performed by the author, and are outlined below.

Merging of Multiple Exposures

Once each exposure has been extracted into an (x, y, λ) data-cube, it is necessary to combine them to create the final global data-cube. The global data-cube consists of a combination of six 1800s exposures, split into two pointings of three dithered exposures (see Figure 4.4). The merging therefore has two functions: 1) to combine the dithered exposures, increasing the signal-to-noise ratio, avoiding systematic effects from bad columns on the CCD, and increasing the effective resolution via 'drizzling'-type sampling; and 2) to form mosaics of several pointings, extending the data over a larger contiguous two-dimensional field.

Each of the two pointings includes the centre of NGC 821 in their field (Figure 4.4). The centre can then be used as a point of reference for defining a common origin for the spatial coordinate system of each of the exposures. The position of the centre can be accurately located by 'reconstructing' the image of the galaxy. This is done by simply summing the total flux in each spectrum, and associating that value with the corresponding spatial element, effectively giving a narrow band-pass filter image (Figure 4.5).

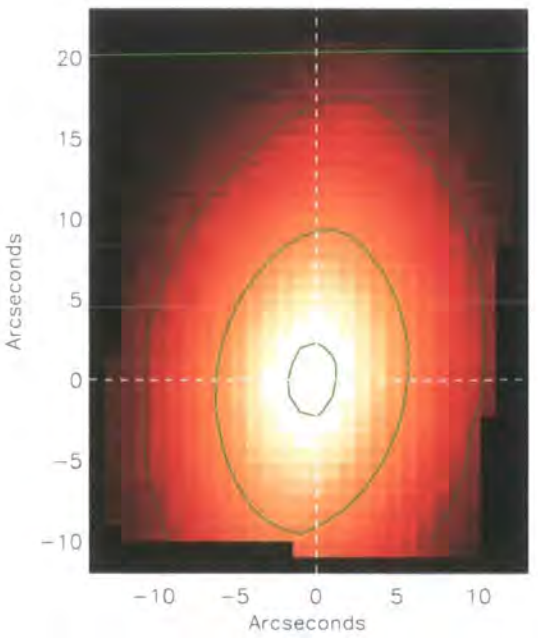

Figure 4.5: Example of a reconstructed *SAURON* image for a single 1800s exposure, created by accumulating the total flux of each spectrum, and associating it with a single spatial element, or lenslet. Such images are used to recentre the coordinates of the data-cube to a common origin, shown here as the galaxy centre. The green lines represent smoothed isophotes of the image, and are included for illustration.

The spectral range varies as a function of position across the CCD, due to a tilt in the interference filter with respect to the plane of the detector. This tilt was introduced to avoid ghost images caused by mutual reflection which were found during the commission-

ing of the instrument. As a result, however, the common wavelength range was reduced by 16%. The red wavelength limit is most affected, and varies from approximately 5275 to 5380 Å between the left and right edges of the field. For many galaxies, in particular those with systemic velocities greater than 2000 $\mathrm{km\,s^{-1}}$, this results in the strong iron feature at 5270 Å being at least partly lost. This feature is not crucial for deriving kinematics, as there are several other strong features in the wavelength range. For absorption line-strength measurements, however, this effectively reduces the field-of-view, as far as Fe5270 is concerned, by more than 30% in some cases (de Zeeuw et al. 2002). This means that truncating the data-cubes to a common wavelength range is often a compromise between field-of-view and wavelength coverage.

For NGC 821, the useful common wavelength range was determined as 4785 - 5370 Å, which includes the Fe5270 absorption feature across the entire field, although it is affected by the filter cut-off towards the right of the field of view. During the flat-fielding, the sharp drop in the filter transmission can introduce a sharp upturn in the extracted spectra at the right-edge (and, to a lesser extent, the left-edge) of the field (Figure 4.6), making line-strength measurements difficult. This feature also presents a problem for deriving the kinematics, since continuum subtraction in the presence of this upturn requires a higher-order polynomial than for spectra in the centre of the field where there is no such feature. However, the spectra are further truncated for the kinematic analysis, and so in the interest of maintaining as much useful information in the data-cube as possible, all the exposures were truncated to this range for the purpose of merging.

After the spectra are truncated, the data-cubes are each individually flux-calibrated. Since photometric standards are not observed after each exposure, all data-cubes are re-normalised using a common spatial aperture on the reconstructed images, thus accounting for differences in transparency between exposures. Each data-cube is then interpolated onto a common grid which has a slightly higher spatial resolution than the original frames to take advantage of the dithered exposures. Each spectrum in the resulting merged data-cube is given by the error-weighted mean of all the spectra overlapping the grid point, weighted by their fractional contribution to the grid aperture.

Adaptive Two-Dimensional Binning

Due to the sharply decreasing light profiles of typical early type galaxies, the signal-to-noise ratio (S/N) varies strongly across the field-of-view. In order to derive accurate and reliable measurements of stellar kinematics, spectra with a minimum S/N are required (Rix & White 1992, van der Marel & Franx 1993, Kuijken & Merrifield 1993). Since this minimum may not be met by a large portion of the data, it is not satisfactory to simply exclude spectra of inferior quality. Rather, it is preferable to combine, or *bin* the information in some way so as to maximise the information in the spectra, albeit at the expense of spatial resolution. Such binning is standard practice with conventional

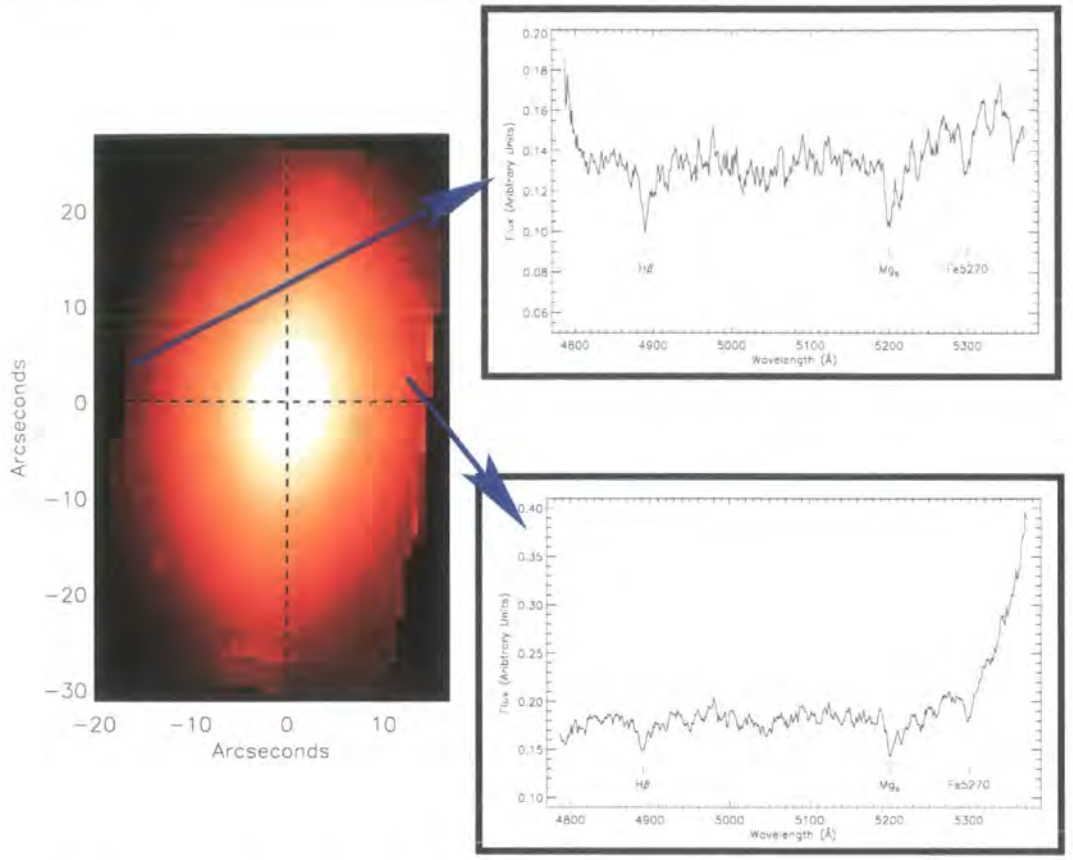

Figure 4.6: Illustration of the effect of the interference filter on the ends of the spectra. The image is reconstructed from the merged data-cubes, truncated in wavelength to 4785 - 5370 Å(before binning). The band-pass of the filter changes as a function of position on the CCD. In order to maintain as much useable information across the entire field as possible, spectra on the right-edge of the field suffer from a significant 'upturn' at their red-end, caused by the difficulty in correcting for the sharp filter cut-off. A similar, but smaller, effect is seen at the blue-end of spectra at the left of the field. The chosen common wavelength range is a compromise between preserving the maximum amount of useful information at the red and blue ends of the spectra across the largest possible field-of-view.

imaging or aperture and long-slit spectroscopy (for example, see §3.3.3); however applying this idea to integral-field spectroscopy is a relatively new concept.

The technique used here is that developed by Cappellari & Copin (2001) as a general approach to the problem, and implemented by Yannick Copin into the XSauron software package. There are two possible methods implemented: the Quadtree method (Samet 1984); and the Voronoi Tesselation method. At the time of writing, only the former can be used with the Schwarzschild modelling code, which requires rectangular-shaped bins such as those constructed by the Quadtree algorithm. Unlike the Voronoi Tesselation, the Quadtree method is not optimal (Cappellari & Copin 2001), and ultimately all applications of the Schwarzschild modelling code to *SAURON* data will use the Voronoi method. To a first order, however, there should be little difference in the overall results of the models. Indeed, §4.6.3 finds that using input data based on the Voronoi

Tesselation method yields a model Distribution Function which is essentially identical to that from the Quadtree-binned data.

The Quadtree method is based on recursively dividing a square aperture into four smaller equal-area squares, until dividing a square results in its corresponding S/N becoming smaller than the threshold minimum value. The *SAURON* data format consists of two parts: one file which contains all the spectral information, including the flux and corresponding noise at each wavelength; and a second file containing information relating each spectrum to a lenslet, and therefore to a spatial position, as well as any derived quantities such as the velocity of the spectrum, its total flux, etc. Before binning the data-cube in the spatial domain, it is necessary to evaluate the S/N of each lenslet of the (merged) data-cube. This is done by evaluating the mean value of the error spectrum for each lens in the data-cube.

Once the S/N map is derived, the binning method involves two stages:

- **Binning computation**: Dividing the field-of-view into bins of comparable S/N using the Quadtree algorithm,
- **Data-cube Binning**: Averages the spectra of the data-cube according to the previously computed bin map.

The first of these has already been described, and results in a map of bins of the requisite S/N. Figure 4.7 (a) shows the S/N map before binning, and clearly a significant portion of the field contains spectra with S/N ≤ 30 pixel^{-1}, for which reliable kinematics (especially h_3 and h_4) will not be obtained. After applying the Quadtree algorithm, the bin map shown in Figure 4.7 (b) is obtained. Clearly, the field-of-view in which reliable kinematic measurements can be made has increased significantly, although the extent of the data, and the spatial resolution in the outer regions, is reduced somewhat.

After the bin map has been created, each lenslet of the original data-cube is assigned an identification number which associates it to a particular bin. The second step of the process combines the spectra associated with each bin, which simply involves taking the sum of all the spectra, weighted by the associated S/N value used to make the bin map. From the Monte Carlo simulations presented in §3.3.3, it has already been shown using a similar wavelength region to *SAURON* that a S/N~ 40 pixel^{-1} is required to determine accurate values of the mean velocity v and velocity dispersion σ; and S/N≥ 50 pixel^{-1} is required to securely determine the higher order h_3 and h_4 terms. To constrain the dynamical model, the higher-order moments are required. Therefore, before any further analysis, the data-cube is binned with a target S/N of 50 pixel^{-1}, and an absolute cut-off of 35, below which no spectra are considered. This results in 589 independent kinematic data points, each with v, σ, h_3 and h_4.

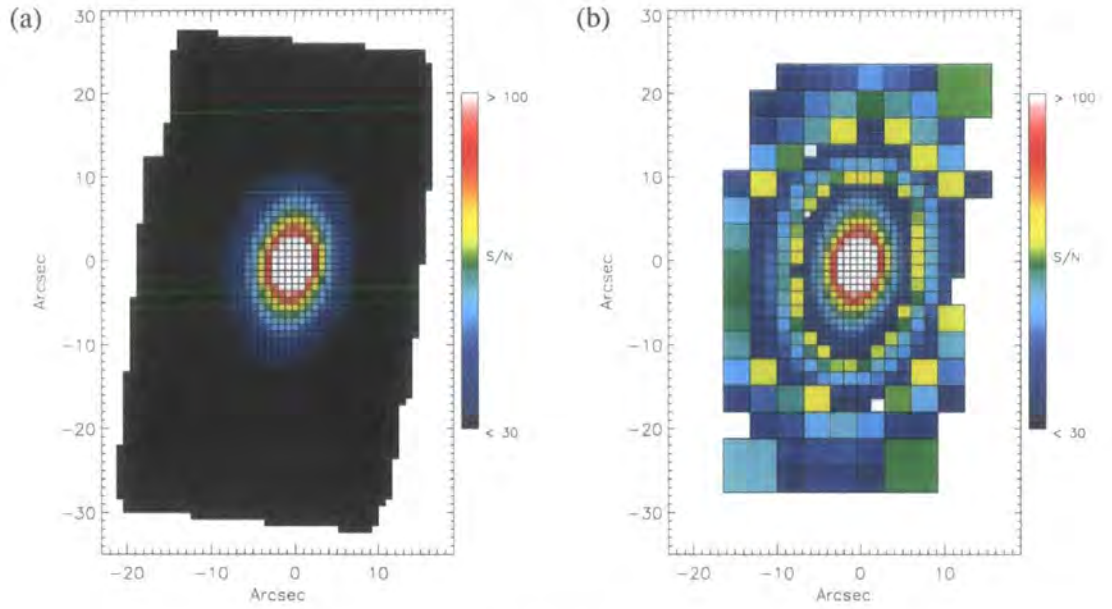

Figure 4.7: Map of S/N across the *SAURON* field (a) before binning, and (b) after binning using the Quadtree algorithm. The extent of the field in which S/N $\geq$ 30 pixel^{-1} is clearly increased significantly by the binning, allowing reliable kinematics to be derived across the entire field.

Deriving the Kinematic Parameters

The stellar kinematics were derived using an implementation of the Fourier Correlation Quotient (FCQ: Bender 1990) written by the Observatoire de Lyon. The reader is referred to §3.3.1 for a description of this method. Since the *SAURON* wavelength range is rather short (only $\sim$ 500 Å), it is necessary to use the entire wavelength range to maximise the kinematic information available. This requires using the Hβ, Mg b and Fe5270 absorption features when calculating the kinematics. These features are notoriously difficult to simultaneously reproduce using a single template star, mainly due to the magnesium overabundance (or 'alpha-enhancement', see §2.2) typically observed in early type galaxies.

For this reason, an 'optimal template' was constructed using a library of template spectra, and finding the linear combination of (non-negative) contributions of the library spectra which best represent the galaxy. The process is similar to that used in determining the emission-line spectra for the long-slit data presented in Chapter 3 (see §3.4 for details), however is performed using a procedure implemented in XSauron by Eric Emsellem which operates directly on the data cube, creating a full data cube of optimal templates fitted to each *SAURON* spectrum. The XSauron implementation differs slightly from the method described in §3.4: rather than initially normalising all spectra by their continuum, it includes a polynomial term in the non-negative least squares solution, which accounts for systematic differences in the continuum. This is preferable to removing the continuum before fitting the spectral library, as the information held in the continuum shape is maintained.

Figure 4.8 illustrates the improvement obtained by using an optimal template rather than a single stellar spectrum. The quality of the optimal template decreases with the S/N of the data, therefore at large distances from the centre of the galaxy, the resulting template is not suitable for using as a kinematic template. Instead, an average optimal template was created by averaging the fitted spectra within 3″ of the galaxy centre. It is this optimal template which is presented in Figure 4.8, and which is used to determine the final kinematics for NGC 821. The resulting kinematic maps are presented in Figure 4.9, which will be used to constrain the dynamical Schwarzschild model.

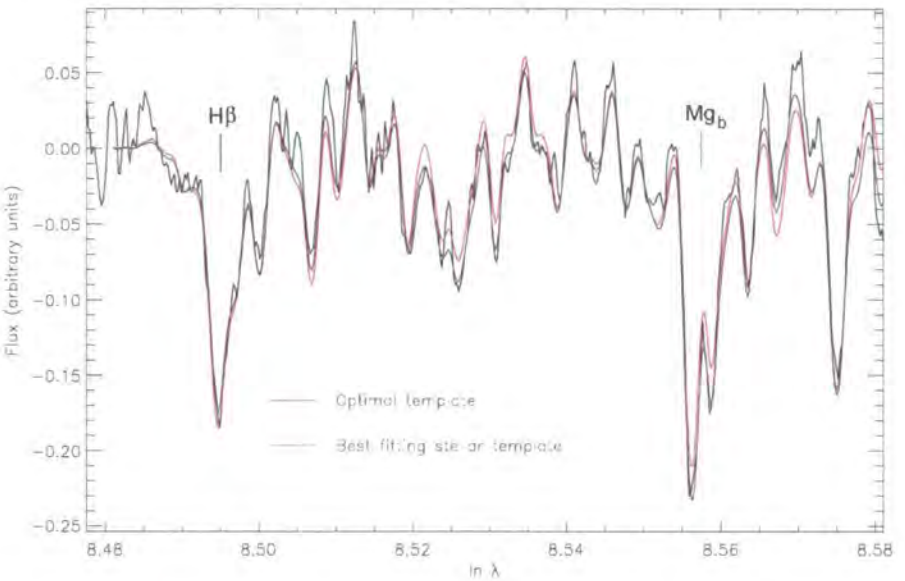

Figure 4.8: Comparison of single stellar template (red line) and optimal template (blue line) on a central spectrum of NGC 821. The stellar template shown here was chosen to give the best fit from several stars observed on the same observing run. The optimal template does provide a better fit to the galaxy spectrum, especially to the Mg b feature.

4.2.5 Comparison with Long-Slit Data

Since there are no integral-field data-sets available in the literature for NGC 821 to compare the *SAURON* data with, it is necessary to extract a narrow aperture from the *SAURON* field in order to simulate long-slit data which can be compared to data from the literature. Here, a comparison of a *SAURON* major-axis 'long-slit' with two available data sets is presented: the data of González (1993), and the ISIS data presented in Chapter 3.

Comparison with Gonzalez Data

For his thesis, Jesús González (1993) presented spatially-resolved (major axis, and minor axis for some galaxies) kinematic profiles and line strengths for 39 nearby early type

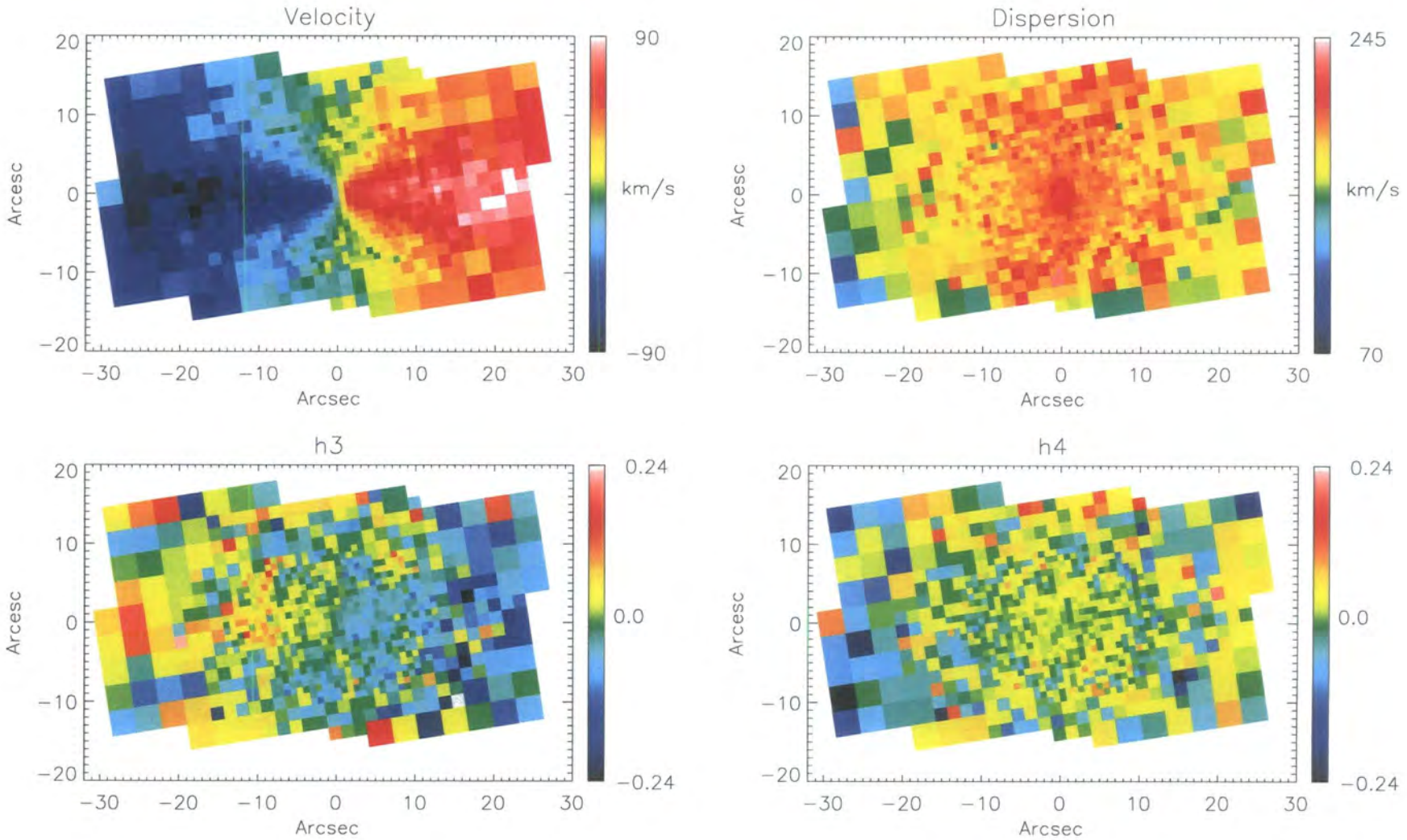

Figure 4.9: Final binned kinematic maps of the *SAURON* data for NGC 821. These data will be used to constrain the Schwarzschild dynamical model. The velocity field clearly shows the rotation and apparent axisymmetry of this galaxy, mirrored by the h_3 field, showing that the LOSVD is distinctly asymmetric due to the disk component.

galaxies, based on data with high signal-to-noise ratio and spectral resolution ($\sim$ 3 Å FWHM). Included in his sample is NGC 821. The data were obtained using the 3m Shane Telescope of Lick Observatory, during the period of August 1985 to September 1989, using a 2.″1 slit. To mimic this observational set-up, bins are extracted which fall within a 2.″1 aperture centred at the origin of the *SAURON* field, and parallel to the major axis as determined from the reconstructed image.

More formally, one would prefer to weight each *SAURON* data point in relation to the area of the bin falling within the slit. However, in the central regions, the bins are generally less than 2.″1×2.″1 in size, and so accounting for fractions of bins is a second-order effect. In the outer parts, the *SAURON* data are taken from bins covering an area larger than the slit. Therefore one should consider the *SAURON* error bars outside $\pm$ 10″ as lower-limits.

Figure 4.10 presents the González (1993) major-axis data overplotted with the equivalent *SAURON* values. The *SAURON* data have been re-binned in the radial direction to match the radial sampling of the González data. This was performed by taking the error-weighted mean of all the *SAURON* data points lying within each of the González radial bins, shown by the radius 'error bar' on the González data. To account for systematic effects, such as template mismatch and filtering differences, the González velocity dispersion data have been scaled such that the median of the two data sets at radii larger than 6″ (to avoid PSF mismatch effects) are the same. Within the uncertainties, the data can be seen to be generally in good agreement.

Comparison with ISIS Data

The González data provides a comparison with kinematics derived from independent observations by another author. However, only the mean velocity and velocity dispersions are available. The *SAURON* data are of sufficient quality to give the higher-order parameters, h_3 and h_4, and one would prefer to also compare these with other data. For this reason, presented here is a comparison of *SAURON* data with the long-slit data presented in Chapter 3 taken with the ISIS spectrograph, also mounted on the WHT 4.2m telescope. The details of this data are described extensively in Chapter 3. The main differences between this ISIS data and that of González are that this data were taken using a 4.2m telescope, with a 1″ slit, and the higher-order parameters have been derived (see Chapter 3).

Following the same procedure as for the González data, bins falling within a 1″ aperture centred on the origin of the *SAURON* field and parallel to the major axis were extracted and binned in radius to the same interval as the ISIS data. Figure 4.11 presents the *SAURON* aperture data overplotted with the ISIS data from Chapter 3. The *SAURON* data is in very good agreement with the ISIS data. The ISIS and *SAURON* data appear to have been observed in similar seeing conditions, as the break in the rotation curve near

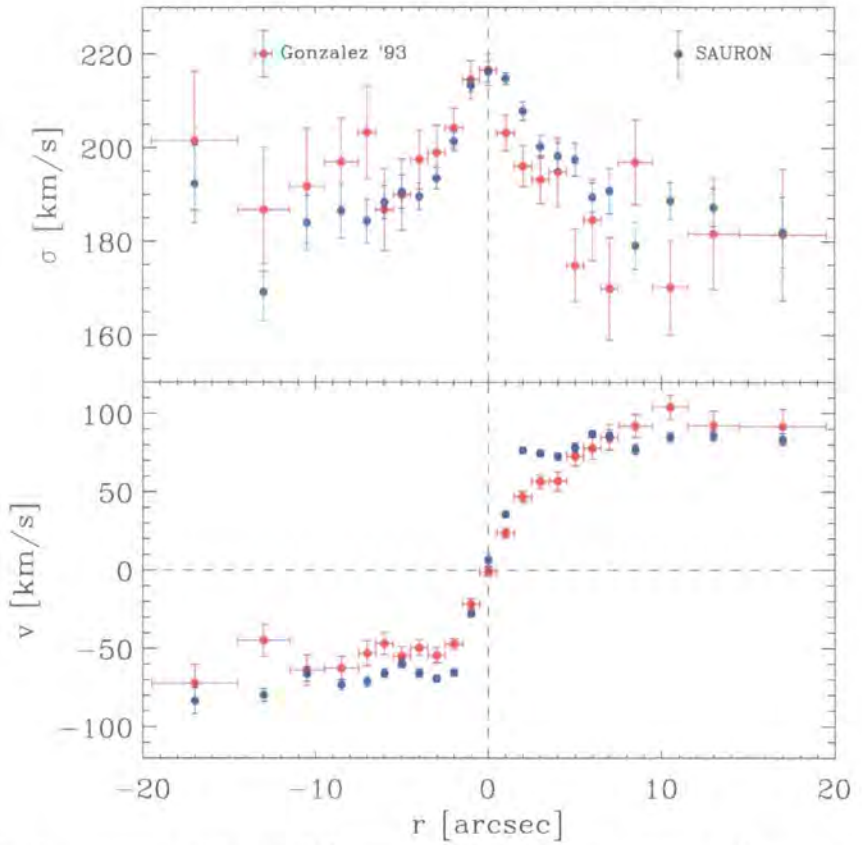

Figure 4.10: Comparison of *SAURON* major-axis aperture with data of González (1993). The *SAURON* data have been rebinned to the same radial sampling as the González data.

the centre is traced equally well by the two data sets. The central velocity dispersion peak is slightly higher in the ISIS data, indicating that the effective *SAURON* seeing (including instrumental PSF) is probably slightly worse than for the ISIS data. However, even in the higher-order terms, the data are in very good agreement with each other.

4.2.6 Other Data Sets

As well as the *SAURON* kinematic constraints, the dynamical model must also have some measurement of the mass distribution of the galaxy. This information comes from the surface brightness distribution, which is related to the mass via some mass-to-light ratio (hereafter M/L). In order to maximise the use of data which is available, it is possible to constrain the model using data from different instruments which sample at different resolutions. For example, to constrain very accurately the mass distribution on wide-field *and* sub-arcsecond scales, one can incorporate imaging data from both ground-based instruments and the Hubble Space Telescope (HST). Likewise, in order to have a strong constraint on the mass of a possible central black hole, it is necessary to use spectroscopic data with high spatial resolution from HST using the Space Telescope Imaging Spectrograph (STIS). Below is a brief description of the other data sets used for the dynamical model.

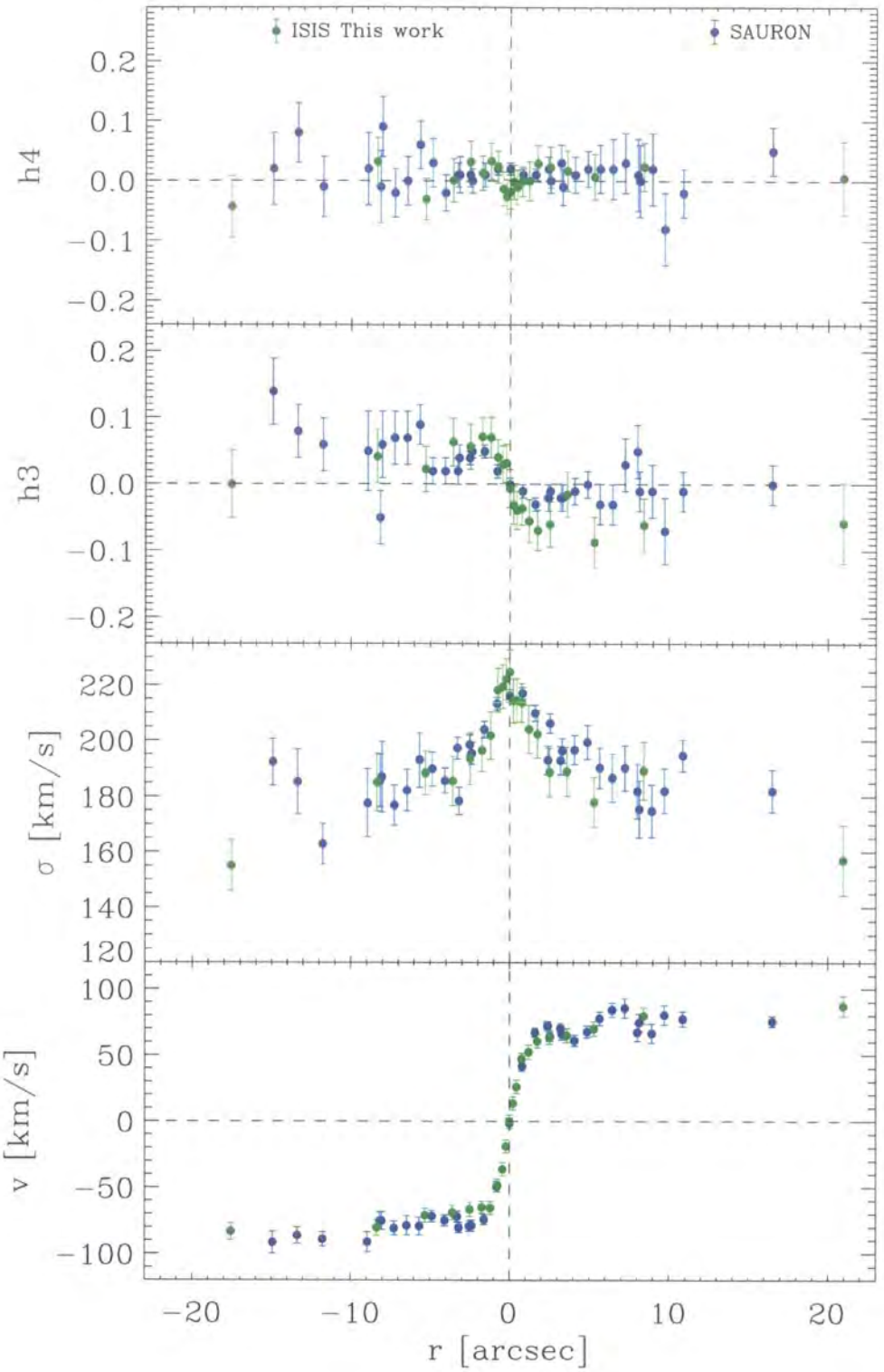

Figure 4.11: Comparison of *SAURON* major axis long-slit aperture with the blue-arm ISIS data presented in Chapter 3.

Imaging

Two imaging data sets were used: 1) Wide-field ground-based data from the 0.9m telescope at the Cerro Tololo Inter-American Observatory (CTIO), in Chile; and 2) archival HST imaging using the Wide-Field and Planetary Camera 2 (WFPC2). Table 4.2 gives a summary of the two data sets. The CTIO imaging was kindly supplied by Harald Kuntschner. The HST data was retrieved from the data archive[2], and is pre-processed using the calibration pipeline of STScI. Figure 4.12 shows the full images from both observatories which form the basis of the imaging information used in the modelling.

	CTIO 0.9m	HST+WFPC2
Filter	R-band	FW814 (I-band)
Exposure Time	160s	1450s
Field-of-View	13.′5 x 13.′5	80″x 80″
Pixel Scale	0.″384 pix^{-1}	0.″05 pix^{-1} (PC chip) 0.″1 pix^{-1} (WF chips)

Table 4.2: Summary of CTIO and HST imaging data.

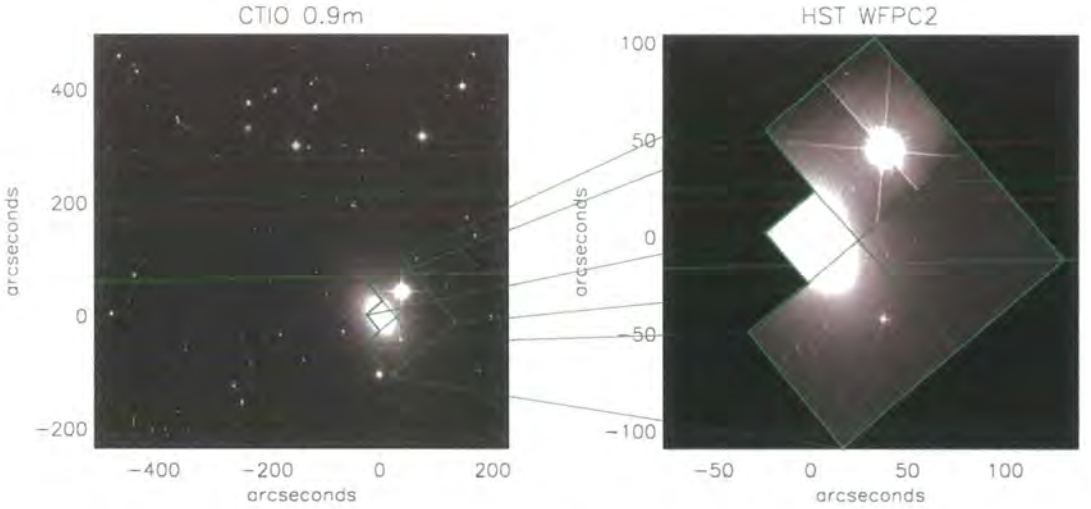

Figure 4.12: Illustration of the two imaging data sets used to map the surface brightness distribution of NGC 821. The CTIO image extends out to large radii, beyond $1R_e$. The HST data, on the other hand, samples only the central regions, but at high resolution. In the HST image, the galaxy has been centred on the Planetary Camera (PC) chip, which samples at a higher spatial resolution (0.″05 pix^{-1}) than the other three Wide Field (WF) chips (0.″1 pix^{-1}). Only the PC chip data is actually used in the modelling. Note the very bright star located about 55″ from the galaxy centre. This star and others in the field, are masked before fitting the MGE model discussed in §4.3. Both images are oriented such that up is north and left is east.

[2]Based on observations made with the NASA/ESA Hubble Space Telescope, obtained from the data archive at the Space Telescope Institute. STScI is operated by the association of Universities for Research in Astronomy, Inc. under the NASA contract NAS 5-26555.

Spectroscopy

In order to constrain the mass of a possible central black hole in NGC 821, it is necessary to probe the dynamics of the central kiloparsec of the galaxy. The radius $r_\bullet$ of the 'sphere of influence' of a black hole (i.e., the radius within which the potential is dominated by the black hole) is given by:

$$r_\bullet \sim \frac{GM_\bullet}{\sigma^2}, \tag{4.1}$$

where G is the gravitational constant, and σ is the characteristic velocity dispersion in the host galaxy (from de Zeeuw 2000). In physical units:

$$r_\bullet \sim 0.4 \left(\frac{M_\bullet}{10^6 M_\odot}\right) \left(\frac{100 \text{ km s}^{-1}}{\sigma}\right)^2 \text{pc}. \tag{4.2}$$

For a galaxy at distance D, $r_\bullet$ corresponds to an angular size $\theta_\bullet$, given by:

$$\theta_\bullet \sim 0\farcs1 \left(\frac{M_\bullet}{10^6 M_\odot}\right) \left(\frac{100 \text{ km s}^{-1}}{\sigma}\right)^2 \left(\frac{1 \text{ Mpc}}{D}\right). \tag{4.3}$$

From the *SAURON* measurements of the velocity dispersion of NGC 821, it is possible to estimate the mass of the black hole, from the black hole mass - velocity dispersion relationship (e.g., Magorrian et al. 1998):

$$\log(M_\bullet/M_\odot) = \alpha + \beta \log(\sigma/\sigma_0), \tag{4.4}$$

where the most recent determination (Tremaine et al. 2002) gives $\alpha = 8.13 \pm 0.06$ and $\beta = 4.02 \pm 0.32$ for $\sigma_o = 200$ km s^{-1}. For NGC 821, with an estimated characteristic velocity dispersion of 200 km s^{-1}, this would imply a black hole of mass $\sim 10^8 M_\odot$. From surface brightness fluctuation measurements (Tonry et al. 2001), the distance to NGC 821 is 24.1 Mpc. Using these values with eq. [4.1] implies that, in order to resolve the black hole, a minimum spatial resolution, $\theta_{res} \sim 0\farcs2$ is required. Detailed modelling has shown that, depending on the internal dynamical structure of the host galaxy, the influence of the black hole is often visible only inside a projected radius significantly smaller than $r_\bullet$ (e.g., eq. [4.2] in Qian et al. 1995). This suggests that a black hole with mass corresponding to $\theta_\bullet \sim \theta_{res}$ is most likely an upper-limit on the true black hole mass, whose sphere of influence lies below the resolution of our data.

Clearly, the resolution of the *SAURON* data is much lower than the $0\farcs2$ required to probe the sphere of influence of a black hole with $M_\bullet \sim 10^8 M_\odot$, and so only an upper limit of $M_\bullet$ can be obtained. Using HST with STIS, however, it is possible to obtain

kinematics on angular scales of 0.″1. Thus, such data is necessary in order to obtain a useful constraint on the black hole mass.

The STIS data used in this work was kindly provided by Karl Gebhardt and the Nuker team in advance of publication, and was obtained by them as part of a larger survey of local elliptical galaxies, aimed at establishing the frequency and demography of central super-massive black holes (Gebhardt et al. 2002, hereafter G02). Such an investigation is not a primary driver of the *SAURON* project. Comparing the results of the dynamical modelling presented in this thesis with that of a completely independent investigation using the same data is, however, a powerful test of the modelling process, and the validity of the assumptions and approximations made by the two codes. Although the modelling presented here uses *SAURON* integral-field data, compared with the major- and minor-axis long-slit data used to constrain the Nuker's models (see G02), the STIS data is a key constraint for the black hole mass, and so consistent estimates of $M_\bullet$ from both codes would be a robust test of the modelling technique employed here.

The details of the acquisition and reduction of the STIS data are given in Pinkney et al. (2002), and a summary of the instrumental set-up is given in Table 4.3. The Calcium II triplet spectral region was used, due to the three strong calcium absorption features, and the lack of strong emission lines which are often found in the central regions of ellipticals. The slit width used was 0.″1. As a result of this very narrow slit, the signal-to-noise ratio of the data is generally rather poor, even with a total combined integration time of 27478 seconds.

Grating	G750M
Slit Size	52″x 0.″1
Wavelength Range	8275-8847 Å
Dispersion	1.1089 Å pix^{-1}
Spatial Scale	0.″05071 pix^{-1}
Integration Time	27478 seconds
Observation Dates	13/10/98, 08/09/99
Position Angle	30°

Table 4.3: Summary of STIS instrumental set-up and data for NGC 821. (From Pinkney et al. 2002)

The kinematics were determined using a maximum-penalised likelihood method (MPL) similar to those developed by Saha & Williams (1994) and Merritt (1997). The technique used for this data employs a symmetric extraction process, whereby spectra at equal radii on either side of the galaxy are fitted *simultaneously*, thus improving the effective S/N of the data, as well as enforcing axisymmetry in the data from the initial extraction stage. Symmetrising the data in this way removes departures from axisymmetry in the data which can adversely affect the model, and is anyway consistent with the assumption of axisymmetry implicit in the modelling process. The final STIS data set used to constrain the modelling is plotted in Figure 4.13, and tabulated in Table 4.4.

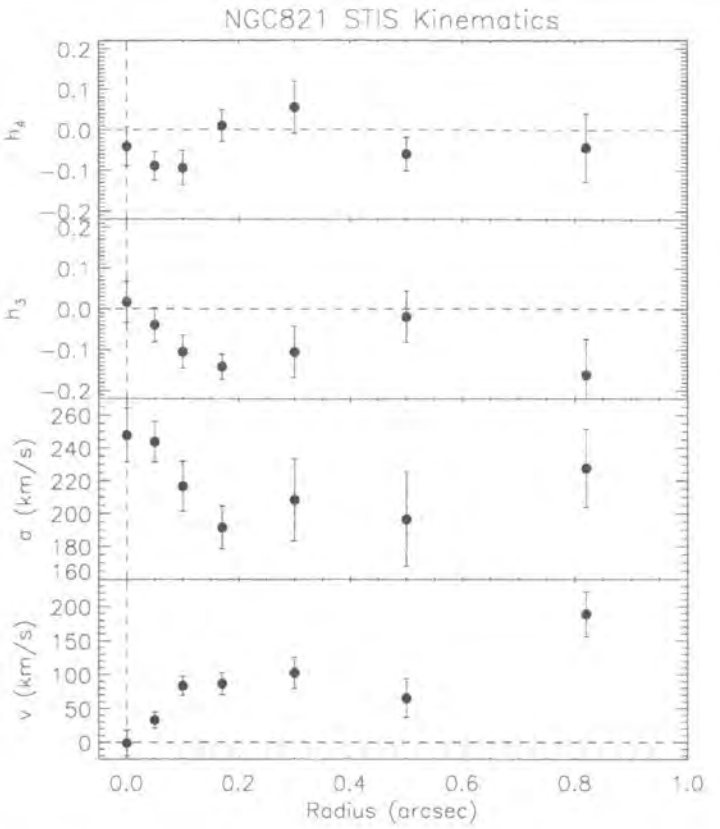

Figure 4.13: The STIS kinematic profile for NGC 821, as described in Pinkney et al. (2002). The kinematics are extracted by applying the MPL method to spectra at equal radii from the galaxy centre along the slit simultaneously, thus imposing folded symmetry directly.

Radius	v	Δv	σ	$\Delta\sigma$	h_3	Δh_3	h_4	Δh_4
0.00	-0.987	19.029	247.842	16.481	0.017	0.050	-0.041	0.048
0.05	32.994	11.993	243.755	12.359	-0.039	0.042	-0.089	0.035
0.10	83.308	14.025	216.651	5.139	0.105	0.040	-0.094	0.042
0.17	86.755	16.284	191.631	13.043	-0.141	0.031	0.010	0.039
0.30	102.552	23.193	208.531	25.089	-0.105	0.063	0.055	0.064
0.50	65.284	28.226	196.581	28.639	-0.019	0.063	-0.060	0.041
0.82	189.023	32.856	227.562	23.808	-0.162	0.088	-0.043	0.084

Table 4.4: STIS kinematic measurements used to constrain the dynamical model. (From Pinkney et al. 2002)

4.2.7 PSF Measurement

The point spread function (PSF) of the spectral data is an important property for the modelling, as this defines the effective resolution limit of the kinematic constraints (see §4.4.2. The PSF of the *SAURON* data is determined via comparison of the *SAURON* reconstructed image of NGC 821, and a high resolution HST image using the XSauron task FITPSF3D. The HST image is convolved with a certain PSF, described by a circular, two-

dimensional double-Gaussian function. The parameters of the double-Gaussian are altered to find the best-fitting solution. The PSF which results in the closest match between the *SAURON* image and the convolved HST image (in this case, the same WFPC2-PC1 image of NGC 821 used in the MGE application) is taken to be the estimate of the PSF. The resulting PSF is shown in Figure 4.14.

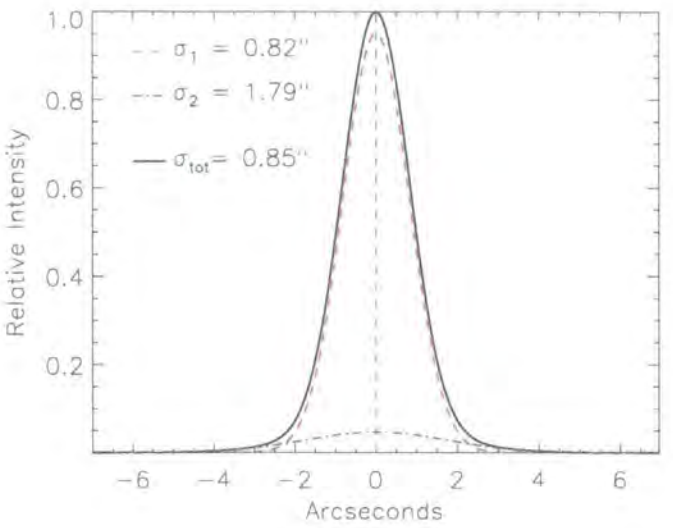

Figure 4.14: Illustration of the double-Gaussian parameterization of the *SAURON* PSF. The dispersions of each Gaussian are given by $\sigma_{1,2}$. $\sigma_{\rm tot}$ corresponds to the dispersion of the best-fitting single Gaussian to the total profile.

From observations of point sources, the STIS PSF is known to have rather asymmetric wings (e.g., Joseph et al. 2001, Bower et al. 2001). The effect of this asymmetry on the derived kinematics and subsequent modelling was shown by Bower et al. (2001) to be negligible. Following the same general procedure of Bower et al. (2001), observations of two stellar point sources ('HR7576' and 'HR6770') taken from the same observing sequence as the NGC 821 data of Pinkney et al. (2002) were obtained from the HST archive. The PSF of HST with STIS is approximately 0.″08 FWHM, which is undersampled by the 0.″05 pixels of the detector. To combat this, one would prefer to have dithered observations of the star at different positions on the slit. Such observations were not obtained during the observing cycle. However, it is possible to make use of the geometric distortions within STIS itself to obtain a well sampled measurement of the PSF.

This was done using the raw spectra (i.e., before corrections of any geometric distortions have been applied). The spectra are binned in the spectral direction, to create high signal-to-noise ratio profiles of the PSF along the detector. Each of the bins is fitted with a single Gaussian function to obtain the centroid of the profile. The profiles are then 'recentred' by changing the relative pixel coordinates, such that the mean of the best-fit single Gaussian is zero. The recentred profiles are then combined by binning *across* the profiles, in units of 0.1 pixels. This final PSF profile is then fitted by a function of multi-

ple, concentric Gaussians. The dispersion of each Gaussian is chosen to minimize the χ^2 residuals between the function and the profile (weighted by the 1-sigma variation within each bin) via a non-linear downhill simplex algorithm (Press et al. 1992). The minimization is optimised by selecting the weight of each Gaussian component via a non-negative least-squares linear combination, thus only the dispersions of each Gaussian component are determined non-linearly. This was conducted on several spectra of the two stars, and the values for the fit were found to vary by insignificant amounts. The fit with the lowest χ^2 value was chosen as the representative case.

The result of this process is shown in Figure 4.15. This shows the overplotted profiles (open symbols) of each spectral bin (normalized by the total flux in the bin within $\pm$ 10 pixels of the centroid), the resampled average profile (red histogram and error bars), as well as the multiple Gaussian fit (blue line) and the individual components (dotted lines). The vertical lines in Figure 4.15 represent the boundaries of the window, centred on the profile peak, which was used to constrain the fit. Note the broad wings, and the prominent asymmetric feature -2 pixels from the centre. The fitting process was initially conducted using three Gaussians, but only two were ever required (i.e., had a non-zero weight), and forcing a third to be included only increased the χ^2 of the fit. The parameters of the multiple-Gaussian description of both the *SAURON* and STIS PSFs are given in Table 4.5.

SAURON	Dispersion	Integral
Component 1	0.″8150	0.9524
Component 2	1.″7947	0.0476
STIS	Dispersion (″)	Integral
Component 1	0.″0335	0.7032
Component 2	0.″0784	0.2968

Table 4.5: Parameters of the multiple-Gaussian models representing the PSF of the two spectrographs. For each PSF, the components are normalised such that the integral of the sum of the components is equal to 1. This ensures that the total flux is conserved during the convolution.

4.3 MGE Mass Model

Before a suitable stellar orbit library can be generated, it is necessary to first of all quantify the gravitational potential in which the stars exist. As discussed in the introduction to this chapter, the gravitational potential of early type galaxies like NGC 821 is composed of essentially three possible components: the stellar mass, a central dark mass, and a possible dark-matter halo. From an observational point of view, only the first of these is directly accessible, being related to the surface brightness distribution we observe. Also, we consider here only models with no dark-matter halo, as the kinematic data only extend to $1/2R_e$, within which the dark halo is not expected to have a significant influence.

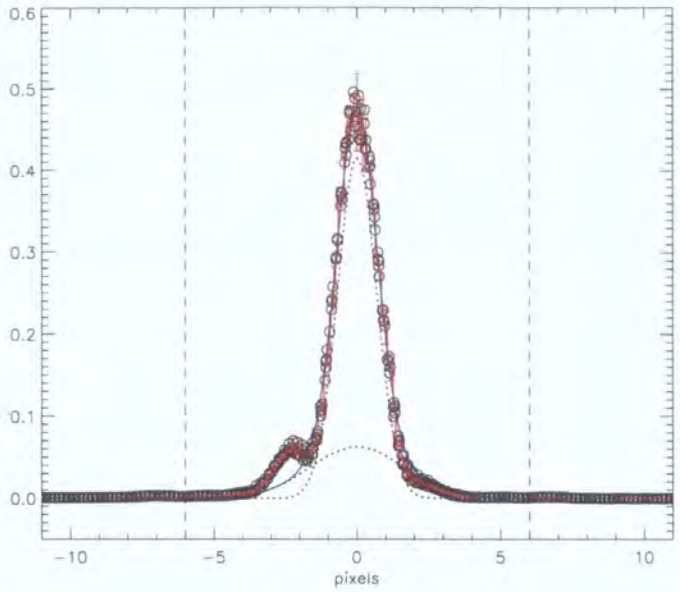

Figure 4.15: PSF profile of STIS, taken from a single stellar spectrum observed at one slit position. Due to the undersampling of the PSF by the detector, the spectrum is binned in the spectral direction, creating profiles of high signal-to-noise ratio, which are then recentred and combined (overplotted as the open symbols). Because of geometric distortions in the spectrograph, the spectrum does not lie perfectly along the detector array. Therefore, by combining profiles along the spectrum, one obtains an increase in the sampling of the PSF. The combined profiles are binned onto a grid of 0.1 pixels ($\equiv 0\farcs005$), with 1-sigma scatter within each bin taken as an error estimate for that pixel. The final profile, shown as the red histogram with error bars, is fitted with a function of multiple, concentric Gaussians. Only two Gaussians are required to fit the profile within the given tolerance. The fit is shown by the blue solid line, and the two components are overplotted as the dotted lines.

From the observed surface brightness distribution, one has to derive a luminosity density, j, which is related to the mass density, ρ, via $\rho = \Upsilon j$, where Υ is the average mass-to-light ratio of the stellar population (hereafter given in solar I-band units). To derive the luminosity density, the surface brightness distribution must be deprojected (transformed from the projected plane of the sky, to the intrinsic three-dimensional volume in space), giving the intrinsic light distribution. This generally involves describing the surface brightness distribution by some analytic function or model, which can then be used to evaluate the gravitational potential, Ψ, for a given inclination.

4.3.1 The MGE Formalism

The parameterization of the surface brightness distribution is performed here using a Multi-Gaussian Expansion (MGE) technique developed by Cappellari (2002). The basic principle of this method is to express the surface brightness, Σ, of a galaxy as a linear combination of two-dimensional Gaussian functions. The first application of this method to the deprojection of galaxy images comes from the work of van Houten (1961), with a

more recent application by Bendinelli (1991), which has since been developed further by several authors (Monnet et al. 1992, Emsellem et al. 1994*a*), and applied to dynamical modelling for a number of galaxies (e.g., Emsellem et al. 1994*b*, 1996, 1999, Emsellem 1995, van den Bosch 1998, van den Bosch & Emsellem 1998, Cretton & van den Bosch 1999, Verolme et al. 2002, Cappellari et al. 2002).

In the projected sky coordinates, (x', y'), the MGE projected surface brightness is given by:

$$\Sigma(x', y') = \sum_{j=1}^{N} I'_j \exp\left[-\frac{1}{2\sigma'^2_j}\left(x'^2_j + \frac{y'^2_j}{q'^2_j}\right)\right], \tag{4.5}$$

where N is the number of Gaussian components with observed axial ratio $0 \leq q'_j \leq 1$, and projected dispersion σ'_j along the major axis of the Gaussian. In the general case, the position angle of each Gaussian is free to vary. However, in the case of axisymmetry, the position angle is constant for all components.

For other than edge-on objects, the deprojection of a galaxy's surface brightness is non-unique (e.g., Rybicki 1986, Franx 1988). In this respect, the MGE model provides only one of a family of possible deprojections. However, the deprojected densities which result from this method are generally smooth and natural-looking, similar to what is observed for intrinsically edge-on objects.

In the oblate axisymmetric case (as is assumed for NGC 821), the projected flattening, q'_j, and intrinsic axial-ratio, q_j, are related by the expression:

$$q^2 = \frac{q'^2 - \cos^2 i}{\sin^2 i}, \tag{4.6}$$

for a given inclination, i. In this case, it can be seen that the deprojection is only defined if $\cos^2 i < q'^2_j$ for all Gaussians. This implies that there is a minimum possible inclination which is determined by the most flattened Gaussian component of the MGE solution. The maximum flattening, $q'_{\rm max}$, is set independently of the MGE model by the axis-ratio of the ellipse which reproduces the galaxy isophotes (along the major axis) where the curvature is greatest (Cappellari 2002). At least one component of the MGE solution must have this limiting axis-ratio to reproduce the maximally-curved isophote.

Finally, the gravitational potential is generated by evaluating the classical Chandrasekhar (1969) formulae for densities stratified on similar concentric ellipsoids (see Binney & Tremaine 1987, p. 61). For the oblate axisymmetric case, the final expression is given by equation 13 of Cappellari (2002).

4.3.2 The MGE Fit

The MGE implementation of Cappellari (2002) used here is designed as a robust, easy-to-use and flexible routine, running within the stable Interactive Data Language (IDL) environment. Multiple resolution images (e.g., ground-based and HST) can be combined very easily, and minimum intervention by the user is required to achieve an excellent fit to the data. The details of the algorithm are given in Cappellari (2002), but a brief outline is given below.

For purposes of efficiency and accuracy, the 2D image of the galaxy is rebinned in logarithmic radial bins. This gives bins of high signal-to-noise ratio in the outer regions, while still sampling the central parts at high resolution. This also prevents the quality of fit evaluation being dominated by the large number of pixels sampling the outer regions of the galaxy compared to the inner regions. The quality of fit is given by the quantity χ^2, defined as:

$$\chi^2 = \sum_{i,j} \left[\frac{C_{i,j} - \Sigma(x'_i, y'_j)}{C_{i,j}} \right]^2, \tag{4.7}$$

where $C_{i,j}$ are the data points and $\Sigma(x'_i, y'_j)$ are the projected model values. Optimising this quantity minimizes the relative error of the fit, thus avoiding a poor fit to the central regions due to the large number of data points at larger radii. The MGE model is fitted to a certain number $N_{\rm sec}$ of photometric profiles, measured along sectors uniformly spaced in angle from the major to the minor axes (see Figure 5 of Cappellari 2002). Sectors in the four quadrants are averaged together before fitting, increasing the effective signal-to-noise ratio of the data, and avoiding the adverse effects of contaminating features in the image (for example, stars or bad pixels). Bright stars (for example, the very bright star around 55″ from the centre of NGC 821, shown in Figure 4.12) are masked before fitting.

The number of Gaussians required to fit a given image depends on the complexity of the light distribution. The methodology employed here is similar to that of Emsellem et al. (1994*a*), in that an initial fit is conducted using $N = 10$ Gaussians. N is then increased until the minimum χ^2 stops decreasing appreciably (e.g., by less than 1 percent).

Table 4.6 presents the parameters of each Gaussian component (surface brightness, major-axis dispersion and flattening) of the best-fitting MGE solution for NGC 821. Figure 4.16 presents the resulting best-fitting MGE model profiles plotted along seven of the nineteen adopted sectors, along with the residuals of the fit. The profiles are shown for the combined HST and CTIO images, which overlap at around 10″. Sky subtraction for the CTIO image was determined by requiring the outer profile to fall off as a power-law; the sky level and relative calibration of the HST image was adjusted to ensure agreement of the profiles in the overlap region. To simplify (PSF) convolution, the central region of the ground-based CTIO image affected by the PSF is excluded from the fit, and the

model is convolved only with the HST PSF. This avoids a poor fit to the high resolution HST image due to any PSF mismatch with the ground-based image. The HST PSF is taken from Table 3 of Cappellari et al. (2002), who derive an MGE approximation of the PSF derived with the TinyTim software (Krist & Hook 2001) using four circular Gaussian components.

Total Luminosity ($10^9 L_{\odot,I}$)	Surface Brightness ($L_{\odot,I}\ pc^{-2}$)	Dispersion (arcsec)	Flattening
0.00903	166715.0	0.0297278	0.714563
0.04883	66011.9	0.110624	0.704732
0.11318	32200.1	0.256883	0.620964
0.22179	15663.4	0.513386	0.626339
0.45887	9282.57	0.979488	0.600700
1.05751	5850.57	1.81099	0.642527
1.58217	2231.99	3.74337	0.589756
2.32437	918.922	6.15615	0.778115
0.72139	290.118	9.83005	0.300000*
5.34021	445.658	15.5601	0.576987
8.09862	141.078	31.7465	0.664043
8.39832	24.5658	70.5837	0.800000
13.78750	4.90344	202.425	0.800000

Table 4.6: Parameters of the 13 Gaussians used to describe the surface photometry of NGC 821. The parameters are given in the units used by the Schwarzschild code. * signifies the most flattened Gaussian of the expansion, corresponding to the $q_{\max}$ component. This limit in q is fixed by the user to ensure the roundest solution possible (see text for details).

Figure 4.17 presents the CTIO and HST images overplotted with the best-fitting MGE model. Clearly, the MGE model is an excellent representation of the data. The diskiness of NGC 821's isophotes is most apparent along the major-axis of the HST image isophotes. These are faithfully reproduced by the MGE model, ensuring that the diskiness of the galaxy is propagated into the dynamical model (since it is of course necessary for the model to reproduce the mass density as well as the kinematics).

The maximum flattening of the MGE model, $q_{\max}$, was determined by limiting the lowest value of q' allowed in the fit, and increasing this value until the χ^2 value increases significantly (ie. by more than $\sim 1\%$), or the fit to the galaxy isophotes becomes unacceptable. In this way, the 'roundest' reasonable solution is ensured. This is important, as flat components can be sensitive to noise in the data, which can result in very flattened components in the MGE fit, which in turn over-estimates the minimum inclination angle, i, for the galaxy. Figure 4.18 illustrates this process by overplotting different MGE solutions with increasing values of $q_{\max}$. The solution corresponding to the determined optimal fit is overplotted as a red line in Figure 4.18, and corresponds to $q_{\max} = 0.3$. It can be seen from the insert in Figure 4.18 that, for $q_{\max} > 0.3$, the fit to the diskiness of the isophotes becomes significantly worse. Similarly, for solutions with $q_{\max} < 0.3$, the improvement in the fit is extremely small. Note that, from eq. [4.6], a value of $q_{\max} = 0.3$ implies a minimum inclination angle $i = 73°$.

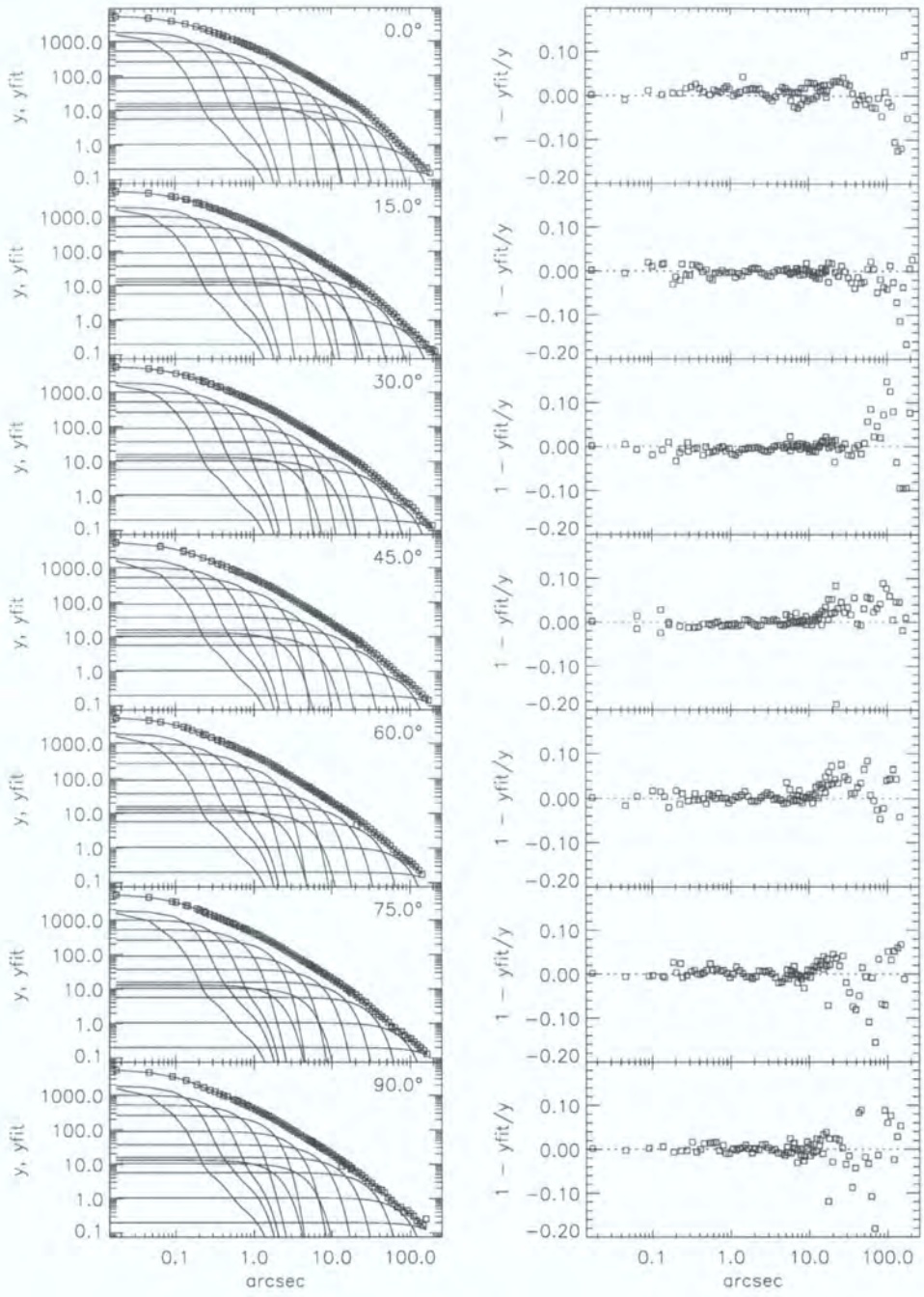

Figure 4.16: Sector profiles (diamonds) and MGE model fit (solid line) to the combined HST and CTIO images of NGC 821 for 7 different sector position angles out of the 19 actually used. The left panel shows the fit to the intensity, and the right panel gives the effective residuals of the fit. The fit is visibly very good, with residuals generally at the level of less than a few percent. In the intensity profiles, there can be seen two Gaussian components which do not follow the even spacing of the other components. These components seem to be associated with the disky component of the surface brightness distribution; however, one must be cautious to attach much physical significance to these essentially arbitrary Gaussian components.

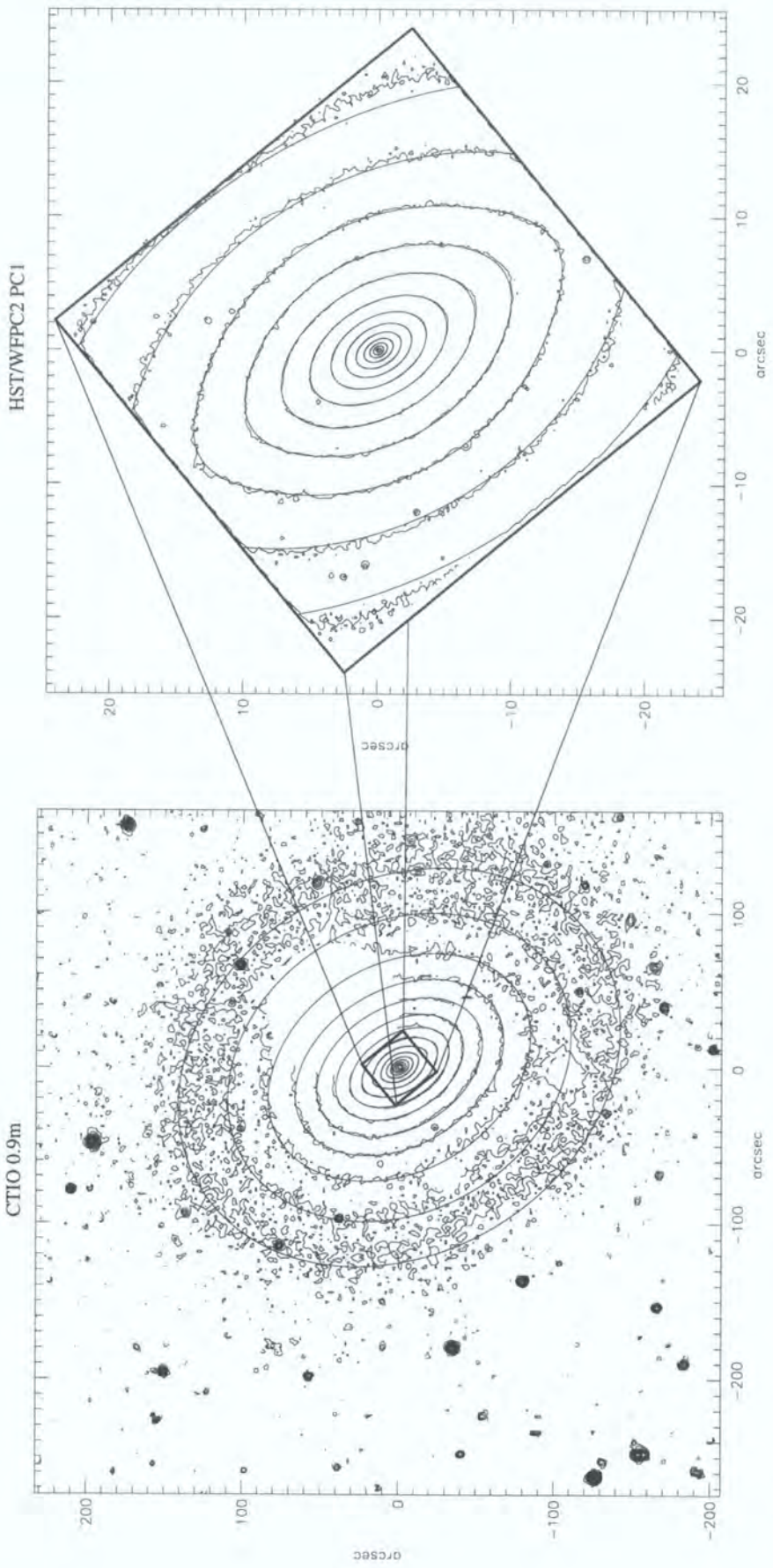

Figure 4.17: Final MGE solution (smooth line) overplotted on the isophotes (noisy line) of the wide-field ground-based CTIO (left frame), and high-resolution HST (right frame) images. The CTIO image shows the HST field of view (PC1 chip only) overplotted to scale. Clearly the quality of the fit is excellent, even where the isophotes show the largest 'disky' distortions. Note that the bright star has been removed from the CTIO image before fitting the model. Both images are oriented such that up is north and left is east.

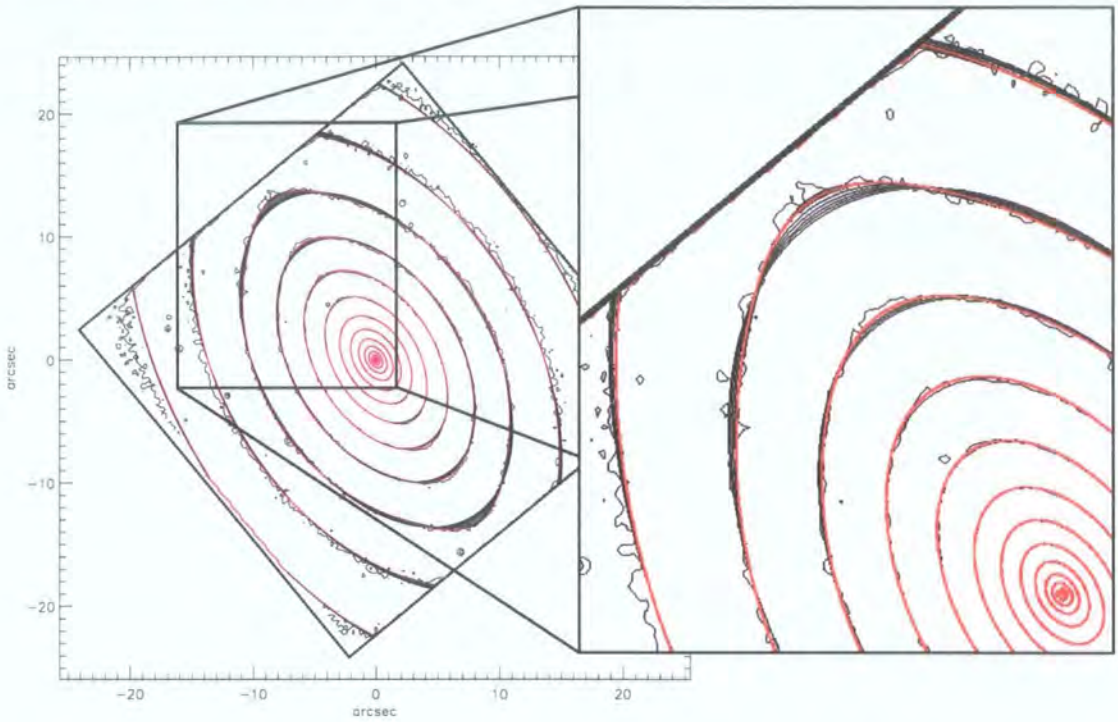

Figure 4.18: HST PC1 image contours for NGC 821 (noisy black contours) overplotted with best-fit MGE models with different maximum flattening limits (smooth contours). To obtain a reliable estimate of the minimum inclination angle, one should use the 'roundest' MGE solution. This is found by varying the lower limit on q'. Shown here are different MGE solutions with increasingly rounder limits on q' (for $q' = 0.17, 0.20, 0.25, ..., 0.60$), which can be seen by the changing quality of fit to the diskiness of the isophotes. The roundest acceptable solution was determined to be for $q_{\max} = 0.3$, which is overplotted as the red smooth line. The insert shows a blow-up of the region where the diskiness is most apparent.

4.4 Schwarzschild Dynamical Model

The modelling technique used here is based on an extension of Schwarzschild's (1979) orbit superposition technique, in which individual stellar orbits are generated, and the optimal linear combination of non-negative contributions from each orbit is found which best fits a set of observables. Early models of this type (e.g., Dressler & Richstone 1988, Richstone et al. 1990) were general, in the sense that they made no assumptions about the dynamical structure of the galaxy. However, only spherical geometries were considered, which may introduce systematic errors when applied to a flattened galaxy such as NGC 821.

Subsequently, axisymmetric models were developed in which the constituent orbits depend on the two classic **integrals of motion** for a static, axisymmetric potential: the binding energy, E, and the component of angular momentum parallel to the symmetry axis, L_z. An integral of motion is any function of the phase-space coordinates $(\mathbf{x}, \mathbf{v})$ that is constant along any given orbit (Binney & Tremaine 1987). These so-called two-integral models are able to reproduce the flattening and rotation of systems like NGC 821. However the resulting models are constrained to be isotropic on the meridional plane, and are not always able to accurately reproduce the observational data. These restrictions

are caused by the fact that orbits in the fully-general axisymmetric case are thought to depend on a third, typically non-analytic integral of motion, I_3.

Apart from computer processing time and memory, there is no physical reason why such fully general axisymmetric models cannot be generated. Motivated by this, independent implementations of three-integral axisymmetric 'Schwarzschild' codes were written by Hans-Walter Rix, Nicolas Cretton and Roeland van der Marel (Rix et al. 1997, Cretton et al. 1999, van der Marel et al. 1998). The latter of these implementations was developed further by the Leiden dynamics group (specifically by Ellen Verolme, Tim de Zeeuw and Michele Cappellari), being extended to incorporate the MGE parameterization (Cappellari et al. 2002) and integral-field data (Verolme et al. 2002), such as that from *SAURON*. It is this code which is used here to model NGC 821.

4.4.1 Generating the Orbit Library

The underlying principle of the orbit superposition technique is that the orbital structure of the galaxy is fully represented by a subset of the library of orbits generated for the galaxy potential. In other words, the resulting model and its properties should not depend on the details of the orbit library. For this reason, it is imperative to sample the orbital parameter space completely and, in the interests of computation time, efficiently.

The orbital trajectories are completely specified by the integrals of motion, defined in phase space by their coordinates (E, L_z, I_3). To sample a representative phase space volume, the scheme described by Cretton et al. (1999) is used. Energy is sampled via a logarithmic grid in radius, which specifies an energy E via the orbit lying on the equatorial plane at a given radius (the 'circular' orbit). This grid should extend from below the resolution limit of the observational data, out to a radius ~ 3.5 times larger than the dispersion of the largest Gaussian component of the MGE mass model. This ensures that essentially all the mass of the galaxy is considered, and that only orbits which are actually constrained by the observations are calculated.

The circular orbit also defines the maximum angular momentum $L_{\max}(E)$ for a given energy. The values of L_z are sampled via a linear grid of $L_z/L_{\max}(E)$. Orbits with $L_z < 0$ are equivalent to their positive counterpart, but rotate in the opposite sense. They are generated by taking a positive L_z orbit and reversing its velocity vector, and so are not explicitly calculated.

I_3 is not usually known analytically, and therefore must be approximated in some way. The numerical representation adopted here uses the fact that every orbit with $L_z \neq 0$ touches the zero-velocity curve (Ollongren 1962). The zero-velocity curve (hereafter ZVC) is the boundary of a region on the meridional plane inside which an orbit of given energy and angular momentum is constrained to move. An orbit can only touch this boundary if its instantaneous velocity on the meridional plane is zero. The third integral is defined

here as the angle between the equatorial plane (i.e., $z = 0$ on the meridional plane) and the point at which the orbit touches the ZVC, as measured from the radius of the circular orbit (see Figure 3 of Cretton et al. 1999).

Finally, one has a grid of parameters which sample the three integrals of motion, (E, L_z, I_3), and completely define the orbit library. Issues concerning the size and sampling of the orbit library are discussed in §4.5.

The technical details of the orbit integration are discussed fully in e.g., Cretton et al. (1999) and van der Marel et al. (1998). Once the orbit trajectories have been generated, it is necessary to store their properties on suitable grids to allow the calculated orbits to be compared to the observables. Both the intrinsic and projected properties are stored, to allow self-consistency checks and comparison with observed data respectively. This results in three grids: 1) a polar grid (r, θ) in the meridional plane, chosen to match the sampling in energy, since a given radius corresponds to a given energy; 2) an (r', θ') grid on the projected (x, y) plane of the sky, sampled in the same way as the meridional grid; and 3) a number of Cartesian $(x, y, v_{\rm los})$ grids, where $v_{\rm los}$ is the line-of-sight velocity, which represent the three phase-space coordinates available from the observations.

The spatial grid size $(\Delta x, \Delta y)$ of the $(x, y, v_{\rm los})$ cube is chosen to give a factor of 2-3 times higher spatial resolution than the data. In this work, data sets of very different spatial resolution are used (ground-based *SAURON* data extending to 1/2 R_e and high-resolution HST/STIS data covering the central arcsec), hence two grids with different spatial sizes and extents are used. The grid size Δv in the $v_{\rm los}$ direction has been chosen to sample the complete range of velocities present in the orbit library and observational data. The Δv bin size itself should be smaller than the effective velocity step of the data, to allow accurate sampling of the observed LOSVDs. The parameters of the two grids used in this work are given in Table 4.7.

Property	Grid 1	Grid 2
Instrument	*SAURON*	STIS
$(\Delta x, \Delta y)$	$0\farcs45 \times 0\farcs45$	$0\farcs03 \times 0\farcs03$
N_x, N_y	90×90	60×60
$\Delta v_{\rm los}$	10 km s^{-1}	10 km s^{-1}
$N_{v_{\rm los}}$	150	150

Table 4.7: Parameters of the Cartesian $(x, y, v_{\rm los})$ grid on which the projected properties of the orbit library are stored for comparison with the observed kinematic constraints. Listed are the relevant spectrographs, the spatial sampling, the number of spatial bins, the velocity sampling, and the number of velocity bins.

4.4.2 Generating the Observed Kinematic Parameters

Before comparing with the observed kinematic data, it is necessary to convolve the projected model properties with an appropriate point spread function (PSF). Since the final

fit to the data is a linear combination of the orbits, the $(x, y, v_{\rm los})$ cubes for each orbit can be convolved individually before the fit is performed. The PSF[3] convolution correlates information in the two spatial dimensions (x, y), but not in $v_{\rm los}$. The convolution is thus given by (using the notation of Cretton et al. 1999):

$$F_{\rm conv}(x_0, y_0, v_{\rm los}) = F \otimes {\rm PSF} = \int\int F(x, y, v_{\rm los})\ {\rm PSF}(x - x_0, y - y_0)\, dx\, dy, \qquad (4.8)$$

where F is the function to convolve, and $F_{\rm conv}$ is the convolution of F with the point spread function, PSF, performed in Fourier space for each velocity 'slice'.

Finally, the convolved orbital properties stored on a given $(x, y, v_{\rm los})$ grid are spatially binned over the apertures of the corresponding kinematic observations. Thus for the STIS data, these apertures are the radial bins formed along the length of the slit; for *SAURON*, the apertures cover the two-dimensional field. This yields, for each calculated orbit, a one-dimensional velocity histogram (i.e., the LOSVD of the orbit) for each observational aperture.

As discussed in §3.3.2, the shape of the LOSVD can be conveniently described by a few parameters. This is more compact than storing the signal in each of the velocity bins, and thus makes the computation less memory intensive. As with the parameterization of the observed LOSVDs, a Gauss-Hermite expansion of the form eq. [3.3] is used to describe the shape of the velocity distribution of each orbit. In principle, one would like to use the LOSVD itself, particularly in the presence of strong departures from Gaussianity (e.g., double-peaked LOSVDs due to the presence of a strongly decoupled component). However, such strong non-Gaussian features are not observed in the derived LOSVDs of NGC 821, and so the LOSVD is, in general, accurately described by the first four Gauss-Hermite moments (hereafter GH moments). As with the observations, the mean velocity, $\bar{v}_{\rm los}$, and velocity dispersion, σ, are taken as the mean and dispersion of the best-fitting Gaussian, implying that $h_1 = h_2 = 0$.

The underlying concept of the orbit superposition method is that a galaxy is composed of a number of orbital 'building blocks'. In this way, the integrated LOSVD is simply the superposition of the individual orbital LOSVDs. Similarly, the observed GH moments are a linear superposition of the GH moments of the individual orbital LOSVDs. The task then of fitting the kinematic observations involves solving for the optimal linear combination of $\bar{v}_{\rm los}$, σ, h_3 and h_4.

[3] Assumed as the atmospheric seeing convolved with the instrumental PSF.

4.4.3 Fitting the Observational Constraints

The final stage in constructing the model is to find the weighted superposition of the orbital properties which best represents the observed information in each observational aperture. This involves fitting two sets of constraints:

1. **Photometric Constraints** Also called *consistency constraints*, this is the mass model (from the MGE fit) integrated over the cells of the various grids. A relevant model should reproduce the stellar density for each cell of the meridional (r, θ) grid, the projected (r', θ') grid, and in each aperture with kinematic constraints.

2. **Kinematic Constraints** The model should reproduce the shape of the observed LOSVD in each kinematic aperture, quantified by the mean velocity, velocity dispersion, and the third and fourth GH moments.

When each orbit is calculated, its properties are averaged over each cell of the various grids, and their fractional contribution to the cell are stored. This results in an orbital matrix of the form:

$$\begin{array}{c} \\ \text{Constraints} \\ \downarrow \end{array} \begin{array}{c} \textit{Orbits} \longrightarrow \\ \begin{pmatrix} O_{11} & \cdots & O_{1N_{\rm orb}} \\ \vdots & \ddots & \vdots \\ O_{N_{\rm con}1} & \cdots & O_{N_{\rm con}N_{\rm orb}} \end{pmatrix} \end{array},$$

for each of the relevant grids, with $N_{\rm orb}$ the number of orbits, and $N_{\rm con}$ the number of constraints. Finding the optimal linear combination[of orbits which best represent the observational constraints involves solving the matrix equation $\mathbf{O}\gamma = D$ (Rix et al. 1997), where $\mathbf{O}$ is the orbital matrix shown above, D is the column vector containing the observed constraints, and γ is the solution vector, containing the optimal set of non-negative weights of the orbits. The problem can be expressed more explicitly as:

$$\begin{pmatrix} O_{11} & \cdots & O_{1N_{\rm orb}} \\ \vdots & \ddots & \vdots \\ O_{N_{\rm con}1} & \cdots & O_{N_{\rm con}N_{\rm orb}} \end{pmatrix} \begin{pmatrix} \gamma_1 \\ \vdots \\ \gamma_{N_{\rm orb}} \end{pmatrix} = \begin{pmatrix} D_1 \\ \vdots \\ D_{N_{\rm con}} \end{pmatrix}, \tag{4.9}$$

where the symbols are defined as before. The solution to this linear problem is found by applying the non-negative least-squares (NNLS) algorithm of Lawson & Hanson (1974). This results in a (not necessarily unique) combination of non-negative occupancies which minimizes the quantity:

$$\chi^2 = \sum_j \left(\frac{D_j - \sum_i \gamma_i O_{ij}}{\Delta D_j} \right)^2, \tag{4.10}$$

where ΔD_j are the observational errors on the constraints D. It should be noted at this point that the error associated with the photometric, or 'mass' constraints, are included artificially by imposing a constant fractional error value ΔM. This is because, in order to use the observational surface brightness errors, it would be necessary to explore a large set of mass densities which are consistent with the surface photometry. This is prohibitively time-consuming, as each density realization requires a complete computation of the orbit library.

Therefore, it is necessary to assign this somewhat arbitrary 'mass error' value to the mass constraints. The result of this error value is to effectively weight the photometric constraints with respect to the kinematic constraints. Therefore, if the mass error used is too small, the model will be over-dependent on the mass constraints. If the value used is too large, however, the resulting dynamical model may not be self-consistent. The appropriate value of the mass error was found by starting with a very small error value (say, 1%) and comparing the resulting fits to the kinematics for increasingly large mass errors. There should be a mass error value for which the fit to the both the kinematics and mass constraints is of similar quality.

Figure 4.19 illustrates the fit to the mass profile and velocity dispersion profile along the major axis of NGC 821 which result from using different values of ΔM. Only the velocity dispersion is shown, as the other kinematic parameters are not so sensitive to the choice of ΔM. From this it can be seen that the fit is over-constrained by the mass for ΔM$= 0.01$, as the fit to the central velocity dispersion is not very good. Likewise, for ΔM≥ 0.2, the fit to the velocity dispersion is good, but the mass is not well reproduced. A value of ΔM$= 0.1$ was deemed to provide the best compromise of fitting both the mass and kinematics. This is consistent with values used by other authors (e.g., Cappellari et al. 2002).

4.4.4 Regularisation

The models generated by the orbit superposition are generally not smoothly varying in integral space, due to the intrinsic ill-conditioning of the inverse problem of reproducing the integrated properties we observe. From observations, elliptical galaxies are known to be very smooth, featureless systems. Based on this, it seems reasonable to assume that the DF of the stars should exhibit some degree of smoothness. Therefore, it is instructive to impose some form of smoothness criterion, which can be most easily implemented as an additional constraint to the NNLS fit (e.g., Press et al. 1992), as described in Rix et al. (1997), Cretton et al. (1999) and van der Marel et al. (1998). The effective 'error'

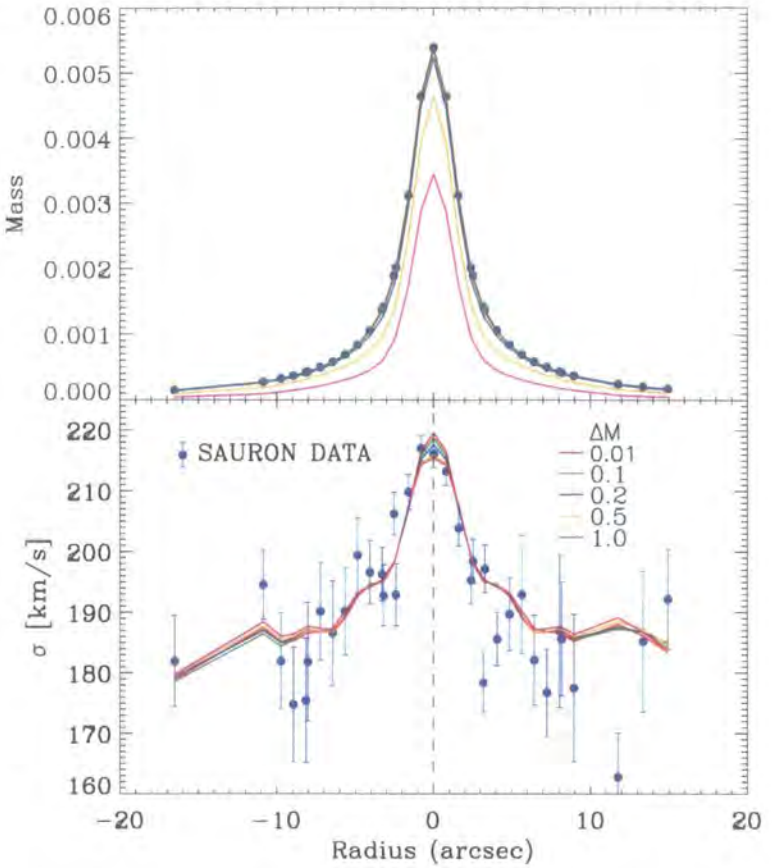

Figure 4.19: Comparison of the model fits (coloured lines) to the mass in the *SAURON* apertures (top panel) and the *SAURON* velocity dispersion (bottom panels) within a 1″ slit along the major axis of NGC 821 for different assumed values of the fractional error on the mass constraints ΔM. For small values of ΔM, the velocity dispersion is not well fitted, but the mass is well reproduced; the reverse is true for large values of ΔM. The choice of ΔM which gives a good fit to both the mass and velocity dispersion was deemed to be ΔM= 0.1, similar to the value used by Cappellari et al. (2002).

on the regularisation constraints act as a weighting scheme, which is controlled by the parameter $1/\Delta$. Models with $\Delta \to \infty$ have no regularisation, while models with $\Delta \to 0$ give infinite weight to the regularisation constraints.

The effect of adding regularisation is explored further in §4.6.3, as is determining the most suitable value of the Δ parameter. Firstly, however, the conservative approach to regularisation of van der Marel et al. (1998) is adopted: if the data cannot be fit with an arbitrarily unsmooth DF, they certainly cannot be fit with a smooth DF. Therefore, unless otherwise stated, no regularisation is applied to the models which follow.

4.5 Determining the Best Fit Parameters

The quantity χ^2 given by eq. [4.10] is a function of three other quantities which must be assumed in constructing a model:

1. **Black Hole Mass** Including a central black hole in the model changes the central potential of the galaxy, which in turn influences any orbits which spend time near the centre. Since the black hole mass, $M_\bullet$, cannot be directly observed, it must be assumed when constructing the model.

2. **Mass-to-Light Ratio** This relates the luminosity density we infer from the surface photometry, to the stellar mass and potential. The stellar mass-to-light ratio, $M/L \equiv \Upsilon$, depends on the mean stellar population present in the galaxy, since for example, metal-poor stars emit more blue light than metal-rich stars of the same mass. For the models presented here, a mean value of Υ is assumed, as there is little evidence of a significant colour gradient in NGC 821. It is possible, however, to assume a spatially varying value of Υ if necessary.

3. **Inclination** The inclination angle, i, of the galaxy must be assumed in order to deproject the surface brightness and kinematics. $i = 90°$ implies an edge-on inclination, for which deprojection is unique (Rybicki 1986). For the face-on case ($i = 0°$), the deprojection is degenerate.

In order to determine the value of these quantities which are most representative of the galaxy being modelled, it is necessary to explore fully this three-dimensional parameter space. This involves constructing 'grids' of models with different values of these three parameters, and evaluating the relative quality of fit to the observational constraints between the different models. In principle, each of the quantities influences the potential, which in turn affects each of the orbits, and one must compute a complete orbit library for each assumed value. The grid can be created more efficiently, however, if one uses the fact that the mass is related to the orbital velocity distribution via $v_{\rm circ}$, the velocity of the circular orbit:

$$v_{\rm circ}^2 = r\frac{\partial \Phi}{\partial r}, \tag{4.11}$$

where r is radius, and Φ is the potential of the galaxy, which is related to the total mass of the system (i.e., inclusive of the black hole). Therefore, any increase in mass is proportional to an increase in the square of the velocity. Likewise, the total mass of the system is given as:

$$M = M_* + M_\bullet, \tag{4.12}$$

where M_* is the mass of the stellar component. Thus, for models with equal values of $M_\bullet/\Upsilon$, the potentials are identical except for a normalisation factor. Therefore, the orbits are also identical, except for a scale factor in velocity, given by the square-root of the proportional increase in $M_\bullet$ or Υ, which can simply be applied to the velocity

histogram of each orbit before computing the NNLS fit. Therefore, the orbit library for a model with $M_\bullet = 1 \times 10^6 M_\odot$ and $\Upsilon = 2.0$ is the same as that with $M_\bullet = 2 \times 10^6 M_\odot$ and $\Upsilon = 4.0$, but with the velocity vectors of each orbit increased by a factor of $\sqrt{2}$. In this way, only orbit libraries with different $M_\bullet/\Upsilon$ need to be calculated and stored for a given inclination. The resulting plane of $(\Upsilon, M_\bullet)$ is then sampled by applying different velocity scale factors to each of the orbit libraries and repeating the NNLS fit to the constraints.

Exploring the inclination parameter involves creating a $(\Upsilon, M_\bullet)$ grid for a number of inclinations, and comparing the relative quality of fit between the models. Typically, determining the inclination (or, equivalently, the intrinsic flattening) of the system with some degree of accuracy from conventional major- and minor-axis long-slit spectroscopy is extremely difficult. The orbital structure of the model is rather poorly constrained by such data, and the model can fit the data equally well for a large range of inclinations (e.g., van der Marel et al. 1998). Multiple slit positions and off-axis exposures can reduce this problem, but such observations are extremely time-consuming, and do not make efficient use of telescope time. Integral-field spectroscopy provides a significant contribution to this problem, capturing a full two-dimensional field of observational constraints, thus better constraining the orbital distribution of the galaxy. The power of IFS data in constraining the inclination was first shown using *SAURON* data for M32 by Verolme et al. (2002).

For NGC 821, the inclination is already rather tightly constrained from photometric considerations (see §4.3). The most flattened Gaussian component from the MGE fit gives, for the assumption of axisymmetry, a lower limit on the inclination angle, such that $i \geq 73°$, equivalent to an intrinsic flattening of 0.3. The range of possible inclinations is therefore reduced to cases where the galaxy is close to edge-on, as one may expect for a galaxy with significant disky isophote distortions (Rix & White 1992). It is unlikely that, through an exploration of the full $(\Upsilon, M_\bullet, i)$ parameter space, it is possible to improve upon this constraint in a significant way from the dynamical modelling. The inclination is therefore not explored with the Schwarzschild model, and the galaxy is assumed to be edge-on (i.e., $i = 90°$). The resulting ($M_\bullet$, M/L) parameter space was sampled on a grid of 308 models, comprising 22 values of black hole mass spaced evenly at $0.5 \times 10^7 M_\bullet$ intervals, and 14 vales of M/L in 0.05 $(M_\odot/L_\odot)_I$ intervals.

Size of the Orbit Library

It was stated in §4.4.1 that the dynamical model should not depend on the size of the orbit library, as the galaxy should be reproduced using only some subset of the library of orbits available. To show that this criterion was met, one would ideally sample integral-space more and more finely until no appreciable difference in the quality of the model was found. In practice, however, one is limited by what is computationally possible.

Determining the optimal size and sampling of the orbit library has recently become a rather controversial topic. A recent preprint by Valluri et al. (2002) explored the effect

of increasing steadily the number of orbits in the library compared to the number of observational constraints in determining the best-fit parameters of an analytic test-case model. These authors find that, in the limit of a sufficiently large orbit library (they suggest a ratio of orbits to constraints of more than $\sim$ 10), the parameters of $M_\bullet$ and Υ are near-indeterminate. Such findings could have serious implications for the validity of black hole mass measurements and related studies, in which much effort has been invested over the past several decades. However, the findings of these authors are yet to be corroborated by other independent groups, and are currently the subject of active debate.

Previous work of van der Marel et al. (1998), Cretton et al. (1999) and others using this Schwarzschild technique (e.g., Cappellari et al. 2002) was based on long-slit data, which generally provide fewer kinematic constraints than integral-field data. In these studies, the (E, L_z, I_3) integral-space was sampled at $(20, 14, 7)$ evenly-spaced points, thus generating 1960 orbits with which to reproduce the kinematic observables. These authors report that using a larger number of orbits results in no change to their models. Verolme et al. (2002) report the same situation for Schwarzschild models using *SAURON* integral-field data, suggesting that the ratio of orbits to constraints is not of primary importance.

Whether or not the orbit library is complete enough to fully describe the galaxy depends primarily on the dynamical structure of the galaxy itself. An orbit library which is sufficiently large for one galaxy, may not be able to reproduce a different galaxy in an equally complete manner. Therefore, χ^2-grids were constructed for two orbit libraries: one sampled with the nominal dimensions $(20, 14, 7)$, and one sampling double the number of energies, giving $(40, 14, 7)$. These grids using 20 and 40 energies are presented in Figures 4.20 and 4.21 respectively, along with their equivalent 1D marginalized profile. These figure show, for each orbit library, the resulting contour plot of $\chi^2(\Upsilon, M_\bullet)$ for an inclination angle of 90°. The displayed χ^2 measures the quality of the fit to the kinematics only, to avoid any systematic effects introduced by the somewhat arbitrary mass error value (see §4.4.3). The actual NNLS fit, however, does include the mass constraints. Neglecting the χ^2 contribution from the mass constraints does not affect the topology of the total χ^2 contours shown in Figure 4.21. The best fitting model is depicted by the large symbol residing within the lowest level χ^2 contour, which corresponds to a $\Delta\chi^2 = 3.53$; equivalent to the $1-\sigma$ confidence level of a three-parameter probability distribution (Press et al. 1992).

Increasing the number of energies has the effect of reducing the variations between neighbouring models, creating a smoother χ^2 topology, and an improved estimate of the black hole mass. This suggests that the galaxy is better reproduced by the finer-sampled orbit library. If doubling the orbit library size noticeably improves the determination of the black hole mass and the quality of the model, it is logical to investigate the effect of doubling the size of the library once more to check whether the limiting size has been reached. Unfortunately, to model the 500+ kinematic apertures provided by the

SAURON data requires a large amount of computing power and time. There are two main limiting factors: 1) the CPU time spent integrating the orbits, and 2) the size of the final orbital matrix (c.f. eq. [4.4.3]) which must be stored in memory by the machine. Within these limitations, an orbit library size of a further factor of two (i.e., using 80 samples in energy) was feasible to explore with the standard PC machines available (1Ghz processor and 1Gb RAM). Exploring models using *SAURON* data and significantly larger orbit libraries (e.g., an order of magnitude larger than the nominal size) would require substantially more computing power. The question of whether such an investment would be scientifically worthwhile remains open.

It should be noted here that all the grids of models presented in this chapter were calculated making use of simplistic parallel computing via IDL scripts. This made it possible to utilise up to 8 CPUs simultaneously, although access was generally restricted to 4. Without such techniques, producing such dense grids with large orbit libraries ($>$ 8000 orbits) and large data sets ($>$ 500 kinematic apertures) becomes prohibitively time consuming.

Figure 4.22(a) presents the equivalent of Figures 4.20(a) and 4.21(a), but using 80 energies, giving a total orbit library size of 7840 orbits. From this it can be seen there is little difference between using 3920 or 7849 orbits. This is emphasised by Figure 4.22(b), which presents the marginalized profiles for all three orbit library sizes. From this, it can be seen that 1960 orbits are not sufficient, as doubling the size of the library to 3920 orbits yields a significantly smoother χ^2 topology. There is very little change, however, by doubling the size again. This largest orbit library still only provides a orbits-to-constraints ratio of 2.5, and so does not probe the indeterminate régime explored by Valluri et al. (2002). Given the computational limitations, however, and the apparent stability of the χ^2 contours for libraries of 3920 orbits or larger, no further increase in the orbit library size is deemed necessary until the Valluri et al. (2002) claims have been substantiated by further and independent tests.

Comparison with Gebhardt et al. 2002

NGC 821 is included in the modelling sample of G02, and uses the same STIS kinematic values used here. Although the input data which constrains the black hole mass most strongly is identical between these two studies, there are numerous significant differences between the other data sets used (i.e., ground-based kinematics, and imaging), as well as the modelling techniques themselves: the modelling code of G02 was developed completely independently of that used in this work, and involves fitting to the actual LOSVD of the kinematic data, rather than the parameterized moments; the ground based kinematics used by G02 involves only major- and minor-axis long-slits, as oppose to full 2D coverage; the models in this work are sampled in the same way as the data (i.e., a Cartesian grid projected on the sky), whereas G02 use angular sectors to rebin their data before com-

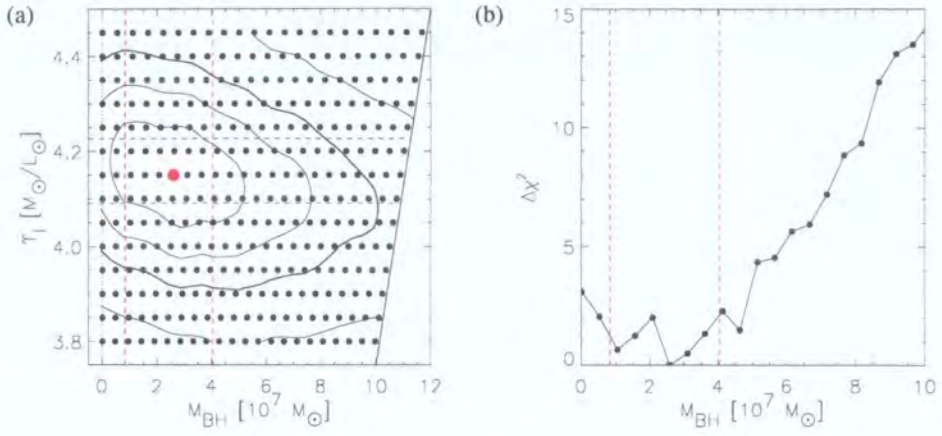

Figure 4.20: (a) Contours of constant χ^2, measuring the goodness of fit of the edge-on axisymmetric models to the combined *SAURON* and STIS data kinematic data for NGC 821. The abscissa is the mass $M_\bullet$ of a central point mass representing the nuclear black hole; the ordinate is the mean I-band mass-to-light ratio of the galaxy. This grid was constructed for models using a total of 1960 orbits. The best-fit model is denoted by the large red circle. The first three contours denote the formal 68.3%, 95.4% and 99.73% (thick contour) confidence regions for the three parameters (i,$M_\bullet$,M/L) jointly. Subsequent contours indicate a factor of 2 increase in $\Delta\chi^2$. The red and blue dashed lines indicate the marginalised (1D) 1-σ confidence limits on $M_\bullet$ and M/L respectively. (b) The marginalised, one-dimensional function of χ^2 as a function of black hole mass. This is determined by fitting a parabola to χ^2 as a function of M/L along a series of vertical slices through the χ^2 surface, giving for each value of $M_\bullet$ the minimum χ^2. The red dashed lines represent the upper- and lower-confidence limits at the 1-σ level.

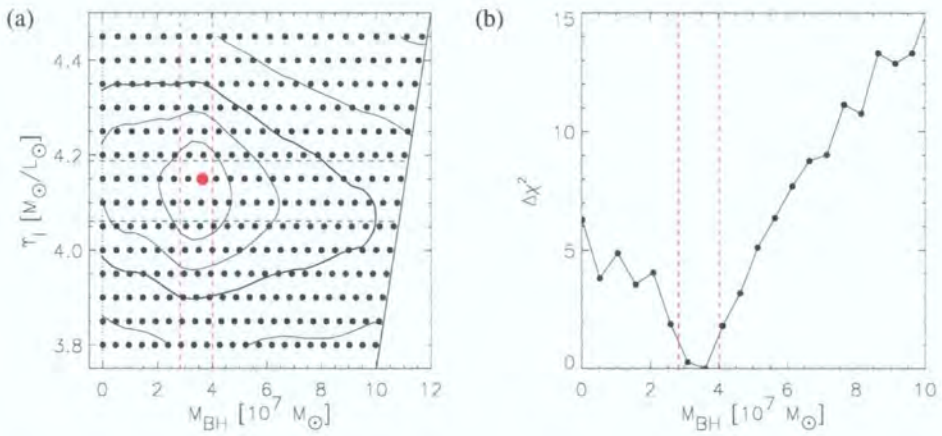

Figure 4.21: Equivalent to Figure 4.20, but using an orbit library which is twice as large (i.e., 3920 orbits in total). There is a noticeable reduction in the variations of χ^2 values between neighbouring models. This is due to the better sampling of the orbit library, which is necessary due to the large number of kinematics constraints provided by the *SAURON* integral-field data. The uncertainty of the black hole mass is most significantly reduced, giving best-fit parameters of $M/L = 4.12 \pm 0.06$ in I-band solar units, and $M_\bullet = (3.41 \pm 0.68) \times 10^7 M_\odot$. These values were determined from a fitting a parabola to the marginalised χ^2 minimum in both M/L and $M_\bullet$. The determined black hole mass is in excellent agreement with the value determined by G02, who find $M_\bullet = (3.7^{+2,4}_{-0.8}) \times 10^7 M_\odot$.

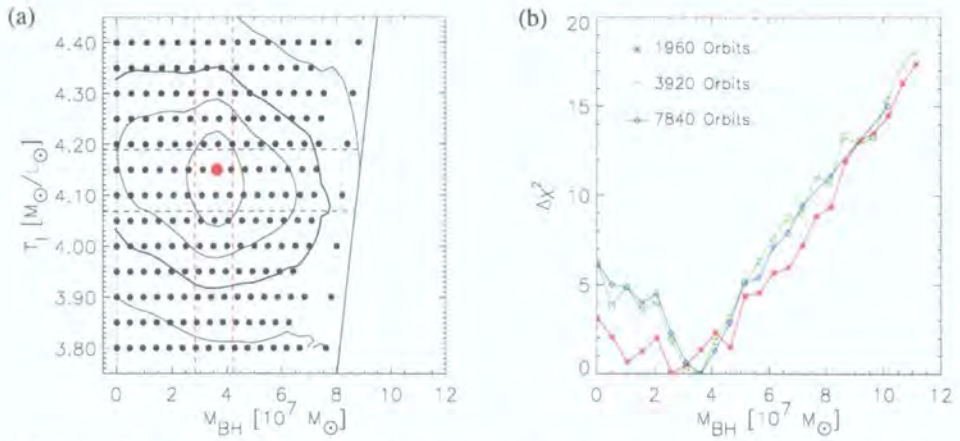

Figure 4.22: (a) Equivalent to Figure 4.20(a), but using an orbit library which is four times larger (i.e., 7840 orbits in total). Comparing this figure with Figure 4.21(a), there is very little change in the shape or size of the χ^2 contours, implying that the optimal orbit library size has been reached, and that adding more orbits does not change the properties of the best-fitting model. This is emphasised by (b), which overplots the marginalised profiles of the grids constructed with different numbers of orbits. The results using either 3920 or 7840 orbits are almost equivalent. Creating a grid with this many orbits using all of the *SAURON* apertures requires a significant amount of computing time and power. Hence why the high black hole mass end is not as well sampled as the other grids.

paring with the model; G02 use a 'maximum entropy' method to obtain the optimum fit of the orbit library to the data (which implies some degree of regularisation), whereas the linear method of non-negative least squares is used in this work. Given these differences, as well as numerous other more subtle variations, it is a strong test of the modelling process (i.e., the validity of the assumptions and approximations) to compare the results of the two studies.

Figure 4.23 presents the χ^2 contour grid of G02 and the current study. The contours are plotted with the same abscissa scale of black hole mass, although the ordinates of Υ are different due to the different photometric band used by G02 to determine the potential (HST F555W filter, close to V-band). What is important from this diagram is the excellent agreement of the black hole mass estimates. The red vertical lines give the 1-σ error around the best-fit value, showing that the two determinations are consistent well within the errors. The G02 grid appears to exclude a zero-mass black hole at the 3-σ level, whereas the grid presented here only excludes it at the 2-σ level. This may be due to inconsistencies between the STIS data and either of the two ground-based kinematic data sets, especially as the black hole mass is constrained primarily by the velocity dispersion, which is susceptible to template mismatch effects at the kinematic extraction stage. Future collaboration between the *SAURON* and G02 groups will aim to determine the cause of this inconsistency.

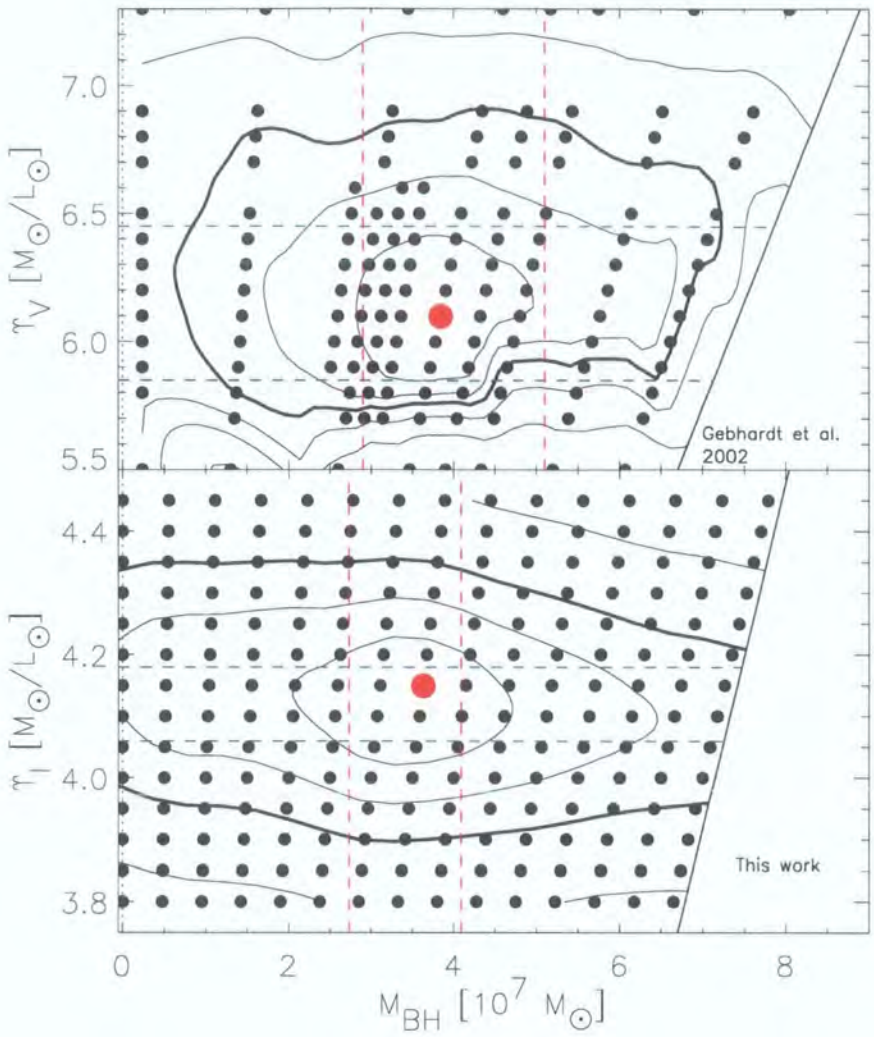

Figure 4.23: Comparison of G02 χ^2 contours with those of this work. The contour levels are the same as Figure 4.20(a), with the thick contour again showing the 3-σ confidence level. The large red filled circle represents the model with the lowest χ^2 value for the grid. The red and blue dashed lines represent the 1-σ marginalised errors on the black hole mass and mass-to-light ratio respectively. The different Υ values are due to the different photometric bands used by the two studies. There is excellent agreement between the two black hole mass estimates, which are consistent within the 1D, 1-σ level.

4.6 Properties of the Best-fit Model

The model with the lowest overall χ^2 value from the grid shown in Figure 4.21 gives the values ($M_\bullet = 3.4 \times 10^7\, M_\odot$, $M/L = 4.15\,(M_\odot/L_\odot)_I$, $i = 90°$) which best represent the photometric and kinematic data. Once these parameters have been established, one can examine the properties of this particular model in detail, which in turn gives information on the dynamical structure of the galaxy. The model is composed of a weighted library of orbits, each of which has known intrinsic properties. The galaxy can now be described by the phase-space distribution of the constituent orbits, giving the Distribution Function of

the galaxy. It is possible to determine the degree of anisotropy at different positions in the galaxy, and hence, ascertain the dominant support mechanisms, and how these relate to other properties of the system.

4.6.1 Comparison with Observational Data

Although the statistically best-fitting model has been determined, this does not imply that the model itself is truly representative of the observational data. Figure 4.24 presents the *SAURON* (left panels) and best-fit model (right panels) kinematic maps for NGC 821. Also shown is the effective mass in each of the *SAURON* apertures taken from the input MGE mass model (left panel) and Schwarzschild model (right panel). Clearly, the model closely resembles the observational data. Figure 4.25 shows an extracted 'long-slit' of the *SAURON* data along the major-axis, overplotted with the equivalent apertures from the model. This figure shows that the *SAURON* data and model are in excellent agreement.

Applying a similar three-integral modelling technique to the dynamically cold galaxy, NGC 4342, it was found by Cretton & van den Bosch (1999) that, at larger radii, their model gave an overabundance of counter-rotating orbits, leading to an erroneous fit to the kinematics. This was determined from examination of the LOSVDs of the model, reconstructed from the $\bar{v}$, σ, h_3 and $h_4$terms, from which a clear counter-rotating component was found. Although the model of NGC 821 fits the data well, even at large radii, it is important to check that the LOSVDs reconstructed from the data are consistent with the velocity histograms of the best-fit model, and that no spurious components are masked by the limitations of only using the first four moments of the LOSVD. Figure 4.26 shows the reconstructed LOSVDs from the data overplotted with the best-fitting velocity histograms for the whole *SAURON* field. Apart from emphasising the enormous amount of information held in these two mosaiced *SAURON* fields, this also shows that the model histograms are remarkably consistent with the parameterized LOSVDs across the entire field. Thus, no spurious counter-rotating components are found in the model.

Although the *SAURON* data places strong constraints on the dynamical structure of the galaxy, the primary constraint on the black hole mass comes from the high-resolution STIS kinematic data. Figure 4.27 shows the best-fit model, overplotted with a model with the same M/L, but with no black hole. The errors on the STIS data are rather large, and so models with no black hole are not strongly excluded by the data. However, the model with the best-fit black hole mass gives a better fit to the data.

4.6.2 Rotational or Pressure Support?

A key finding in the study of elliptical galaxies is that the amount of rotation required to explain the observed flattening of these systems is generally much higher than the observed rotation speed. Therefore, the shape and structure of the galaxy must be supported by

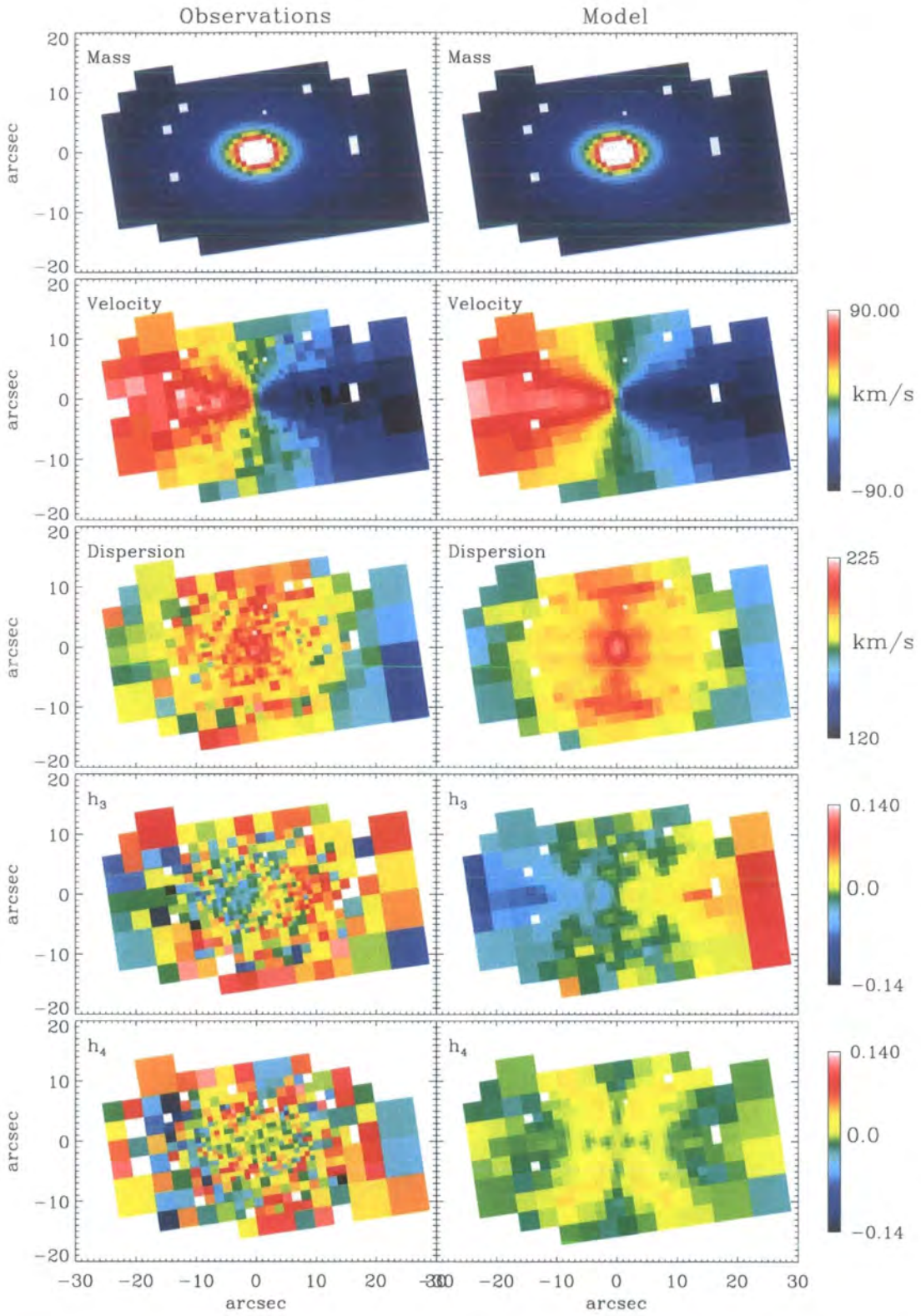

Figure 4.24: Comparison of input *SAURON* data (left panels) with the best-fit Schwarzschild model (right panels). The velocity field is very well reproduced by the model. The kinematic fields are visibly well reproduced, although it is difficult to perceive the consistency between data and model, as one cannot present the error bars at each aperture.

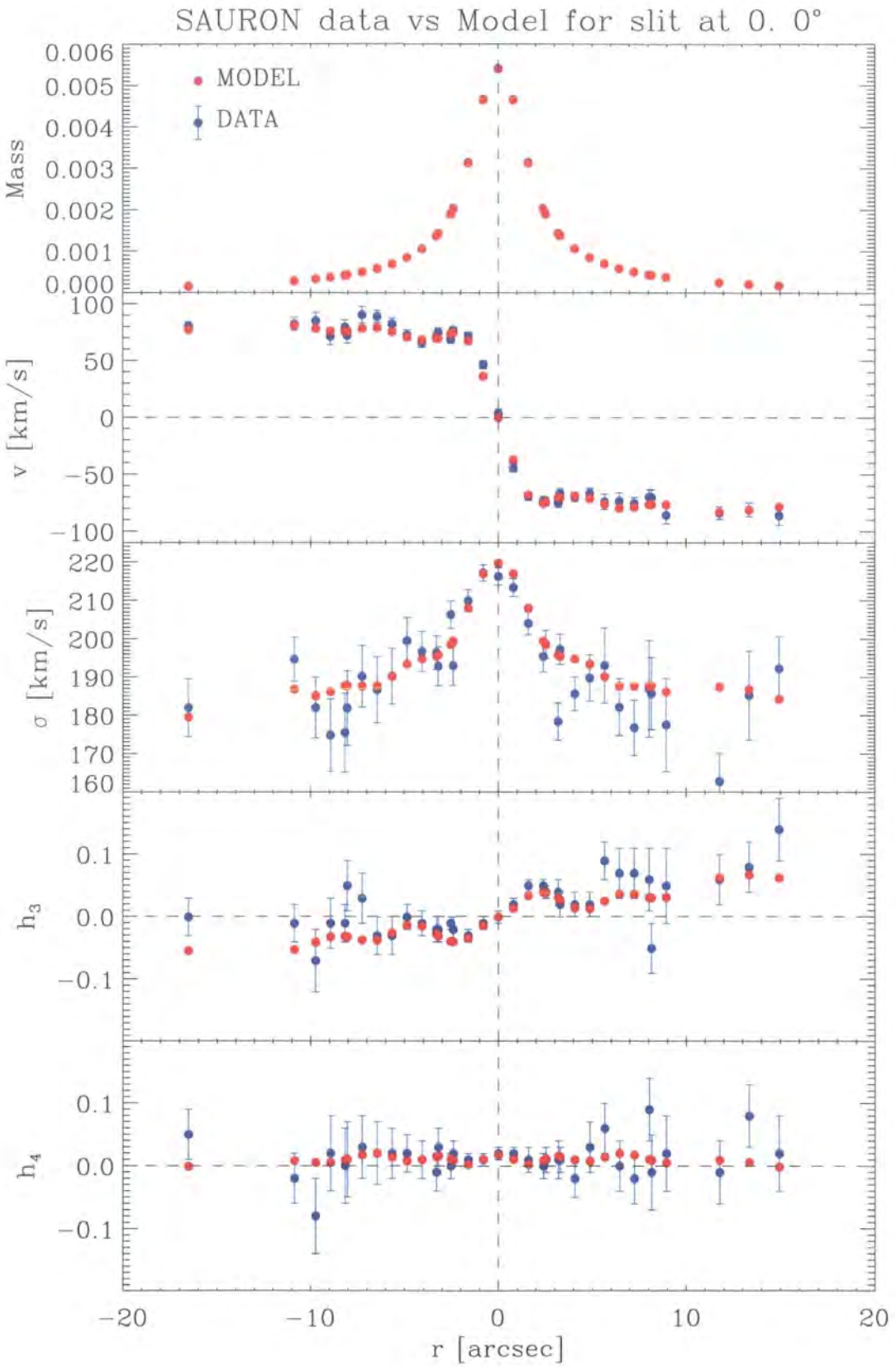

Figure 4.25: Comparison of input *SAURON* data (blue symbols) with the best-fit Schwarzschild model (red symbols) for an extracted 'slit' along the major-axis of the *SAURON* field of NGC 821 presented in Figure 4.24. Each panel presents (from top to bottom) the mass distribution, the rotation velocity, velocity dispersion, h_3 and h_4 terms. This 1D slice through the 2D field shows more clearly the consistency of the data and model with respect to the observational errors.

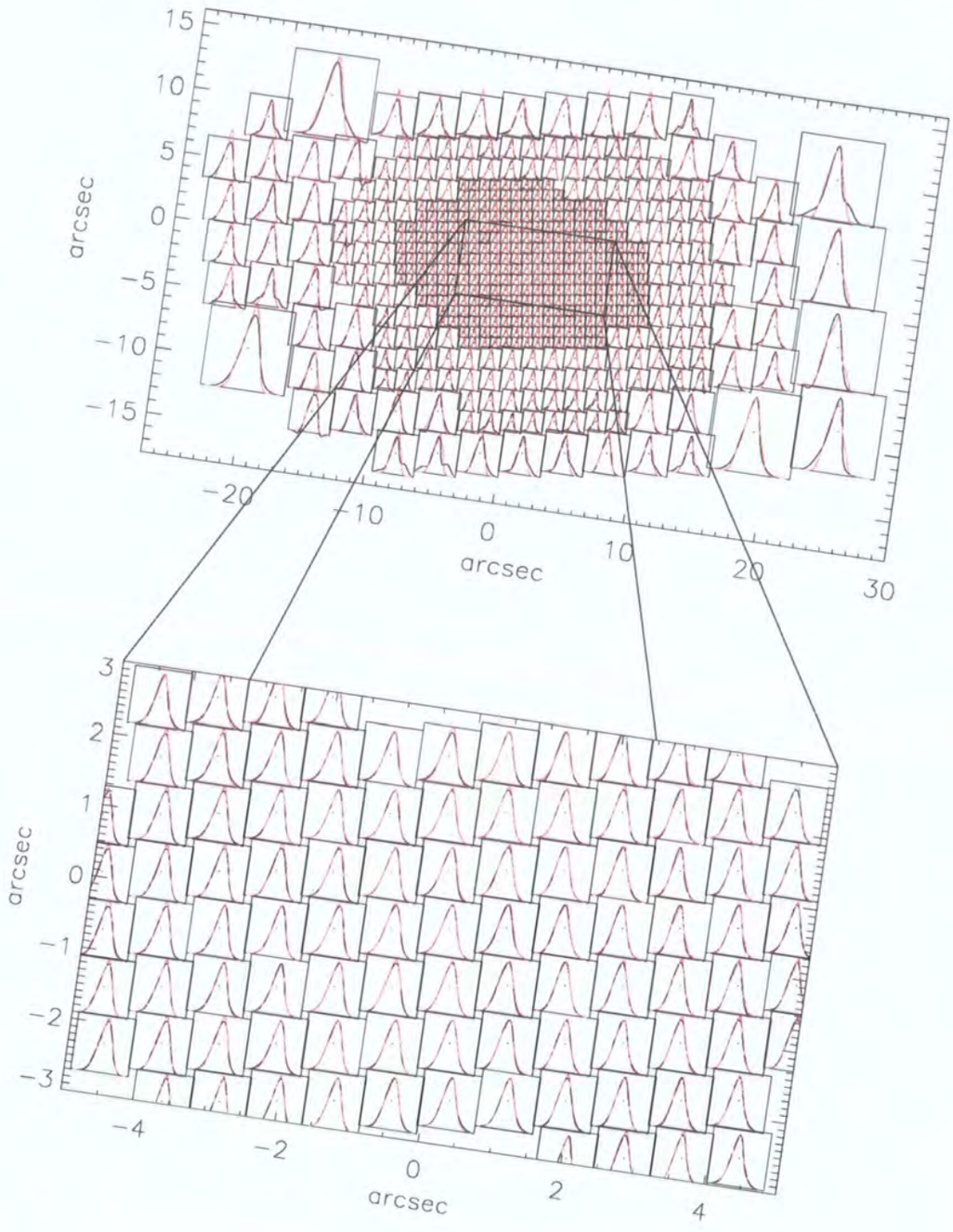

Figure 4.26: Reconstructed *SAURON* LOSVDs (using $\bar{v}$, σ, h_3 and h_4) shown by the black curves, overplotted with the total velocity histograms of the best-fitting model (red lines) in each *SAURON* aperture. The insert shows an expansion of the central regions, where the data are not binned, and the aperture size is $0\farcs8^2$. The model used to plot the histograms has a regularisation parameter $\Delta = 4.0$.

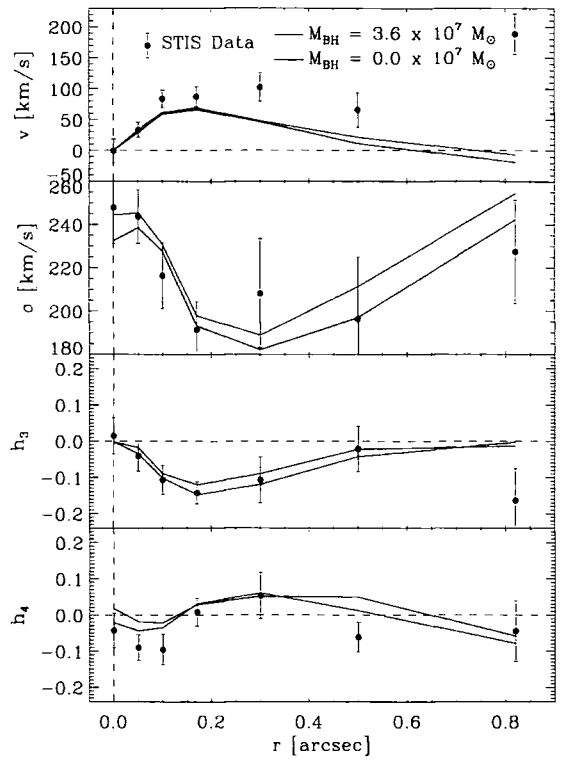

Figure 4.27: Comparison of STIS kinematic data (blue points) with a model which has no black hole (blue line), and the model closest to the best-fit values, which has a central dark mass of $3.6 \times 10^7 M_\odot$. On visual inspection, the model which includes a black hole is only a marginally better fit to the STIS data than that with no black hole. Statistically, however, the difference between their quality of fit is at the 2-σ level. The most significant difference between the models occurs for the central velocity dispersion, which is what one expects for the addition of a central dark mass.

some other mechanism. It was shown by Binney (1978) that this could be explained by anisotropies in the velocity dispersion tensor of the galaxy, thus supporting the figure of the system via random, rather than streaming motion.

A useful quantification of which support mechanism is more important, i.e., pressure or rotation, is given by the ratio of the rotation velocity and velocity dispersion: v/σ. Since only projected quantities can be observed, and one would like to compare this property between different galaxies, this ratio is usually given as a global quantity for a galaxy, defined generally as the maximum observed rotation velocity, $\bar{v}_{\rm max}$, divided by some averaged central velocity dispersion, σ_0. In this way, one can quantify the balance between random and ordered motions, thus indicating the mechanism of support for a given galaxy.

For an individual galaxy, it is instructive to consider the ratio of rotation velocity and velocity dispersion simply as a function of position on the meridional plane for a galaxy, from which it may be possible to infer substructure in the galaxy. Specifically, for NGC 821, there is photometric evidence (disky isophotes) and kinematic evidence

(asymmetric LOSVD) for an embedded stellar disk. Such a structure is expected to have a higher degree of rotational support compared to the spheroidal component.

Figure 4.28 presents the intrinsic v/σ in the meridional plane of the model. To be consistent with previous authors (van der Marel et al. 1998, Verolme et al. 2002, Cappellari et al. 2002), this was calculated as the ratio of the velocity in the ϕ direction and the quadrature sum of the trace of the tensor describing the velocity ellipsoid of the best-fitting model:

$$v/\sigma = \frac{\langle v_\phi \rangle}{\sqrt{\langle v_r^2 \rangle + \langle v_\theta^2 \rangle + \langle v_\phi^2 \rangle}}. \tag{4.13}$$

Note that $\langle v_\phi^2 \rangle \equiv \sigma_\phi^2 + \langle v_\phi \rangle^2$, and so includes both random and streaming motion (i.e., it represents the second moment of the azimuthal velocity relative to the systemic velocity, rather than relative to the mean rotational speed).

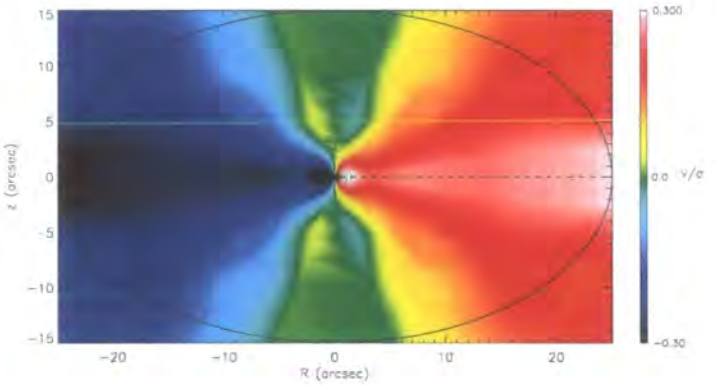

Figure 4.28: Intrinsic ratio of rotational velocity and velocity dispersion on the meridional plane. Large absolute values imply a higher degree of rotational support. Overplotted are points which indicate the sampling of the meridional plane by the orbit library. Specifically, the radial interval is determined by the sampling in E, and the angular interval by the sampling in L_z. The sector closest to the minor-axis has been omitted, as it is generally poorly sampled by the model, and thus contains little useful information. The ellipse indicates the position of the 0.5 R_e isophote. The v/σ rises sharply on the major-axis compared to off-axis positions. This very 'pinched' field may indicate the presence of the embedded stellar disk.

Figure 4.28 resembles somewhat the velocity field of the *SAURON* data. However, this figure uses the *intrinsic* moments of the stellar orbits, rather than projected values integrated along the line of sight. In principle, this should reveal more clearly the structure of the galaxy. Indeed, the flattened region of high $\mid v/\sigma \mid$ extending along the major axis is probably due to the embedded stellar disk.

To help interpret the intrinsic v/σ of the model, it would be instructive to compare the result of the NGC 821 model with that of an analytic case: for example, an oblate, isotropic rotator model. This would highlight where the structure of v/σ differs from that

of a simple system, flattened by rotation. A full exploration of this, however, is beyond the scope of this chapter.

However, a useful comparison can be made between the intrinsic v/σ of NGC 821 and that of a galaxy thought to be consistent with the oblate, isotropic case. The nearby dwarf elliptical, M32, is just such a galaxy. This object was recently studied in detail using the same Schwarzschild orbit superposition software used here, as well as *SAURON* integral-field data (Verolme et al. 2002). This object is clearly not directly comparable to NGC 821, but it is a constructive exercise to compare the two objects in this respect. Figure 4.29 (a) and (b) show the intrinsic v/σ field for NGC 821 and M32 respectively. To allow a comparison, the spatial coverage has been scaled in both cases to extend 0.25 R_e along the effective major-axis. This value was chosen as the *SAURON* data for M32 was

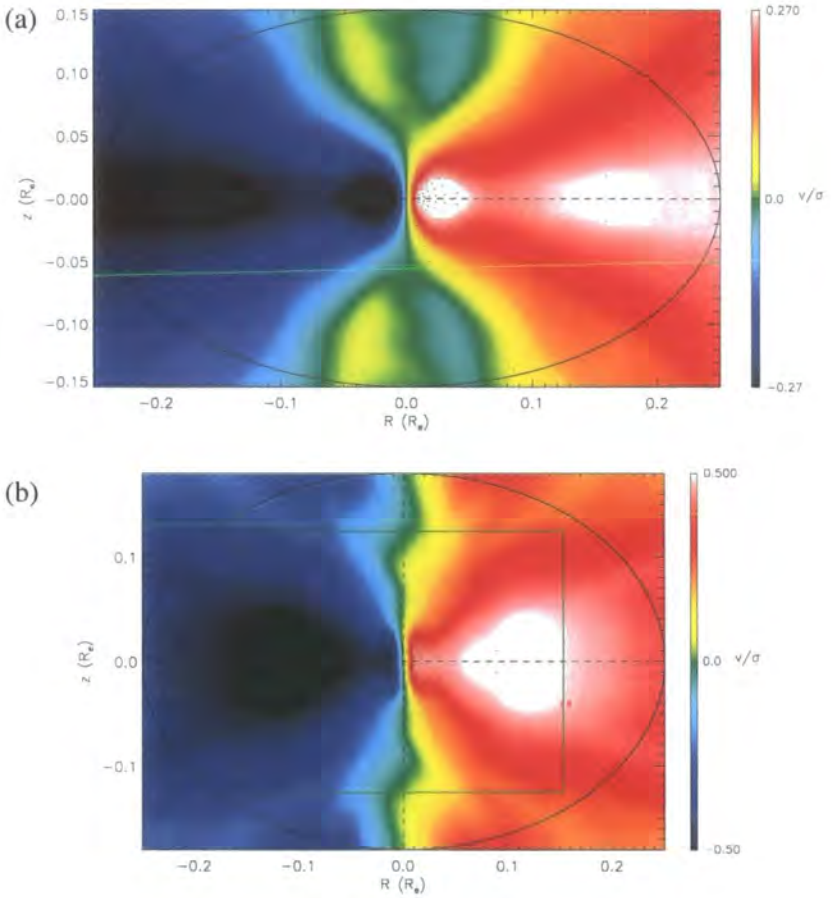

Figure 4.29: Comparison of the intrinsic v/σ of (a) NGC 821 with that of (b) M32 (courtesy of Ellen Verolme, private communication). M32 is thought to be close to an oblate, isotropic rotating system (van der Marel et al. 1998, Verolme et al. 2002). The spatial coverage is scaled to compare the models at the same effective radius. The M32 model is based on high-resolution *SAURON* data, covering the central region within $\sim \pm 1/6\ R_e$, indicated by the green box. The overplotted ellipse represents the intrinsic flattening on the meridional plane, with a major-axis length of 0.25 R_e. The relatively flat structure in NGC 821 is not present in M32, suggesting that it may be associated with the disk component.

only obtained in the high-resolution mode, and so the field of view is reduced to around $9'' \times 11''$, equivalent to $0.25 \times 0.30\ R_e$. The green box in Figure 4.29 (b) indicates the coverage of the *SAURON* data for M32.

This simplistic comparison show that, in the case of M32, the change in v/σ as one moves from the minor- to the major-axis is rather gradual. For NGC 821, however, there is a steep increase in the v/σ which is localised along the major-axis. Off-axis positions, by comparison, show lower values for the same elliptical radius. This behaviour adds support to the interpretation of the v/σ field of the NGC 821 model being caused by the presence of a disk.

4.6.3 The Distribution Function

The Distribution Function (DF) of a galaxy specifies how the orbits are distributed over position and velocity, and is therefore of primary importance for understanding the dynamical structure of the system. Information on the form of the DF is held in the dynamical model by the distribution of weights allocated to each orbit in the orbit library. Each orbit is defined uniquely by the three integrals of motion E, L_z and I_3. Therefore, the weights applied to each orbit form a distribution in the 3-dimensional integral-space, which represents the DF for the galaxy. By examining the integral-space distribution from the model, one can gain an understanding of the types of orbits which make the galaxy, and perhaps link this with other properties of the system.

Figure 4.30 shows the full integral-space distribution for the best fitting model. Each panel of this plot shows the distribution of orbital weights as a function of the third integral (x-axis) and the vertical component of the angular momentum (y-axis) for a given energy. The energy decreases from left to right, and from top to bottom, corresponding to an increase in galactocentric radius indicated by the values at the bottom of each panel. No regularisation constraints have been added for this model, therefore the distribution of weights is rather discretised, or 'spikey'. For smooth systems like elliptical galaxies, however, one intuitively expects the DF to vary slowly as radius increases, with the most of the stars sharing similar regions of phase-space.

For this reason, some form of regularisation can be imposed on the model to allow a more physically meaningful, rather than statistically optimal, interpretation of the DF. As described in §4.4.4, this regularisation takes the form of additional constraints included in the NNLS fit which force the distribution of weights towards a smooth function of E, L_z, and I_3. The degree of smoothness imposed is determined primarily by the fractional error Δ associated with the smoothness constraints; thus by assigning a large Δ parameter, little regularisation is applied.

Determining the optimal value of Δ is a somewhat subjective process. It is clear, however, that the degree of regularisation applied should not significantly alter the quality

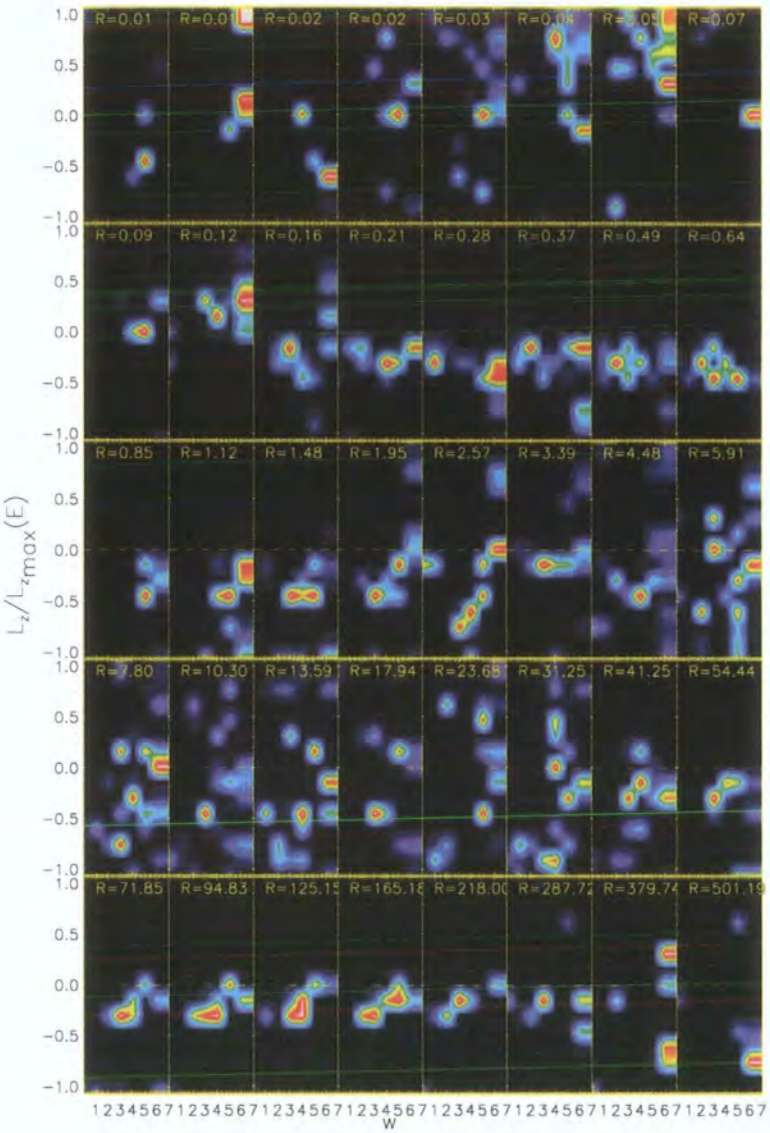

Figure 4.30: Distribution of orbital weights in integral-space for the best-fit model of NGC 821 using 3920 orbits. Each panel of this plot shows the distribution of orbital weights as a function of I_3 (x-axis) and L_z (y-axis) for a given energy. The energy decreases from left to right, and from top to bottom, corresponding to an increase in galactocentric radius indicated by the values at the bottom of each panel. No regularisation constraints have been added for this model.

of the model's fit to the data. Figure 4.31 presents the χ^2 value of the best-fitting model as a function of Δ (similar to Figure 4 of Verolme et al. 2002). From Figure 4.31 it can be seen that, for $\Delta \gtrsim 4.0$, the χ^2 value of the model is increased at the level of less than 15%. For values of $\Delta \lesssim 4.0$, the χ^2 begins to increase significantly, and the model is not able to fit the input data. The value of $\Delta = 4.0$ is therefore chosen, as it gives a smooth solution which provides a similar quality of fit to the data as the statistically best-fit model.

Figure 4.32 presents the integral-space distribution of the same model as shown in 4.30, but for $\Delta = 4.0$. By comparison with Figure 4.30, the regularised integral-space

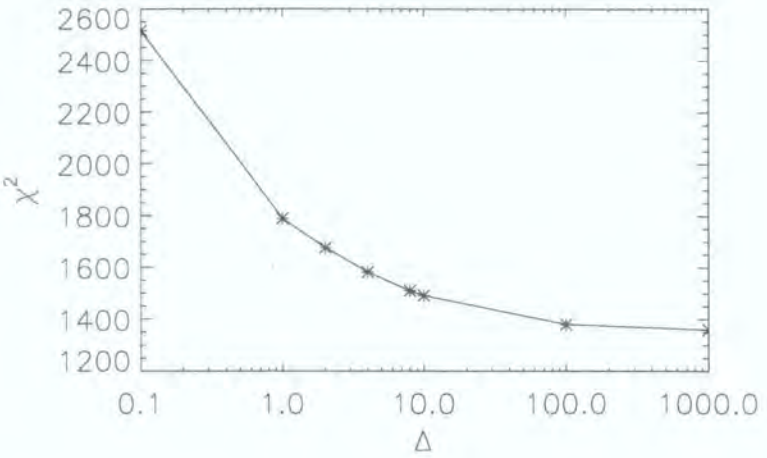

Figure 4.31: Absolute χ^2 value of a model with the best-fit input parameters for different degrees of regularisation, quantified by the 'error' parameter Δ. Note that the decrease in the quality of fit for $\Delta \gtrsim 4$ is less than $\sim 15\%$. For all regularised models which follow, a value of $\Delta = 4$ is assumed, which is consistent with values used in other studies (van der Marel et al. 1998, Verolme et al. 2002, Cappellari et al. 2002).

distribution is much clearer to interpret. It is possible to determine by visual inspection that there are certain regions of integral-space which are preferred over others, and that the weights assigned to these regions vary smoothly from the peak values to zero. This is what one intuitively would expect for a system composed of stars which share a common dynamical origin.

On closer inspection of Figure 4.32, it is evident that there is a significant degree of sub-structure at certain energies, which remains even with regularisation imposed. At all radii $\lesssim 30''$(where the model is most strongly constrained by the *SAURON* kinematic data), there exists a component with $L_z \sim 0$, and generally high ($w \geq 6$) values of I_3. This 'primary' component approximates to a structure composed generally of orbits which can pass high above the equatorial plane, and which do not exhibit strong rotation about the symmetry axis. Between circular radii of $\sim 0''.37 - 40''$, there is evidence of a secondary component. This component, unlike the primary component, occupies only a subset of energies. It is distinct from the primary component in both its values of L_z and I_3, tending towards higher absolute values of angular momentum (extending to $|L_z| \gtrsim 0.5$), and lower values of I_3 (extending to $w \lesssim 3$). This suggests a component composed of orbits which lie closer to the equatorial plane (i.e., is flattened) and exhibits relatively stronger rotation about the symmetry axis.

Figure 4.33 illustrates this by presenting the orbital paths on the meridional plane of two orbits representative of the two components from integral-space. This demonstrates the qualitative difference between these two components, and suggests that the flattened component with higher angular momentum may be attributed to the disk component housed in this galaxy; and that the low-angular momentum, high-I_3 component may

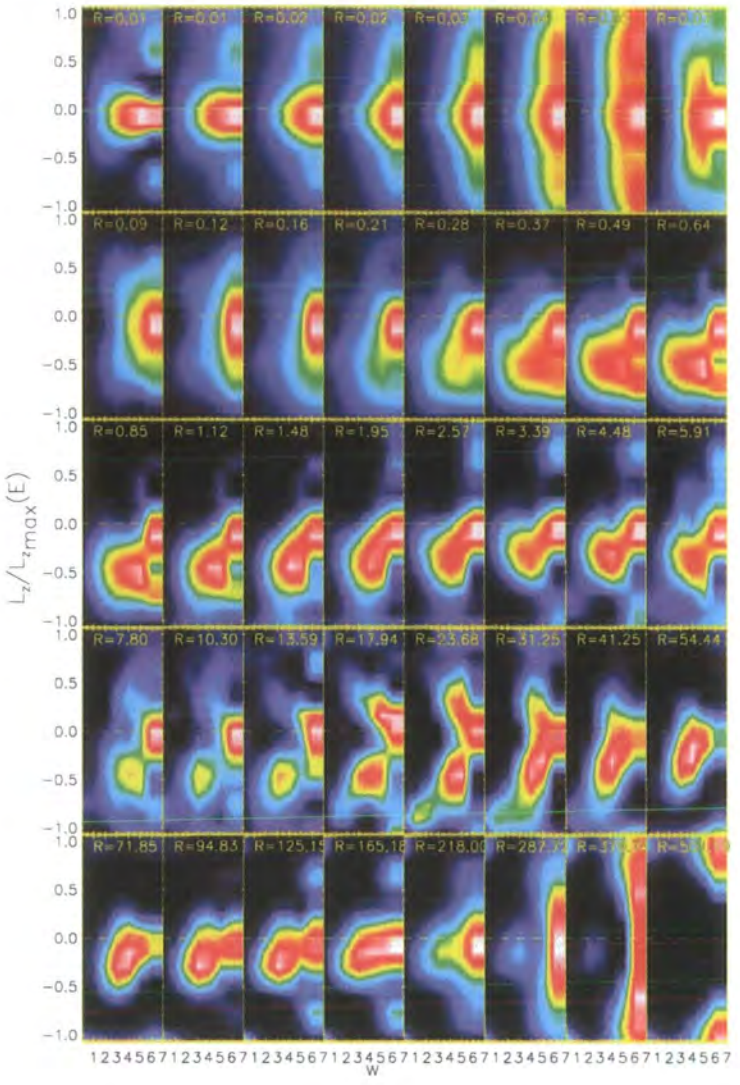

Figure 4.32: Distribution of orbital weights in integral-space for the best-fit model of NGC 821 with regularisation parameter = 4.0.

represent the spheroidal, or 'bulge' component of the galaxy. This possible interpretation is developed in the following section.

Before embarking on a decomposition of the integral-space distribution of the model, it is worthwhile trying to establish how robust the structure in integral-space is to variations or noise in the input data. Ultimately, one would prefer to establish the character of integral-space using some analytic test-model, for which the DF is known, and so one can test to what extent the DF can be recovered. With such a model not presently available, a less formal, but still useful exercise is to use a different input data set of the same galaxy, and see whether the structure in integral-space remains unchanged.

For this purpose, a set of kinematic data was produced using the same original *SAURON* data-cube, but treating it in a somewhat different way to the data and re-

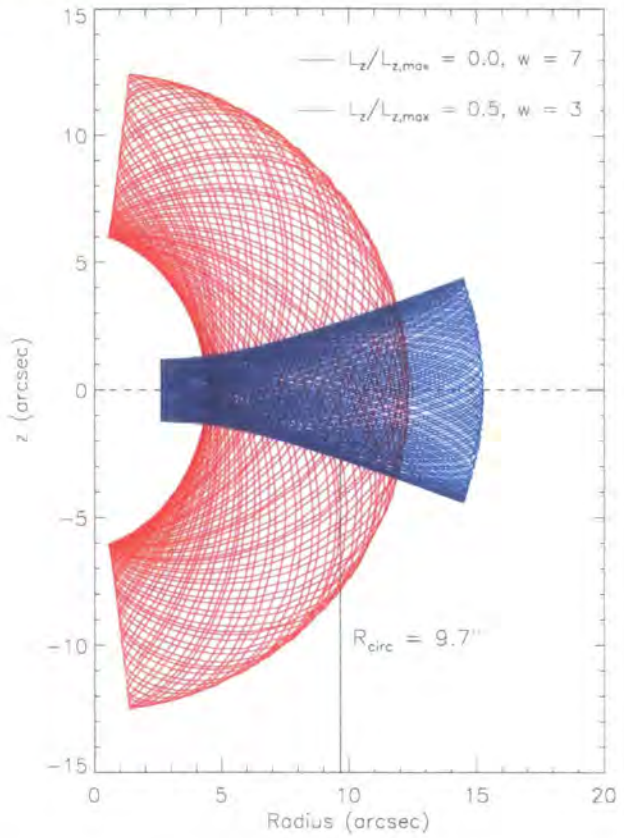

Figure 4.33: Comparison of two orbits representative of the two peaked components observed in the integral-space distribution of NGC 821, taken at a circular radius of $\sim 10''$. The red line represents an orbit typical of the 'primary' integral-space component, which is characterised by low angular momentum, and high values of I_3. The blue line represents the trajectory typical of the 'secondary' component, which has generally higher angular momentum and lower values of I_3. The secondary component is more flattened, than the primary, giving rise to a two-component, disk-and-bulge type structure. Note, however, that the secondary component is not a thin disk, but has an appreciable thickness. This suggests that the disk in NGC 821 may have an appreciable pressure support.

duction described earlier in this chapter. The data are binned using the optimal Voronoi tessellation (Cappellari & Copin 2001), to a minimum S/N of around 50 as before. The kinematics were independently derived from this binned data-cube by the *SAURON* data-reduction pipeline, using a different spectral template, and with different FCQ configurations (e.g., continuum order, wavelength bounds, filtering et.). Rather than using this data directly, however, the kinematic maps (i.e., $\bar{v}$, σ, h_3 and h_4) are firstly parameterized using a Fourier expansion of the 2D fields. This process is similar to what is conventionally conducted on images of elliptical galaxies in order to quantify deviations from true elliptical isophotes (e.g., Franx et al. 1989*a*). For photometry of regular objects like elliptical galaxies, usually the first four terms of a Fourier series are adequate to describe the shape to below the 1% level. The analogy of this is the technique of 'kinemetry' (Schoenmakers et al. 1997, Copin et al. 2001), which can quantify the general parameters of velocity fields (e.g., the opening angle of the velocity field, kinematic misalignments, twists in the zero-velocity contour etc.). The application here, however, is slightly different, in that the

Fourier expansion is being used purely to reproduce as well as possible the input data. It was found that, to reproduce the sharpness of the angular variations in the velocity field of NGC 821, the first twelve terms of the Fourier series were required. Clearly all twelve terms do not each contain new diagnostic information. However, they are required to properly reproduce the input data. Therefore, this process differs from kinemetry, which uses only the significant terms to parameterise the general features of the velocity field.

A useful consequence of describing the data by this Fourier expansion is that the kinematic maps are implicitly symmetrised. The data are also effectively filtered of high-frequency spatial variations. The result of the Fourier expansion is to produce input maps which are visibly smooth and regular, as will as being axisymmetric. Figure 4.34 presents the pipeline-reduced data (after 2D binning with the Voronoi tessellation method) and the resulting Fourier expansion, kindly provided by Michele Cappellari. It is clear that the features of the input data are very well reproduced. The Fourier expanded data is within the uncertainties of the original data, but is naturally smoother, as the high-frequency spatial variations are effectively removed. It is also clear, however, that the Fourier-expanded kinematic data is sufficiently different from the original Quadtree-binned data, such that if the two-component structure of integral-space is very sensitive to aspects of the input data which are not physically useful (e.g., noise, 2D-binning), it is unlikely that it will be reproduced using this smooth, regular input data.

Figure 4.35 presents the input kinemetry and the resulting model, which uses the best-fit parameters of $M_\bullet$, M/L and i derived from the previous section. One would prefer to determine the true best-fit parameters by computing a complete grid for this data, but for the purpose of this test, it is sufficient to use the previously determined values. Clearly the model fits the input data extremely well. Figure 4.36 presents the equivalent of Figure 4.32, but for the Fourier-expanded input data. A visual comparison the two plots (both have the same regularisation parameter, $\Delta = 4.0$) shows that they are almost identical, implying that the two-component structure in integral-space appears to be robust to significant alterations (within the uncertainties) to the character of the input data, suggesting that the presence of this structure is a robust result, of which further analysis is justified.

4.6.4 Decomposition of Phase Space

The distribution of orbital weights in integral-space completely defines the number and type of orbits which reproduce the galaxy being modelled. If the distribution of weights shows a significant indication of substructure, even when regularisation is optimally applied, this suggests that the model may be composed of two or more stellar components which occupy separate phase-space regions. In principle, this may hold information concerning the origin and formation of the object, which may also be linked with other observable evidence of substructure in the galaxy, both dynamical and in the stellar populations.

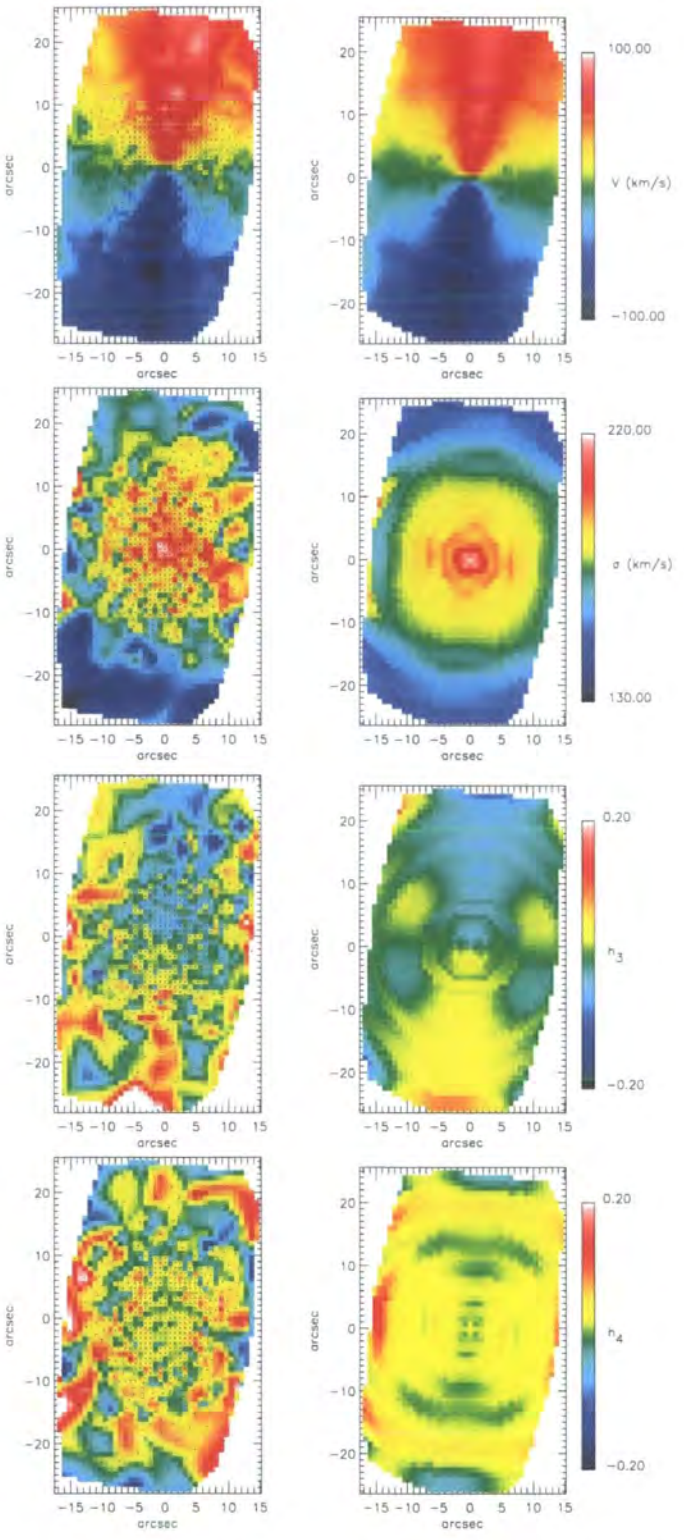

Figure 4.34: Comparison of the pipeline-reduced *SAURON* data of NGC 821 binned using the Voronoi Tesselation method (left panels), and the symmetric Fourier-expansion of this data using the first twelve terms of the expansion (right panels). The Fourier expansion is performed along circular annuli, and is consistent with the original data within the observational errors. The Fourier expansion is used for two reasons: 1) it allows the modelling code to use the Voronoi-binned data by resampling on a fine, regular grid of square apertures, and 2) reduces the spatial variations in the parametric maps caused by noise in the data. (Courtesy of Michele Cappellari)

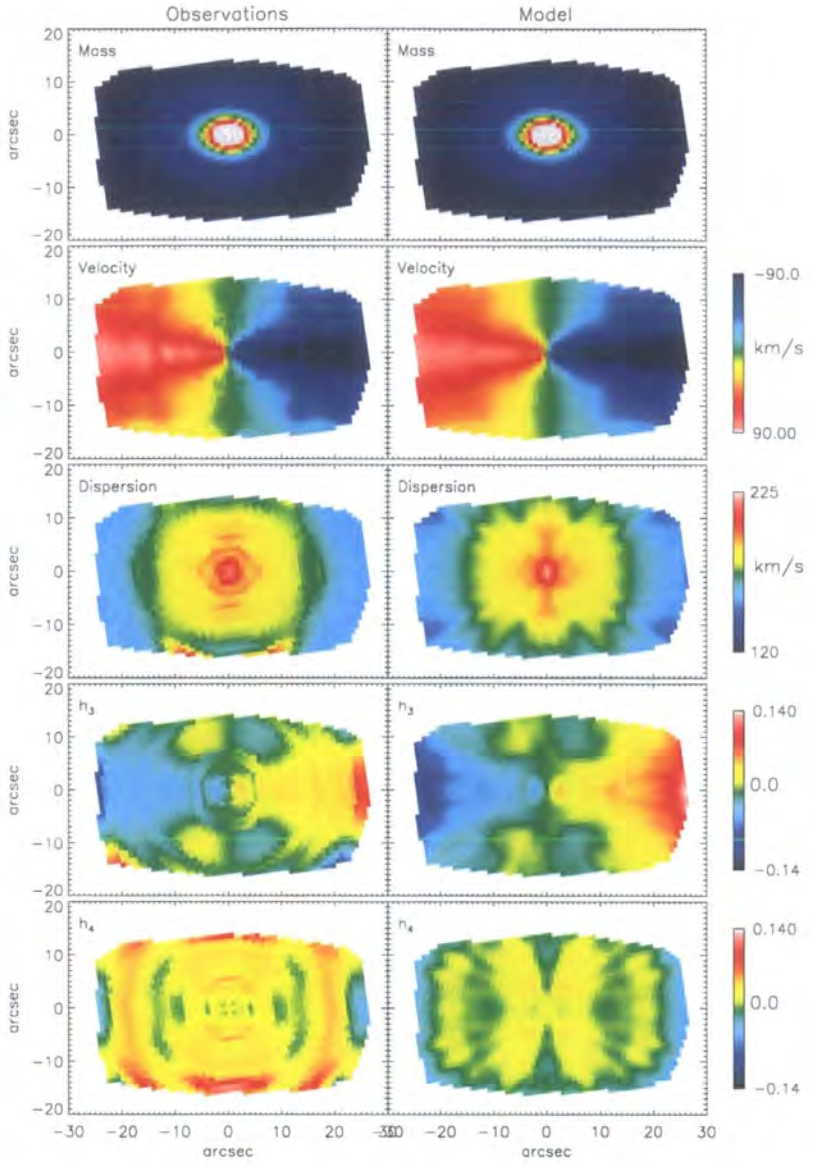

Figure 4.35: Comparison of Fourier-expanded *SAURON* data of NGC 821 (left panels) with the fitted Schwarzschild dynamical model (right panels). The model uses the same best-fit parameters for $M_\bullet$, M/L and i as derived from the original Quadtree-binned data (see §4.5). The fit to the input data is clearly very good.

For this reason, it is instructive to explore the possibility of 'decomposing' the integral-space distribution into the constituent components, in order to reconstruct the orbital distribution of these structures, and hopefully learn about the nature of the galaxy. There are conceivably a number of ways to do this; however, examples in the literature of separating distinct integral-space components are few. The main reason for this is that typical kinematic data used to constrain the model consists of long-slit data with generally major-, minor- and intermediate-axis position angles. Such data can constrain the general features of the model; however, with integral-field data such as that delivered by *SAURON*, it is possible to constrain very well the orbital distribution over the entire

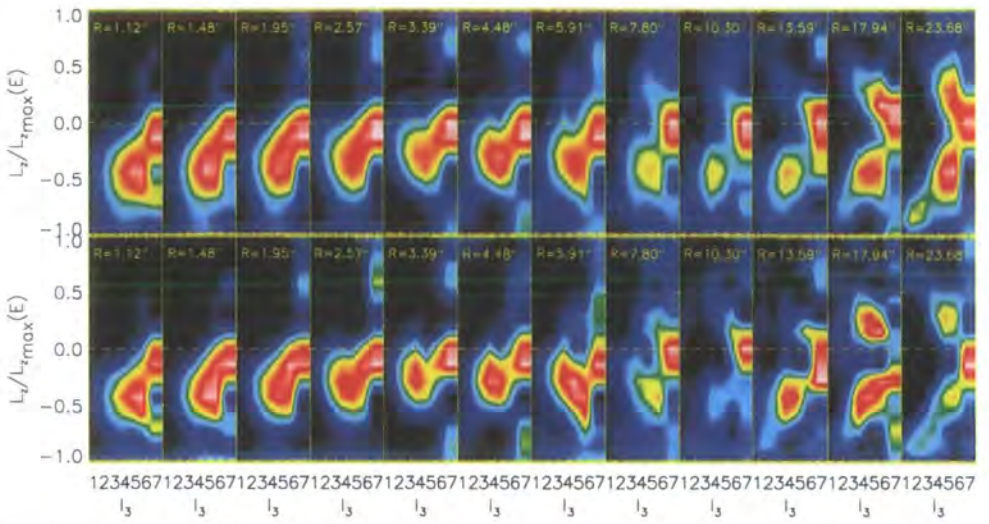

Figure 4.36: Comparison of the integral-space distribution for NGC 821 derived from the Quadtree-binned data (top row of panels) and from the Fourier-expanded data (bottom row of panels) shown in Figure 4.35. Both models have a regularisation parameter value of $\Delta = 4.0$, equivalent to Figure 4.32. Comparison of the two integral-space distributions shows very good agreement, implying that the two-component structure within the range of the *SAURON* data is insensitive to small variations in the input data. This suggests that this structure is a robust feature of the model, rather than an artefact of noise.

two-dimensional (2D) field of the data, and thus more reliably recover substructure in the galaxy.

Using multiple-position angle long-slit observations, Cappellari et al. (2002) provide the first quantitative analysis of a sub-component of phase-space, estimating the mass of the prototypical counter-rotating core housed in the centre of IC1459. This was possible for two reasons: 1) The kinematic data were of excellent quality, and at five different position angles, which sampled the central regions of the galaxy very well, and 2) The sub-component is very well separated in phase-space, given that it is rapidly counter-rotating with respect to the main body of the galaxy.

The case of NGC 821 is more subtle. There is clearly no evidence of a counter-rotating component, and the sub-structure in integral-space is most prominent at large radii, away from the core where strongly decoupled components are typically found. NGC 821 does, however, have strong disky isophote distortions, quantified by the C4 term of a Fourier expansion of the surface photometry. The galaxy is also very flattened, with relatively strong rotation about the symmetry axis. Thus, it is likely that any sub-structure in the phase-space distribution of the stellar orbits can be attributed to the disk-like properties of the galaxy.

To properly address the nature of the subcomponents of integral-space, it is first necessary to separate them in an objective way. This is, in principle, similar to deblending photometric images of extended galaxies, where the morphology and intensity distribution

of the objects in question are not known a priori. Prompted by this analogy, a similar approach to that adopted by Bertin & Arnouts (1996) for the widely-used 'SExtractor' software was applied to the integral-space distribution at different energies.

The implementation was greatly simplified by the assumption of an intrinsic two-component structure in phase-space, thus required only deciding what fraction of the orbital weights should be attributed to each component. This was done by a simple, but effective, statistical approach. Firstly, the two integral-space components are fitted non-linearly with two 2D Gaussian functions. The two Gaussians are optimised for their independent centre coordinates, normalisation, dispersion, axis-ratio, and position angle. This twelve-parameter fit was conducted using an adaptation of the robust Levenberg-Marquardt method implemented by Moré et al. (1980)[4]. This method varies smoothly between two different optimisation methods: the 'steepest descent' method, most suitable when the function is far from the optimal solution; and the 'inverse-Hessian' method, which converges rapidly when in the parabolic régime found close to the χ^2 minimum.

This 2D double-Gaussian fit is then used to form a probability distribution that a certain fraction of any given pixel belongs to one of the two Gaussian-fitted components. Thus, at any position, the fraction of the orbital weight assigned to either component is given by the relative contribution of the Gaussians at that point, which is effectively the probability for that pixel to belong to either of the two components. The important advantage of this approach over, for example, just using the 2D double-Gaussian fit, is that no assumption is made about the shape of the component in integral-space: something which is as yet not well understood. Also, the total mass of the model is conserved: essential to properly reproduce the galaxy in a consistent manner.

Figure 4.37 presents an example of the resulting separation of two components in phase space. The left-most panel shows the original data, overplotted with the contours of the two 2D Gaussians from the fitting process to show how the probabilities are distributed. The two middle panels show the two individual components, separated, and plotted with the same levels. Note how the overlapping region is recovered, as well as the deviations in shape from pure Gaussians. The right-most panel shows the sum of the two individual components, showing that the original mass is conserved.

Clearly, from Figure 4.32 it can be seen that the integral-space distribution is not always composed of two distinct components. Also, the model is only constrained by kinematics within the range of the *SAURON* field ($\lesssim 30''$). It is therefore not meaningful to separate regions which are clearly not composed of two distinct components. Likewise, it is not meaningful to analyse in detail regions of the model where no kinematic data exist, as this is the principle constraint on the orbital distribution. Therefore, the integral-space distribution is deblended within a range of energies which correspond to regions where a two-component analysis is justified, and where there also exists a reasonable number of

[4]The actual package used was an IDL porting of the MINPACK-1 code by Craig B. Markwardt that is available from http://cow.physics.wisc.edu/~craigm/idl

SAURON data points. This is taken to be the range from 1–25″. Figure 4.38 presents the total orbital weights for this volume of integral-space, along with the two assumed components, which have been separated using the above deblending technique. All weights outside the energy range shown are assigned to the primary component.

Having separated the components in integral-space, it is possible to apply the weights assigned to each component to the orbit library, thus evaluating the matrix equation (4.9) for a subset of the total weights. In this way, the observable projected properties (i.e., the mass distribution and kinematic parameters) of the two components can be reconstructed and examined separately. The predicted observables are generated by the modelling software as though the model were being 'observed' with the *SAURON* instrument. Thus the mass and kinematics are reproduced in each of the *SAURON* apertures used to constrain the original total model.

Figure 4.39 presents the original *SAURON* data, along with the total best-fitting model. Also shown are the two components reconstructed from the separated weights in integral-space. As expected, the reconstructed primary and secondary integral-space components form a spheroidal and flattened structure respectively. What is rather surprising is how distinct these two components are. The projected mass of the primary component appears very rounded, and the velocity field shows only a low-level indication of rotation. The velocity dispersion is also generally high. The secondary component, in contrast, is much more flattened, and has a strong rotation field. The velocity dispersion, although centrally peaked, is generally low, especially at larger radii ($\gtrsim 10''$).

This qualitative comparison is suggestive that the integral-space decomposition yields two distinct components, with similar properties to the classical 'disk and bulge' compo-

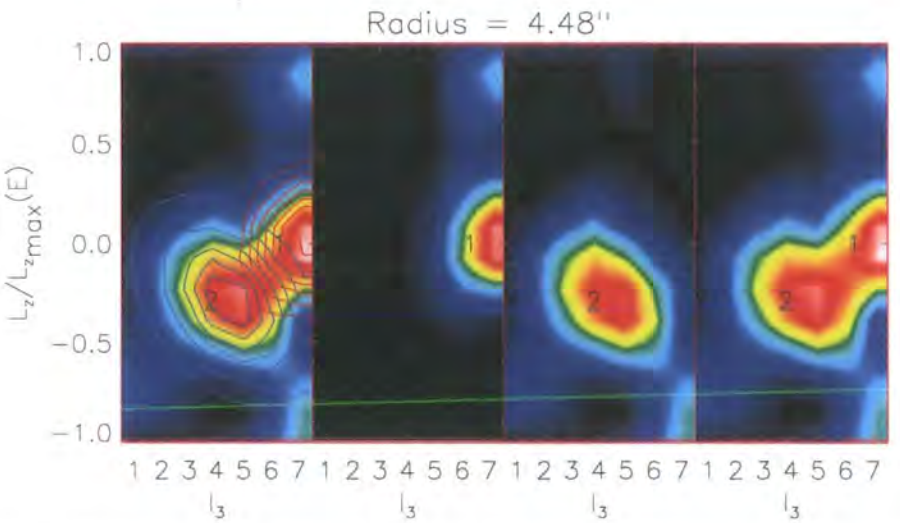

Figure 4.37: Demonstration of the deblending technique used to separate the integral-space components. From left to right: original integral-space distribution for an energy corresponding to a circular radius of 4.5″, overplotted with contours showing the probability distribution resulting from the 2D double-Gaussian fit; 'primary' component; 'secondary' component; sum of the primary and secondary components. All panels are plotted with the same intensity scale, in the sense that white indicates the maximum weight allocated at this energy, and black indicates zero weight.

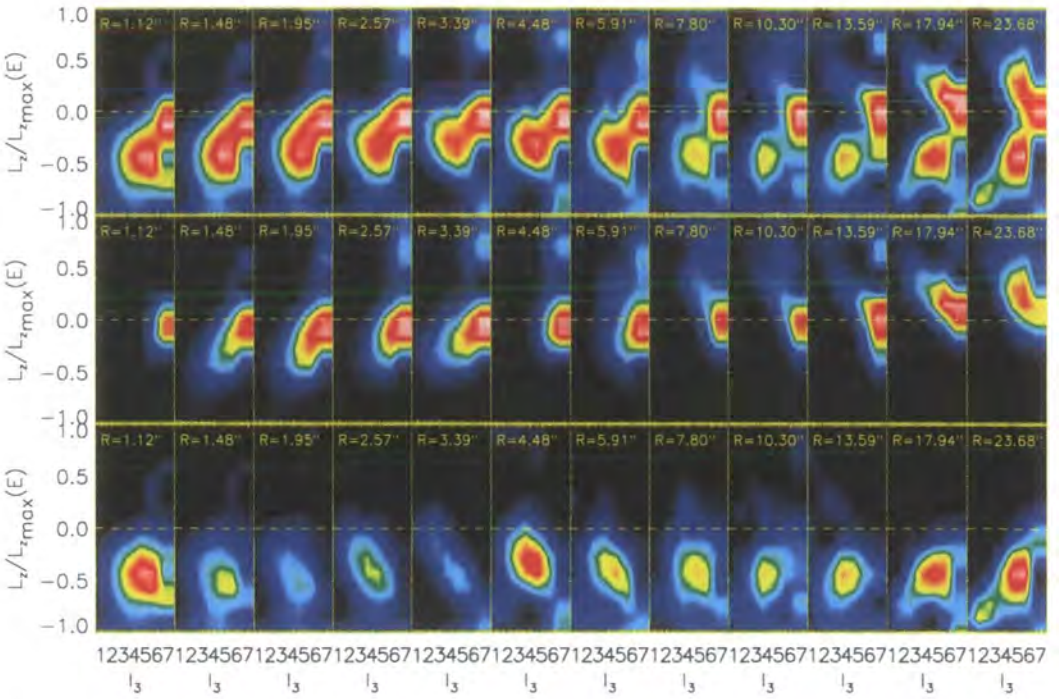

Figure 4.38: Resulting decomposition of the two-component structure found in integral-space within the range of the *SAURON* data. The circular radius increases from left to right as indicated on the plots. The top row presents the total integral-space distribution, and is a sub-set of the panels shown in Figure 4.32. The middle and bottom rows of panels show the separated components resulting from the deblending process described in the text. Outside the radii shown in this figure, either the data are not sufficient, or the two-component structure not strong enough to justify this decomposition.

nents. It is difficult to understand the limitations of this integral-space separation without having an analytic model to establish the sensitivity of the method. However, it seems apparent that there are two strong components in the phase-space of NGC 821, and that these correspond to a spherical component with generally low rotation and high velocity dispersion, and a secondary component, which accounts for the galaxy's integrated flattening and strong rotation. At this stage, it is difficult to determine whether these two components can be interpreted as being physically distinct, with different origins or formation mechanisms; or if they merely appear to occupy separate regions of integral-space due to the limitations of the data or model. By comparing this decomposition with other techniques, it should be possible to obtain a clearer understanding of what information the integral-space distribution actually contains.

4.6.5 Comparison With Other Decomposition Techniques

It is intuitive that the apparently strong sub-components resulting from the integral-space decomposition should be evident through standard photometric decomposition techniques. Indeed, NGC 821 is known to have rather strong disky isophote distortions (Scorza & Bender 1995), resulting in a C4 profile which peaks at around 16″ (e.g., see Figure 3.35). It is tempting, therefore, to associate this flattened component determined from integral-space directly with the disky isophotes.

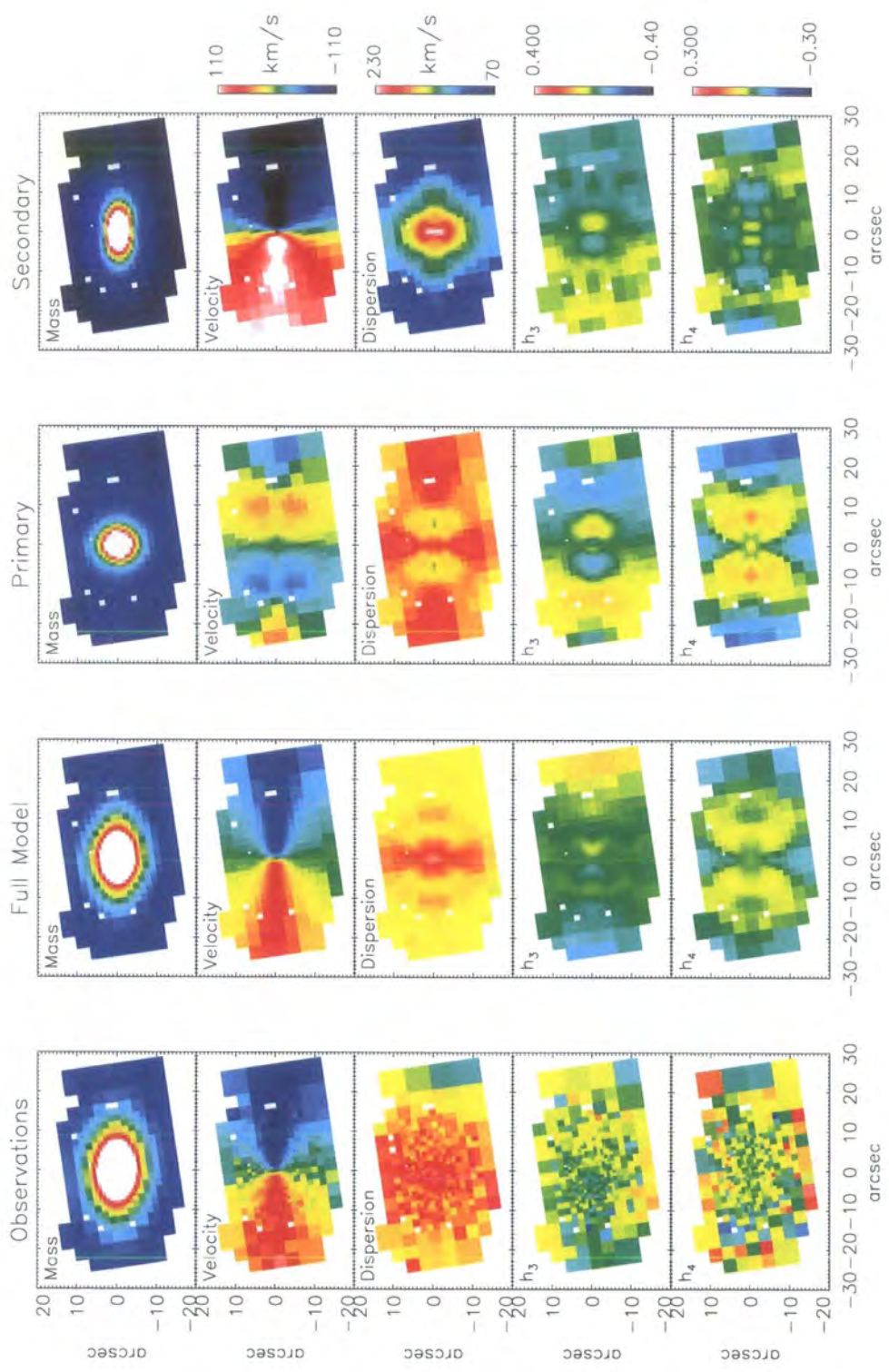

Figure 4.39: From left to right: input kinematic data and MGE model in *SAURON* apertures; the full best-fit model; the primary integral-space component; the secondary integral-space component. Note that the primary component also includes all the orbital weights assigned outside the radius constrained by *SAURON*. The primary component is clearly very rounded in comparison to the secondary. The secondary component is also strongly rotating, and has a much lower velocity dispersion compared to the primary component. The Gauss-Hermite coefficients are less obvious to interpret.

Disky isophote distortions are generally considered to result from thin disks which are close to edge-on. The inclination of NGC 821 is well constrained from the photometry alone, as the axis-ratio of the ellipse which can fit the isophote with the smallest radius of curvature places a lower limit on the inclination angle. The contribution from this highly-flattened component to the total flux can be determined, to first order, from the results of the MGE fit from Section 4.3. The fit, using 13 Gaussians, resulted in a single component with a flattening of 0.3, and all other Gaussians having a flattening of more than 0.57. It is clear that this highly-flattened component is responsible for the disky isophote distortions, visible even by eye on the HST and ground-based images. By isolating this distinct component, one can estimate its fractional contribution to the mass of the galaxy, which can be directly compared to the integral-space components already discussed.

Since disks are generally thought to have exponential light distributions, it is possible that, by using only a single Gaussian to represent the disk, the mass may be underestimated. Therefore, a second MGE fit was made, this time using 19 Gaussian components in order to trace the most flattened galaxy component with more than one Gaussian, and obtain a reasonable estimate of this components relative mass contribution. Table 4.8 presents the parameters of the Gaussians fitted to the combined HST and CTIO imaging as before (c.f. Table 4.6). Inspection of this table highlights three Gaussians for which the flattening is much lower than the other components. Figure 4.40(a) illustrates this component by subtracting off all the other, rounder Gaussian components to reveal this very flattened disky component. Figure 4.40(b) presents the HST field, with contours showing the galaxy light, the light from the rounder components, and the effect of the three most flattened Gaussians on the diskiness of the isophotes.

Figure 4.41 illustrates the effect of the flattened component on the photometric profile of the galaxy. The blue and red symbols indicate the ellipticity ϵ and C4 parameters before and after subtracting the flattened component respectively. The total mass fraction of this flattened three-Gaussian component is only 2%, yet it alone is able to account for the strong diskiness observed. The ellipticity is not significantly lower after the disk is removed, indicating that the galaxy is still significantly flattened even in the absence of this disky component. This is consistent with the decomposition of phase-space, where it is found that the observed flattening is due to a component consisting of 15% of the total mass: significantly more than can be attributed to the disky isophotes alone. Indeed, recovering features at the level of 2% from integral-space may be beyond what is possible, even with the exceptional constraint placed on the orbital structure with integral-field spectroscopy.

Total Counts (counts)	Dispersion (pix)	Flattening
7177.36	0.495147	0.800000
9741.97	1.16697	0.641270
69750.6	2.55020	0.800000
17882.5	5.26705	0.253837*
158460.	6.08572	0.661476
348596.	12.2162	0.680969
45186.6	18.6813	0.241611*
638670.	24.7685	0.579650
737623.	34.6102	0.770073
915430.	53.7701	0.534223
1.91274e+006	85.6618	0.612492
2.82197e+006	133.602	0.698794
1.35141e+006	190.456	0.800000
523637.	274.697	0.181235*
6.36630e+006	345.104	0.553177
8.50899e+006	625.772	0.680712
3.60472e+006	890.819	0.633462
1.13050e+007	1569.94	0.800000
1.89814e+007	4448.91	0.800000

Table 4.8: Parameters of the 19 Gaussians used to describe the surface photometry of NGC 821. Note the occurrence of three components (marked *) which are much more flattened than the other components. In total, these three Gaussians contribute only $\sim 2\%$ of the total galaxy mass.

4.7 Conclusions

This chapter presents the detailed dynamical modelling of the disky elliptical galaxy NGC 821 using a three-integral, axisymmetric application of Schwarzschild's orbit superposition technique. This study concentrates on the use of kinematic data, obtained by integral-field spectroscopy using the *SAURON* instrument, to constrain the model. The comparatively vast number of individual constraints this data format provides over conventional long-slit based studies reduces the uncertainties on the model parameters and orbital distribution, as well as allowing a more detailed analysis of the resulting dynamical model. Here the main findings of this investigation are summarised.

4.7.1 Determining the Best-Fit Model

Before analysing a particular dynamical model, it is necessary to optimise the three input parameters which must be assumed for each model; specifically the inclination i, the mass-to-light ratio Υ, and the central dark mass $M_\bullet$. The first of these, the inclination, is already rather strongly constrained by the photometry alone. NGC 821 exhibits strongly disky isophotes, requiring that a thin, disk-like component exists in the galaxy and is close to edge-on. From the Multi-Gaussian Expansion (MGE) fitting process, it is possible to

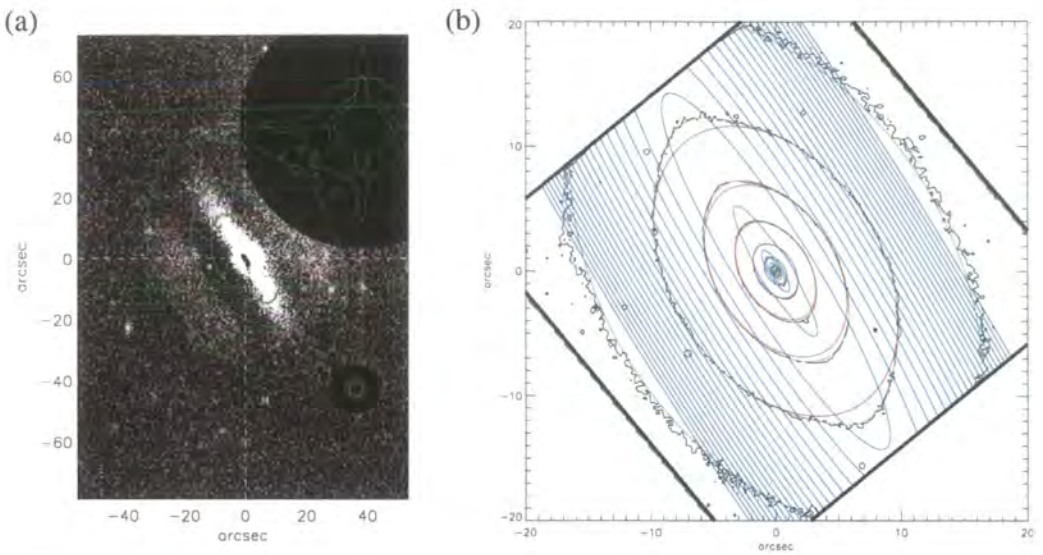

Figure 4.40: (a) Residual CTIO image of NGC 821 after subtraction of the MGE components with axis-ratio larger than 0.57, showing the intensity of the underlying highly-flattened component. Overplotted in green are the contours of the original image, including the bright stars which were masked for the MGE fit. (b) Contour plot of the HST PC1 image (black contours) overplotted with the MGE components with axis-ratio larger than 0.57 (red contours) and the residual flattened component (blue contours). This shows how the flattened component, which contributes not more than 2% of the total light, accounts for the diskiness of the isophotes. The 2% component does not account for all the flattening of the galaxy, which remains to be around 0.6.

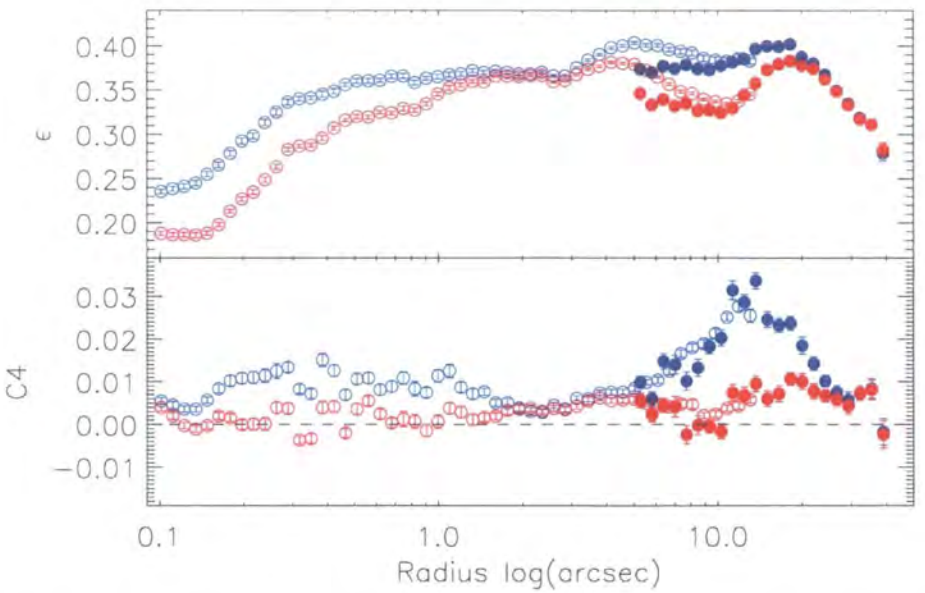

Figure 4.41: Illustration of the ellipticity ϵ and C4 photometric parameters before (blue symbols) and after (red symbols) subtraction of the three flattest Gaussians from the MGE fit. Both ground-based (CTIO, filled symbols) and space-based (HST PC1 chip, open symbols) data are shown. The data used are the same as for the original MGE fit in Section 4.3. The parameters were derived using the IRAF package, **GALPHOT** (Franx et al. 1989*b*).

put a lower limit on the inclination angle (90° implies edge-on) from the axis-ratio $q_{\rm max}$ of the flattest Gaussian component. From the MGE model fitted to the ground- and space-based photometry, it was found that $q_{\rm max} = 0.3$, implying an inclination of greater than $\sim 73°$. The inclination is therefore already well-constrained, and for this reason, was not explored with the dynamical models, as this would not yield a significantly improved constraint on the inclination.

A full exploration of the (Υ,$M_\bullet$) parameter space was conducted, and the best-fitting model, determined as having the lowest χ^2 value when fitted to the data, gave $M/L = 4.12 \pm 0.06$ in I-band solar units, and $M_\bullet = (3.41 \pm 0.68) \times 10^7 M_\odot$. NGC 821 was also in the sample of G02, whom modelled the galaxy using the same principles (i.e., using an axisymmetric, three-integral Schwarzschild method), but a completely independent code. The photometric data used by these authors for NGC 821 was based on the HST F555W (V-band) filter, and so their determination of Υ is correspondingly higher ($\Upsilon = 7.6V$-band solar units) as one expects for an early-type galaxy with a relatively old stellar population. A notable difference between the two determinations of Υ is the respective uncertainties. The G02 study, based on major- and minor-axis long-slit kinematic data, finds a 1-σ uncertainty in Υ of around ± 0.35. The present study, using *SAURON* integral-field data, finds an uncertainty almost one order of magnitude smaller at the same confidence level. This is significant, and is clearly due to the panoramic nature of the integral-field data.

G02 find a black hole mass of $M_\bullet = (3.7^{+2.4}_{-0.8}) \times 10^7 M_\odot$, which is very close to the value determined in this work, and the two values are consistent within the 1-σ uncertainties. Both studies use the exact same HST-STIS central kinematic data, with all other input data being completely independent. The modelling codes used are based on the same techniques, but were developed completely independently, and use different numerical methods, and make different assumptions. This remarkably consistent result is a strong test of the axisymmetric, three-integral Schwarzschild modelling technique, as well as the codes currently being used by the different groups. At a time when other competing groups seem overly concerned by fitting empirical relation's using the results from various published models (e.g., Merritt & Ferrarese 2001, Tremaine et al. 2002), it is reassuring that two dynamical modelling groups obtain consistent results given the same data.

4.7.2 Global Properties of the Best Fit Model

Once the free parameters have been optimised, it is possible to investigate in detail the best-fitting model in order to learn about the dynamical structure of the galaxy. A principle property of a galaxy is the mechanism which supports its shape; i.e., is the galaxy flattened by rotation, or by random motions? The relative importance of these two mechanisms can be estimated by investigating the ratio of the intrinsic rotation velocity and velocity dispersion: v/σ. From the Schwarzschild model it is possible to infer the

intrinsic v/σ from the moments of the velocity distributions derived in each direction of motion. From the resulting map of v/σ, it was found that the ratio has a peak value which extends along the major-axis, with a steep gradient across the minor-axis. When compared to the same map of M32 (thought to resemble a simple oblate, isotropic rotator) from the model of Verolme et al. (2002), the contours of constant ratio for NGC 821 form a comparatively small 'opening' angle, suggesting the presence of a cold, rotationally supported component, such as a disk. The presence of such a component in NGC 821 is already known from other studies (e.g., Scorza & Bender 1995); however, it is reassuring that this feature is also reproduced by the model.

4.7.3 Integral-Space Distribution

A natural result of the orbit superposition technique is the distribution of weights assigned to each orbit in the orbit library. The orbits are defined by their position in the three-dimensional space which describes an orbit's integrals of motion. The allocation of weights in this 'integral-space' describes the Distribution Function for the galaxy, and consequently allows the galaxy's dynamical structure to be completely defined.

Within the range of the *SAURON* kinematic constraints, the integral-space distribution of NGC 821 shows a distinct two-component structure. The typical trajectory of the orbits associated with these two components suggests that they are characterised by a primary spheroidal component with little rotation, combined with a more flattened secondary component with a higher degree of rotation. Given the known disky isophotes of this galaxy, it is intuitive to suspect that this secondary component is associated directly with this. To determine the nature of the two components, the integral-space distribution was decomposed into two representative components over the range where the *SAURON* data has good coverage, and where the two-component structure is clear. Since the Distribution Function of each component is then known, it is possible to reconstruct the two components, and measure their physical properties (i.e., mass distribution and kinematics).

As expected, the primary component takes the form of a near-spherical component, with little rotation and generally high velocity dispersion. This would be analogous to a pressure-supported bulge component. The secondary component accounts for the general observed ellipticity of NGC 821, forming a flattened component with strong rotation, and generally low velocity dispersion. The secondary component contributes around 15% of the total mass of the system. However, from analysis of the photometry using an MGE model, it is found that the disky isophotes are due to a highly flattened (axis ratio $\sim 0.1 - 0.2$) component which contributes as little as 2% of the total mass. After subtraction of this disky component, the ellipticity of the galaxy is not significantly changed. Therefore, the secondary component in integral-space cannot be exclusively associated with the component which gives rise to the disky isophotes. Rather, the sec-

ondary integral-space component seems to be a result of the flattened, strongly-rotating nature of this galaxy, of which disky isophotes may be a consequence, given the favourable inclination of the system.

The ubiquity of such secondary integral-space components in flattened, rotating galaxies will be addressed by similar three-integral Schwarzschild modelling of the galaxies consistent with axisymmetry from the full *SAURON* survey. Preliminary results for two other flattened, rotating galaxies in the sample, NGC 2974 (Krajnovic, D. et al. 2003, in prep.) and NGC 4473 (van den Bosch, R. et al. 2003, in prep.), also show a secondary integral-space component similar to that found for NGC 821. This suggests that the detailed analysis of integral-space, which becomes feasible using the unprecedented number of constraints supplied by integral-field data, may yield fundamental information on the dynamical structure of these objects.

Chapter 5 | *Conclusions*

The aim of this thesis has been to investigate the nature and origin of disky elliptical galaxies, with emphasis on understanding the origin of the disk component in these objects. This aim has been tackled in two distinct, but complementary approaches: firstly, investigating whether the disk component is composed of stars which have an origin distinct from that of the rest of the galaxy; and by detailed dynamical modelling, which recovers the dynamical properties of the disk based on the orbital distribution. The conclusions drawn from these two approaches are discussed separately below, followed by a discussion of general conclusions pertaining to both. This chapter concludes with an outline of future work, both proposed and currently underway.

5.1 Young Disks in Elliptical Galaxies

Using simple stellar population (SSP) model spectra, it was found that comparing kinematics derived from the Calcium II triplet and Hβ absorption lines can reveal the presence of a young stellar population in the form of a rotationally-supported disk embedded in an old, pressure-supported spheroid population. There are three different indicators of the young disk component, which depend on the fraction of the total system mass contributed by the disk:

- For disks which are close in age to the spheroid population, and which implicitly contribute the greatest possible mass fraction (typically more than 10%), the young disk is detectable by examining the LOSVD shapes. The disk component gives a significant contribution to the LOSVD, which is then either strongly double-peaked, or is dominated by the low-dispersion disk, especially for the Hβ kinematics.

- For disks of 'intermediate' age (typically around 25-50% of the total system age) and mass (between 2-10% of the total mass), the young disk is most apparent in the derived LOSVD parameters. Specifically, there is a measurable offset in the rotation velocities determined from the two wavelength regions, such that Hβ gives a higher rotation velocity than the Calcium II triplet. These offsets are coupled with other differences in the higher-order moments of the two LOSVDs, but the mean rotation velocity is generally easier to recover from the data, and so is a more useful initial indicator.

- For disks which are very young (less than 25% of the system age) and are very low mass (less than around 2% of the total mass), the signature of the disk is only visible as small offsets in the higher-order moments of the LOSVD, parameterised by the Gauss-Hermite coefficients h_3 and h_4. These small offsets are difficult to detect, which makes the presence of such a very young, very low mass disk difficult to establish.

These indicators were established under the assumptions of a cold, rotationally supported disk, and with both components composed of solar-metallicity stellar populations. The results were very similar when different metallicities were used for the disk and bulge component: specifically for the 'worst case scenario' of a metal-poor old spheroidal population combined with a metal-rich young disk. Increasing the pressure-support of the disk, however, (i.e., using a disk with an appreciable velocity dispersion) reduced the prominence of the young disk by a factor of ~ 2. Therefore dynamically hot young disks are significantly more difficult to detect than dynamically cold ones.

The strength of the separation of the young and old components depends on the total luminosity-weighted age of the system, which is indicated by the strength of the Hβ absorption. By creating disk+spheroid models with varying input parameters, such as disk mass fraction, disk age, and the total Hβ absorption strength of the model, it is possible to make predictions about how easily a young disk can be detected, and what its possible physical properties are. These predictions can be used to help interpret observational results.

From a small observed sample of four disky elliptical galaxies with enhanced Hβ absorption, two galaxies show measurable offsets in their major-axis rotation velocity profiles. Comparing these with the model predictions, it is found that the observational results are not consistent with the picture of a simple old spheroid combined with a young, dynamically cold disk created by a single burst of star formation. The disk component seems equally apparent from both the Hβ and Calcium II triplet kinematics, which is consistent with a formation scenario in which the disk is built up over time, and thus contains a significant portion of old and young stars with similar dynamical properties.

5.2 Dynamical Modelling of NGC821

NGC 821 is a disky elliptical galaxy taken from the *SAURON* survey of nearby early type galaxies, and is also included in the small long-slit sample of disky ellipticals. It has strong evidence for containing an embedded stellar disk, both from the photometry (disky isophote distortions) and from the kinematics (strong rotation gradient and h_3 values). By constructing a general dynamical model of this object constrained by integral-field spectroscopy, as well as ground- and space-based imaging, it is possible to investigate the dynamical structure of this galaxy.

NGC 821 is also included in the modelling sample of Gebhardt et al. (2002), in a study of black hole mass determinations via stellar dynamical modelling of HST STIS kinematics, which uses independently developed modelling software. Using the same STIS kinematic data, and combining this with the large number of *SAURON* apertures, excellent agreement is found between the black hole masses determined in this thesis ($(3.4 \pm 0.7) \times 10^7 M_\odot$) and Gebhardt et al. (2002) ($(3.7 \pm 1.4) \times 10^7 M_\odot$). Such agreement between independent software is a strong test of the general assumptions of the axisymmetric modelling technique.

Detailed analysis of the velocity ellipsoid of the best-fitting dynamical modelling shows evidence for a flattened, rotationally supported component which lies along the major-axis of NGC 821. This is interpreted as being due to the presence of the disk component.

The distribution of orbits in integral-space also shows an interesting two-component structure. By separating these two components in phase space, and reconstructing the projected observable quantities, these two components are found to relate to a spheroidal 'primary' component, which shows little rotation, and generally high dispersion; and a flattened 'secondary' component which rotates rapidly about the minor axis, having relatively low velocity dispersion. The secondary component accounts for 15% of the total mass, which is far in excess of the 2% required to reproduce the disky isophote distortions.

5.3 General Discussion and Conclusions

The underlying theme of this thesis is to make connections between the photometric properties, dynamical components and stellar populations of disky elliptical galaxies, with methods which can be applied to early type galaxies in general. By comparing the Calcium II triplet and Hβ kinematics derived from stellar population models, using the same techniques which are applied to observations, it was found that these different spectral features can reveal, preferentially, kinematic information about the old and young stellar populations respectively. This has potential to be a powerful tool, especially for galaxies which have more distinct dynamical and stellar population components.

In this respect, disky ellipticals represent something of a challenge. The disks which are embedded in these systems are not generally well separated from their host galaxy. Indeed, they are only apparent through deviations from perfect elliptical isophotes at the level of 1%. The Hβ enhancement found in disky ellipticals by de Jong & Davies (1997), and corroborated as a lower luminosity-weighted age by Trager (1997), is only a subtle effect, with many galaxies only showing moderately young total ages, making the disks either close in age to the rest of the galaxy, or with very low mass, both of which are difficult to detect.

No strong cases of a young disk embedded in an old spheroid were found in the observed sample. However, through use of the SSP modelling results, it is possible to put constraints on what cannot be present, as well as what could be present, but is below the sensitivity of the method. By applying the model predictions, no cases are found to be consistent with the model assumptions. This is not greatly surprising, as the formation of disk structures is generally the result of dissipational processes. For this to occur in galaxies, there has to be an appreciable amount of gaseous material available, which cannot be used in star formation too quickly. Therefore the assumption of a disk formed as a single star-burst is not realistic.

From the dynamical modelling of NGC 821 using *SAURON* integral-field data, two distinct components were found in the phase-space distribution of the stellar orbits. The model includes fitting to photometric constraints as well as the 2D kinematics, thus includes both forms of evidence for the disk component. The two components appear to conform to the qualitative properties of a rotating disk and a non-rotating spheroidal component. Their separation in phase-space also suggests that these components have physically distinct origins. Extracting information about the disk and spheroidal components directly from the galaxy phase-space, rather than through some parametric decomposition, provides a more physically motivated technique for quantifying the structural components of a galaxy. However, more rigorous tests are required involving analytic test models to fully understand how the recovered Distribution Function relates to the intrinsic galaxy properties.

The findings of this thesis seem to indicate that disky ellipticals are consistent with having formed through merging processes, since the component responsible for the flattened appearance of these objects appears as distinct in phase-space. From the long-slit study, the signature of the disk in these galaxies is equally apparent in the Calcium II triplet and Hβ absorption features, which cannot be explained by a purely young disk unless the mass fraction of the disk is either low ($< 2\%$) or high ($> 10\%$). The secondary component in the phase space of NGC 821 contributes around 10-15% of the total mass, suggesting that, if this component is associated with the disk, the disk has a luminosity weighted age only a little less than the rest of the galaxy, implying that the disk formed early in the galaxy's evolutionary history.

5.4 Future Work

5.4.1 The *SAURON* Survey and Other IFU Studies

The *SAURON* observations of a representative sample of galaxies have now been completed. The analysis of this rich data set is well underway, and initial findings are that early type galaxies exhibit a diverse array of characteristics, which will be quantified with unprecedented accuracy using this integral-field data. This will address issues such as the

demography of kinematically decoupled components; the distribution of age and metallicity within galaxies; characteristic differences, if any, between isolated galaxies and those in cluster environments; evolution of dynamical structure with morphology; and linking the distribution of stellar populations in galaxies with their dynamical structure.

From the full *SAURON* sample of galaxies, there are a subset of around twenty objects which appear consistent with the assumption of axisymmetry. As in the case of NGC 821, these objects will be modelled using the three-integral Schwarzschild method, yielding detailed dynamical information for a large sample of objects based on integral-field data. Initial findings suggest that the phase-space structure found in NGC 821 may also be present in a number of other flattened galaxies. A full exploration of this will determine whether this is physically significant, and establish the range of dynamical structure in this large, and homogeneously observed sample. This work will also incorporate rigorous comparison with other modelling groups to ensure the security of the method and findings.

There are now several IFU instruments currently available on 8 m class telescopes: VIMOS at the VLT, GMOS on Gemini North, CIRPASS on Gemini South; and several more coming online in the near future: GNIRS on Gemini South, SINFONI+SPIFFI at the VLT. Such instruments will allow integral-field observations of fainter and more distant galaxies which will have similar quality to those obtained by *SAURON* for nearby objects. A recently proposed survey using the VIMOS IFU to probe more distant galaxies in contrasting environments will compliment and extend upon the findings from the *SAURON* data set. These combined surveys will provide a complete picture of early type galaxies in the local universe, and will act as a benchmark for future studies in this field.

5.4.2 Modelling Dynamics and Stellar Populations

The fact that this thesis finds no clear signatures of young disks in ellipticals reflects two aspects of this work: 1) the difficulty of separating the stellar populations and kinematics of components in early type galaxies, and 2) the limitations of our technique. The first of these is, of course, implicit in the nature of the problem. The second, however, can be improved upon. This thesis makes use of a standard algorithm, FCQ, developed as a general purpose tool for determining stellar kinematics. By focusing on a particular absorption feature (in this case, the Calcium II triplet and Hβ lines), the derived kinematics were sensitive to different putative stellar populations. However, this does not make efficient use of the information held in the integrated spectrum of a galaxy. All the absorption features in the spectrum generally tell us something about the stellar populations we are observing, with varying degrees of sensitivity to different populations. Even the shape of the continuum holds useful information, which is effectively removed by using the FCQ technique.

Likewise for the Schwarzschild dynamical modelling, the representative orbits of the

stars are determined, and detailed kinematic structure is recovered, but there is no consideration of the stellar populations involved. The distribution of age and metallicity within a galaxy, combined with a detailed picture of the dynamical structure, provides powerful constraints on the possible formation mechanisms and evolutionary path of the object.

A more satisfactory, and potentially more powerful, approach would be to combine the techniques of dynamical modelling and stellar population synthesis. This thesis takes an initial step towards this by directly inferring information on stellar populations through derived kinematics. The next stage in amalgamating these two key aspects of galaxy studies is to incorporate information concerning the stellar populations into the orbit-based dynamical modelling machinery which currently exists. By utilising SSP model spectra, such as those used in Chapter 2, it is possible to associate a given orbit with several possible stellar populations. Rather than determining the orbital distribution based on a handful of derived parameters, the distribution of orbits, based on their kinematics *and* population characteristics, will be determined by using the observed *spectrum* as the constraint.

This work poses many potential hurdles: computational constraints, limitations in the stellar population models, as well as the intrinsic degeneracies inherent in untangling composite stellar populations and kinematics. However, advances in computing power, extensive new stellar libraries becoming available, and the high-quality, two-dimensional observational data sets delivered by instruments such as *SAURON*, put this important goal within reach.

Bibliography

Arimoto, N. (1996), Stellar Population Synthesis Models for Elliptical Galaxies, *in* 'ASP Conf. Ser. 98: From Stars to Galaxies: the Impact of Stellar Physics on Galaxy Evolution', p. 287.

Bacon, R., Adam, G., Baranne, A., Courtes, G., Dubet, D., Dubois, J. P., Emsellem, E., Ferruit, P., Georgelin, Y., Monnet, G., Pecontal, E., Rousset, A. & Say, F. (1995), '3D spectrography at high spatial resolution. I. Concept and realization of the integral field spectrograph TIGER.', A&AS **113**, 347.

Bacon, R., Copin, Y., Monnet, G., Miller, B. W., Allington-Smith, J. R., Bureau, M., Carollo, C. M., Davies, R. L., Emsellem, E., Kuntschner, H., Peletier, R. F., Verolme, E. K. & de Zeeuw, P. T. (2001), 'The SAURON project - I. The panoramic integral-field spectrograph', MNRAS **326**, 23–35.

Bacon, R., Emsellem, E., Copin, Y. & Monnet, G. (2000), Supermassive Black Hole Searches with 3-D Spectroscopy, *in* 'ASP Conf. Ser. 195: Imaging the Universe in Three Dimensions', p. 173.

Barnes, J. E. (2002), 'Formation of gas discs in merging galaxies', MNRAS **333**, 481–494.

Bekki, K. & Shioya, Y. (1997), 'Formation of Boxy and Disky Elliptical Galaxies in Early Dissipative Mergers', ApJ **478**, L17.

Bender, R. (1988), 'Velocity anisotropies and isophote shapes in elliptical galaxies', A&A **193**, L7–L10.

Bender, R. (1990), 'Unraveling the kinematics of early-type galaxies - Presentation of a new method and its application to NGC4621', A&A **229**, 441–451.

Bender, R. & Surma, P. (1992), 'Mg2 line-strength profiles of elliptical galaxies with kinematically decoupled cores', A&A **258**, 250–254.

Bender, R., Burstein, D. & Faber, S. M. (1993), 'Dynamically hot galaxies. II - Global stellar populations', ApJ **411**, 153–169.

Bender, R., Doebereiner, S. & Moellenhoff, C. (1988), 'Isophote shapes of elliptical galaxies. I - The data', A&AS **74**, 385–426.

Bender, R., Surma, P., Doebereiner, S., Moellenhoff, C. & Madejsky, R. (1989*a*), 'Isophote shapes of elliptical galaxies. II - Correlations with global optical, radio and X-ray properties', A&A **217**, 35–43.

Bender, R., Surma, P., Doebereiner, S., Moellenhoff, C. & Madejsky, R. (1989*b*), 'Isophote shapes of elliptical galaxies. II - Correlations with global optical, radio and X-ray properties', A&A **217**, 35–43.

Bendinelli, O. (1991), 'Abel integral equation inversion and deconvolution by multi-Gaussian approximation', ApJ **366**, 599–604.

Bendo, G. J. & Barnes, J. E. (2000), 'The line-of-sight velocity distributions of simulated merger remnants', MNRAS **316**, 315–325.

Bertin, E. & Arnouts, S. (1996), 'SExtractor: Software for source extraction.', A&AS **117**, 393–404.

Bertola, F. & Capaccioli, M. (1975), 'Dynamics of early type galaxies. I - The rotation curve of the elliptical galaxy NGC 4697', ApJ **200**, 439–445.

Binette, L., Magris, C. G., Stasinska, G. & Bruzual, A. G. (1994), 'Photoionization in elliptical galaxies by old stars', A&A **292**, 13–19.

Binney, J. (1976), 'Is the flattening of elliptical galaxies necessarily due to rotation', MNRAS **177**, 19–29.

Binney, J. (1978), 'On the rotation of elliptical galaxies', MNRAS **183**, 501–514.

Binney, J. & Merrifield, M. (1998), *Galactic astronomy*, Galactic astronomy / James Binney and Michael Merrifield. Princeton, NJ : Princeton University Press, 1998. (Princeton series in astrophysics) QB857 .B522 1998 ($35.00).

Binney, J. & Tremaine, S. (1987), *Galactic dynamics*, Princeton, NJ, Princeton University Press, 1987, 747 p.

Bower, G. A., Green, R. F., Bender, R., Gebhardt, K., Lauer, T. R., Magorrian, J., Richstone, D. O., Danks, A., Gull, T., Hutchings, J., Joseph, C., Kaiser, M. E., Weistrop, D., Woodgate, B., Nelson, C. & Malumuth, E. M. (2001), 'Evidence of a Supermassive Black Hole in the Galaxy NGC 1023 from the Nuclear Stellar Dynamics', ApJ **550**, 75–86.

Bower, R. G., Kodama, T. & Terlevich, A. (1998), 'The colour-magnitude relation as a constraint on the formation of rich cluster galaxies', MNRAS **299**, 1193–1208.

Bower, R. G., Lucey, J. R. & Ellis, R. S. (1992), 'Precision Photometry of Early Type Galaxies in the Coma and Virgo Clusters - a Test of the Universality of the Colour / Magnitude Relation - Part Two - Analysis', MNRAS **254**, 601.

Bowers, R. L. & Deeming, T. (1984), *Astrophysics. Volume 2 - Interstellar matter and galaxies*, Research supported by the University of Texas, Los Alamos National Laboratory, and Digicon Geophysical Corp. Boston, MA, Jones and Bartlett Publishers, Inc., 1984, 283 p.

Brown, B. A. & Bregman, J. N. (1998), 'X-Ray Emission from Early-Type Galaxies: A Complete Sample Observed by ROSAT', ApJ **495**, L75.

Brown, R. J. N., Forbes, D. A., Kissler-Patig, M. & Brodie, J. P. (2000), 'Imaging of the protoelliptical NGC 1700 and its globular cluster system', MNRAS **317**, 406–420.

Burstein, D., Faber, S. M. & Gonzalez, J. J. (1986), 'Old stellar populations. III - The metallicities of M5, M71, and M67', AJ **91**, 1130–1139.

Burstein, D., Faber, S. M., Gaskell, C. M. & Krumm, N. (1984), 'Old stellar populations. I - A spectroscopic comparison of galactic globular clusters, M31 globular clusters, and elliptical galaxies', ApJ **287**, 586–609.

Buson, L. M., Sadler, E. M., Zeilinger, W. W., Bertin, G., Bertola, F., Danzinger, J., Dejonghe, H., Saglia, R. P. & de Zeeuw, P. T. (1993), 'The distribution of ionized gas in early-type galaxies', A&A **280**, 409–425.

Butcher, H. & Oemler, A. (1978), 'The evolution of galaxies in clusters. I - ISIT photometry of C1 0024+1654 and 3C 295', ApJ **219**, 18–30.

Butcher, H. & Oemler, A. (1984), 'The evolution of galaxies in clusters. V - A study of populations since Z approximately equal to 0.5', ApJ **285**, 426–438.

Cannon, A. J. & Pickering, E. C. (1918), 'Corrected version available on magnetic tape and microfiche at CDS Strasbourg Henry Draper Catalogue .', *Annals of Harvard College Observatory.*

Caon, N., Macchetto, D. & Pastoriza, M. (2000), 'A Survey of the Interstellar Medium in Early-Type Galaxies. III. Stellar and Gas Kinematics', ApJS **127**, 39–58.

Cappellari, M. (2002), 'Efficient multi-Gaussian expansion of galaxies', MNRAS **333**, 400–410.

Cappellari, M. & Copin, Y. (2001), Adaptive 2D-Binning, *in* 'Galaxies: the Third Dimension, proceedings of a conference held in Cozumel, Mexico, 3-7 December 2001. Organized by the Instituto de Astronomía, UNAM. Edited by Margarita Rosado, Luc Binette, and Lorena Arias. To be published in ASP Conf. Series'.

Cappellari, M., Verolme, E. K., van der Marel, R. P., Verdoes Kleijn, G. A., Illingworth, G. D., Franx, M., Carollo, C. M. & de Zeeuw, P. T. (2002), 'The Counterrotating Core and the Black Hole Mass of IC 1459', ApJ.

Cardiel, N. (1999), *Ph.D. Thesis.*

Carollo, C. M., Franx, M., Illingworth, G. D. & Forbes, D. A. (1997), 'Ellipticals with Kinematically Distinct Cores: V-I Color Images with WFPC2', ApJ **481**, 710.

Carrasco, L., Buzzoni, A., Salsa, M. & Recillas-Cruz, E. (1995), Probing Turn Off Location of Stellar Populations in Early-type Galaxies: H-Beta Radial Gradients, *in* 'ASP Conf. Ser. 86: Fresh Views of Elliptical Galaxies', p. 235.

Cenarro, A. J., Cardiel, N., Gorgas, J., Peletier, R. F., Vazdekis, A. & Prada, F. (2001), 'Empirical calibration of the near-infrared Ca ii triplet - I. The stellar library and index definition', MNRAS.

Chandrasekhar, S. (1969), *Ellipsoidal figures of equilibrium*, The Silliman Foundation Lectures, New Haven: Yale University Press, 1969.

Clegg, R. E. S. (1992), *ISIS Astronomers' Guide. Version 1.0*, User Manual, La Palma: Isaac Newton Group, 1992, edited by Clegg, R.E.S.

Colless, M., Burstein, D., Davies, R. L., McMahan, R. K., Saglia, R. P. & Wegner, G. (1999), 'The peculiar motions of early-type galaxies in two distant regions - V. The Mg-sigma relation, age and metallicity', MNRAS **303**, 813–825.

Copin, Y. (2000), 'Dynamique des Galaxies de type Précoce: Observations 3D et Modélisations', *Ph.D. Thesis.*

Copin, Y. et al. (2001), 'Kinemetry: quantifying kinematic maps'.

Corsini, E. M., Pizzella, A. & Bertola, F. (2002), 'The orthogonal gaseous kinematical decoupling in the Sa spiral NGC 2855', A&A **382**, 488–494.

Cretton, N. & van den Bosch, F. C. (1999), 'Evidence for a Massive Black Hole in the S0 Galaxy NGC 4342', ApJ **514**, 704–724.

Cretton, N., de Zeeuw, P. T., van der Marel, R. P. & Rix, H. (1999), 'Axisymmetric Three-Integral Models for Galaxies', ApJS **124**, 383–401.

Davies, R. L., Efstathiou, G., Fall, S. M., Illingworth, G. & Schechter, P. L. (1983), 'The kinematic properties of faint elliptical galaxies', ApJ.

Davies, R. L., Kuntschner, H., Emsellem, E., Bacon, R., Bureau, M., Carollo, C. M., Copin, Y., Miller, B. W., Monnet, G., Peletier, R. F., Verolme, E. K. & de Zeeuw, P. T. (2001), 'Galaxy Mapping with the SAURON Integral-Field Spectrograph: The Star Formation History of NGC 4365', ApJ **548**, L33–LL36.

de Jong, R. S. & Davies, R. L. (1997), 'The Shapes and Ages of Elliptical Galaxies', MNRAS **285**, L1–LL4.

de Vaucouleurs, G. & Capaccioli, M. (1979), 'Luminosity distribution in galaxies. I - The elliptical galaxy NGC 3379 as a luminosity distribution standard', ApJS **40**, 699–731.

de Vaucouleurs, G., de Vaucouleurs, A., Corwin, H. G., Buta, R. J., Paturel, G. & Fouque, P. (1991), *Third Reference Catalogue of Bright Galaxies*, Volume 1-3, XII, 2069 pp. 7 figs.. Springer-Verlag Berlin Heidelberg New York.

de Zeeuw, P. T. (2000), 'Evidence for Massive Black Holes in Nearby Galactic Nuclei', *In ESO Conference on Black Holes in Binaries and Galactic Nuclei eds L. Kaper and E.P.J. van den Heuvel.*

de Zeeuw, P. T., Bureau, M., Emsellem, E., Bacon, R., Marcella Carollo, C., Copin, Y., Davies, R. L., Kuntschner, H., Miller, B. W., Monnet, G., Peletier, R. F. & Verolme, E. K. (2002), 'The SAURON project - II. Sample and early results', MNRAS **329**, 513–530.

de Zeeuw, T., Peletier, R. & Franx, M. (1986), 'Mass models with Staeckel potentials', MNRAS **221**, 1001–1022.

Diaz, A. I., Terlevich, E. & Terlevich, R. (1989), 'Near-IR features in late type stars - Their relation with stellar atmosphere parameters', MNRAS **239**, 325–345.

Donahue, M. & Voit, G. M. (1991), 'A photoionization model for the optical line emission from cooling flows', ApJ **381**, 361–372.

Dressler, A. (1980), 'Galaxy morphology in rich clusters - Implications for the formation and evolution of galaxies', ApJ **236**, 351–365.

Dressler, A. & Richstone, D. O. (1988), 'Stellar dynamics in the nuclei of M31 and M32 - Evidence for massive black holes?', ApJ **324**, 701–713.

Dressler, A., Schechter, P. L. & Rose, J. A. (1986), 'The mass of the isolated elliptical NGC 720 as determined from the dynamics of its companions', AJ **91**, 1058–1061.

Eggen, O. J., Lynden-Bell, D. & Sandage, A. R. (1962), 'Evidence from the motions of old stars that the Galaxy collapsed.', ApJ **136**, 748.

Ellis, R. S., Smail, I., Dressler, A., Couch, W. J., Oemler, A. J., Butcher, H. & Sharples, R. M. (1997), 'The Homogeneity of Spheroidal Populations in Distant Clusters', ApJ **483**, 582.

Emsellem, E. (1995), 'The Sombrero galaxy. I. Modelling the dust content.', A&A **303**, 673.

Emsellem, E., Bacon, R., Monnet, G. & Poulain, P. (1996), 'The Sombrero galaxy. II. Colours, kinematics and line strengths of the central region.', A&A **312**, 777–796.

Emsellem, E., Dejonghe, H. & Bacon, R. (1999), 'Dynamical models of NGC 3115', MNRAS **303**, 495–514.

Emsellem, E., Monnet, G. & Bacon, R. (1994*a*), 'The multi-gaussian expansion method: a tool for building realistic photometric and kinematical models of stellar systems I. The formalism', A&A.

Emsellem, E., Monnet, G., Bacon, R. & Nieto, J.-L. (1994*b*), 'The multi-gaussian expansion method: a tool for building realistic photometric and kinematical models of stellar systems II. Application to the central region of the Sombrero Galaxy (NGC 4594)', A&A.

Faber, S. M. (1973), 'Variations in Spectral-Energy Distributions and Absorption-Line Strengths among Elliptical Galaxies', ApJ **179**, 731–754.

Faber, S. M., Friel, E. D., Burstein, D. & Gaskell, C. M. (1985), 'Old stellar populations. II - an analysis of K-giant spectra', ApJS **57**, 711–741.

Faber, S. M., Tremaine, S., Ajhar, E. A., Byun, Y., Dressler, A., Gebhardt, K., Grillmair, C., Kormendy, J., Lauer, T. R. & Richstone, D. (1997), 'The Centers of Early-Type Galaxies with HST. IV. Central Parameter Relations.', AJ **114**, 1771.

Fosbury, R. A. E., Boksenberg, A., Snijders, M. A. J., Danziger, I. J., Disney, M. J., Goss, W. M., Penston, M. V., Wamsteker, W., Wellington, K. J. & Wilson, A. S. (1982), 'Very extended ionized gas in radio galaxies. I - A radio, optical and ultraviolet study of PKS 2158-380', MNRAS **201**, 991–1008.

Franx, M. (1988), 'The projection of galaxy models with a Staeckel potential', MNRAS **231**, 285–308.

Franx, M., Illingworth, G. & Heckman, T. (1989*a*), 'Major and minor axis kinematics of 22 ellipticals', ApJ.

Franx, M., Illingworth, G. & Heckman, T. (1989*b*), 'Multicolor surface photometry of 17 ellipticals', AJ.

Gebhardt, K., Richstone, D., Tremaine, S., Lauer, T. R., Bender, R., Bower, G., Dressler, A., Faber, S. M., Filippenko, A. V., Green, R., Grillmair, C., Ho, L. C., Kormendy, J., Magorrian, J. & Pinkney, J. (2002), 'Axisymmetric dynamical models of the central regions of galaxies', *astro-ph/0209483*.

Gerhard, O. E. (1993), 'Line-of-sight velocity profiles in spherical galaxies: breaking the degeneracy between anisotropy and mass.', MNRAS **265**, 213.

González, J. J. (1993), 'Line strength gradients and kinematic profiles in elliptical galaxies', *Ph.D. Thesis*.

Goudfrooij, P. & Emsellem, E. (1996), 'Ionized gas in early-type galaxies: its effect on Mgb and other stellar line-strength indices.', A&A **306**, L45.

Goudfrooij, P., Hansen, L., Jorgensen, H. E. & Norgaard-Nielsen, H. U. (1994), 'Interstellar matter in Shapley-Ames elliptical galaxies. II. The distribution of dust and ionized gas', A&AS **105**, 341–383.

Heckman, T. M., Baum, S. A., van Breugel, W. J. M. & McCarthy, P. (1989), 'Dynamical, physical, and chemical properties of emission-line nebulae in cooling flows', ApJ **338**, 48–77.

Henry, R. B. C. & Worthey, G. (1999), 'The Distribution of Heavy Elements in Spiral and Elliptical Galaxies', PASP **111**, 919–945.

Hernquist, L. (1993), 'Structure of merger remnants. II - Progenitors with rotating bulges', ApJ **409**, 548–562.

Heyl, J. S., Hernquist, L. & Spergel, D. N. (1994), 'Structure of merger remnants. 4: Isophotal shapes', ApJ **427**, 165–173.

Ho, L. C., Filippenko, A. V. & Sargent, W. L. W. (1993), 'A Reevaluation of the Excitation Mechanism of LINERs', ApJ **417**, 63+.

Hoffleit, D. & Jaschek, C. (1982), *The Bright Star Catalogue*, The Bright Star Catalogue, New Haven: Yale University Observatory (4th edition), 1982.

Hubble, E. & Humason, M. L. (1931), 'The Velocity-Distance Relation among Extra-Galactic Nebulae', ApJ **74**, 43+.

Hubble, E. P. (1936), 'Realm of the Nebulae', *Yale University Press.*

Idiart, T. P., Thevenin, F. & de Freitas Pacheco, J. A. (1997), 'The Infrared Ca II Triplet as a Metallicity Indicator of Stellar Populations', AJ **113**, 1066.

Illingworth, G. (1977), 'Rotation in 13 elliptical galaxies', ApJ **218**, L43–LL47.

Jones, L. A. (1998), 'Differential Spectral Synthesis of Low-Luminosity Elliptical Galaxies', *Ph.D. Thesis.*

Joseph, C. L., Merritt, D., Olling, R., Valluri, M., Bender, R., Bower, G., Danks, A., Gull, T., Hutchings, J., Kaiser, M. E., Maran, S., Weistrop, D., Woodgate, B., Malumuth, E., Nelson, C., Plait, P. & Lindler, D. (2001), 'The Nuclear Dynamics of M32. I. Data and Stellar Kinematics', ApJ **550**, 668–690.

Kim, D. (1989), 'Interstellar matter in early-type galaxies - Optical observations', ApJ **346**, 653–674.

Knapp, G. R., Guhathakurta, P., Kim, D. & Jura, M. A. (1989), 'Interstellar matter in early-type galaxies. I - IRAS flux densities', ApJS **70**, 329–387.

Knapp, G. R., Turner, E. L. & Cunniffe, P. E. (1985), 'The statistical distribution of the neutral-hydrogen content of elliptical galaxies', AJ **90**, 454–468.

Kodama, T. & Arimoto, N. (1997), 'Origin of the colour-magnitude relation of elliptical galaxies.', A&A **320**, 41–53.

Kodama, T., Arimoto, N., Barger, A. J. & Arag'on-Salamanca, A. (1998), 'Evolution of the colour-magnitude relation of early-type galaxies in distant clusters', A&A **334**, 99–109.

Kormendy, J. & Bender, R. (1996), 'A Proposed Revision of the Hubble Sequence for Elliptical Galaxies', ApJ **464**, L119+.

Kormendy, J. & Illingworth, G. (1982), 'Rotation of the bulge components of disk galaxies', ApJ **256**, 460–480.

Krajnovic, D. et al. (2003), 'Dynamical Modelling of NGC 2974', *in preperation.*

Krist, J. & Hook, R. (2001), 'The Tiny Tim User's Guide, Version 6.0'.

Kuijken, K. & Merrifield, M. R. (1993), 'A New Method for Obtaining Stellar Velocity Distributions from Absorption-Line Spectra - Unresolved Gaussian Decomposition', MNRAS **264**, 712.

Kuntschner, H. (2003), 'Photometry of Disky Ellipticals', *in preperation.*

Larson, R. B. (1975), 'Models for the formation of elliptical galaxies', MNRAS **173**, 671–699.

Larson, R. B., Tinsley, B. M. & Caldwell, C. N. (1980), 'The evolution of disk galaxies and the origin of S0 galaxies', ApJ **237**, 692–707.

Lauer, T. R., Ajhar, E. A., Byun, Y.-I., Dressler, A., Faber, S. M., Grillmair, C., Kormendy, J., Richstone, D. & Tremaine, S. (1995), 'The Centers of Early-Type Galaxies with HST.I.An Observational Survey', AJ **110**, 2622.

Lawson, C. L. & Hanson, R. J. (1974), *Solving least squares problems*, Prentice-Hall Series in Automatic Computation, Englewood Cliffs: Prentice-Hall, 1974.

Magorrian, J., Tremaine, S., Richstone, D., Bender, R., Bower, G., Dressler, A., Faber, S. M., Gebhardt, K., Green, R., Grillmair, C., Kormendy, J. & Lauer, T. (1998), 'The Demography of Massive Dark Objects in Galaxy Centers', AJ **115**, 2285–2305.

Merritt, D. (1997), 'Recovering Velocity Distributions Via Penalized Likelihood', AJ **114**, 228–237.

Merritt, D. & Ferrarese, L. (2001), 'The $M_\bullet$-σ Relation for Supermassive Black Holes', ApJ **547**, 140–145.

Michard, R. (1999), 'Colour distributions in E-S0 galaxies . IV. Colour data and dust in E's from Nieto's B, R frames', A&AS **137**, 245–268.

Monnet, G., Bacon, R. & Emsellem, E. (1992), 'Modelling the stellar intensity and radial velocity fields in triaxial galaxies by sums of Gaussian functions', A&A **253**, 366–373.

Moré, J. J., Garbow, B. S. & Hillstrom, K. E. (1980), User guide for MINPACK-1, Technical Report ANL-80-74.

Naab, T. & Burkert, A. (2001), 'The Formation of Disks in Elliptical Galaxies', ApJ **555**, L91–LL94.

Naab, T., Burkert, A. & Hernquist, L. (1999), 'On the Formation of Boxy and Disky Elliptical Galaxies', ApJ **523**, L133–LL136.

Nieto, J.-L., Capaccioli, M. & Held, E. V. (1988), 'More isotropic oblate rotators in elliptical galaxies', A&A **195**, L1–L4.

Ollongren, A. (1962), 'Three-dimensional galactic stellar orbits', Bull. Astron. Inst. Netherlands **16**, 241.

Osterbrock, D. E. (1989), *Astrophysics of gaseous nebulae and active galactic nuclei*, Research supported by the University of California, John Simon Guggenheim Memorial Foundation, University of Minnesota, et al. Mill Valley, CA, University Science Books, 1989, 422 p.

Pastoriza, M. G., Winge, C. ., Ferrari, F., Macchetto, F. D. & Caon, N. (2000), 'A Photometric and Kinematic Study of the Stars and Interstellar Medium in the Central 2 Kiloparsecs of NGC 3379', ApJ **529**, 866–874.

Peletier, R. F. & Valentijn, E. A. (1989), 'Stellar populations as a function of radius in giant elliptical galaxies', Ap&SS **156**, 127–131.

Peletier, R. F., Davies, R. L., Illingworth, G. D., Davis, L. E. & Cawson, M. (1990), 'CCD surface photometry of galaxies with dynamical data. II - UBR photometry of 39 elliptical galaxies', AJ **100**, 1091–1142.

Peletier, R. F., Vazdekis, A., Arribas, S., del Burgo, C., García-Lorenzo, B., Gutiérrez, C., Mediavilla, E. & Prada, F. (1999), 'Two-dimensional line-strength maps in three well-studied early-type galaxies', MNRAS **310**, 863–878.

Phillips, M. M., Jenkins, C. R., Dopita, M. A., Sadler, E. M. & Binette, L. (1986), 'Ionized gas in elliptical and S0 galaxies. I - A survey for H-alpha and forbidden N II emission', AJ **91**, 1062–1085.

Pignatelli, E., Corsini, E. M., Vega Beltrán, J. C., Scarlata, C., Pizzella, A., Funes, J. G., Zeilinger, W. W., Beckman, J. E. & Bertola, F. (2001), 'Modelling gaseous and stellar kinematics in the disc galaxies NGC 772, 3898 and 7782', MNRAS **323**, 188–210.

Pinkney, J. et al. (2002), *in prep.*

Press, W. H., Teukolsky, S. A., Vetterling, W. T. & Flannery, B. P. (1992), *Numerical recipes in FORTRAN. The art of scientific computing*, Cambridge: University Press, —c1992, 2nd ed.

Qian, E. E., de Zeeuw, P. T., van der Marel, R. P. & Hunter, C. (1995), 'Axisymmetric galaxy models with central black holes, with an application to M32', MNRAS **274**, 602–622.

Richstone, D., Bower, G. & Dressler, A. (1990), 'Constraints on the mass distribution near the centers of M31 and M32', ApJ **353**, 118–122.

Rix, H. & White, S. D. M. (1990), 'Disks in elliptical galaxies', ApJ **362**, 52–58.

Rix, H. & White, S. D. M. (1992), 'Optimal estimates of line-of-sight velocity distributions from absorption line spectra of galaxies - Nuclear discs in elliptical galaxies', MNRAS **254**, 389–403.

Rix, H., de Zeeuw, P. T., Cretton, N., van der Marel, R. P. & Carollo, C. M. (1997), 'Dynamical Modeling of Velocity Profiles: The Dark Halo around the Elliptical Galaxy NGC 2434', ApJ **488**, 702.

Rybicki, G. B. (1986), '', *in Structure and Dynamics of Elliptical Galaxies, ed. P.T. de Zeeuw (Dodrecht Reidel).*

Saglia, R. P., Maraston, C., Thomas, D., Bender, R. & Colless, M. (2002), 'The Puzzlingly Small Ca II Triplet Absorption in Elliptical Galaxies', ApJ **579**, L13–L16.

Saha, P. & Williams, T. B. (1994), 'Unfolding kinematics from galaxy spectra: A Bayesian method', AJ **107**, 1295–1302.

Salaris, M. & Weiss, A. (1998), 'Metal-rich globular clusters in the galactic disk: new age determinations and the relation to halo clusters', A&A **335**, 943–953.

Salasnich, B., Girardi, L., Weiss, A. & Chiosi, C. (2000), 'Evolutionary tracks and isochrones for alpha -enhanced stars', A&A **361**, 1023–1035.

Samet, H. (1984), 'The quadtree and related hierarchical data structures', *ACM Computing Surveys* **16**(2), 187–260.

Sandage, A. & Visvanathan, N. (1978), 'The color-absolute magnitude relation for E and S0 galaxies. II - New colors, magnitudes, and types for 405 galaxies', ApJ **223**, 707–729.

Sargent, W. L. W., Schechter, P. L., Boksenberg, A. & Shortridge, K. (1977), 'Velocity dispersions for 13 galaxies.', ApJ **212**, 326–334.

Schoenmakers, R. H. M., Franx, M. & de Zeeuw, P. T. (1997), 'Measuring non-axisymmetry in spiral galaxies', MNRAS **292**, 349.

Schwarzschild, M. (1979), 'A numerical model for a triaxial stellar system in dynamical equilibrium', ApJ **232**, 236–247.

Schweizer, F. . (1998), Observational Evidence for Interactions and Mergers, *in* 'Saas-Fee Advanced Course 26: Galaxies: Interactions and Induced Star Formation', p. 105.

Schweizer, F. & Seitzer, P. (1992), 'Correlations between UBV colors and fine structure in E and S0 galaxies - A first attempt at dating ancient merger events', AJ **104**, 1039–1067.

Schweizer, F., Seitzer, P., Faber, S. M., Burstein, D., Dalle Ore, C. M. & Gonzalez, J. J. (1990), 'Correlations between line strengths and fine structure in elliptical galaxies', ApJ **364**, L33–LL36.

Scorza, C. & Bender, R. (1990), 'A disk in the elliptical galaxy NGC 3610', A&A **235**, 49–54.

Scorza, C. & Bender, R. (1995), 'The internal structure of disky elliptical galaxies.', A&A **293**, 20–43.

Shields, J. C. (1991), 'Optical nebulosity in X-ray-selected, early type galaxies', AJ **102**, 1314–1334.

Simkin, S. M. (1974), 'Measurements of Velocity Dispersions and Doppler Shifts from Digitized Optical Spectra', A&A **31**, 129.

Smith, R. J., Lucey, J. R., Schlegel, D. J., Hudson, M. J., Baggley, G. & Davies, R. L. (2001), 'Streaming motions of galaxy clusters within 12,000 km s^{-1} - II. New photometric data for the Fundamental Plane', MNRAS **327**, 249–264.

Sparks, W. B., Macchetto, F. & Golombek, D. (1989), 'Imaging observations of gas and dust in NGC 4696 and implications for cooling flow models', ApJ **345**, 153–162.

Springel, V. (2000), 'Modelling star formation and feedback in simulations of interacting galaxies', MNRAS **312**, 859–879.

Stanford, S. A., Elston, R., Eisenhardt, P. R., Spinrad, H., Stern, D. & Dey, A. (1997), 'An IR-Selected Galaxy Cluster at z=1.27', AJ **114**, 2232.

Statler, T. S. & Smecker-Hane, T. (1999), 'The Stellar Kinematic Fields of NGC 3379', AJ **117**, 839–854.

Statler, T. S., Smecker-Hane, T. & Cecil, G. N. (1996), 'The Post-Merger Elliptical NGC 1700: Stellar Kinematic Fields to Four Effective Radii', AJ **111**, 1512.

Stiavelli, M., Londrillo, P. & Messina, A. (1991), 'Dissipationless collapse and the shape of isophotes', MNRAS **251**, 57P–59PP.

Tonry, J. & Davis, M. (1979), 'A survey of galaxy redshifts. I - Data reduction techniques', AJ **84**, 1511–1525.

Tonry, J. L., Dressler, A., Blakeslee, J. P., Ajhar, E. A., Fletcher, A. ., Luppino, G. A., Metzger, M. R. & Moore, C. B. (2001), 'The SBF Survey of Galaxy Distances. IV. SBF Magnitudes, Colors, and Distances', ApJ **546**, 681–693.

Toomre, A. (1977), 'Theories of spiral structure', ARA&A **15**, 437–478.

Trager, S. C. (1997), 'The Stellar Population Histories of Elliptical Galaxies', *Ph.D. Thesis.*

Trager, S. C., Faber, S. M., Worthey, G. & González, J. J. . (2000), 'The Stellar Population Histories of Early-Type Galaxies. II. Controlling Parameters of the Stellar Populations', AJ **120**, 165–188.

Tremaine, S., Gebhardt, K., Bender, R., Bower, G., Dressler, A., Faber, S. M., Filippenko, A. V., Green, R., Grillmair, C., Ho, L. C., Kormendy, J., Lauer, T. R., Magorrian, J., Pinkney, J. & Richstone, D. (2002), 'The Slope of the Black Hole Mass versus Velocity Dispersion Correlation', ApJ **574**, 740–753.

Valluri, M., Merritt, D. & Emsellem, E. (2002), 'Difficulties with recovering the masses of supermassive black holes from stellar kinematical data'.

van den Bosch, F. C. & Emsellem, E. (1998), 'Bar-driven evolution of S0s: the edge-on galaxy NGC 4570', MNRAS.

van den Bosch, F. C., Jaffe, W. & van der Marel, R. P. (1998), 'Nuclear stellar discs in early-type galaxies. I - HST and WHT observations', MNRAS.

van den Bosch, R. et al. (2003), 'Dynamical Modelling of NGC 4473', *in preperation.*

van der Marel, R. P. & Franx, M. (1993), 'A new method for the identification of non-Gaussian line profiles in elliptical galaxies', ApJ **407**, 525–539.

van der Marel, R. P., Cretton, N., de Zeeuw, P. T. & Rix, H. (1998), 'Improved Evidence for a Black Hole in M32 from HST/FOS Spectra. II. Axisymmetric Dynamical Models', ApJ **493**, 613.

van Houten, C. J. (1961), 'Surface photometry of extragalactic nebulae (Errata: 17 310)', Bull. Astron. Inst. Netherlands **16**, 1–+.

VandenBerg, D. A., Swenson, F. J., Rogers, F. J., Iglesias, C. A. & Alexander, D. R. (2000), 'Models for Old, Metal-poor Stars with Enhanced α-Element Abundances. I. Evolutionary Tracks and ZAHB Loci; Observational Constraints', ApJ **532**, 430–452.

Vazdekis, A. (1999), 'Evolutionary Stellar Population Synthesis at 2 Å Spectral Resolution', ApJ **513**, 224–241.

Vazdekis, A., Casuso, E., Peletier, R. F. & Beckman, J. E. (1996), 'A New Chemo-evolutionary Population Synthesis Model for Early-Type Galaxies. I. Theoretical Basis', ApJS **106**, 307+.

Vazdekis, A., Cenarro, A. J., Gorgas, J., Cardiel, N. & Peletier, R. F. (2003), 'Empirical calibration of the near-infrared CaII triplet - IV. The stellar population synthesis models', MNRAS **340**, 1317–1345.

Verolme, E. K., Cappellari, M., Copin, Y., van der Marel, R. P., Bacon, R., Bureau, M., Davies, R. L., Miller, B. M. & de Zeeuw, P. T. (2002), 'A SAURON study of M32: measuring the intrinsic flattening and the central black hole mass', MNRAS **335**, 517–525.

Wagner, S. J., Bender, R. & Dettmar, R.-J. (1989), 'Stellar kinematics of bulge, disk and nucleus in NGC 4594', A&A **215**, 243–252.

Weiss, A., Peletier, R. F. & Matteucci, F. (1995), 'Synthetic metal line indices for elliptical galaxies from super metal-rich {alpha}-enhanced stellar models.', A&A **296**, 73+.

Wiener, N. (1949), *Extrapolation, Interpolation and Smoothing of Stationary Time Series*, MIT Press, Cambridge, Mass. and Wiley, New York.

Wiklind, T. & Rydbeck, G. (1986), 'Detection of CO (J = 1-0) in the dwarf elliptical galaxy NGC 185', A&A **164**, L22–L24.

Worthey, G. (1992), 'The controlling parameters of the integrated flux of a stellar population', *Ph.D. Thesis.*

Worthey, G. (1994), 'Comprehensive stellar population models and the disentanglement of age and metallicity effects', ApJS **95**, 107–149.

Worthey, G., Faber, S. M. & Gonzalez, J. J. (1992), 'MG and Fe absorption features in elliptical galaxies', ApJ **398**, 69–73.

Ziegler, B. L. & Bender, R. (1997), 'The Mg(b)-sigma relation of elliptical galaxies at Z of about 0.37', MNRAS **291**, 527.